

Fast scintillating ZnO ceramics for relativistic heavy-ion beam diagnostics

Schnell szintillierende ZnO Keramiken zur Diagnostik von relativistischen Schwerionenstrahlen

Zur Erlangung des Grades eines Doktors der Naturwissenschaften (Dr. rer. nat.)

Genehmigte Dissertation von Maxim Saifulin aus Astana, Kasachstan

Tag der Einreichung: 02.10.2023, Tag der Prüfung: 11.12.2023

1. Gutachten: Prof. Dr. Christina Trautmann
 2. Gutachten: Prof. Dr. Ralph Krupke
- Darmstadt, Technische Universität Darmstadt



TECHNISCHE
UNIVERSITÄT
DARMSTADT

Materials and Earth
Sciences Department

Institute of Materials
Science

Ion-Beam Modified Materials

Fast scintillating ZnO ceramics for relativistic heavy-ion beam diagnostics
Schnell szintillierende ZnO Keramiken zur Diagnostik von relativistischen Schwerionenstrahlen

Accepted doctoral thesis by Maxim Saifulin

Date of submission: 02.10.2023

Date of thesis defense: 11.12.2023

Darmstadt, Technische Universität Darmstadt

Bitte zitieren Sie dieses Dokument als:

URN: urn:nbn:de:tuda-tuprints-265252

URL: <http://tuprints.ulb.tu-darmstadt.de/26525>

Jahr der Veröffentlichung auf TUprints: 2024

Dieses Dokument wird bereitgestellt von tuprints,
E-Publishing-Service der TU Darmstadt

<http://tuprints.ulb.tu-darmstadt.de>

tuprints@ulb.tu-darmstadt.de

Die Veröffentlichung steht unter folgender Creative Commons Lizenz:

Namensnennung – Weitergabe unter gleichen Bedingungen 4.0 International

<https://creativecommons.org/licenses/by-sa/4.0/>

This work is licensed under a Creative Commons License:

Attribution–ShareAlike 4.0 International

<https://creativecommons.org/licenses/by-sa/4.0/>

Erklärungen laut Promotionsordnung

§ 8 Abs. 1 lit. c PromO

Ich versichere hiermit, dass die elektronische Version meiner Dissertation mit der schriftlichen Version übereinstimmt.

§ 8 Abs. 1 lit. d PromO

Ich versichere hiermit, dass zu einem vorherigen Zeitpunkt noch keine Promotion versucht wurde. In diesem Fall sind nähere Angaben über Zeitpunkt, Hochschule, Dissertationsthema und Ergebnis dieses Versuchs mitzuteilen.

§ 9 Abs. 1 PromO

Ich versichere hiermit, dass die vorliegende Dissertation selbstständig und nur unter Verwendung der angegebenen Quellen verfasst wurde.

§ 9 Abs. 2 PromO

Die Arbeit hat bisher noch nicht zu Prüfungszwecken gedient.

Darmstadt, 02.10.2023

M. Saifulin

Abstract

This thesis focuses on the study of inorganic scintillating ceramics based on zinc oxide prepared by uni-axial hot pressing in vacuum and doped with different elements such as indium and gallium. The optical and luminescent properties of these samples were tested under heavy-ion irradiation. The investigations are motivated by the need to eventually replace plastic scintillators, which are currently standard for beam diagnostics in fast-counting scintillation detectors but suffer severely from radiation damage. ZnO-based ceramic scintillation detectors are expected to be radiation hard and as such particularly suitable for beam diagnostics at heavy-ion accelerator facilities for absolute beam intensity measurements and calibration of beam current measuring devices such as ionization chambers and secondary electron transmission monitors.

The ion irradiation experiments were performed at the universal linear accelerator UNILAC and at the heavy-ion synchrotron SIS18 of the GSI Helmholtz Center for Heavy Ion Research (Darmstadt, Germany). The ceramic samples were irradiated under various beam conditions, including ions between ^{40}Ar and ^{238}U ions, beam energies from 4.8 to 500 MeV/u, and fluences up to 10^{13} ions/cm². The light output and emission spectra of ion-induced luminescence were recorded in-situ during sample irradiation.

Under all beam conditions, the intensity of the luminescent light decreases with increasing ion fluence. The evolution of the light intensity as a function of fluence is described with the model suggested by Birks and Black, yielding the critical fluence of 50% intensity loss for the stopping powers of the respective ions. The ZnO-based ceramics show more than 100 times higher radiation hardness compared to standard plastic scintillators used in heavy-ion beam diagnostics. Non-irradiated In-doped and Ga-doped ZnO ceramics exhibit intense exciton-related near-band-edge emission combined with very low defect-related deep-level emission.

When exposed to heavy ions, the intensity of the near-band-edge emission decreases, but no new emission bands associated with radiation-induced defects are observed. In-situ optical light transmission measurements were performed in the wavelength range of 300 to 1000 nm. With increasing ion fluence, the spectra show a more and more pronounced reduction in transmission in the 390–600 nm range, while no change is observed at higher wavelengths. Important to note is that the ionoluminescence intensity decreases faster than the optical transmission. The kinetics of luminescent light emission was characterized using fast photomultiplier tube signals. Before ion exposure, both In-doped and Ga-doped ZnO ceramics exhibit ultrafast scintillation decay times of less than a nanosecond. No change in scintillation decay time is observed as a result of ion irradiation.

The second part of the thesis concentrated on the design and construction of a prototype ZnO(In) based scintillation detector. The performance of this prototype was tested with various 300 MeV/u ions (^{40}Ar – ^{238}U) including a variation of the beam spot position across the active area of the prototype detector. Compared to the plastic reference detector, the ZnO ceramic prototype showed 100% counting efficiency. Considering the radiation hardness results, the ceramic detector is expected to have an operational lifetime at least 100 times longer than the plastic scintillation detectors currently used for beam diagnostics at GSI. The new detector prototype represents a tool with significantly improved properties for heavy-ion beam diagnostics.

Zusammenfassung

Diese Dissertation befasst sich mit der Untersuchung von anorganischen keramischen Szintillatoren auf Basis von Zinkoxid, die durch einachsiges Heißpressen im Vakuum hergestellt und mit verschiedenen Elementen wie Indium und Gallium dotiert wurden. Die optischen und Lumineszenzeigenschaften dieser Proben wurden unter Schwerionenbestrahlung getestet. Die Untersuchungen sind durch die Notwendigkeit motiviert, Plastikszintillatoren zu ersetzen, welche derzeit standardmäßig in schnell zählenden Szintillationsdetektoren eingesetzt werden, aber stark unter Strahlungsschäden leiden. Es wird erwartet, dass keramische Szintillationsdetektoren auf ZnO-Basis strahlungsfest sind und sich daher besonders für die Strahldiagnostik an Schwerionenbeschleunigeranlagen für absolute Strahlintensitätsmessungen sowie die Kalibrierung von Strahlstrommessgeräten wie Ionisationskammern und Sekundärelektronentransmissionsmonitoren eignen.

Die Bestrahlungsexperimente wurden am universellen Linearbeschleuniger UNILAC und am Schwerionensynchrotron SIS18 des GSI Helmholtzzentrums für Schwerionenforschung (Darmstadt, Deutschland) durchgeführt. Die Proben wurden unter verschiedenen Strahlbedingungen bestrahlt, darunter Ionen zwischen ^{40}Ar und ^{238}U , Strahlenergien von 4,8 bis 500 MeV/u und Ionenfluenzen bis zu 10^{13} cm^{-2} . Die Lichtausbeute und ioneninduzierte Lumineszenzspektren wurden in-situ während der Probenbestrahlung aufgezeichnet.

Unter allen Bestrahlungsbedingungen nimmt die Lumineszenzintensität mit steigender Ionenfluenz ab. Der Intensitätsverlauf als Funktion der Fluenz wird gut durch das von Birks und Black vorgeschlagene Modell beschrieben und liefert kritische Fluenzwerte (50% Intensitätsverlust) für die Energieverluste der verschiedenen Ionen. Die auf ZnO basierten Keramiken weisen eine mehr als 100-mal höhere Strahlenresistenz auf als Standard-Szintillatoren aus Kunststoff. In-dotierte und Ga-dotierte ZnO-Keramiken zeigen eine intensive exzitonenbasierte Nahbandkantenemission zusammen mit einer sehr geringen sogenannten deep-level Emission, die auf Defekte zurückzuführen ist.

Bei der Bestrahlung mit schweren Ionen nimmt die Intensität der bandnahen Emission ab, es werden jedoch keine neuen Emissionsbänder beobachtet, die mit strahleninduzierten Defekten in Verbindung stehen. Messungen der optischen Lichtdurchlässigkeit wurden im Wellenlängenbereich von 300 bis 1000 nm durchgeführt. Mit zunehmender Ionenfluenz zeigen die Spektren eine immer ausgeprägtere Verringerung der Transmission im Bereich von 390 bis 600 nm, während bei höheren Wellenlängen keine Veränderung zu beobachten ist. Es wurde gezeigt, dass die Intensität der Ionenlumineszenz schneller abnimmt als die optische Transmission. Die Kinetik der Lumineszenzemission wurde an Hand der Signale einer schnellen Photomultiplier Röhre analysiert. Vor der Bestrahlung weisen sowohl In-dotierte als auch Ga-dotierte ZnO-Keramiken ultraschnelle Abklingzeiten von weniger als einer Nanosekunde auf, welche sich durch die Bestrahlung nicht ändert.

Der zweite Teil der Arbeit konzentrierte sich auf den Entwurf und die Konstruktion eines Szintillationsdetektor-Prototypen. Die Leistung dieses Prototyps wurde mit verschiedenen Ionen (^{40}Ar – ^{238}U) bei 300 MeV/u getestet, einschließlich einer Variation der Strahlfleckposition über den aktiven Bereich des Detektors. Bezogen auf den Kunststoffdetektor zeigte der ZnO-Keramik-Prototyp eine Zähleffizienz von 100%. In Anbetracht der Ergebnisse zur Strahlenresistenz ist davon auszugehen, dass der Keramikdetektor eine mindestens 100-mal

längere Lebensdauer als Szintillationsdetektoren aus Kunststoff haben wird und somit besser für die Diagnostik von Schwerionen geeignet ist.

Contents

Abstract	v
List of Figures	xi
List of Tables	xvii
List of Acronyms	xix
1 Introduction and Motivation	1
2 Theoretical Basis	7
2.1 Characteristics of heavy-ion interaction with matter	7
2.1.1 Nuclear and electronic stopping power	7
2.1.2 Radial distribution of energy deposited by electronic stopping	9
2.1.3 Formation of radiation damage due to electronic stopping	12
2.2 Characteristics of inorganic scintillators	13
2.2.1 Generation of electron-hole pairs	14
2.2.2 Excitation and emission of luminescent centers	15
2.2.3 Duration of scintillation pulse	17
2.3 Radiation hardness and damage accumulation models	17
2.4 Influence of radiation damage on scintillation properties	20
2.4.1 Scintillation light absorption by crystal defects	21
2.4.2 Undesirable luminescence and afterglow	21
2.4.3 Radiation-stimulated losses of scintillation efficiency	22
3 Review of Investigated Materials	23
3.1 General physical properties of ZnO	23
3.2 Luminescence and optical properties of ZnO	24
3.3 Uni-axial hot pressing in vacuum	26
3.4 Description of investigated ZnO samples	27
3.5 Other investigated materials	27
4 Experimental Characterization of Samples Irradiated with Heavy-Ion Beams	31
4.1 Irradiation details	31
4.1.1 Irradiation experiments at UNILAC	31
4.1.2 Irradiation experiments at SIS18	34
4.2 In-situ ionoluminescence and UV/Vis spectroscopy at the M3 beam line	37
4.3 Characterization with Raman spectroscopy	39
4.4 X-ray induced luminescence spectroscopy	40

4.5	UV/Vis transmission spectrometry	41
4.6	Ionoluminescence with relativistic heavy ions	42
4.6.1	In-situ ionoluminescence spectroscopy at HTP	43
4.6.2	Light output and scintillation decay times measurement at HTP	46
4.7	Beam intensity and irradiation fluence monitoring for experiments at SIS18	48
4.7.1	Beam intensity measurements with scintillation detector	49
4.7.2	Beam intensity measurements with ionization chamber	51
4.7.3	Beam intensity measurements with secondary electron transmission monitor	53
5	Samples Characterization Results and Discussion	55
5.1	In-situ ionoluminescence results under swift heavy ion irradiation	55
5.2	In-situ UV/Vis transmission results under swift heavy ion irradiation	57
5.3	X-ray induced luminescence of pre-irradiated ZnO(In) samples	60
5.4	Changes of total optical transmission under swift heavy ion irradiation	62
5.5	Raman spectroscopy characterization results	63
5.6	Ionoluminescence spectroscopy under relativistic heavy ion irradiation	65
5.7	Scintillation light output as a function of stopping power and fluence	67
5.8	Fitting the IL intensity change as a function of fluence	71
5.9	Fast-PMT signal rise and decay time characterization using relativistic ions	74
6	Development of ZnO-Based Scintillation Detector Prototype	77
6.1	Detector layout, description of the main parts and concepts of prototype	77
6.2	Modeling of light propagation in prototype detector using OpenGATE	77
6.2.1	Finding an optimal thickness and surface finishing of a radiation-hard light guide	79
6.2.2	Experimental characterization of a light diffusion by BK7G18 glass used as a light guide	83
6.2.3	Simulation of the transmission efficiency by BK7G18 glass at various source positions	85
6.3	Step-by-step description of the prototype detector assembly	87
7	Test of ZnO-Based Scintillation Detector Prototype	91
7.1	Experimental setup description	91
7.2	Prototype detector signal amplitude variation across the detector active area	92
7.3	Counting efficiency variation across detector active area	94
7.4	Counting efficiency at high counting rates	94
8	Summary and Outlook	97
8.1	Summary	97
8.2	Future prospective for improvement	98
8.3	Possible other applications	98
8.3.1	Beam diagnostics and accelerator physics applications	98
8.3.2	Applications in nuclear and high energy physics	99
8.3.3	Medical applications	99
	Bibliography	101
	Appendixes	111
	Curriculum Vitae	115
	Acknowledgements	117

List of Figures

1.1	Schematic view of the existing GSI accelerator facility (blue), the future FAIR complex (red), and experimental stations at FAIR (black) taken from [5].	2
1.2	Schematic view of a plastic scintillation counter used in particle detector combinations at GSI beam diagnostics. The incident heavy ions enter the active volume perpendicular to the image plane. Scintillation photons travel from the active volume through the light guide to the photosensor, experiencing multiple reflections. In the photomultiplier tube used as a photosensor, light photons that reach the photocathode are converted to photoelectrons. The number of electrons is multiplied by passing through the dynodes chain. The resulting electric signal is read out from the anode of the photomultiplier tube.	3
2.1	Stopping power of Ar and U ions as a function of their specific energy in ZnO (a) and as a function of penetration depth for 300 MeV/u (b). Both curves in (a) and (b) are simulated using SRIM2013 [37], assuming a ZnO density of 5.6 g/cm ³	9
2.2	Radial distribution of dose deposited by different ions into the electronic subsystem of ZnO according to Equation 2.3 for (a) UNILAC and (b) SIS18 ion beams.	11
2.3	General relaxation scheme of excited electronic states in an intrinsic scintillator from [67]. The scheme depicts the energy transfer processes after the excitation of electrons (red) and holes (blue) by an ionizing radiation. In the scheme, <i>e</i> — electron, <i>h</i> — hole, <i>ph</i> — phonon, <i>c</i> — electron capturing trap, <i>V_k</i> — self-trapped hole, <i>exc</i> — exciton (electron-hole pair), <i>hv</i> — scintillation photon.	14
3.1	Crystal systems that can be formed by ZnO (left to right) — cubic rocksalt, cubic zinc blende, and hexagonal wurtzite. The blue and red spheres correspond to zinc and oxygen, respectively.	23
3.2	ZnO photoluminescence spectrum measured at 4.2 K temperature with a HeCd laser excitation from [99]. Excitonic, donor acceptor pair (DAP) and deep level emission bands are visible. The corresponding phonon replica with longitudinal optical phonons (LO) are indicated.	25
4.1	UNILAC linear accelerator scheme, adapted from [130].	32
4.2	Schematic view of the M3 beam line at the UNILAC accelerator at GSI, adapted from [131].	33
4.3	Schematic view of the X0 beam line of the UNILAC accelerator at GSI.	33
4.4	SIS18 ring accelerator scheme with experimental areas available after extraction, adapted from [5]. The experiment of this work was performed at HTP.	35
4.5	Schematic view of the HTP target area provided with the beam from the SIS18 accelerator at GSI.	35

4.6	Schematic view of the experimental setup at the M3 beam line. For ionoluminescence measurements (a), the Faraday cup (FC) is removed from the beam path. The luminescence light spectrum is recorded with the spectrometer (SP). Transmission measurements (b) are performed by inserting the Faraday cup to block the ion beam. The transmission of light from a continuous light source (LS) is quantified by the same spectrometer (SP) used in measurement (a). The dashed line indicates the walls of the vacuum chamber. L1 and L2 are optical biconvex lenses and RS a remotely controllable shutter.	37
4.7	Photo of target holder used for ionoluminescence and transmission spectrometry at M3 beam line. CROMOX scintillating screen is attached to the front side of the holder, exposed to an ion beam. The investigated sample is mounted to the upper hole on the back side of the holder. The lower hole is used for reference light source spectrum measurements.	38
4.8	Photo of target holder and lenses placed inside the spectroscopy chamber at M3 beam line to perform ionoluminescence and transmission spectroscopy measurements. The ion beam enters the chamber from right to left.	39
4.9	Schematic representation of Raman spectrometer used for post-irradiation samples characterization, adapted from [133]. Two lasers are available: a solid state (473.05 nm) and He-Ne gas (632.82 nm) lasers. Measurements are performed in back-scattering geometry.	39
4.10	Schematic view of the X-ray induced luminescence spectrometer used for post-irradiation samples investigation.	40
4.11	Schematic view of the total transmission spectra measurement setup used to investigate samples after irradiation.	41
4.12	Photo of the upper part of the integrating sphere with the 2 mm diameter mask and sample placed with the irradiated surface down.	42
4.13	Photo of the experimental setup for ionoluminescence measurements under relativistic heavy ion beams. The black box is partially opened to see the insights. The yellow arrow shows the direction of the beam from SIS18 synchrotron. 1 — stainless-steel exit window, 2 — collimator, 3 — ionization chamber, 4 — photo-multipliers, 5 — video camera, 6 — target holder, 7 — spectrometers.	43
4.14	Photo of the target holder used in relativistic heavy ion irradiation experiments.	44
4.15	Schematic view of scintillation light spectrum measurement under relativistic heavy ion beam irradiation. The inset on top shows a photo of the Horiba CP 140-202 spectrograph attached to the PCO.1600 camera.	44
4.16	Calibration spectra recorded by spectrometer assemblies with “PCO SensiCam QE” (dashed blue line) and “PCO.1600” cameras (solid green line). Both first and second order diffraction lines of mercury emission are visible by “PCO SensiCam QE”. Only the first order lines are registered by “PCO.1600” due to its low sensitivity in the UV range.	45
4.17	An example of the PCO camera image containing an ionoluminescence light spectrum originating from the ZnO(Ga) ceramic. The color map represents the number of counts at each pixel position. The wavelength resolution is along the X–coordinate. The position resolution along the spectrometer slit is on Y–coordinate of the camera image.	46
4.18	Typical response signals of the Hamamatsu H7415 at different supply voltages (a) and Hamamatsu H13661 at +5 V supply and +2.2 V control voltage for different intensity of the laser light (b). The inset plots show the response signals zoomed in around the maximum amplitude. All signals from (a) and (b) are scaled by the maximum amplitude.	47
4.19	Gain of Hamamatsu H7415 slow photomultiplier assemblies placed on the front (a) and back (b) side of the target holder (identification numbers are LA4852 and LA4857, respectively). The dashed lines show the fit of the experimentally measured points.	48

4.20	Standard signal of plastic scintillation detector created by a single 300 MeV/u ^{74}Kr ion impact (a). Typical amplitude distribution of signal of plastic scintillation detector (b). PMT was operating at 1000 V supply voltage ($\sim 3 \times 10^5$ gain value).	49
4.21	True counting rates versus registered counting rate for scintillation detector (a). Blue and green lines show true vs. registered rate calculated according to the paralyzable model from Equation 4.1 for 25 and 50 ns dead time, respectively. The dashed line shows “ $y = x$ ” line. Figure (b) shows the increase in systematic error due to signals pile-up for counts registered by scintillation detector with 25 and 50 ns dead time, according to Equation 4.2.	51
4.22	Typical current to frequency convertor (IFC) calibration in three different operation ranges. . .	52
4.23	Correlation of ionization chamber output current and calibrated ion counts from secondary electron transmission monitor for 300 MeV/u ^{209}Bi ion beam. The black dashed line shows the linear dependency region. The red dashed line shows IC current upper limit around 5 μA at which IC counts linearity beaks down.	53
4.24	Schematic view of SEETRAM working principle (left) and a photo of the SEETRAM mounted in PDC used for experiments (right). The picture is taken from [138].	54
5.1	Ionoluminescence spectra of thermally-treated ZnO(In) scintillating ceramics. The irradiation was performed with 4.8 MeV/u ^{48}Ca (a) and ^{197}Au (b) ions under an angle of beam incidence of 45°	56
5.2	Evolution of the ionoluminescence peak position measured with increasing fluence for thermally-treated ZnO(In) scintillating ceramics. Irradiation was performed with 4.8 MeV/u ^{197}Au (open blue circles) and ^{48}Ca (open orange triangles) under an angle of beam incidence of 45° . The uncertainty is of position is ± 1 nm position.	56
5.3	Gaussian peaks fit of the ionoluminescence spectrum of thermally-treated ZnO(In) sample irradiated with 4.8 MeV/u ^{197}Au to 1.7×10^8 ions/cm 2 . The thick blue line represents the experimentally measured spectrum. The dashed yellow line is the fit by the sum of multiple Gaussian peaks. Thin color lines represent individual Gaussian peaks of the sum. The parameters of the peaks are listed in Table 5.1.	57
5.4	In-situ transmission spectra of thermally-treated ZnO(In) samples irradiated with swift heavy ions	58
5.5	Thermally-treated ZnO(In) ceramic at various fluences of 4.8 MeV/u ^{48}Ca ion irradiation at 45° beam incidence. Relative ionoluminescence intensity I_Φ/I_{init^*} (a) and relative optical transmission T_Φ/T_{init} (b) spectra. The initial IL spectrum corresponds to 6×10^9 Ca — ions/cm 2 fluence.	59
5.6	Thermally-treated ZnO(In) ceramic at various fluences of 4.8 MeV/u ^{197}Au ion irradiation at 45° beam incidence. Relative ionoluminescence intensity I_Φ/I_{init^*} (a) and relative optical transmission T_Φ/T_{init} (b) spectra. The initial IL spectrum corresponds to 2×10^8 Au — ions/cm 2 fluence.	59
5.7	Ionoluminescence (a) and light transmission (b) spectra of a plastic scintillator irradiated at various fluences with 4.8 MeV/u ^{48}Ca ions. The ion incidence angle with respect to the sample surface was 45°	60
5.8	X-ray induced luminescence spectra of initial (a) and thermally-treated (b) ZnO(In) ceramic scintillators irradiated at various fluences with 8.3 MeV/u ^{197}Au ions. The peak at 389 nm is assigned to near-band-edge emission (NBE).	61
5.9	Relative change of the X-ray induced luminescence NBE intensity (a) and shift of the NBE peak position (b) for initial and thermally-treated ZnO(In) ceramic samples irradiated at various fluences with 8.3 MeV/u ^{197}Au ions.	61

5.10	Total transmission spectra of initial (a) and thermally-treated (b) ZnO(In) ceramic scintillators irradiated at various fluences with 8.3 MeV/u ^{197}Au ions.	62
5.11	Wavelength of absorption edge cut-off as a function of fluence (a) and correlation of the cut-off wavelength vs. NBE luminescence peak position (b) for ZnO(In) ceramic scintillators irradiated at various fluences with 8.3 MeV/u ^{197}Au ions.	63
5.12	Raman spectra of pure ZnO single crystals and ceramic (a). Raman spectra of In- and Ga-doped ZnO ceramics (b).	64
5.13	Raman spectra of initial (a) and thermally-treated ZnO(In) (b) ceramics irradiated with 8.3 MeV/u Au ions of different fluences.	64
5.14	Ionoluminescence spectra of pristine ZnO samples prepared with different doping and with-/without thermal treatment. The luminescence is induced by 300 MeV/u ^{238}U ions.	66
5.15	Ionoluminescence spectra of initial ZnO(Ga) ceramic sample exposed to 250 MeV/u Ar and 300 MeV/u U ions, corresponding to various electronic stopping powers of 0.66 and 24.36 MeV/(mg cm ²), respectively.	66
5.16	3D representation of the evolution of the ionoluminescence spectra of thermally-treated ZnO(In) ceramic as a function of 300 MeV/u Bi ion fluence.	67
5.17	Comparison of ionoluminescence (a) and Raman spectra (b) for initial ZnO(Ga) irradiated with Bi at 300 MeV/u. The ionoluminescence of the pristine sample corresponds to 2.9×10^{10} Bi—ions/cm ²	67
5.18	Typical PMT signals (a) and anode charge of the PMT (b) recorded for pristine plastic scintillator and ZnO(In) exposed to 300 MeV/u Kr ions. The PMT gain is 3.6×10^5	68
5.19	Number of photoelectrons generated at PMT input as a result of various samples irradiation with relativistic heavy ions at different stopping power.	69
5.20	Number of photoelectrons generated at PMT input as a result of 300 MeV/u ^{209}Bi ion-induced luminescence in thermally-treated ZnO(In) sample at different fluence.	70
5.21	Relative IL intensity change measured by different methods as a result of 300 MeV/u ^{209}Bi ion-induced luminescence in thermally-treated ZnO(In) sample at different fluence. The dashed line corresponds to the Birks-Black model fit.	71
5.22	Number of photoelectrons generated at PMT input as a result of 300 MeV/u ^{238}U ion-induced luminescence in pristine ZnO(In) sample (blue) and pre-irradiated and annealed ZnO(In) sample (yellow).	71
5.23	Relative IL intensity as a function of fluence measured for thermally-treated ZnO(In) ceramic exposed to 4.8 MeV/u Ca and Au beams (a), and relative IL intensity and relative PMT N_{phe} values as a function of fluence measured for initial ZnO(Ga) sample (b). Dashed lines correspond to the simplified Birks-Black model fits (Equation 2.21).	72
5.24	The number of photoelectrons measured for the pristine thermally-treated ZnO(In) sample (blue) together with data of the same sample irradiated with 300 MeV/u Bi up to 9×10^{11} ions/cm ² (green). The dark gray and white bar plots correspond to the simulated N_{phe} distributions assuming Gaussian and homogeneous ion beams, respectively. The Gaussian beam is assumed to have $\sigma = 1.25$ mm, and both simulations assume $\Phi_{1/2} = 3.6 \times 10^{11}$ ions/cm ²	73
5.25	Critical fluence values extracted via Birks-Black model from experimental measurements of this work in comparison to previously reported critical fluences for BC400 plastic scintillator by Gardes <i>et al.</i> [146]. Dashed lines are used to guide the eye.	75

5.26	Fast PMT signals recorded for 300 MeV/u Bi ion irradiated ZnO(Ga) initial sample and reference plastic scintillator (a). The black dashed line corresponds to the fast PMT response obtained using 44 ps, 373 nm laser pulse excitation. In Figure (b), the orange dashed line corresponds to the convolution of the scintillation pulse shape approximated with Eq. 2.17 and the fast PMT response signal. All signals are scaled by the maximum signal amplitude.	76
6.1	Principal scheme of the multi-tile ZnO-based radiation-hard scintillation detector prototype. ZnO(In) tiles are on both sides of the glass, i.e., the BK7G18 glass is sandwiched between two layers of ZnO tiles.	78
6.2	Schematic (not in scale) representation of the scintillation light propagation through radiation-hard glass light guide. As a result of the ion impacts, N_{tot} scintillation photons are emitted from ZnO(In) surface. N_{in} photons enter the BK7G18 light guide, thus, defining the light guide collection efficiency as $\eta_c = N_{in}/N_{tot}$. As a result of multiple reflections inside the BK7G18, N_{out} photons exit the light guide further towards PMT, thus, defining the light guide transmission efficiency as $\eta_{tr} = N_{out}/N_{tot}$	79
6.3	Reflection types (a) and micro-facet tilt angle α (b) as simulated in OpenGATE using the UNIFIED model [33].	80
6.4	Simulated light collection efficiency of BK7G18 glass light guide as a function of surface roughness parameter σ_α	81
6.5	Transmission efficiency of the glass plate for different surface finishing (case (1) front and back surfaces are smooth, (2) front surface rough and back smooth, (3) front smooth and back rough, (4) front and back are rough) and different optical coupling from PMT side (air – blue bars, optical silicon – orange bars).	82
6.6	Simulated glass light guide transmission efficiency as a function of thickness and surface roughness σ_α . Different colors correspond to different transmission efficiency values η_{tr}	83
6.7	Schematic view of the setup used to characterize the BK7G18 light guide roughness with respect to the σ_α roughness parameter of the UNIFIED model.	84
6.8	The image of the laser beam spot observed on the screen, when no sample is inserted (a). Comparison of the measured laser spot projection with the one simulated using OpenGATE (b).	84
6.9	Image of laser beam spot observed on screen, when BK7G18 light guide is inserted (a). Comparison of the measured laser spot projection with the one simulated using OpenGATE (b). The best simulation versus experiment match is observed when $\sigma_\alpha = 20^\circ$	85
6.10	2D map of the transmission efficiency of scintillation detector prototype simulated for scintillation light occurring at different horizontal and vertical positions in the detector active volume. Thick black lines define the boundaries of the BK7G18 glass light guide, while dashed lines show the boundaries of the region covered by ZnO(In) tiles. The upper side of the color map corresponds to the glass light guide region that is coupled to PMT via optical silicon and plastic light guide.	86
6.11	Horizontal (a) and vertical (b) projection of the simulated transmission efficiency of the scintillation detector prototype along the x- and y-axes passing through the center of the detector active volume.	87
6.12	Detector components and prototype assembly from top to bottom.	89
7.1	Experimental layout used for in-beam tests of the prototype detector.	91
7.2	2D color map of the prototype detector performance tests under 300 MeV/u Au beam, showing the amplitude of the output signal(a). The signal amplitude plotted along horizontal and vertical axis across the active volume center (b). Color points correspond to experimental measurements, while dashed lines correspond to OpenGATE simulations.	92

7.3	Amplitude distributions of the prototype detector output signals recorded when a 300 MeV/u Pb beam hits different ZnO(In) tiles on the detector active area (a). Photo of the prototype detector active area taken after the in-beam tests, showing the upper row of ZnO(In) tiles contaminated with the optical silicon (b). The two peaks in the amplitude distribution of Tile-3 (left figure) are ascribed to a contamination with optical silicon.	93
7.4	Prototype detector output signal amplitude distribution, when 300 MeV/u Pb beam hits the edge of the prototype (see Figure 7.3b), covering three distinctive regions: 1 – beam passes only through the BK7G18 light guide, 2 – beam passes through BK7G18 light guide and ZnO(In) tile on one side, 3 – beam passes through BK7G18 light guide and ZnO(In) tiles on both front and back sides.	94
7.5	Counting efficiency of the prototype detector relative to the reference plastic scintillator measured for 300 MeV/u U ions.	95
7.6	Comparison of the counting rate of the prototype detector versus the current in the ionization chamber for 300 MeV/u Au ions.	95
A1.1	Ion-induced luminescence spectra of BK7G18 borosilicate glass exposed to 4.8 MeV/u Ca (a), Au (b), and 300 MeV/u Bi (c) ions at various fluences, and X-ray-induced luminescence spectra of pristine and ion-irradiated BK7G18 samples (d). X-ray-induced luminescence spectra (d) were measured one year after ion exposure.	112
A1.2	Relative intensity (a) and wavelength (b) changes of BK7G18 borosilicate glass ionoluminescence as a function of fluence of various heavy ions.	113
A1.3	X-ray-induced luminescence kinetics of BK7G18 glass (a) and typical photomultiplier signals due to a heavy-ion impact in BK7G18 in comparison to ZnO(In) scintillating ceramics (b). . .	113
A2.1	Optical transmission spectra of pristine and 4.8 MeV/u Au ion irradiated BK7G18 glass. . . .	114

List of Tables

1.1	Basic properties of some inorganic scintillators compared to the BC400 plastic *	4
3.1	Physical properties of hexagonal wurtzite zinc oxide [94, 96]	24
3.2	List of the samples characterized within this work	29
4.1	Irradiation parameters of the samples investigated at M3 and X0 beam lines	34
4.2	Irradiation parameters of the samples investigated at the HTP experimental cave (measurements at normal beam incidence)	36
5.1	Parameters of Gaussian peaks found in thermal-treated ZnO(In) sample irradiated with 4.8 MeV/u Au at 1.7×10^8 fluence. Within the experimental errors, 98% of the measured spectral data points match the fit curve (R^2 of the fit is 0.9998)	57
5.2	Critical fluence values extracted from characterization experiments of this work	74
5.3	Scintillation decay times extracted from the experiments using fast PMT characterization	76

List of Acronyms

ATIMA ATomic Interaction with MAtter, computer code.

BE Bound exciton.

CCD Charge-coupled device.

DAP Donor-acceptor pair.

DL Deep level emission.

FAIR Facility for Antiproton and Ion Research.

FC Faraday cup.

HEST Hochenergie Strahlführung, heigh energy beam transfer lines at GSI facility.

i-TS Inelastic Thermal Spike model.

IC Ionization chamber.

IFC Current to frequency converter.

IL Ion-induced luminescence, or ionoluminescence.

LO Longitudinal optical phonon.

NBE Near-band-edge emission.

PDC Particle detectors combination.

PETG Polyethylene terephthalate glycol.

PMT Photomultiplier tube.

SEETRAM Secondary electron transmission monitor.

SIS100 Schwerionensynchrotron, ring accelerator with maximum magnetic rigidity of particles of 100 T m, that belongs to FAIR facility.

SIS18 Schwerionensynchrotron, ring accelerator with maximum magnetic rigidity of particles of 18 T m that belongs to GSI facility.

SRIM Stopping and Range of Ions in Matter, computer code.

STE Self-trapped exciton.

STH Self-trapped hole.

TEM Transmission Electron Microscopy.

TO Transversal optical phonon.

UV Ultraviolet, the form of electromagnetic radiation with the wavelength shorter than the visible light.

UV/Vis Ultraviolet–Visible, spectral range that covers ultraviolet and visible part of the electromagnetic spectrum.

XRL X-ray-induced luminescence.

1 Introduction and Motivation

Materials that exhibit light emission when exposed to ionizing radiation are called scintillators. Since the beginning of the last century, scintillators have become an indispensable material for detecting ionizing radiation, which is not visible to the human eye. Light-emitting materials are the basis of scintillation counters — devices that count light flashes produced by individual ionizing particles.

The first device that provided counts of individual ionizing particles was built in 1903 by Crookes, using a ZnS scintillating screen [1]. The light flashes produced on the screen were visible in a darkened room with the help of optical instruments or by the naked eye. This technique led to a number of important discoveries. In 1911, Rutherford used it to count the scattered alpha-particles in his historic alpha-scattering experiment [2]. Scintillators gained additional attention in 1944 when Curran and Baker replaced the naked eye measurement with the newly developed photomultiplier tube (PMT) [3]. Since then, a similar concept has been preserved in modern scintillation detectors, where scintillation material serves as an active volume converting ionizing radiation into light flash.

Scintillator materials vary widely and can be categorized into two main types: organic and inorganic scintillators. Organic scintillators typically consist of organic compounds (usually a polymer) containing hydrogen, carbon, and other elements. The scintillation mechanism in organic scintillators is due to the transition of electrons between molecular orbitals. Organic scintillators have fast scintillation decay times in the order of few nanoseconds. Inorganic scintillators, on the other hand, are composed of crystalline or non-crystalline solid materials, often doped with specific elements to enhance their scintillation properties. The scintillation process in inorganic materials is due to the electronic band structure found in crystals and is not molecular in nature as is the case with organic scintillators. Inorganic scintillators usually have decay times longer than organic scintillators. However, inorganic scintillators exhibit higher light output and are more tolerant to radiation-induced damage.

Due to the large variety of materials with different scintillating properties providing high efficiency in detecting different types of ionizing radiation, scintillators have found applications in many fields. They are of interest in national security applications, monitoring gamma- and neutron-radiation from nuclear materials. They are also used in X-ray scanners for security checks, medical imaging and in geoscience for the exploration of mineral deposits. They are used in medicine for gamma-ray detection in positron emission tomography (PET) and mammography (PEM), or single positron emission tomography (SPECT) techniques for early detection of diseases such as cancer, Alzheimer's, and heart disease. Finally, scintillators are used for numerous basic research; examples include detectors at various accelerator facilities around the world aimed at elementary particles and nuclear structure research, as well as fundamental studies of matter in extreme conditions.

This thesis focuses on the application of scintillators used in scintillation counters for beam diagnostics at particle accelerator facilities. For example, in the future FAIR accelerator facility (*Facility for Antiproton and Ion Research*), scintillators will be used for heavy-ion beam intensity monitoring [4]. The layout of the FAIR with the existing GSI facility is schematically shown in Figure 1.1.

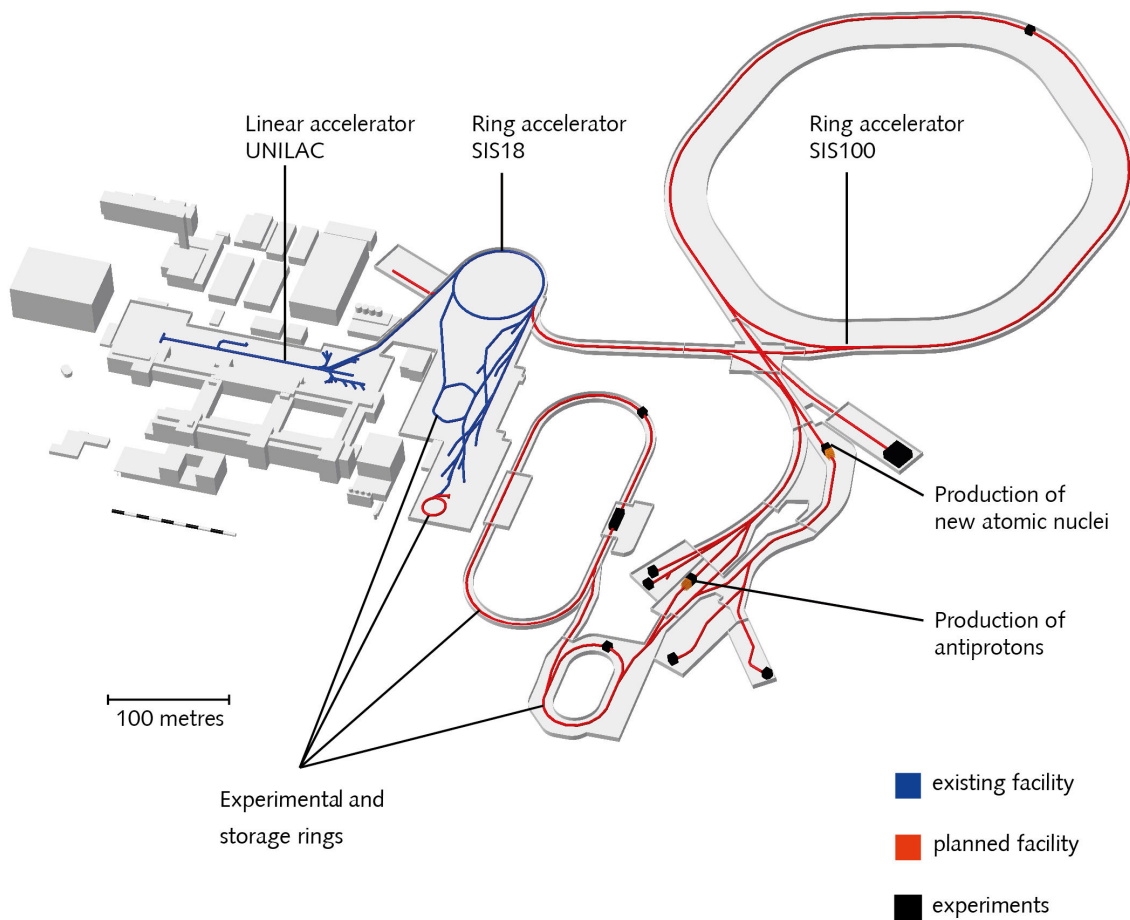


Figure 1.1: Schematic view of the existing GSI accelerator facility (blue), the future FAIR complex (red), and experimental stations at FAIR (black) taken from [5].

Heavy-ion beams from proton to uranium are accelerated by the Universal Linear ACcelerator (UNILAC) up to energies of 3.6–11.4 MeV/u, and distributed to numerous experimental stations. UNILAC beams are also injected into the heavy-ion synchrotron SIS18, where the beam energy is further increased. The maximum beam energy that can be gained by the SIS18 is limited by the charge state of the accelerated ion and the maximum magnetic rigidity of 18 T m. Therefore, depending on ion species, the maximum ion energy produced by the SIS18 ranges from 4.5 GeV for protons to 1 GeV/u for uranium. Beams from the SIS18 synchrotron are delivered to different experimental stations via high-energy beam transfer lines (referred to as HEST for Hochenergie Stahlführung).

Scintillation counters are routinely used as a part of Particle Detector Combinations (PDC) at HEST for measuring the absolute beam intensity and calibrating ionization chambers and secondary electron monitors located at different points along beam lines [6]. Beam intensity measurements along the HEST allow for optimizing the beam transmission from the accelerator to the final experimental stations. Also, scintillation counters are useful for characterizing the time structure of slowly extracted spills from the SIS18 accelerator. The information about the time structure of the spill helps to improve the parameters of the SIS18 beam extraction and provides a more in-depth understanding of the physics that occurs during the acceleration process.

With respect to beam diagnostics, scintillation counters are going to be used as a part of PDC assemblies located along the beam transfer/injection channel from the SIS18 to the SIS100 synchrotron, as well as standard PDCs located at the high-energy beam transfer lines to the experiments after the SIS100 extraction.

It is important to note that, due to the high beam energies provided by the SIS18 and SIS100 accelerators, the ion beams have large ranges and completely pass through the diagnostic devices without being stopped. In the case of the scintillator detectors discussed in this thesis, the energy loss per unit length along the active volume of the detector can be considered constant.

The currently used plastic scintillation counters in the beam diagnostics PDCs at GSI consist of three main components: detector active volume, light guide, and photosensor (see Figure 1.2).

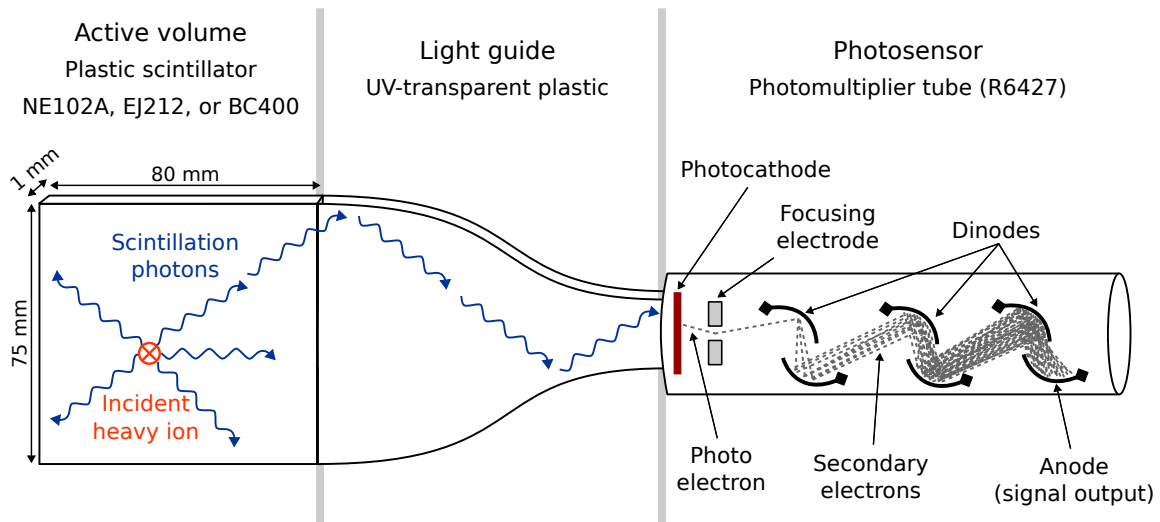


Figure 1.2: Schematic view of a plastic scintillation counter used in particle detector combinations at GSI beam diagnostics. The incident heavy ions enter the active volume perpendicular to the image plane. Scintillation photons travel from the active volume through the light guide to the photosensor, experiencing multiple reflections. In the photomultiplier tube used as a photosensor, light photons that reach the photocathode are converted to photoelectrons. The number of electrons is multiplied by passing through the dynodes chain. The resulting electric signal is read out from the anode of the photomultiplier tube.

The active volume of the detector is a 75 mm × 80 mm × 1 mm plate, that is made of NE102A, EJ212 (Eljen Technology), or BC400 (Saint Gobain) plastic scintillator. These plastics are well-known fast scintillators, that emit scintillation light with a maximum intensity at around 423 nm wavelength and have typical decay times of about 2.4 ns.

The detector's active volume is followed by the ultraviolet UV light transparent plastic light guide glued to the active volume from the side that is not exposed to the ion beam. It collects the scintillation light from the active volume and efficiently transports it to the photosensor. The photomultiplier tube, e.g., Hamamatsu R6427, is typically used as the photosensor for PDC scintillation detectors at GSI. It converts scintillation light flashes into electrical signals corresponding to individual ions passing through the detector's active volume. The PMT has a round-shaped alkali photocathode of 25 mm diameter. The PMT entrance window is made of borosilicate glass. The typical PMTs used for PDC scintillation detectors have a dynode chain that results in a gain of 5×10^6 at 1500 V supply voltage. They exhibit a signal raise time of 1.7 ns, fall time of 4.5 ns, and

signal width at half maximum of 2 ns. As a result, such plastic scintillation counters are capable of detecting a wide range of particles from protons to uranium, providing high amplitude signals above 100 mV with a pulse width below 20 ns. This ensures high counting efficiency up to beam intensities of 10^6 ions/s.

The weak point of the plastic scintillation counters is their limited radiation hardness. Due to radiation damage, scintillation counter signals become distorted, and signal amplitude goes down, leading to inaccurate particle counting. The damaged plastic scintillators have to be replaced frequently, disrupting beam and causing other operation inconveniences. With this work, we aim to identify and characterize more radiation-hard scintillator alternatives that can substitute plastic scintillators. This will enable longer operation times for scintillation detectors in beam diagnostics and avoidance of particle miscounting due to radiation damage not only at the GSI/FAIR facility, but also at numerous heavy-ion accelerator facilities worldwide.

Inorganic scintillators in various forms (single crystals, ceramics, thin deposited layers, or powders) are known to be, in general, more resistant to ionizing radiation than plastic scintillators. They have been widely used in high-energy and nuclear physics experiments, medical instruments, and homeland security applications. Manufacturing of nanosecond- and sub-nanosecond-fast high-quality inorganic scintillators is a hot topic in the scintillating materials community.

To date, there is a rather limited selection of inorganic scintillators, exhibiting nanosecond or shorter decay times, that could be used for fast scintillation counter. Regarding the application in fast counting of heavy ions, investigations of $\text{Gd}_2\text{SiO}_5(\text{Ce})$, $\text{YAlO}_3(\text{Ce})$, CsI, BaF_2 , $\text{ZnO}(\text{In})$, $\text{ZnO}(\text{Ga})$ have been reported previously [7–10]. Some basic properties of the above-mentioned inorganic scintillators are summarized in Table 1.1. It is important to note that properties of scintillators can vary depending on numerous factors, including crystal structure, purity, and measurement method, so it is not uncommon to find some variation in the presented values.

Table 1.1: Basic properties of some inorganic scintillators compared to the BC400 plastic *

	BC400	BaF_2	CsI	Gd_2SiO_5	YAlO_3	ZnO
Density (g/cm³)	1.03	4.88	4.51	6.71	5.37	5.6
Melting point (°C)	70 #	1280	621	1950	1875	1975
Emission peak^a (nm)	423	310 220	450 310, 340	430	370	550 390
Light yield^{a,b} (photons/MeV)	11200	9500 1400	varies 2000	9000	18000	varies 14700
Refractive index^{a,b}	1.58	1.5	1.8 1.68	1.85	1.95	2.1 2.3
Decay time^a (ns)	2.4	650 0.9	\gtrsim 1000 6, 30	400 (10 %) 56 (90 %)	27	\gtrsim 1000 0.7

* The values in this table may vary depending on crystal structure, purity, and measurement conditions

Softening point

^a Top line: slow component, bottom line: fast component

^b At the maximum emission wavelength

This work focuses on zinc oxide as a promising alternative to plastic scintillators. ZnO exhibits high scintillation light output with an ultra-fast decay time (< 1 ns) at room temperature. This means that within a very short time, it produces numerous photons per unit of energy deposited in the scintillator and makes particle detection

to be fast and easy. Finally, as an inorganic scintillator, ZnO is expected to exhibit a higher radiation hardness compared to plastic scintillators.

ZnO has attracted scientific interest as a promising fast scintillating material for ionizing particle detector application already since the 1960s [11, 12]. In the various forms of ZnO, two luminescence bands can be observed [13]. The first band is characterized by an ultra-fast luminescence with a decay time below one nanosecond. It is a short-wavelength band of exciton nature and situated close to the material absorption edge (so-called near-band-edge emission, NBE). The second band is due to slow photon emission with a decay time in the order of microseconds. The band is rather broad and comes from native defects present in the material. Its maximum intensity is around the green light spectral region (frequently referred to in literature as deep-level emission, DL). Impurities such as In, Ga, and Al can significantly enhance NBE and suppress the DL component, allowing ZnO to provide the fastest luminescence response speed of any known inorganic scintillator [9, 14–20].

There have been several attempts to use ZnO in the form of powders, nanostructures, thin layers, single-crystals, and ceramics to build X-ray, neutron, proton, and alpha-particle detectors for medical, industrial and scientific purposes [14, 21–25]. Despite the interest in ZnO for radiation detector application, there is limited information on ZnO radiation hardness. This is because the dominant part of applications, driving the scintillating materials development, deals with low ionizing radiation that induces negligible radiation damage in ZnO. In contrast to these, ZnO application at heavy-ion accelerator facilities is a special case, where information about radiation hardness becomes especially important.

High radiation resistance of ZnO has been reported previously for single- and poly-crystals, nanostructures, and NiO/ZnO hetero-junctions irradiated with protons and heavy ions [26–32]. These studies mainly focused on electric, structural, and optical properties for electronics and solar cell applications in space. Regarding the light emission properties, one can note the work by Koike *et al.*, where room temperature photoluminescence of ZnO thin films and bulk single-crystals was studied as a function of 8 MeV proton fluence [26]. The photoluminescence intensity remained nearly unchanged and deterioration starts only from 2×10^{12} protons/cm² for ZnO bulk crystal, and 5×10^{14} protons/cm² for thin film samples. The NBE emission was predominantly observed without evolving DL emission. In the work of Pal *et al.* [28], the formation of a new sub-bandgap absorption band around 407 nm was observed for ZnO single crystals irradiated with 700 keV ¹⁶O at 3×10^{15} ions/cm² fluence. This absorption band was associated with neutral oxygen vacancies and was responsible for the red-brown coloration of the irradiated crystal.

Further investigations are needed to understand in more detail the change in optical and luminescence properties of ZnO exposed to high radiation doses. Comprehensive characterization of ZnO-based materials exposed to energetic heavy-ion beams is performed as a part of R&D, aimed at the design and construction of new radiation-hard fast scintillation counters. The new detector development requires investigation of ZnO-based scintillators response (i.e., light output, scintillation pulse rise and decay times, emitted and absorbed light spectra, and effects of the accumulated radiation damage) at various deposited energies that are due to different ion species with different energies.

This thesis focuses on investigations of In-doped and Ga-doped ZnO transparent scintillating ceramics made by uni-axial hot pressing in vacuum. These ceramics are of potential interest for substituting plastic scintillators in fast scintillation counters used for heavy-ion beam diagnostics. Due to the lack of literature data on ZnO-based ceramic scintillators' performance under swift and relativistic heavy-ion exposure, comprehensive samples characterization is required before building a detector prototype.

For GSI, the ion energy range of main interest for ZnO ceramics characterization is located around 300 MeV/u and higher. This corresponds to SIS18 energies at which plastic scintillation detectors used at experimental

beam lines for beam diagnostics purposes face the highest rates of radiation damage. In particular, we investigate how much longer ZnO-based ceramics preserve their scintillating properties and stay in operational conditions compared to plastic scintillators for this ion energy region. Therefore, the experiments were performed with Pb, Bi, and U ions of at 300 MeV/u energy. Characterizations using these ion species represent realistic radiation hardness tests of ZnO ceramics for the future scintillation detector application in the most challenging radiation conditions.

However, reaching high radiation damage in ZnO samples at SIS18 experiments requires long ion exposure times above a day, which is hard to afford for a detailed study. Therefore, additional high radiation damage exposures were performed using swift heavy ions at experimental stations of the UNILAC linear accelerator at GSI. Here, complementary data on high radiation damage to ZnO samples was obtained within a shorter beam time because of the higher energy deposition at lower ion velocities (close to the Bragg maximum) ^{48}Ca and ^{197}Au ions at 4.8 and 8.3 MeV/u energies. Given by the broad variety of beam parameters allowed us to collect a unique data set on ion and X-ray-induced luminescence, light transmission, and Raman spectroscopy. These data served as solid evidence that ZnO ceramics can be used for fast scintillation detector applications, and also served as important input when designing the scintillation detector prototype based on ZnO ceramics.

As the ultra-fast scintillation component in ZnO is known to be emitted close to the self-absorption edge of the material, ZnO ceramic could not serve as a light guide to transport scintillation light directly to a photo-sensor. The scintillation light can escape from the ZnO ceramic only from a thin near-surface region where a charged particle enters and exits the scintillator, while the light generated in the bulk of the ceramic is self-absorbed. Therefore, a dedicated system of light guides consisting of borosilicate radiation hard glass that is inserted into the beam together with the scintillator, and a plastic light guide, coupled to a photo-multiplier tube, has been designed. The performance of the radiation hard glass light guide in terms of propagation of optical photons was modeled and optimized using the OpenGATE simulation tool based on Geant4 [33].

The second challenge in designing the detector was to develop a detector that has a sufficiently large detecting area to cover large beam spots. This requirement was satisfied by stacking 3×3 arrays of $15 \text{ mm} \times 15 \text{ mm}$ ZnO(In) scintillator tiles on the front and back side of the borosilicate glass light guide. Thus, a prototype scintillation detector with an active area of $45 \text{ mm} \times 45 \text{ mm}$ was assembled. Its performance was tested with Ar, Au, Bi, and U ions at 300 MeV/u energy and compared to a plastic scintillation detector commonly used at high-energy beam transfer lines at GSI.

After this introduction, the thesis presents the following chapters:

- Chapter 2 introduces basic theoretical concepts of investigated phenomena and applied characterization methods;
- Chapter 3 summarizes information about the investigated materials and samples preparations;
- Chapter 4 describes experimental setups and specific devices used for sample characterization before and after ion irradiation;
- Chapter 5 presents and discusses the results obtained during materials characterization;
- Chapter 6 describes different stages of the design of the prototype detector based on the ZnO(In) ceramic scintillator;
- Chapter 7 summarizes the results of the prototype detector performance test;
- Chapter 8 provides the summary of the work, conclusions, and further outlook.

2 Theoretical Basis

This chapter provides general information about the interaction between ions and matter, as well as the phenomenon of scintillation, based on existing literature. The chapter includes an overview of how energy is transferred from ions to solid matter, common types of radiation damage, and how radiation damage is formed. Additionally, the chapter includes basic definitions and essential information on how radiation damage can affect scintillation properties.

2.1 Characteristics of heavy-ion interaction with matter

2.1.1 Nuclear and electronic stopping power

When a heavy ion travels through a solid, it is involved in various Coulomb-force-driven interactions with the solid material. The Coulomb interactions are represented by: (i) attraction forces between projectile ions and electrons of the target, and (ii) repulsion forces between projectile ions and atomic nuclei of the target. The projectile ion can also change its charge state while passing through the material. Depending on the projectile ion velocity and its charge state before entering the target, electrons that belong to the projectile ion can be stripped by the target (increasing the positive ion charge), or, the other way around, electrons that belong to the target material can be captured by the projectile ion (reducing the positive ion charge). As a result of these interactions, the projectile ion loses part of its kinetic energy and excites the target material.

The amount of the kinetic energy lost by the projectile ion in the target is referred to as *energy loss*. It is represented by the parameter dE , and expressed in units of keV or MeV. It describes the reduction of the projectile ion energy, and, therefore, it always takes negative value.

In some applications, the energy loss per unit path length of the projectile, dE/dx , is used to describe the ion stopping. Therefore, it is expressed in units of keV/nm. In the case, when the material thickness is normalized by its density, dE/dx is expressed in units of MeV/(mg/cm²).

The interconnected parameter that is opposite to the energy loss per unit path length is *stopping power*. It is given as $S = -dE/dx$ and represents a measure of how effectively a material stops a charged particle as it passes through. In other words, stopping power represents the rate at which a charged particle transfers its energy to the target material as it moves through. The stopping power is an essential parameter for determining the response of a specific material to the ion beam.

The character of the Coulomb-force-driven interactions between the projectile and target depends on the *specific energy* of the projectile, E_i (which is expressed as the projectile kinetic energy per number of nucleons of the projectile, MeV/u). Depending on the specific energy, two stopping power terms are distinguished for an ion passing through matter:

- **Nuclear stopping power** (S_n) is dominating for low-energy ions ($E_i < 0.1$ MeV/u). In this case, the incident ions mainly scatter elastically at the nuclei of the target atoms. Due to the ion-nucleus collisions, some target atoms can be knocked out from their original positions. The nuclear stopping power can be calculated if one knows the form of the repulsive potential energy between the incident ion and the target atoms. Typically, it is represented by the Coulomb repulsion force with a certain screening function, which takes into account that at greater distances, the electron clouds screen the target nuclei from the projectile ion. The damage to the material along the low-energy ion path is mainly characterized by the formation of vacancies and interstitial atoms, but also leads to amorphization at high fluences.
- **Electronic stopping** (S_e) is dominating for high-energy ions ($E_i > 0.1$ MeV/u). In this case, the energy from the projectile ion is mainly transferred to the electrons of the target atoms. The damage processes due to electronic stopping are far more complex than for the nuclear stopping and remain an open topic for scientific discussions also nowadays.

The electronic stopping power at high projectile ion energies can be approximated by the Bethe–Bloch formula [34]:

$$\left\langle -\frac{dE}{dx} \right\rangle = K z^2 \frac{Z}{A} \frac{1}{\beta^2} \left[\frac{1}{2} \ln \frac{2m_e c^2 \beta^2 \gamma^2 W_{max}}{I^2} - \beta^2 - \frac{\delta(\beta\gamma)}{2} \right], \quad (2.1)$$

where $K = 4\pi N_A r_e^2 m_e c^2$ is a constant coefficient, z is the charge of the incident particle, Z is the atomic number of the target material, A is the atomic mass of the target, $\beta = v/c$ is the projectile velocity (v) relative to the speed of light (c), m_e is the electron rest mass, $\gamma = 1/\sqrt{1 - \beta^2}$ is the Lorentz factor, W_{max} is the maximum energy that can be transferred from projectile to the target electron, $\delta(\beta\gamma)$ is a density effect correction, and I is the average excitation and ionization potential of the target material. Normally, the I value is an experimentally determined parameter for each element. However, it can also be roughly estimated in electron volts as, $I = 13.5 \times Z$, [35].

It should be noted that at relativistic energies the Bethe-Bloch formula assumes fully stripped ions, thus the incident ion charge equals to the nuclear charge. At lower energies where $\beta \ll 1$, the electrons, remaining bound to the ion, screen part of the nuclear charge, thus, leading to lower energy losses. The so-called effective charge, z_{eff} , is used in this case instead of the nuclear charge. The Barkas formula provides the relevant effective charge as [36]:

$$z_{eff} = z \left(1 - \exp(-125\beta z^{-\frac{2}{3}}) \right). \quad (2.2)$$

Figure 2.1a shows the stopping power as a function of kinetic energy for Ar and U ions in ZnO. The two regimes of nuclear and electronic stopping are marked with dashed and solid lines, respectively. Depending on the charge of the projectile, the maximum of the electronic energy loss is located around 1–5 MeV/u. The stopping power varies depending on the projectile-target combination and can be calculated for any setting using various simulation programs or taken from the tables (e.g., The Stopping and Range of Ions in Matter (SRIM) [37], or ATOMIC Interaction with MATter (ATIMA) [38].) A more detailed overview of various tables and computer programs providing the stopping power values for positive ions in matter can be found in [39].

When the stopping power is plotted as a function of the penetration depth of the projectile inside the target, the so-called Bragg curve is obtained. Figure 2.1b shows the Bragg curves of ^{40}Ar and ^{238}U ions with the incident kinetic energy of 300 MeV/u in ZnO. The stopping power is rather constant at the beginning of the projectile path (withing the first 1 mm for uranium, or 10 mm for argon). It is dominated by the electronic stopping power, following the Bethe-Bloch formula. The maximum stopping power is reached close to the end of the ion path (the so-called Bragg peak). The depth at which the Bragg peak is observed depends on the particular projectile and target combination. The heavy-ion projectile trajectory before reaching the Bragg

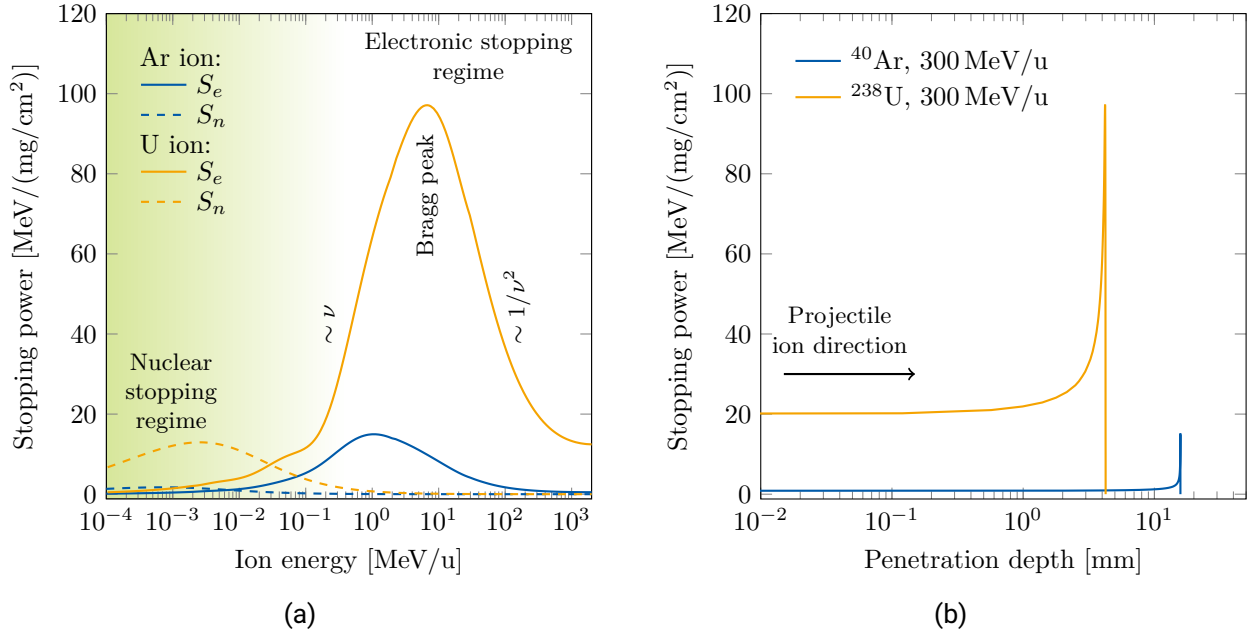


Figure 2.1: Stopping power of Ar and U ions as a function of their specific energy in ZnO (a) and as a function of penetration depth for 300 MeV/u (b). Both curves in (a) and (b) are simulated using SRIM2013 [37], assuming a ZnO density of 5.6 g/cm³.

peak is a rather straight line with negligible deviations. After the Bragg peak, the electronic stopping power reduces according to Firsov/Lindhard-Scharff models [40–42], and the contribution of the nuclear stopping power starts to increase. Therefore, the projectile scatters at target atoms and starts to deviate more and more from its original direction. However, this occurs only within a few micrometers after the Bragg peak before the projectile is completely stopped.

The irradiation experiments with relativistic heavy ions carried out as part of this work were in the range of $250 \text{ MeV/u} < E_i < 500 \text{ MeV/u}$, with E_i representing the specific energy of ions when they are extracted from the SIS18 accelerator. The thickness of the targets used for investigations was $\sim 0.5 \text{ mm}$, that is orders of magnitude smaller than the range of the relativistic heavy ions (the range is $\gtrsim 5 \text{ mm}$, depending on the ion, see Figure 2.1b). Therefore, ions from SIS18 could pass through the entire sample thickness and exit from the back side. Moreover, as one could see from Figure 2.1b, the electronic stopping power is nearly constant versus depth for 0.5 mm thick ZnO samples.

The situation is different when using ions from the UNILAC. The range of ions with specific energies between 4.8 and 8.3 MeV/u is $\sim 30\text{--}100 \mu\text{m}$. As a result, ions from the UNILAC are completely stopped inside the investigated samples. The electronic stopping power has its dominant contribution to effects observed within a few micrometers near the sample's surface. When approaching the depth where the projectile ions completely stop, the combination of nuclear and electronic stopping power has to be considered.

2.1.2 Radial distribution of energy deposited by electronic stopping

As described in the previous section, electronic stopping dominates at high ion energies. In this case, the ion passage through matter is characterized by collisions of the projectile ion with target electrons, generating an

electron cascade around the ion trajectory. According to Sternglass [43] and Koschar *et al.* [44], the primary-knocked-out electrons are represented by high-energy δ -electrons (resulting from violent binary close collisions with a small impact parameter between projectile and electron) and low-energy electrons (resulting from soft collisions with a large impact parameter).

The δ -electrons fly outward from the ion trajectory, creating a further cascade of secondary electrons. As a result of the primary and secondary electron's cascade, excited states are created in the conduction and valence bands of the target. These states relax and decay in different channels within 10^{-15} – 10^{-12} s. In particular, such electron cascades may result in material luminescent light emission and formation of structural defects.

In order to explain various complex effects of heavy ions in matter, the electron kinetics plays an important role. The electron kinetics can be described by various *ab initio* methods, such as time-domain density functional theory, non-equilibrium Green functions, or simplified approaches like Boltzmann's kinetic equation, Fokker–Planck equation, or Monte Carlo methods. The recent publication by Medvedev *et al.* gives the latest update on frontiers, challenges, and solutions in modeling electron kinetics to understand various swift heavy ion effects in materials [45].

One of the simple examples to describe the radial distribution of the energy deposited to the target through the generation of primary-knocked-out electrons is given by [46, 47], as:

$$D(r) = \left(\frac{z_{eff}^2 N e^4}{\beta^2 m_e c^2} \right) \times \left(\frac{1}{r} + 0.6 + 1.7 \times \beta \right)^{-1} \times \left(\frac{1}{r^2} \right) \times \left(\exp \left[- \left(\frac{r}{0.37 \times r_{max}} \right)^2 \right] \right), \quad (2.3)$$

where z_{eff} and β are effective charge and relative speed of projectile ions, e is the elementary charge, c is the speed of light, and m_e is the rest mass of the electron, N describes the number of available free electrons per unit volume, r_{max} is the maximum range of the generated primary-electrons in the material, which depends on the maximum energy that can be transferred to target electrons, W_{max} , as:

$$r_{max} = kW_{max}^\alpha, \quad (2.4)$$

where $k = 6 \times 10^{-6} \text{ cm}^{-2} \text{ keV}^{-\alpha}$, and $\alpha = 1.079$ for $W_{max} < 1 \text{ keV}$, or $\alpha = 1.667$ for $W_{max} > 1 \text{ keV}$.

The maximum energy that can be transferred in a binary collision between the incident ion and the primary-knocked-out-electron is estimated as:

$$W_{max} = 2m_e c^2 \beta^2 / (1 - \beta^2), \quad (2.5)$$

where m_e is the rest mass of the electron, c is the speed of light, β is the relativistic velocity of an incident ion.

Thus, the maximum energy transferred from an incident ion to a primary-knocked-out electron of a target is ranging within 10–1400 keV, and the corresponding maximum range of δ -electrons in ZnO is 0.5 μm to 1.9 mm for excitation with ^{40}Ar to ^{238}U ions with energies of 4.8 to 500 MeV/u.

The $1/r^2$ drop of the third term of Equation 2.3 is characteristic of the course of the radial dose. For large radii $r \sim r_{max}$, the last term of the formula comes into play and the function rapidly decays exponentially.

Figure 2.2 shows the course of the excitation density in ZnO calculated according to Equation 2.3, starting radially from the path of different ions provided by the UNILAC and SIS18 accelerators. The faster the projectile, the broader the dose distribution into the material, i.e., the greater the maximum range r_{max} of the δ -electrons. Although the Au ions at 4.8 and 8.3 MeV/u have a rather similar energy loss, i.e., 75 and 74 MeV/(mg/cm²), respectively, the deposited energy density of the slower ions is higher (since the energy is deposited within a smaller volume).

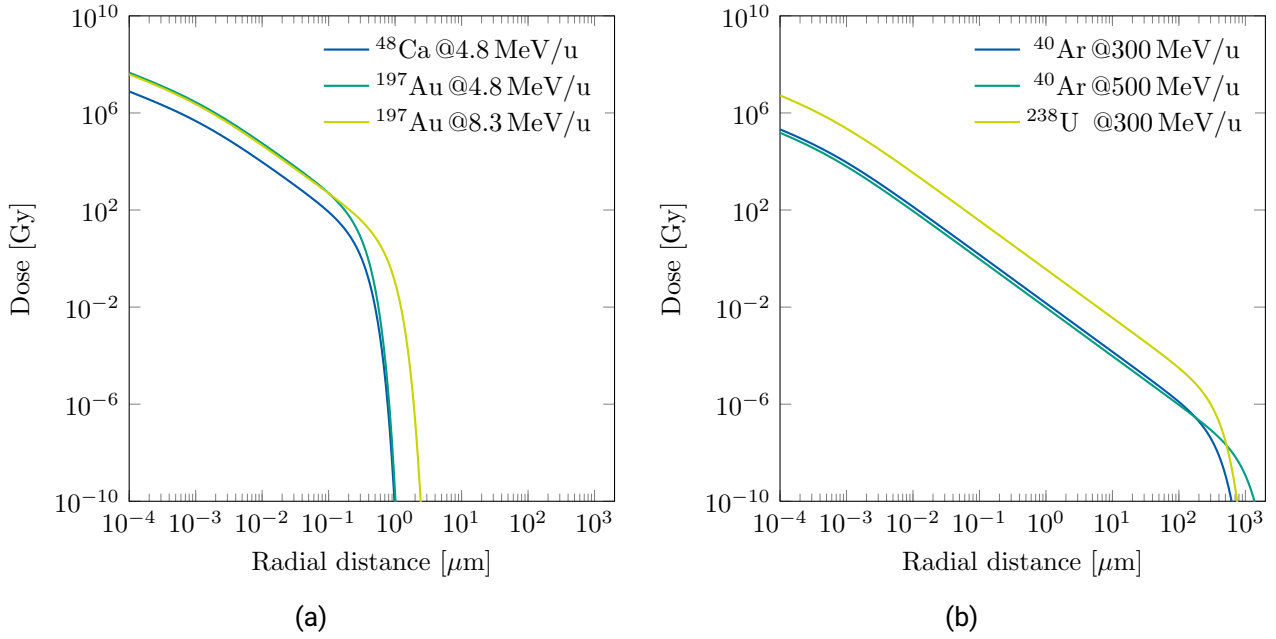


Figure 2.2: Radial distribution of dose deposited by different ions into the electronic subsystem of ZnO according to Equation 2.3 for (a) UNILAC and (b) SIS18 ion beams.

The deposited energy density plays an important role for both luminescence (scintillation) and radiation damage formation phenomena. In particular, the light output of a scintillator depends not only on the stopping power value of the penetrating particles, but also on the deposited energy density. Although the S_e value increases with the mass and charge state of the projectile, the light output of the scintillator can decrease. This means that less light can be produced for heavy ions than for light ions at the same energy [35, 48, 49].

Luminescence light emission is quenched if the deposited energy density is too high [50, 51]. This non-linear behavior was previously described by Birks and Black when they experimentally investigated the scintillation light output of anthracene as a function of stopping power due to the irradiation with different particle beams [52]. From these observations, the authors developed a semi-empirical model which describes the specific light output per unit length in scintillator, dL/dx , as a function of the dE/dx value (or electronic stopping power, S_e) [52, 53].

$$\frac{dL}{dx} = \frac{L_0 \times \frac{dE}{dx}}{1 + KB \times \frac{dE}{dx}}, \quad (2.6)$$

where L_0 is the absolute luminescence efficiency representing the fraction of energy deposited by the particle that is converted to luminescent light without quenching, $B \times \frac{dE}{dx}$ is the number density of luminescence centers along the ion path and K is a quenching factor. The factor KB is usually treated as a single parameter — the so-called Birks factor [54].

In the model proposed by Michaelian *et al.*, electron-hole pairs are generated starting from the track of the ion, whose excitation density ρ (number density of luminescence centers) follows the course of the radial dose $D(r)$ (Equation 2.3 and Figure 2.2) [51]. The model further assumes that above a material-specific limit value ρ_q , the input energy can no longer be converted into luminescence centers and, thus, quenching of the material luminescence starts. The course of the light output, for a region where $\rho > \rho_q$, is therefore constant, i.e., proportional to ρ_q up to a radius $r < r_q$. For radii with $r > r_q$, the density of the generated luminescence

centers and thus the light output is proportional to the course of the radial dose up to the maximum range of the δ -electrons [48].

Concerning the radiation damage and deposited energy density, the so-called *velocity effect* is mentioned in literature [55–61]. The effect can be formulated as follows: For two ions that have the same electronic stopping power in the target material, the ion with a lower velocity (or specific energy) produces larger damage in the material than the ion with higher velocity.

Two ions having the same S_e generate different energy distributions in the target (as shown in Figure 2.2). The energy deposited by high-velocity ions spreads into a larger area around the ion path, leading to a lower deposited energy density than that for low-velocity ions. This results in more pronounced damage around the ion path of slower ions than those produced by faster ions with the same S_e .

2.1.3 Formation of radiation damage due to electronic stopping

Various models have been developed over time to explain the large number of radiation damages that occur due to the electronic stopping of heavy ions [45, 62–64]. As compared to nuclear collisions, for which damage results from direct atom–atom collisions, the damage resulting from electronic stopping is a complex process including multiple stages. For the past decades, some semi-empirical models have proved their predictive capability with satisfactory precision.

In the model of the so-called *Coulomb Explosion*, the resulting radiation damage is interpreted as the result of mutual repulsion of the positively charged atomic nuclei around the ion track. Since the excited electrons relax within 10^{-12} – 10^{-14} s, the positively charged atomic nuclei can repel each other, which can result in a large number of vacancies, interstitials and other defects along the ion track [65].

Another explanation for the development of radiation damage is provided by the so-called *Inelastic Thermal Spike Model* (i-TS) [66]. This is one of the most commonly used semi-empirical models to predict the size of the latent track (damaged material region along the ion path). Here, the energy of the ions is first transferred and redistributed between the electrons of the solid. Then, after thermalization within the electron subsystem, hot electrons transfer their energy to the atomic lattice through electron-phonon interaction. The energy thus converted into heat leads to a sharp increase in temperature within a very short time, with the material surrounding the ion track being able to be melted. Due to the equally rapid solidification of the molten phase, defect formation and amorphization of the material can occur.

According to the i-TS model, the size of the damaged region can be estimated by solving a system of two heat equations:

$$\begin{cases} C_e(T_e) \frac{\partial T_e}{\partial t} = \frac{1}{r} \frac{\partial}{\partial r} \left[r K_e(T_e) \frac{\partial T_e}{\partial r} \right] - g(T_e - T_a) + A(r, t) \\ C_a(T_a) \frac{\partial T_a}{\partial t} = \frac{1}{r} \frac{\partial}{\partial r} \left[r K_a(T_a) \frac{\partial T_a}{\partial r} \right] + g(T_e - T_a), \end{cases} \quad (2.7)$$

where $C(T)$, $K(T)$ are heat capacity and thermal conductivity as a function of temperature (subscript e and a correspond to electrons and atoms subsystems, respectively), g is the electron-phonon coupling constant, t is time, and r is a radial distance from the ion path. The $A(r, t)$ is the distribution of the energy deposited into the electronic subsystem.

Despite some criticisms of the thermal spike model, e.g., that processes taking place on the atomic scale are described with macroscopic quantities (temperature, thermal conductivity, specific heat capacity), and that the model uses the electron-phonon coupling as a free parameter, the i-TS model is generally accepted because

it provides a helpful orientation of the track formation processes, and can predict the experimentally observed track radii.

In addition to these two semi-empirical models, complex multiscale *ab initio* models are developed. For example, the approach based on a combination of: (i) the Monte Carlo code TREKIS describing time resolved kinetics of electron excitations and energy transfer from target electrons to target atoms, and (ii) Molecular Dynamics (MD) code LAMMPS that describes time-resolved relaxation of target atoms in a crystal lattice after receiving energy from the electrons subsystem. The advantage of MD simulations is that they include additional processes such as recrystallization in the atomic system, and also they can be directly compared to experimental results from transmission electron microscopy (TEM).

2.2 Characteristics of inorganic scintillators

In general, scintillation can be understood as the energy conversion of ionizing radiation (X-ray, electron, proton, heavy ion) into low-energy photons. An external excitation brings the material into a non-equilibrium state with regard to the charge carrier concentration, and then, it relaxes into an equilibrium state. Depending on the type of excitation, one speaks, for example, of photoluminescence (excitation by light), electroluminescence (excitation by applying an electric current), radioluminescence (excitation by applying X-rays or electrons), or ionoluminescence (excitation by irradiation with ions).

The term luminescence describes the radiant transition of an excited atom into the ground state after direct excitation. In contrast to this, scintillation is a consequence of the energy loss of ionizing radiation in matter followed by light emission [67].

The scintillation process can be described as a sequence of five steps [68]:

1. *Energy deposition* by absorption of ionizing radiation and ionization of the atoms to form primary electrons in the conduction band and holes in the valence band or states close to the core (less than 10^{-16} s);
2. *Relaxation* of the primary electrons and holes, i.e., generation of secondary electrons, holes, photons, and plasmons (10^{-16} – 10^{-14} s);
3. *Thermalization* of the excited electrons and holes towards the band edges (10^{-14} – 10^{-12} s);
4. *Excitation* of the luminescent centers by energy transfer from the electron-hole pairs (10^{-12} – 10^{-10} s);
5. *Radiative recombination* with emission of a photon (more than 10^{-10} s).

The scintillation stages listed above can be visualized in time using the electronic band structure scheme shown in Figure 2.3. In this general scheme, the energy is plotted against a timescale, as well as the near-nuclear states of the solid and the valence and conduction bands separated by a band gap. The densities of states of the electrons (red) and holes (blue) are plotted as a function of time. In the following subsections, we discuss each stage in more detail.

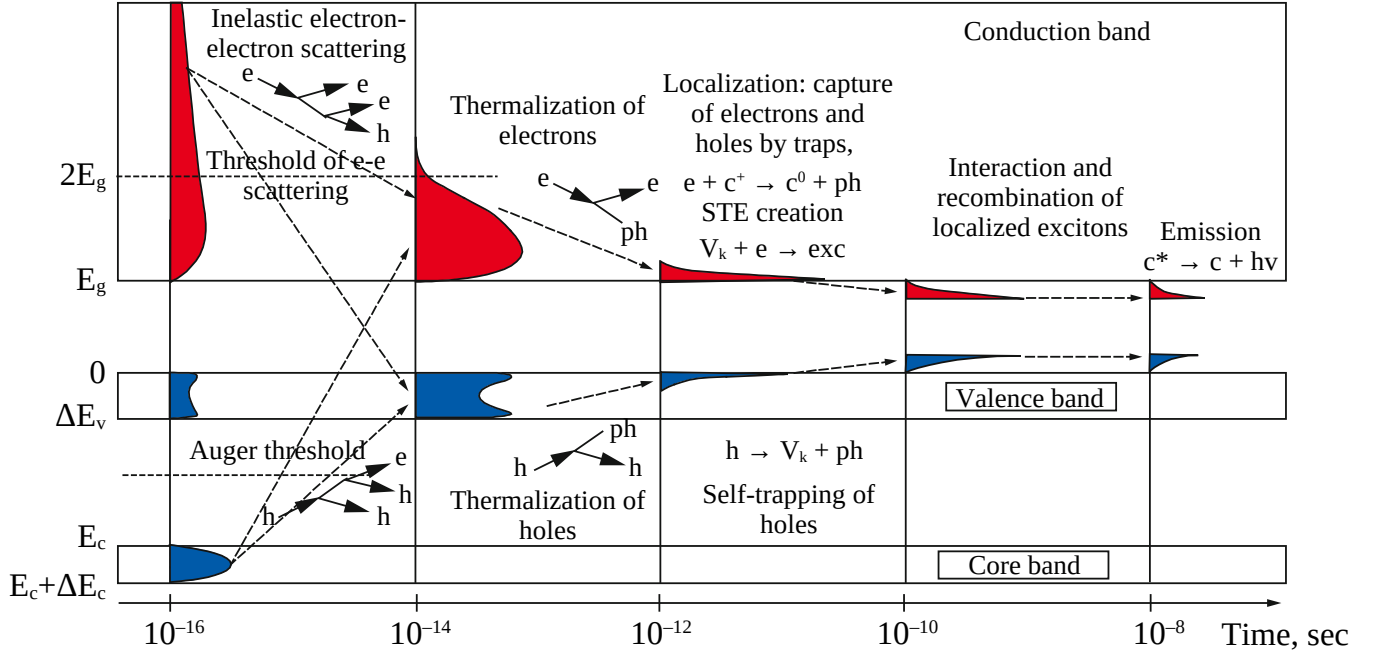


Figure 2.3: General relaxation scheme of excited electronic states in an intrinsic scintillator from [67]. The scheme depicts the energy transfer processes after the excitation of electrons (red) and holes (blue) by an ionizing radiation. In the scheme, e – electron, h – hole, ph – phonon, c – electron capturing trap, V_k – self-trapped hole, exc – exciton (electron-hole pair), hv – scintillation photon.

2.2.1 Generation of electron-hole pairs

According to [35], the scintillation efficiency η is defined as the number $N_{h\nu}$ of light quanta generated by ionizing radiation of the energy E_i .

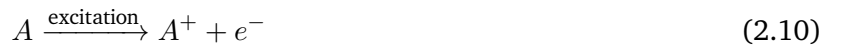
$$\eta = \frac{h\nu_m \times N_{h\nu}}{E_i}, \quad (2.8)$$

where $h\nu_m$ is the mean energy of the emitted photons. The number of generated photons $N_{h\nu}$ can also be written as the product of the efficiencies of the steps described above in the relaxation of a material [68]:

$$N_{h\nu} = N_{eh} \times P \times q, \quad (2.9)$$

N_{eh} represents the conversion efficiency (i.e., the number of electron-hole pairs or excitons formed by ionizing radiation of energy E_i); P describes the probability of transfer to a luminescent center and q is the quantum efficiency of the material for radiative recombination.

In the first step, an atom of the solid-state compound is ionized by excitation with high-energy radiation, which leads to the formation of a deep hole (e.g., in the K -shell) and a hot electron.



In addition, secondary and tertiary ionization steps can occur in a cascade-like manner, caused by collision processes between electrons, by the generation of primary X-rays or by Auger processes, until the energy of the electrons or holes produced is no longer sufficient to trigger new ionizations. Due to these inelastic

collision processes, numerous secondary electrons and holes are generated in the conduction or valence band within a very short time (10^{-16} – 10^{-14} s). The number of electron-hole pairs formed is determined in a first approximation by the energy of the incident radiation E_i [68]:

$$N_{eh} = \frac{E_i}{E_{eh}}, \quad (2.11)$$

where E_{eh} is an average energy required for (thermalized) electron–hole pair production. According to Shockley, the electron–hole pair production can be written as: $E_{eh} = (2...3) \times E_g$ [69]. Thus, the size of the band gap E_g is the key limiting factor in the generation of e – h pairs. It should be noted that N_{eh} is relevant only for a limited number of scintillators; in materials with complex electronic systems, additional types of excitation can occur, such as core-valence transitions in BaF_2 [70], or the coexistence of Ce-Frenkel and F-Wannier excitons in the scintillator CeF_3 [71].

In the second step, the charge carriers relax towards the band edges with subsequent recombination. At the end of this step, all the electrons are at the bottom of the conduction band and all the holes are at the top of the valence band.

Below the threshold energy for the creation of an electron-hole pair, free charge carriers can no longer be created. The energy is dominantly released to the lattice with the creation of phonons (heat). The thermalization of the charge carriers takes place within a period of 10^{-12} to 10^{-11} s.

It must be noted that ultimately only a fraction of the excited primary electrons and holes result in radiative recombination. As discussed in the previous section, processes also occur in the solid in which the excited electrons and holes recombine in a non-radiative manner. These include, for example, the formation of color centers and other defects (resulting in phosphorescence or loss of luminescent light yield), as well as thermal losses and the generation of phonons.

2.2.2 Excitation and emission of luminescent centers

Following the thermalization of the charge carriers, the localization of the excited states takes place through the trapping of electrons and holes or with the formation of excitons (self-trapped exciton, STE). This step is critical in that the excited excitons can either recombine in a stepwise radiative manner or decay non-radiatively into stable defects. The impurities and lattice defects present in the solid (e.g., vacancies, grain boundaries) play a major role in trapping the charge carriers. For example, an anion vacancy acts as a very effective trap to capture electrons. These defects are often referred to as color centers. The consequence of trapping the charge carriers is that they can no longer participate in the recombination process. Since the location of the defect states is usually within half the band gap, recombination across such a level is more likely than direct recombination since it requires less energy.

Finally, for a material to be able to emit light, luminescent centers must be present. The luminescence centers can be of either intrinsic, or extrinsic nature.

In the case of extrinsic type, luminescence is determined by the presence of an activator impurity (e.g., $\text{NaI}(\text{Tl})$, $\text{CaF}_2(\text{Eu})$, $\text{Al}_2\text{O}_3(\text{Cr})$). The luminescence efficiency can thus be significantly increased by the controlled addition of activator ions. Since the light emission process is directly related to the number of luminescent centers present, one might assume that an increased number of defects should lead to more luminescence. In fact, however, many experiments indicate that the intensity of the emission first increases and then decreases again when the defect concentration has exceeded a certain value [72, 73]. This phenomenon is called

concentration quenching and was first described by Johnson and Williams [74, 75]. The effect is caused by the increased probability of energy transfer between neighboring impurity centers [76].

The intrinsically activated luminescence is observed for materials with defect states within the atomic structure, which have a radiant transition between an excited state and a ground state (e.g., BaF₂, ZnO, or PbWO₄). These intrinsic states can trap and localize charge carriers. A conceivable process would look like this:



By capturing an electron from the conduction band, the F^+ center is transformed into an (excited) F^* center, which then emits light, corresponding to $F^* \rightarrow F + h\nu$. This possible type of recombination is in turn limited by the formation and emission of self-trapped excitons (STE), i.e., the interaction of a hole center with an electron of the conduction band.

If a hole h^+ is at the top of the valence band at the end of the thermalization step, it can be localized on an anion, i.e. $X^- + h^+ \rightarrow X^0$. The state X^0 in turn polarizes the environment and forms together with another anion molecule X_2^- . This state is also referred to as the V_K center or self-trapped hole (STH). The time for the formation of the STH is between 10^{-12} – 10^{-10} s (Figure 2.3). Since this period is much shorter than the average lifetime of a free exciton (10^{-10} – 10^{-6} s), most holes are localized at V_K centers. In addition, the probability of direct recombination of excited electrons and holes decreases with the energy of the exciting radiation. This is due to the higher mobility of electrons than holes.

By capturing free electrons from the conduction band at the V_K center, the STE is formed, which recombines with the emission of a photon:



For the practical application of a scintillator, the relative light output (or scintillation yield) L represents a more significant quantity than the efficiency η (Equation 2.8). The relative light output L is defined as the number $N_{h\nu}$ of emitted photons per absorbed energy E_i (unit: photons/MeV) [35]:

$$L = \frac{N_{h\nu}}{E_i} = \frac{\eta}{h\nu_m} \quad (2.14)$$

A combination of Equation 2.14 with Equation 2.11 and 2.8 yields:

$$L = \frac{N_{eh} \times P \times q}{E_i} \quad (2.15)$$

Since the solid-state physical processes that take place here (i.e., transport to the luminescent center with a probability P and emission, characterized by a quantum efficiency q) are difficult to determine, a light yield, L , was characterized in the context of this work. The light yield was measured using various detectors, which output signals are proportional to the number of incident scintillation photons. In our experiments, the detectors were the CCD chip of a camera/spectrometer and the cathode of a photomultiplier tube, which were exposed to scintillation light of the investigated sample.

2.2.3 Duration of scintillation pulse

In most scintillators, the intensity of the emission rises infinitely fast compared to the decay time. It is frequently assumed that the scintillation pulse reaches its maximum intensity at the time $t = 0$, and then, decays with a certain constant. The intensity of the emission $J(t)$ (in photons/s) of the scintillator with one type of luminescent center decays exponentially with a time constant τ :

$$J(t) = J_0 \exp\left(-\frac{t}{\tau}\right), \quad (2.16)$$

where J_0 is the initial intensity, i.e., photons/s at $t = 0$. This case corresponds to a linear recombination (first-order kinetics) when the concentration of luminescent centers is greater than the concentration of non-equilibrium carriers (electrons and holes).

For scintillators with a finite rise time τ_R and decay time τ , the emission intensity follows:

$$J(t) = \frac{N_{eh}}{\tau - \tau_R} \left[\exp\left(-\frac{t}{\tau}\right) - \exp\left(-\frac{t}{\tau_R}\right) \right]. \quad (2.17)$$

If a crystal has a rise time and two decay modes, the kinetic equation can be written as:

$$J(t) = J_1 \left[\exp\left(-\frac{t}{\tau_1}\right) - \exp\left(-\frac{t}{\tau_R}\right) \right] + J_2 \exp\left(-\frac{t}{\tau_2}\right), \quad (2.18)$$

where J_1 and J_2 are the intensity contributions and τ_1 and τ_2 the decay time constants from decay modes 1 and 2, respectively.

When the scintillation light pulse is registered with a photomultiplier tube connected to a measuring device (e.g, an oscilloscope), the scintillation intensity function is convoluted with a response function of the photomultiplier and the measuring device. Thus, the measured scintillation signal is written as:

$$V(t) = (f * J)(t) = \int_0^t f(\tau) J(t - \tau) d\tau, \quad (2.19)$$

where $V(t)$ is the measured scintillation signal, $f(t)$ is the response function of the photomultiplier and oscilloscope, $(f * J)(t)$ is the convolution operation. The response function $f(t)$ can be represented as the convolution itself. In the simplest assumption, this is the convolution of the photomultiplier, signal cable, and oscilloscope response.

Also, the scintillator response $J(t)$ can be represented as a convolution of the true scintillation light generation and propagation of the light through the scintillator towards the photomultiplier. However, most commonly propagation of light from scintillator to photomultiplier is negligible due to the specific geometries of the experimental setups.

2.3 Radiation hardness and damage accumulation models

The interaction of ionizing radiation with the scintillator crystal inevitably causes radiation damage in the material. The development of radiation damage is based on complex processes in which not only the matrix atoms but also impurities or defects are involved. The defect formation mechanisms are described in more

detail in the next chapter. At this point, however, the concept of the radiation hardness of a scintillator should be explicitly discussed. It should be noted in advance that the term “radiation hardness” is not well-defined. However, to be able to specify the radiation hardness of a material, the dose is often chosen at which the intensity of a previously defined optical transition has fallen to 60–80% of the original value [77].

In this context, the type of ionizing radiation and the quality and composition of the non-irradiated material are not considered. For example, the optical absorption of a material can be increased by targeted doping compared to the non-doped material, but at the same time the radiation hardness can be improved by creating luminescent centers [78].

In principle, the luminescence properties of a scintillator can be impaired by the following types of damage:

- Concentration quenching. At large defect concentration, the probability of energy transfer between neighboring luminescent centers increases. For example, if anion vacancies are generated by the irradiation, but at the same time the primary scintillation process is dominated by the recombination of F centers, this luminescence will be effectively quenched when a critical number of defects is accumulated.
- Formation of color centers whose absorption bands can absorb the light emitted by luminescent centers. In most crystals, the decrease in transmittance of the material is the main cause of degradation in light output.
- Radiation-induced defects can trap free charge carriers and prevent them from radiative recombination. This also results in additional modifications in the properties of the luminescent centers, such as a shift in the emission spectrum, a change in the decay times, etc.
- The formation of shallow trap states leads to increased afterglow.
- Occurrence of nuclear reactions and the associated radioactive decay processes create additional defects in the material.

Numerous models have been developed to provide predictions about the long-term behavior and radiation hardness of scintillators. However, all are based on the first approach by Birks and Black, who developed a model as early as the 1950s to describe the light yield of anthracene under irradiation with α -particles as a function of the applied dose [79]. The model described in [53, 79, 80] was also used in this work to describe the dynamic scintillation behavior of ZnO ceramics as a function of the ion fluence.

In contrast to the irradiation with high-energy photons (X-rays, γ -radiation), the dose deposited by heavy ions is not homogeneously but rather heterogeneously distributed within the sample volume. Each individual ion produces a cylindrical damage zone along the ion path. This so-called ion track is surrounded by the undamaged material. Under extended ion bombardment, tracks start to overlap and finally, at large enough fluences, cover the entire sample volume.

Various models have been developed for description of heavy ion irradiation damage [79, 81]. A common parameter of these models is the effective damage cross-section around the ion trajectory. Four selected models are listed below:

The Birks-Black model : This model has been extensively used since the 1950s for describing the scintillation light output reduction due to radiation damage in various organic and inorganic scintillators [79, 82, 83]. According to this model, the luminescence intensity changes as a function of fluence follows:

$$I(\Phi) = \frac{I_0}{1 + k[\exp(\sigma_e \Phi) - 1]}, \quad (2.20)$$

where $I(\Phi)$ is the light intensity at fluence Φ , I_0 is the initial emission intensity at zero fluence, σ_e is the effective damage cross-section of an individual ion, and k is the ratio between non-radiative and radiative transition rates for luminescence in the irradiated material. It is important to emphasize that σ_e is an effective cross-section, which represents a collective effect of different defect types created in a damaged region. The same is valid for the parameter k , which can vary for different defect types.

In many experiments, $\sigma_e \Phi$ is much smaller than 1. Hence, equation 2.20 can be simplified to:

$$I(\Phi) = \frac{I_0}{1 + \Phi/\Phi_{1/2}}, \quad (2.21)$$

where $\Phi_{1/2} = 1/(k\sigma_e)$ represents an ion fluence at which the luminescence intensity is reduced to 50%. This value is used for a quantitative radiation hardness comparison of different scintillators, as well as damage efficiency comparison of various ionizing particle types.

The Birks-Black model provides an estimate of the relative change in scintillation light output (i.e, the characteristic of a bulk material property). In reference [81], authors consider various radiation damage formation models that estimate the fraction of the amorphous phase in material as a function of fluence ($f_a(\Phi)$). Compared to the Birks-Black model, these models are focused more on estimation of the material structure change, rather than the change of physical properties of irradiated material.

Direct-impact model : Each impacting ion contributes equally to the damage formation by triggering a respective collision cascade [84]. The course of the relative damage f_a can then be written as a function of the fluence Φ as:

$$f_a(\Phi) = 1 - \exp(-\sigma\Phi) \quad (2.22)$$

where σ represents an effective damage cross-section caused by the impacting ion, which is a measure of the radiation hardness of a material.

The direct-impact model and the Birks-Black model are almost identical for swift heavy ions because they consider that each ion damages the material (e.g., amorphization). However, when the ion hits an already damaged material region, it does not contribute to the overall damage.

Cascade-overlap model : This model assumes that permanent damage to the material only occurs when a certain limit value of the fluence is exceeded. If the ion tracks overlap at higher fluences, very high defect concentrations can be accumulated locally in the area where the ion tracks intersect together, which accounts for the damage. This model can be used well for materials whose damage shows a sigmoidal behavior depending on the fluence [84]. The development of the relative damage as a function of the fluence is then:

$$f_a(\Phi) = 1 - \left(\left(1 + \sigma\Phi + \frac{\sigma^2\Phi^2}{2} \right) \exp(-\sigma\Phi) \right) \quad (2.23)$$

Combination of processes : The development of a composite model from the Direct-impact/Cascade-overlap model is based on the observation that for some materials damage already starts at the beginning of the irradiation, but with prolonged irradiation, the damage to the material is less pronounced than in the Direct-impact model, what is attributed to an additional necessary accumulation of defects [85].

Furthermore, the purity of a crystal is of great importance for a high radiation hardness, since the effectiveness of the generation of defects generally depends on the concentration of impurities present [67]. The intrinsic radiation hardness depends on the generated self-trapped holes (V_K centers) in the material, the formation rate of which in turn depends on the type of substitution atom, its size and the crystal structure.

For example, scintillators without V_K centers, such as alkaline earth oxides, have a high radiation hardness [67]. However, the rule that particularly pure crystals have a high level of radiation hardness must be extended to include the fact that targeted doping may also contribute to an improvement in radiation hardness if the number of precursors used to create point defects (e.g., as a compensator for oxygen voids that form color centers) can be reduced. This is the case, for example, with $Gd_2SiO_2:Ce$ if the Ce concentration is between 0.5–2.5 mol% [86].

Some radiation-damaged materials regain their optical properties over time. However, such processes are diffusion-linked and recovery at room temperature is extremely slow. Almost complete recovery of the material can be achieved by annealing at elevated temperatures [87–89]. The temperature and the duration of the annealing strongly depend on the properties of the material's color centers. Photo-stimulated healing (optical bleaching) of the color centers at a defined wavelength for a certain period of time is also possible [77].

2.4 Influence of radiation damage on scintillation properties

The scintillating properties of crystals are strongly related to their crystallographic structure. In fact, all the components of the scintillation light yield, mentioned earlier, depend to some extent on the structural quality of the lattice.

Defects are produced in scintillating materials when exposed to ionizing radiation. Even light particles such as electrons can produce local defects and charge imbalance in the crystal. Heavier particles, such as protons, α -particles, and heavier ions, deposit more energy when interacting with the crystal lattice and produce relatively large damage zones extending over several crystallographic cells. Based on the size, classification of crystal lattice defects include point defects as well as two- and three-dimensional defects.

Point defects include ion vacancies and interstitials, impurity atoms or ions and their aggregates, and radiation induced defects like color centers. Such defects are characterized by quick internal stress relaxation with distance from the point defect and weak interaction with other defects. In thermodynamic equilibrium, there always exists a certain concentration of point defects in a crystal. The point defects concentration can increase with irradiation. An increase in vacancies concentration leads to the formation of bi-, three-, or more vacancies clusters. Such defects do not influence the crystal transparency, although they can initiate the capture of carriers and energy storage mechanisms in the crystal. Other internal defects can introduce absorption bands (especially in the UV range) which are likely to decrease the crystal transparency at the light emission wavelength.

Impurities in crystals are far more diverse in comparison to internal point defects and, in general, one can distinguish activating impurities (i.e, impurity influencing the scintillation process itself) and parasitic impurities that decrease the scintillation efficiency.

Two-dimensional, or linear defects, are dislocations of all possible configurations. These defects are the source of internal stresses, particularly when they appear in clusters. In general, it is assumed that linear defects, like dislocations, have a small contribution to scintillator performance and radiation damage. Nevertheless, in the early 80-s the “deformation luminescence” phenomenon was discovered and described [90]. This effect embraces a range of phenomena during crystal deformation that give rise to the excitation of luminescence when dislocations are displaced. In practice, the internal stresses are not large enough to produce the displacement of dislocations, but stresses can increase with radiation dose. Moving dislocations cause the formation of numerous vacancies and vacancy complex in crystals, also they contribute to the activator impurities homogenization which can be initially localized in the crystal lattice in a non-random way.

Three-dimensional defects appear in different kinds as macroscopic inclusions into the crystal lattice, for instance, foreign phases, voids, pores, and so on. These defects can have a complex influence on optical transparency, diffuse light scattering and scintillation light emission efficiency of the crystal.

2.4.1 Scintillation light absorption by crystal defects

Absorption bands as well as internal non uniformities, for example, scattered inclusions, gas bubbles, and voids influence the light collection and contribute to light losses by scattering and absorption. This is particularly important for large scintillators. This is why the study of the optical absorption spectrum in the scintillation emission is an important tool to probe the intrinsic quality of the crystal.

The most essential contribution to optical absorption is related to internal point defects, impurities, and radiation-induced point defects.

2.4.2 Undesirable luminescence and afterglow

The scintillation efficiency losses are related to carrier capture. It occurs at trap sites originating from impurities or radiation defects.

CsI scintillator represents a unique example of intrinsic luminescence in the alkali halite scintillators family. Besides the fast 10 ns scintillation component, other slowly decaying emission bands are also observed. In particular, the emission caused by the presence of oxygen ions in the crystal has been identified. This emission in the green range has the decay time of several microseconds, which is typical of such ions as O_2^- [67]. Moreover, under irradiation and (or) temperature treatment, reactions easily occur from O^{2-} ions to O_2^- . All these centers introduce both additional harmful luminescence, quench the fast emission and cause afterglow to scintillation. The methods to prevent undesirable luminescence and afterglow are generally related to crystal production technology. This includes (i) preliminary purification of raw material, (ii) additional melt purification, (iii) attempts to reach the best structure performance.

In activated scintillators, one of the mechanisms at the origin of high afterglow level is related to the formation of complex activator luminescence centers. For example, in CsI(Tl) the radiation-induced spectrum shows the contribution from Tl_2^0 and Tl^{2+} activator centers. Such centers are formed under UV irradiation. Their combination with F-centers is responsible for the afterglow. To prevent the formation of such centers and decrease the amount of afterglow, such crystals need to be stored in the dark.

The stability of such centers is not high, and dissociation temperature for Tl_2^0 and Tl^{2+} reach 70 °C and 140 °C, respectively. Consequently, low-temperature (130–140 °C) annealing of the crystal is also a way to lower the afterglow level and to increase the radio luminescence output by 40–50%.

2.4.3 Radiation-stimulated losses of scintillation efficiency

Radiation defects depend on the initial structure of the target material and also specific to the kind of ionizing radiation.

From a pragmatic perspective, the question of scintillator radiation hardness is most commonly reduced to the estimation of the change of the detected scintillation efficiency when exposed to different kinds of radiation. The practical criterion of the scintillator resistance to radiation is the value of the scintillator efficiency losses under radiation, i.e., the reduction of its light yield. The radiation damage does not have an unambiguous interpretation, as it depends on many parameters (projectile particles, the dose, dose rate, irradiation temperature, recovery (aging) conditions).

From the physical perspective, the problem is to study mechanisms of the optical transparency and of the luminescence light yield deterioration in materials.

For many materials, the crystal transparency drops as a result of the formation of color centers under irradiation. This process obviously affects the light transport efficiency from the point of emission to the photodetector. The luminescence yield can also be modified if the luminescence centers are subject to transformations under irradiation. Fortunately, the scintillation mechanism itself is very stable in many crystals.

For self-activated crystals, like PbWO_4 and $\text{Bi}_3\text{Ge}_4\text{O}_{12}$, the radiation damage is only related to the optical transmission damage through the formation of color centers. In activated scintillators (such as $\text{NaI}(\text{Tl})$, $\text{CsI}(\text{Tl})$), both the scintillation efficiency and the crystal transparency can be potentially damaged under irradiation. ZnO is a self-activated scintillator, but it has a different behavior than the one described above. This is shown further in the results of this work.

3 Review of Investigated Materials

This chapter focuses on the general properties of ZnO-based materials, with a particular emphasis on their optical and luminescence properties, which are of great interest for scintillation detector applications. It includes a description of the manufacturing process for transparent ZnO ceramics. The chapter concludes with a summary of all the samples that were investigated in this work.

3.1 General physical properties of ZnO

Zinc oxide is a direct-gap semiconductor with a considerable fraction of ionic bonding. It crystallizes in three primary crystal systems: cubic rocksalt, cubic zinc blende, and hexagonal wurtzite, as shown in Figure 3.1. The hexagonal wurtzite is the most frequently observed ZnO phase, which is stable at room temperature. It belongs to the $P6_3mc$ space symmetry group and has lattice parameters: $a = 3.2495 \text{ \AA}$ and $c = 5.2069 \text{ \AA}$. Each zinc atom of the crystal lattice is surrounded by four oxygen atoms located at the corners of a nearly regular tetrahedron. The Zn–O spacing along the c -axis is slightly shorter than the other Zn–O bonds (1.90 \AA and 1.98 \AA , respectively).

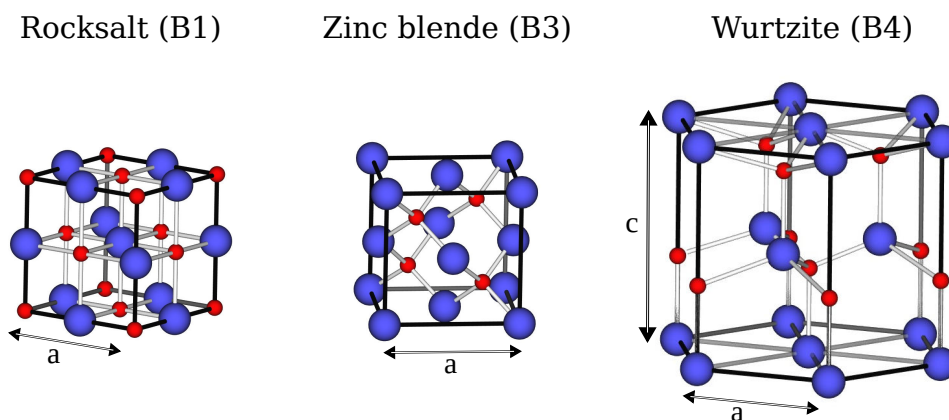


Figure 3.1: Crystal systems that can be formed by ZnO (left to right) – cubic rocksalt, cubic zinc blende, and hexagonal wurtzite. The blue and red spheres correspond to zinc and oxygen, respectively.

The nature of chemical bonding of ZnO lies in the intermediate range between covalent and ionic. Given the considerable ionic nature of the connections linking Zn and O atoms (~ 0.62 on the Phillips scale), the two elements forming the bonds can be indicated as Zn^{2+} and O^{2-} ions, respectively [91, 92].

Due to its physical properties, ZnO has been used in biomedical applications, electronic devices, energy industry, gas sensors, optical devices, and ionizing radiation detectors [93–95]. The selected physical properties of wurtzite zinc oxide are summarized in Table 3.1.

Table 3.1: Physical properties of hexagonal wurtzite zinc oxide [94, 96]

Property	Value
Molecular formula	ZnO
Molar mass	81.39 g/mol
Density at room temperature	5.606 g/cm ³ (crystal theoretical density 5.61 g/cm ³)
Solubility in water (25 °C)	1.6 mg/L
Melting temperature	1975 °C
Boiling temperature	2360 °C
Stable phase at room temperature	wurtzite
Structure	Hexagonal
Space group symmetries	C46v (P63mc)
Bulk effective piezoelectric constant	9.9 pm/V
Hardness	5.0 ± 0.1 GPa
Lattice parameters (at 300 K)	a = 3.2495 Å c = 5.2069 Å
Thermal conductivity	0.6, 1–1.2 W/(cm K)
Specific heat	0.494 J/(g °C)
Band gap	3.437 eV (at 1.6 K) 3.37 eV (at 300 K)
Exciton binding energy	60 meV
Exciton diameter	~2 nm
Longitudinal optical phonon energy	72 meV
Low-frequency dielectric permittivity, ϵ_0	8.75 () 7.8 (\perp)
High-frequency dielectric permittivity, ϵ_∞	3.75 () 3.7 (\perp)

3.2 Luminescence and optical properties of ZnO

For various forms of ZnO, single- and poly-crystals, thin films and threads, nanocrystals and powders, one can distinguish two luminescence bands. The first is a short-wavelength band, located near the absorption edge of the crystal (frequently mentioned in literature as edge luminescence, or near-band-edge emission), and the second is a broad long-wavelength band, the maximum of which is in the green spectral range (referred to as green luminescence or defect band emission). Although zinc oxide has been known as an efficient phosphor and investigated for many decades, no consensus has been achieved on the light emission mechanism that leads to the observed bands. Moreover, there are several models of luminescence that contradict each other [94, 97, 98].

The photoluminescence spectrum of bulk ZnO at 4.2 K excited by a HeCd laser is shown in Figure 3.2 [99]. The dominating line of the spectrum at 3.35 eV (~ 370 nm) originates from bound exciton (BE) recombination (excitons bound to neutral donors (D^0X) and/or acceptors (A^0X)) followed by longitudinal optical (LO) phonon replicas with an energy separation of 72 meV. In some samples, a donor–acceptor pair (DAP) transition is found around 3.22 eV (~ 385 nm). The chemical identity of the acceptor A_x is unknown according to Ref. [99].

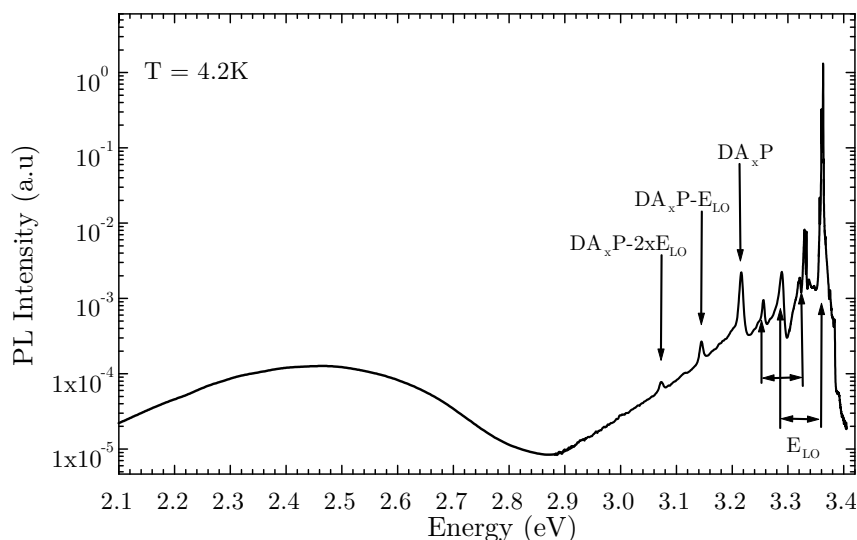


Figure 3.2: ZnO photoluminescence spectrum measured at 4.2 K temperature with a HeCd laser excitation from [99]. Excitonic, donor acceptor pair (DAP) and deep level emission bands are visible. The corresponding phonon replica with longitudinal optical phonons (LO) are indicated.

The luminescence decay time for the near-band-edge emission is of the order of 0.5–1 ns and, thus, is of high interest for detector applications where a fast signal response is required [95].

The nature of the green luminescence occurring as a broad band with a maximum at 2.32 eV (535 nm) and full width at half maximum 0.33 eV in Figure 3.2 is yet to be understood. As a result of an extended review in Ref. [94], the authors came to the conclusion that various centers may be involved in green luminescence simultaneously. The green luminescence can be caused by imperfections of the crystal lattice, instability of certain point defects, and a variety of their forms. Impurity Cu^{2+} ions, zinc vacancies V_{Zn} , oxygen vacancies V_O , interstitial zinc ions Zn_i , oxygen antisites Zn_O , and transitions $Zn_i - V_{Zn}$ are considered by various authors to be the luminescence centers responsible for the green luminescence [94, 100–107]. The luminescence decay times of the green luminescence band are known to be in the microsecond timescale, which is much larger compared to near-band-edge luminescence. Therefore, it is desirable to avoid the presence of green luminescence for fast applications.

As it has been previously reported by a number of authors, the fraction of fast near-band-edge luminescence can be enhanced relative to the slow defect band luminescence by introducing group 3A elements such as Ga, In, or Al, which results in obtaining ultra-fast scintillating material [9, 14–16, 18, 19, 21, 108–110].

3.3 Uni-axial hot pressing in vacuum

In the majority of cases, zinc oxide is used in the form of thin films and powders or in the form of small size single crystals. Obtaining large single crystals, which are favorable for scintillators applications, is difficult. It has been reported previously, that the ordinary method of growing crystals from melt does not yield satisfactory results in the case of ZnO because of its high vapor pressure [111, 112]. Mainly, large ZnO crystals are obtained using the hydrothermal growth method, known as an expensive and prolonged process. Thus, crystals with a size of $30 \times 30 \times 12 \text{ mm}^3$ can be grown within the order of 100 days [113]. In addition, such crystals inevitably contain ionic impurities of K, Li, and other contaminants.

Optically transparent ZnO ceramics, which are prepared by the methods of uni-axial hot pressing and iso-static pressing, serve as alternatives to single crystalline ZnO synthesis. In particular, a successful use of the uni-axial hot pressing method to obtain transparent pure, In-doped and Ga-doped zinc oxide ceramics has been reported [15, 16, 18, 114–117].

The hot uni-axial pressing method is a high-pressure, high-temperature and low strain rate synthesis process designed to form a dense, bulk material pieces with powders as starting material. During sintering, densification is achieved by simultaneously heating and pressing of the powder inside a mold. The high temperature and pressure applied to the powder are typically independent of each other. The hot pressing method is known to be used to synthesize ceramic carbides, borides, nitrides, oxides, etc. However, it is not limited only to ceramics. Various ceramic/metal composites and metal composites can also be fabricated by the hot pressing [118–121]. Generally, densification is due to particle rearrangement, plastic deformation, grain boundary diffusion and pore elimination. The loose powder or the pre-compacted raw body is put into a graphite die, which is heated up to a high temperature of the order of 1000–2500 °C. At the same time, a high pressure of up to 150 MPa is applied along one of the sample axis. The treatment is performed in a vacuum, air or a gas controlled atmosphere, and usually lasts for several hours.

The high temperatures are typically achieved by inductive, direct or indirect heating. In inductive heating, the heat is produced by a high-frequency electromagnetic field within an electrically and thermally conductive mold placed into an induction coil. In the case of the direct heating method, the heating is caused by an electric current generated directly in a pressing mold containing the powder. It is used as a spark plasma sintering with a pulsed DC current. Inductive and direct sintering techniques are dependent on the intrinsic physical properties of the pressing mold.

Indirect heating, is considered as the most easy to use technique. The mold is placed inside a heating chamber in a vacuum or a controlled atmosphere. The chamber is heated by graphite elements heated by an electric current, and the mold is heated by heat convection. Indirect resistance heating is preferred because higher temperatures can be reached. Moreover, it is independent of the conductivity of the mold as well as the heat and pressure within the mold. Finally, in the case of indirect heating, the temperature distribution in the mold is homogeneous and allows obtaining large ceramic samples [121].

A comprehensive overview of different ZnO-based ceramics prepared by uni-axial hot pressing and spark plasma sintering has been given by Sahani *et.al.* [95]. This summary reports about a number of undoped and doped (e.g., Zn, Ga, Ga&N, In and Li) transparent ceramic ZnO scintillators that have been explored [18, 110, 115, 117, 122–126].

The reported ceramics have a poly-crystalline structure with large grain sizes of 5–30 μm , and exhibit light transparency for approximately 390 nm wavelength and higher. The emission ratio of near-band-edge and defect band was controlled by changing the doping concentration of the impurities mentioned above. Also, it was shown that luminescence properties of ZnO can be improved by H_2 treatment.

3.4 Description of investigated ZnO samples

Samples that were characterized within this work are listed in Table 3.2. ZnO-based scintillating ceramics characterized within this work were produced by the Joint Stock Company “Research and Production Corporation S.I. Vavilova” (St. Petersburg, Russia) using uni-axial hot pressing in vacuum. These samples can be divided into four groups based on manufacturing process:

- **Initial In-doped samples:** are ZnO(In) ceramics;
- **Thermally-treated In-doped samples:** are ZnO(In) ceramics with a successive thermal treatment in (Ar/H₂) atmosphere;
- **Initial Ga-doped samples:** are ZnO(Ga) ceramics;
- **Thermally-treated Ga-doped samples:** are ZnO(Ga) ceramics with a successive thermal treatment in (Ar/H₂) atmosphere.

It should be noted that initial In-doped and initial Ga-doped samples were mechanically polished after hot pressing. Therefore, these samples have a roughness around 0.1 μm. Thermally treated In-doped and thermally treated Ga-doped samples were polished before the treatment. As a result of the thermal treatment in a static (Ar/H₂) atmosphere, the surface of the samples was etched, increasing the roughness up to ~ 10 μm. One ZnO(In) sample was thermally treated using (Ar/H₂) gas flow. In this case, the surface roughness remained unchanged.

The fact that ceramic samples are produced from pressed powder mixtures, leads to the presence of voids in the sample volume. These voids result in a density value (measured as sample mass and volume ratio) that is lower than the density of single crystalline ZnO. The average bulk sample density of initial In- and Ga-doped samples is 2–4% lower than the density of bulk single-crystalline ZnO. For thermally treated In- and Ga-doped samples, the average bulk sample density is 10–30% lower than the density of single-crystalline ZnO.

The doping concentrations for all In-doped and Ga-doped samples were 0.13 and 0.1 wt.%, respectively.

Further manufacturing conditions (temperatures, pressure, gas mixture proportions, and processing times) of the hot-pressing of the initial ceramics, as well as conditions of the further thermal treatment, cannot be disclosed due to the trade secrets of the Joint Stock Company “Research and Production Corporation S.I. Vavilova”.

3.5 Other investigated materials

In addition to ZnO ceramics, commercially purchased plastic scintillators, single-crystalline ZnO, and BK7G18 borosilicate glass were investigated. While not the main focus of this work, these materials also have relevance in scintillation detector development and utilization in high radiation environments.

Plastic scintillators are one of the most frequently used materials for fast-counting detector applications. Applications include industrial and health physics measurement of alpha, beta, gamma, and neutron radiation as well as in numerous medical instruments and scientific research ranging from low background shields in nuclear physics to space-borne astrophysics systems. In this work, EJ-212 plastic scintillator purchased from ELJEN TECHNOLOGY served as a reference for ZnO-based scintillators comparison. EJ-212 is identical to the well-known NE-102A and BC-400 referenced in numerous scientific articles over the past forty years. It is based on polyviniltoluene polymer with 1.023 g/cm³ density and exhibits the light output of 65% of

anthracene. The wavelength of the maximum light emission is at 423 nm. The material scintillation decay time is 2.4 ns [127].

Pure hydrothermally grown **single-crystalline ZnO** plates were purchased from Crystal GmbH. Single-crystalline ZnO samples were available in three different crystal plane orientations perpendicular to $\langle 0001 \rangle$, $\langle 10-10 \rangle$ and $\langle 11-20 \rangle$ directions. These single crystals were used as additional commercially available ZnO reference compared to the doped ZnO-based ceramics produced by the uni-axial hot pressing.

Borosilicate radiation-hard glass is known for applications in space and nuclear power. In this work, the material represents interest for the detector application as a medium guiding scintillation light in the UV/Vis light range. We investigated the borosilicate glass with 1.8% cerium oxide produced by SCHOTT (product name BK7G18). Cerium oxide doping changes the intrinsic color of the glass and is used to stabilize the transmittance loss caused by ionizing radiation [128]. According to the manufacturer specifications, the BK7G18 glass exhibits good transmission in soft UV and visible range starting from approximately 370 nm [129].

Table 3.2: List of the samples characterized within this work

Sample name	Doping (wt.%)	Density (g/cm ²)	Surface roughness (μm)	Comments
Plastic scintillator	—	1.023	0.09	Reference scintillator (EJ212, or BC400)
BK7G18	—	2.52	< 0.01	Radiation-hard glass (light guide material)
ZnO <0001>	—	5.61	< 0.01	Single-crystalline zinc oxide, <0001> orientation
ZnO <10-10>	—	5.61	< 0.01	Single-crystalline zinc oxide, <10-10> orientation
ZnO <11-20>	—	5.61	< 0.01	Single-crystalline zinc oxide, <11-20> orientation
ZnO_In-851-18	In ³⁺ , 0.13	5.40	0.12	Initial ZnO(In) ceramic sample
ZnO_In-904-19-init	In ³⁺ , 0.13	5.39	0.03	Initial ZnO(In) ceramic sample
ZnO_In-956-21	In ³⁺ , 0.13	5.4	0.07	Initial ZnO(In) ceramic sample
ZnO_Ga	Ga ³⁺ , 0.1	5.44	0.07	Initial ZnO(Ga) ceramic sample
ZnO_Ga-845-18	Ga ³⁺ , 0.1	5.45	0.10	Initial ZnO(Ga) ceramic sample
ZnO_In	In ³⁺ , 0.13	5.49	0.09	Thermally-treated ZnO(In) ceramic sample (Ar/H ₂ gas flow, 600 °C, 2 hours)
ZnO_In-851-18-to	In ³⁺ , 0.13	4.66	11	Thermally-treated ZnO(In) ceramic sample (static Ar/H ₂ atmosphere)
ZnO_In-890-19-therm	In ³⁺ , 0.13	4.91	6.23	Thermally-treated ZnO(In) ceramic sample (static Ar/H ₂ atmosphere)
ZnO_In-897-19-therm	In ³⁺ , 0.13	4.46	10.39	Thermally-treated ZnO(In) ceramic sample (static Ar/H ₂ atmosphere)
ZnO_In-904-19-therm	In ³⁺ , 0.13	4.12	9.68	Thermally-treated ZnO(In) ceramic sample (static Ar/H ₂ atmosphere)
ZnO_Ga-858-18-to	Ga ³⁺ , 0.1	5.17	2.95	Thermally-treated ZnO(Ga) ceramic sample (static Ar/H ₂ atmosphere)
ZnO_Ga-901-19-therm1	Ga ³⁺ , 0.1	5.12	3.28	Thermally-treated ZnO(Ga) ceramic sample (static Ar/H ₂ atmosphere)
ZnO_Ga-901-19-therm2	Ga ³⁺ , 0.1	4.60	8.90	Thermally-treated ZnO(Ga) ceramic sample (static Ar/H ₂ atmosphere)

4 Experimental Characterization of Samples Irradiated with Heavy-Ion Beams

This chapter describes the experiments that were performed to characterize samples listed in the previous chapter. The experiments can be divided into two groups, depending on ion energies used for samples exposure. In the first group, experiments were performed at the UNILAC linear accelerator using swift heavy ion beams of 4.8–8.3 MeV/u. These experiments include the irradiation of samples followed by offline measurements using X-ray induced luminescence, total optical transmission, and Raman spectrometry. This group also includes irradiations, where ion induced luminescence and transmission spectra were measured in-situ. In the second group, experiments using relativistic heavy ions of 250–500 MeV/u energy from the SIS18 synchrotron are presented. These experiments had the aim of measuring in-situ ion induced luminescence spectra and scintillation light output. The measurements also recorded scintillation pulse rise and decay times in comparison to a reference plastic scintillator. Measurements were done for pristine samples before irradiation and also as a function of fluence using various ion species.

4.1 Irradiation details

The heavy ion irradiation experiments were performed at the linear accelerator UNILAC and synchrotron ring accelerator SIS18 at the GSI Helmholtz Center for Heavy Ion Research. Figure 1.1 schematically shows the locations where the irradiation experiments were conducted. The M3 and X0 beam lines of the UNILAC were used to perform samples characterization with swift heavy ions at 4.8–8.3 MeV/u energies, providing high energy loss and fast damage accumulation. The HTP beam line of the SIS18 was used to perform samples characterization using relativistic heavy ion beams at energies of 250–500 MeV/u, providing materials performance tests under conditions similar to the beam diagnostics applications of interest mentioned earlier.

4.1.1 Irradiation experiments at UNILAC

Figure 4.1 shows a schematic view of the UNILAC linear accelerator adapted from [130]. The UNILAC is capable of accelerating various ion species from proton to uranium to the maximum energy of 11.4 MeV/u (i.e., 15.5% of the velocity of light). The accelerator is equipped with three ion source terminals. The first terminal provides high-charge-state ion beams using the electron cyclotron resonance (ECR) source. The second terminal is equipped with four different ion sources, including MEtal Vapor VAcuum Arc (MEVVA) source, MUlti-Cusp Ion Source (MUCIS), or Cold or HOt Reflex Discharge ion Source (CHORDIS), and provides low-charge-ion beams. The third terminal is equipped with the Penning ion gauge (PIG) source and delivers low to intermediate charged ions.

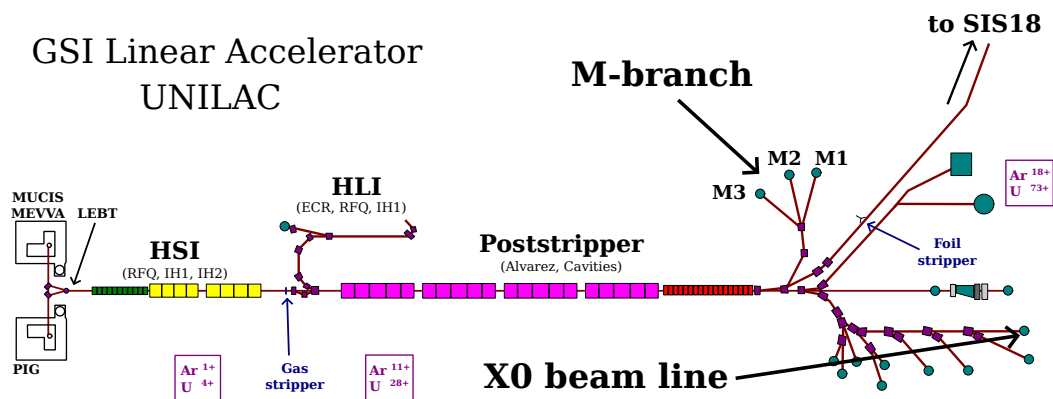


Figure 4.1: UNILAC linear accelerator scheme, adapted from [130].

After the electrostatic extraction from the low and intermediate charge state ion sources (e.g., MEVA, MUCIS, or PIG source), the DC-beam goes to the high current injector (HSI) where the beam is bunched using a radio frequency quadrupole (RFQ) and pre-accelerated with the Inter-Digital (IH) cavities up to 1.4 MeV/u. To enhance the efficiency of further acceleration of low-charged beams, the outer electrons of the ions are stripped off by passing through a gas stripper, thus increasing the ion charge state. The use of the gas stripper is not required for highly charged beams (e.g., ECR source). After the stripper, the final acceleration stage is done using five Alvarez-type cavities. The acceleration in cavities can be individually switched on and off; thus, the UNILAC can quickly provide 3.6, 4.8, 5.9, 8.6, and 11.4 MeV/u beam energies. The beam from the UNILAC can be further passed to one of the experimental target areas or be sent via a transfer channel to the SIS18 heavy ion synchrotron for a further acceleration.

In this work, the beams from the UNILAC were delivered to the target stations of the M3- and X0 beam lines. The beams had a pulse length of 5 ms and frequency of 3–50 Hz. The pulse frequency varied depending on the sharing factor with multiple users of the other UNILAC beam lines. $^{48}\text{Ca}^{10+}$ and $^{197}\text{Au}^{26+}$ beams at 4.8 MeV/u were used at the M3 beam line to perform in-situ ionoluminescence and UV/Vis light spectroscopy measurements. $^{197}\text{Au}^{26+}$ ion beam at 8.6 MeV/u energy was used at the X0 beam line to perform high fluence samples irradiation. After the irradiation at X0 beam line, samples were characterized off-line by X-ray induced luminescence, UV/Vis transmission, and Raman spectroscopy.

Figure 4.2 shows a schematic view of the M3 beam line. The beam coming from the accelerator is defocused using quadrupole and steered using dipole magnets. In order to uniformly irradiate the samples, the central part of the beam is cut to a rectangular spot of a few centimeters in size using a system of horizontal and vertical slits. The system of slits is additionally used for beam flux monitoring during samples irradiation. This is achieved by monitoring the current on the slits due to interaction with ions from the periphery of the beam. The charge from the slits is calibrated to the beam flux that passes through the slits opening and measured by a Faraday cup placed inside the diagnostics chamber in front of the sample position. The beam spot size and homogeneity is checked by inserting a luminescence screen made of Cr-doped Al_2O_3 (CROMOX). The uncertainty of the accumulated fluences measured by the calibrated slits is estimated to be 20%. The Faraday cup and the luminescence screen are moved out from the beam during the sample irradiation. The setup for in-situ ion induced luminescence and UV/Vis transmission measurements is mounted inside the spectroscopy chamber with the sample tilted to 45° beam incidence angle. The irradiation at the M3 beam line was performed at room temperature in vacuum. A more detailed description of the in-situ ion induced luminescence and UV/Vis transmission measurement setup is given further in this chapter.

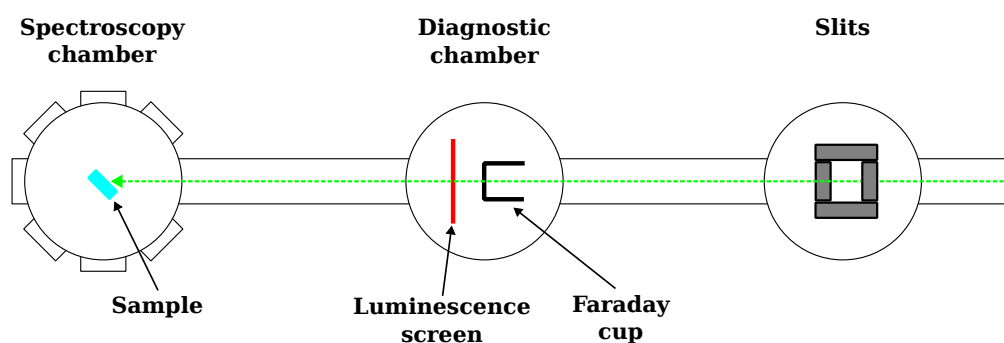


Figure 4.2: Schematic view of the M3 beam line at the UNILAC accelerator at GSI, adapted from [131].

Figure 4.3 shows a schematic view of the X0 beam line. The ion beam is defocused and steered using quadrupole and dipole magnets such that the beam covers the entire area of the irradiated sample. Before hitting the sample, the beam passes through a SEcondary Electron TRANSMISSION Monitor detector (SEETRAM) that consists of three 1 μm thick aluminum foils that are used to monitor the beam flux during the sample exposure.

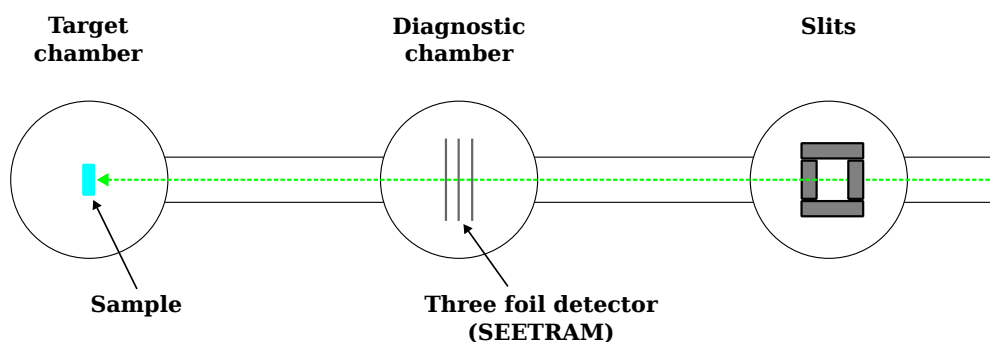


Figure 4.3: Schematic view of the X0 beam line of the UNILAC accelerator at GSI.

As it was mentioned above, samples at X0 beam line were irradiated with $^{197}\text{Au}^{26+}$ ions of 8.6 MeV/u energy. Due to the SEETRAM detector inserted in front of the sample, the beam energy is reduced by 0.3 MeV/u and Au ions equilibrate their charge state; thus, the Au ion beam that reaches the sample surface has an energy of 8.3 MeV/u energy and ions are at the equilibrium charge state (for Au: $\langle q \rangle \sim 60$). The samples at the X0 beam line were placed at normal incidence to the beam, and samples exposure was performed at room temperature in vacuum.

The SRIM2013 code was used to calculate the penetration depth and the energy loss of various beams in the investigated samples [37]. A summary of the irradiation conditions for various beams and samples investigated with swift heavy ions at the UNILAC is presented in Table 4.1. It should be noted that in all irradiations the beam penetration depth was significantly shorter than the sample thickness. This means that the incident ions are stopped in the sample, and only the top layer of the samples is directly influenced by the beam.

Table 4.1: Irradiation parameters of the samples investigated at M3 and X0 beam lines

Beam line	Ion	Energy (MeV/u)	Incidence angle	Sample	Penetration depth (um)	Energy loss at surface (MeV/(mg cm ²))	Investigated fluences (ions/cm ²)
M3	⁴⁸ Ca	4.8	45 °	ZnO(In) thermal	24.4	12.6	0–5 × 10 ¹²
				Borosilicate glass	31.3	16.6	0–1 × 10 ¹²
				Plastic scintillator	49.8	19.9	0–1 × 10 ¹²
	¹⁹⁷ Au	4.8	45 °	ZnO(In) thermal	26.8	75.3	0–2 × 10 ¹¹
				Borosilicate glass	33.8	99.9	0–1 × 10 ¹³
	X0	¹⁹⁷ Au	8.3	90 °	ZnO(In) initial	50.1	73.7
ZnO(In) thermal					62.8	73.7	0–1 × 10 ¹³

4.1.2 Irradiation experiments at SIS18

Pre-accelerated ion beams from the UNILAC are injected into the SIS18 heavy ion synchrotron via a transfer channel on a pulse to pulse basis using the multi-turn injection. SIS18 is a ring accelerator with a 216 m circumference length and maximum magnetic rigidity of 18 Tm. The ion pulses injected from the UNILAC circulate inside the ring and with each turn are accelerated to higher energies using two radio-frequency (RF) cavity systems. Depending on the ion species, the energy can be increased up to 1 GeV/u for uranium, 2 GeV/u for neon, or up to 4.5 GeV for protons, reaching approximately 90 % of the velocity of light. The acceleration process typically takes about 1–3 s, during which the beam particles make millions of revolutions inside the ring. The relativistic ion beams from SIS18 can be extracted in two modes: (i) *fast extraction* with a pulse length of 0.2 to 1 μs; (ii) *slow extraction* of a spill with a duration time of 0.01–8 s. In this work, beams from SIS18 were obtained by slow extraction, with the spill extraction times within 1–5 s. The relativistic ion beams were sent to the HTP target area shown in Figure 4.4.

A schematic view of the HTP target area, where in-situ ion induced luminescence spectra, scintillation light output, and scintillation pulse rise and decay time measurements were recorded, is shown in Figure 4.5. The beam from the SIS18 is optimized using quadrupole and dipole magnets placed along the beam transfer line, under a high vacuum. At the end of the transfer line, the beam flux is monitored using an ionization chamber (IC) filled with the Ar/CO₂ gas mixture and a secondary electron transmission monitor (SEETRAM), which consists of three Al-foils of 100 μm thickness. The experimental setup with the sample holder is placed in air behind an exit window (100 μm thick stainless-steel window, AISI 302 alloy, Fe₇₄Cr₁₈Ni₈).

Next, after passing 40 cm of air gap, the beam enters the experimental setup cover box through a black paper window and cut by a cylindrical collimator made from aluminum (60 mm base diameter, 70 mm thickness), with a 5 mm diameter circular hole at the center. The collimator thickness is sufficient to stop all the primary particles. The secondary particles produced as a result of the interaction of the beam and collimator that can reach samples are mainly protons and helium, which produce negligible signals compared to the primary beam. Thus, a well-defined circular beam of 5 mm diameter exits the collimator and its flux is monitored

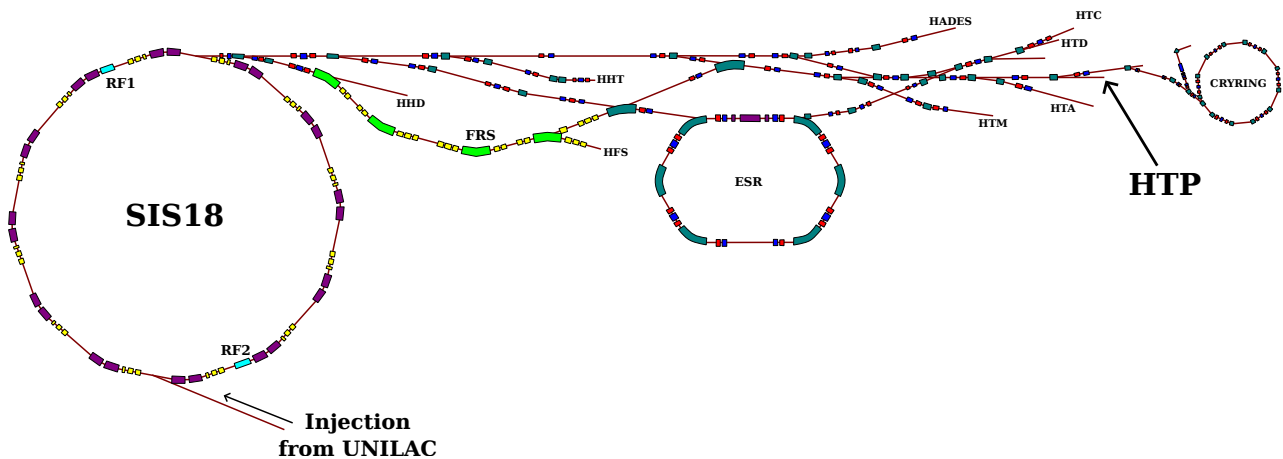


Figure 4.4: SIS18 ring accelerator scheme with experimental areas available after extraction, adapted from [5]. The experiment of this work was performed at HTP.

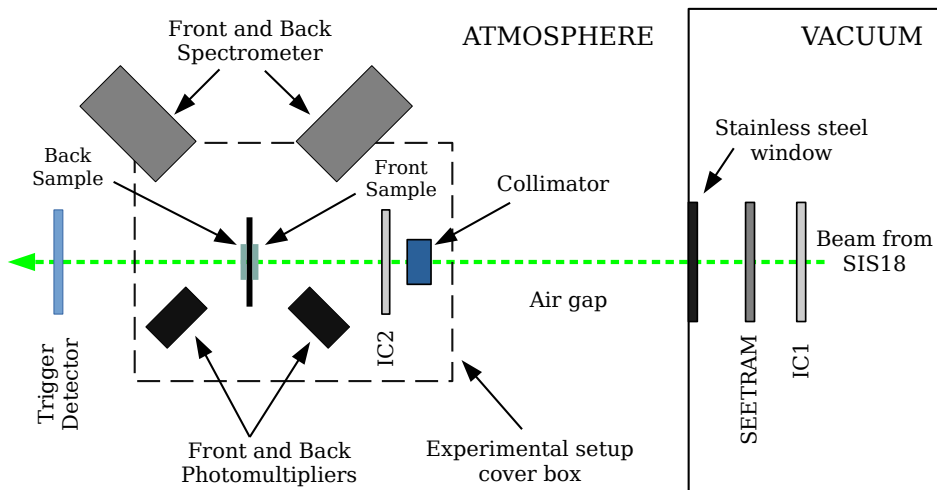


Figure 4.5: Schematic view of the HTP target area provided with the beam from the SIS18 accelerator at GSI.

using an ionization chamber. After the ionization chamber, the beam interacts with samples on a movable target holder placed at normal incidence to the beam. The investigated samples were fixed at the front and back side of the remotely controllable target holder to speed up the exchange of the samples and recording data within a limited beam time.

In this work, ^{40}Ar beams with energies of 250, 300, and 500 MeV/u, as well as ^{78}Kr , ^{208}Pb , ^{209}Bi , and ^{238}U beams with energy of 300 MeV/u were used for irradiation experiments at the HTP experimental area. For all ion species, the energy was sufficient to pass through the entire sample and exit from the back side. The BC400 plastic scintillator mounted on the target holder served as a reference to compare signals from PMTs and spectrometers placed on the front (ion enter) and back (ion exit) sides of the target holder. For scintillation light output, and scintillation pulse rise and decay times characterizations, an additional plastic scintillation detector was inserted behind the experimental setup and was used as a trigger detector to monitor single ion impact events that occur in the investigated samples.

The energy loss of relativistic ion beams along the HTP experimental beam line and irradiation parameters of the investigated samples were calculated using the ATIMA code [132]. Due to the high energy of the ion beams used, the variation of the energy loss inside the investigated samples can be neglected and thus represented by an energy loss average along the whole sample thickness. Table 4.2 summarizes the irradiation parameters for the samples exposed to relativistic heavy ion beams.

Table 4.2: Irradiation parameters of the samples investigated at the HTP experimental cave (measurements at normal beam incidence)

Ion	Energy (MeV/u)	Sample	Average energy loss (MeV/(mg cm ²))	Investigated fluence range (ions/cm ²)
⁴⁰ Ar	250	ZnO-based samples	0.9	—
		Plastic scintillator	1.3	—
	300	ZnO-based samples	0.9	—
		Plastic scintillator	1.2	—
	500	ZnO-based samples	0.7	—
		Plastic scintillator	0.9	—
⁷⁸ Kr	300	ZnO-based samples	3.4	—
		Plastic scintillator	4.6	—
²⁰⁸ Pb	300	ZnO-based samples	16.0	0–5×10 ¹¹
		Plastic scintillator	21.3	—
		Borosilicate glass	18.8	—
²⁰⁹ Bi	300	ZnO-based samples	16.9	0–3×10 ¹²
		Plastic scintillator	22.6	0–5.5×10 ¹⁰
		Borosilicate glass	19.9	0–1×10 ¹²
²³⁸ U	300	ZnO-based samples	20.1	0–1.5×10 ¹¹
		Plastic scintillator	26.8	—

4.2 In-situ ionoluminescence and UV/Vis spectroscopy at the M3 beam line

Figure 4.6 shows the schematic view of the experimental measurements performed at the M3 beam line. Ion-induced luminescence spectra were recorded online during irradiation, while for UV/Vis transmission measurements the beam was interrupted at selected fluences. The beam intensity and irradiation fluence were monitored by a system of horizontal and vertical slits. The shutters of the system of slits were individually read out via charge integrators. They were calibrated compared to the charge measured with a Faraday cup (FC) placed downstream from the slits in front of the measured sample. The FC was also used for stopping the beam during the light transmission measurements, see Figure 4.6b. All characterizations were performed at room temperature in vacuum.

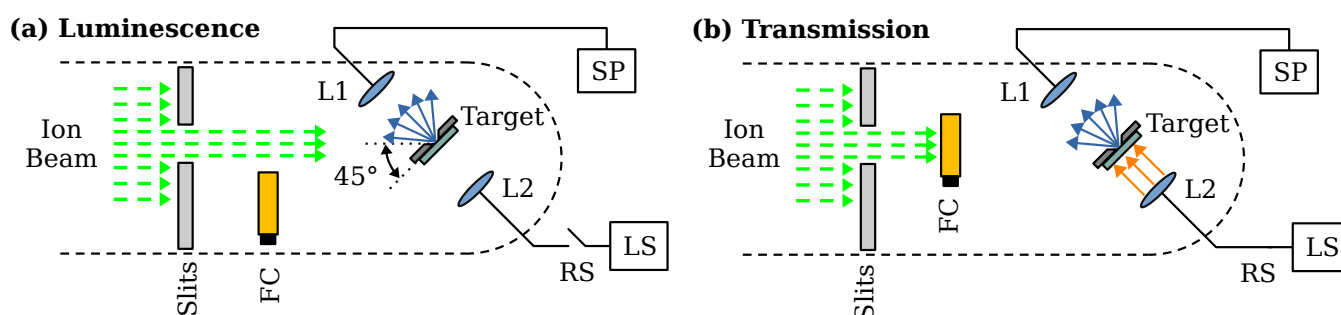


Figure 4.6: Schematic view of the experimental setup at the M3 beam line. For ionoluminescence measurements (a), the Faraday cup (FC) is removed from the beam path. The luminescence light spectrum is recorded with the spectrometer (SP). Transmission measurements (b) are performed by inserting the Faraday cup to block the ion beam. The transmission of light from a continuous light source (LS) is quantified by the same spectrometer (SP) used in measurement (a). The dashed line indicates the walls of the vacuum chamber. L1 and L2 are optical biconvex lenses and RS a remotely controllable shutter.

The investigated sample is mounted on a target holder behind a 6 mm diameter circular mask as shown in Figure 4.7. The circular hole defines the region of the sample exposed to the ion beam. The target holder has a second 6 mm diameter hole below the sample. This was to acquire the reference spectrum of a light source used for transmission measurements. At the bottom of the holder, a CROMOX luminescence screen is mounted to see and adjust the beam spot. The target holder is fixed between two biconvex lenses inside the spectroscopy chamber, as shown in Figure 4.8. In order to prevent that the ion beam hits the lens L1, the sample holder and lenses were rotated 45° with respect to the ion beam, see Figure 4.6a. The lens L1 was used to collect light emitted from the irradiated sample and transmit it to a spectrometer via optical fiber. A second lens L2 placed on the back side of the sample was connected to a continuous light source used for transmission measurements.

Both ionoluminescence and transmission spectra were recorded with Ocean Optics QE-Pro spectrometer. The signal-to-noise ratio was optimized via variation of the spectrum acquisition time, ranging from 1 to 10 s. Each spectrum was corrected for dark counts and normalized by the number of ions that hit the sample during the spectrum acquisition.

The incident light source for the UV/Vis transmission measurements was a Mikropac DH-2000-BAL UV/VIS/NIR equipped with deuterium and tungsten halogen lamps. It provided a continuous spectrum with a stable light intensity in a wavelength range from 210 to 2500 nm. The source was supplied with a remotely controllable

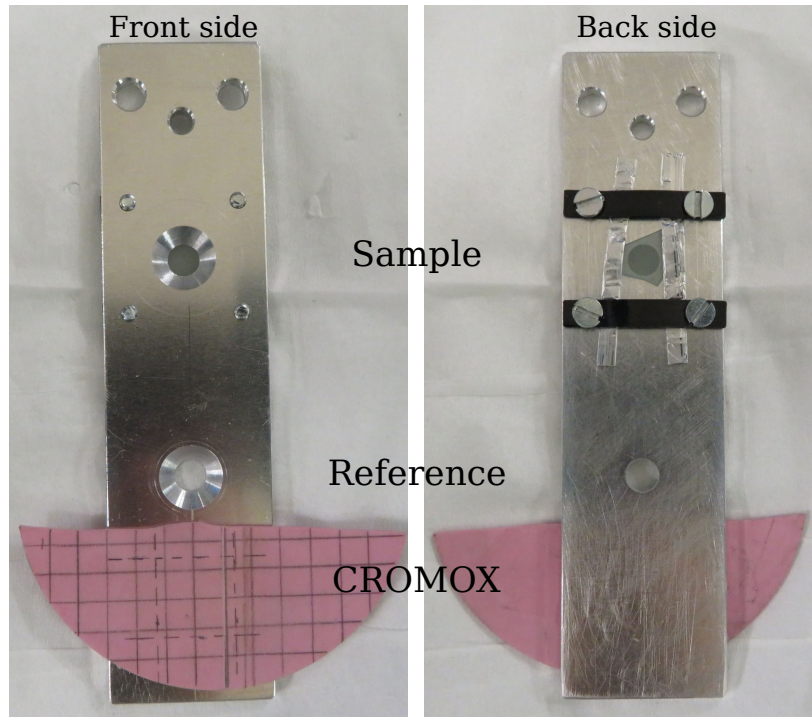


Figure 4.7: Photo of target holder used for ionoluminescence and transmission spectrometry at M3 beam line. CROMOX scintillating screen is attached to the front side of the holder, exposed to an ion beam. The investigated sample is mounted to the upper hole on the back side of the holder. The lower hole is used for reference light source spectrum measurements.

shutter, which allows leaving the source lamps switched on during the IL measurements. The transmitted light was collected from the surface of the sample exposed to the ion beam. For each selected fluence, the transmitted light spectra were recorded with an acquisition time of 10 s. The measured ten spectra were averaged for each fluence. Before the sample irradiation, a spectrum of the incident light was recorded with the empty target holder with an acquisition time of 0.5 s. All spectra were corrected for dark counts and normalized by the corresponding acquisition time.

It should be noted that due to diffuse light scattering, a part of the light transmitted through the sample was not collected by the lens L1. Therefore, the values of transmission measured in this setup configuration is expected to be smaller than the total transmission value. In this work, we assume that the angular distribution of the diffuse scattered light does not change with ion irradiation. Thus, we consider only the relative change of transmission T_{Φ}/T_{init} , where T_{Φ} is transmission measured at fluence Φ , and T_{init} is initial transmission of the non-irradiated sample.

The ionoluminescence as a function of fluence is also measured relative to the initial ionoluminescence intensity. It is represented as $I_{\Phi}/I_{\text{init}}^*$, where I_{Φ} is ionoluminescence intensity at fluence Φ , and I_{init}^* is initial ionoluminescence intensity. It is important to note that the initial ionoluminescence spectrum fluence is not equal to zero, since the sample must be exposed to the beam to produce a spectrum. Therefore, the star in I_{init}^* indicates that the initial value denotes ionoluminescence at small fluence, but not at zero.

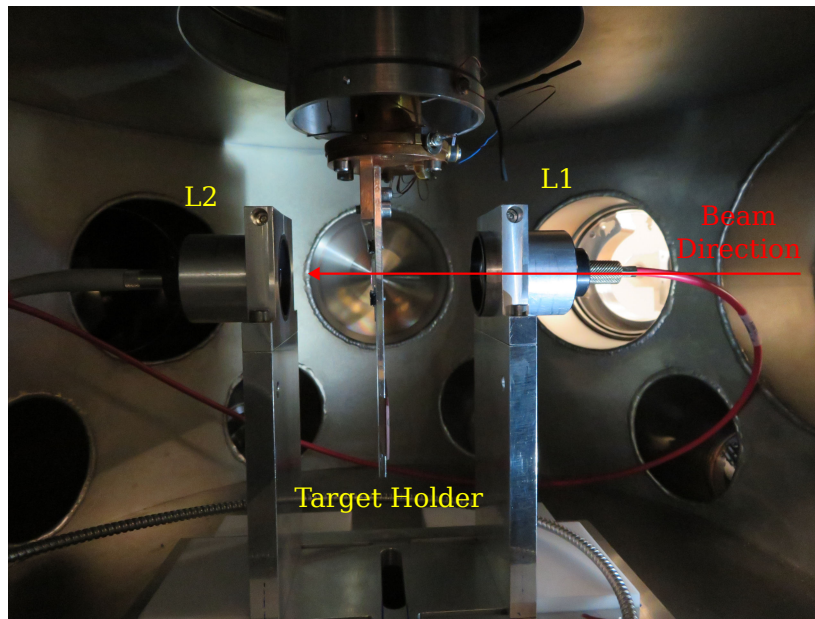


Figure 4.8: Photo of target holder and lenses placed inside the spectroscopy chamber at M3 beam line to perform ionoluminescence and transmission spectroscopy measurements. The ion beam enters the chamber from right to left.

4.3 Characterization with Raman spectroscopy

Raman spectroscopy characterization of irradiated samples was performed at room temperature in ambient atmosphere using a commercial Raman spectrometer HORIBA Jobin Yvon (LabRAM HR800). The system has access to two lasers: He-Ne gas laser with the excitation wavelength of 632.82 nm and a solid state laser with the wavelength of 473.05 nm. For both lasers, the power is 8 mW which avoids sample heating or annealing by the laser beam. The absence of the sample heating and damage annealing by the laser beam has been confirmed by multiple spectra acquisitions at the same spot.

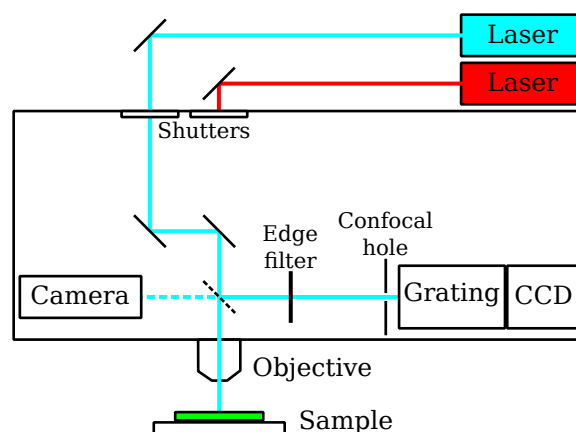


Figure 4.9: Schematic representation of Raman spectrometer used for post-irradiation samples characterization, adapted from [133]. Two lasers are available: a solid state (473.05 nm) and He-Ne gas (632.82 nm) lasers. Measurements are performed in back-scattering geometry.

In this work, the Raman spectroscopy measurements were performed using 473.05 nm laser in a back-scattering geometry as shown in Figure 4.9. Samples were placed with the spectrometer objective facing the irradiated surface. The internal edge filter was used to cut out the Rayleigh scattered light from the sample surface. This allows measurements up to Raman shifts below 100 cm^{-1} . A confocal hole is installed in Raman system to provide good depth resolution and cut off the Raman signal close or far in z-direction from the objective focal point. The set of microscope objectives available for Raman measurements ranges from $\times 5$ magnification up to $\times 100$. With the adjustment of the confocal hole and selecting a high magnification objective, the Raman spectra were collected from the near surface layer that is much less than the penetration depth of ions in the samples. A grating with 600 gr/mm was used for all measurements in this work. Peltier cooling is used for the charge-coupled device (CCD) detector installed in the system, providing a detector operating temperature of $-70\text{ }^{\circ}\text{C}$. A silicon wafer was used as calibration standard for the Raman shift.

4.4 X-ray induced luminescence spectroscopy

X-ray induced luminescence (XRL) spectroscopy was performed at room temperature in ambient atmosphere using an original experimental setup at Peter the Great Polytechnical University (St. Petersburg, Russia). Figure 4.10 shows a schematic view of the XRL setup. Spectra were recorded in reflected light geometry using a continuous X-ray source operated at 40 kV. The X-ray source was equipped with a copper anode, providing X-rays of copper K-alpha energy of $\sim 8\text{ keV}$. X-rays hit the sample at 45° incidence relative to the ion-irradiated sample surface. The investigated sample region was covered with a copper mask with 3 mm diameter aperture. The emitted light exits the sample chamber through a quartz window placed at 45° angle to the investigated sample surface. The luminescence spectra of the samples were acquired using an MDR-2 monochromator with a 1200 gr/mm grating and a Hamamatsu H8259-01 counting head as a photon detector. This allowed us to get emission spectra in the range from 350 to 650 nm. The resulting spectra were corrected with respect to the transmittance through the quartz window and monochromator, as well as the spectral sensitivity of the counting head.

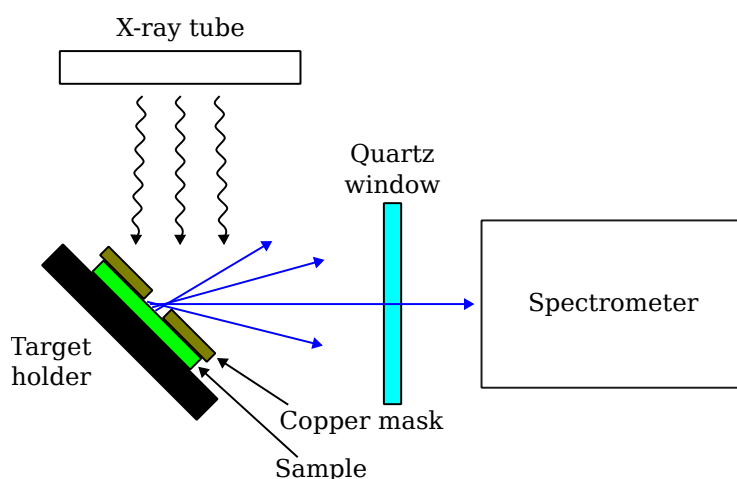


Figure 4.10: Schematic view of the X-ray induced luminescence spectrometer used for post-irradiation samples investigation.

4.5 UV/Vis transmission spectrometry

A commercial double-beam computer-controlled spectrophotometer SPECORD-200-plus with an integrating sphere module was used to record the total transmission spectra in the 350 to 1100 nm wavelength range (including diffused scattered light). Irradiated samples were placed with the irradiated surface facing the integrating sphere entrance window. Therefore, the incident light penetrated the sample through a non-irradiated surface, and the transmitted light escaped through the irradiated surface.

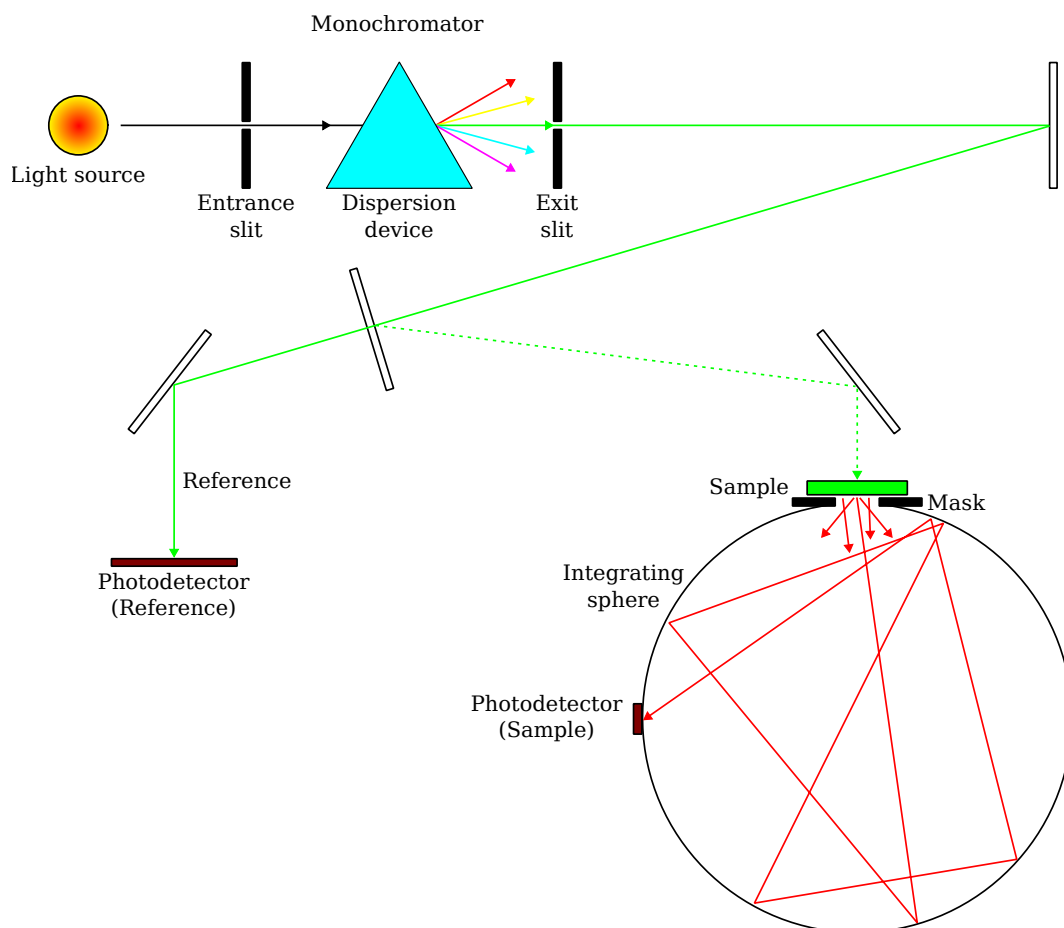


Figure 4.11: Schematic view of the total transmission spectra measurement setup used to investigate samples after irradiation.

Figure 4.11 shows the scheme of the total transmittance measurement setup. A light from a continuous UV/Vis/NIR light source passes through a monochromator and beam splitting system in order to select light with a specific wavelength (λ), shape the beam and split it into two. One beam goes to a reference photodetector, while the second beam illuminates the sample. The light is transmitted through the sample and collimated by the 2 mm diameter mask in order to collect the transmitted light only from a selected region of the sample, see Figure 4.12. The light passed through the mask enters the integrating sphere and then goes to the sample photodetector. The number of counts from sample $I_{\text{sample}}(\lambda)$ and reference photodetectors $I_{\text{ref}}(\lambda)$ are sent to a computer to create $I_{\text{sample}}/I_{\text{ref}}$ output as a function of λ . Total transmission characterizations were performed at room temperature in air.

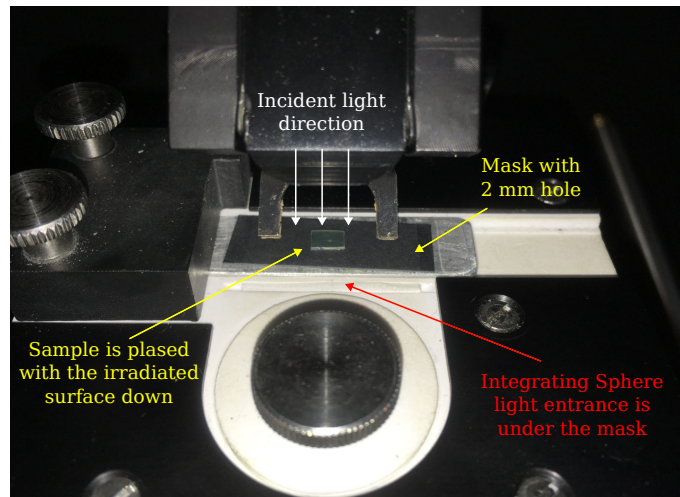


Figure 4.12: Photo of the upper part of the integrating sphere with the 2 mm diameter mask and sample placed with the irradiated surface down.

4.6 Ionoluminescence with relativistic heavy ions

In order to measure ionoluminescence of samples exposed to relativistic heavy ions, a dedicated experimental setup was developed within this work. The setup was mounted at the HTP experimental area, where relativistic heavy ion beams are delivered from the SIS18 synchrotron. The photo of the setup is shown in Figure 4.13. Investigated samples and part of the measurement equipment were enclosed inside a black box in order to avoid the external light, allowing PMT detection of a few photons. The box consists of an optical breadboard at the bottom to mount the setup components and a frame built from ITEM profiles. The walls of the box are made of Thorlabs' TB4 black construction hardboard (4.78 mm thick, plastic-coated cardboard panels with foam core). The black hard-boards which protect the setup from external light were partially removed in Figure 4.13 to be able to see the inside.

The relativistic heavy ion beam from the SIS18 synchrotron enters from right to left, as indicated by the yellow arrow. It exits the high vacuum beam transfer line into the air atmosphere through a stainless-steel window indicated as (1) in Figure 4.13. The beam enters the black box and passes through a cylindrical collimator indicated as (2). After collimation, the beam passes through an ionization chamber (3) and then penetrates the sample fixed on a target holder (6). Luminescence light from the sample under irradiation is emitted in all directions. The luminescent light is registered by photo-multipliers (4) for time and light yield measurements, video camera (5) for beam adjustments, and spectrometers (7) for wavelength measurements of the emitted light.

A closer view of a target holder is shown in Figure 4.14. The target holder was built so that two samples could be mounted one behind another from the front (beam incident) and back (beam exit) sides of the holder. The front and back samples were separated by a layer of a black paper to prevent scintillation light transition from one sample to the other. The target holder was mounted on a remotely controllable stepper-motor drive to be able to move the stage in a horizontal direction into beam position. This allows to mount a number of samples in front and back of the holder and perform irradiation of several samples without interrupting the beam, entering the radiation controlled area, and opening the black box to exchange samples.

CROMOX screen mounted on the sample holder (see Fig. 4.14) was used to control the homogeneity, size,

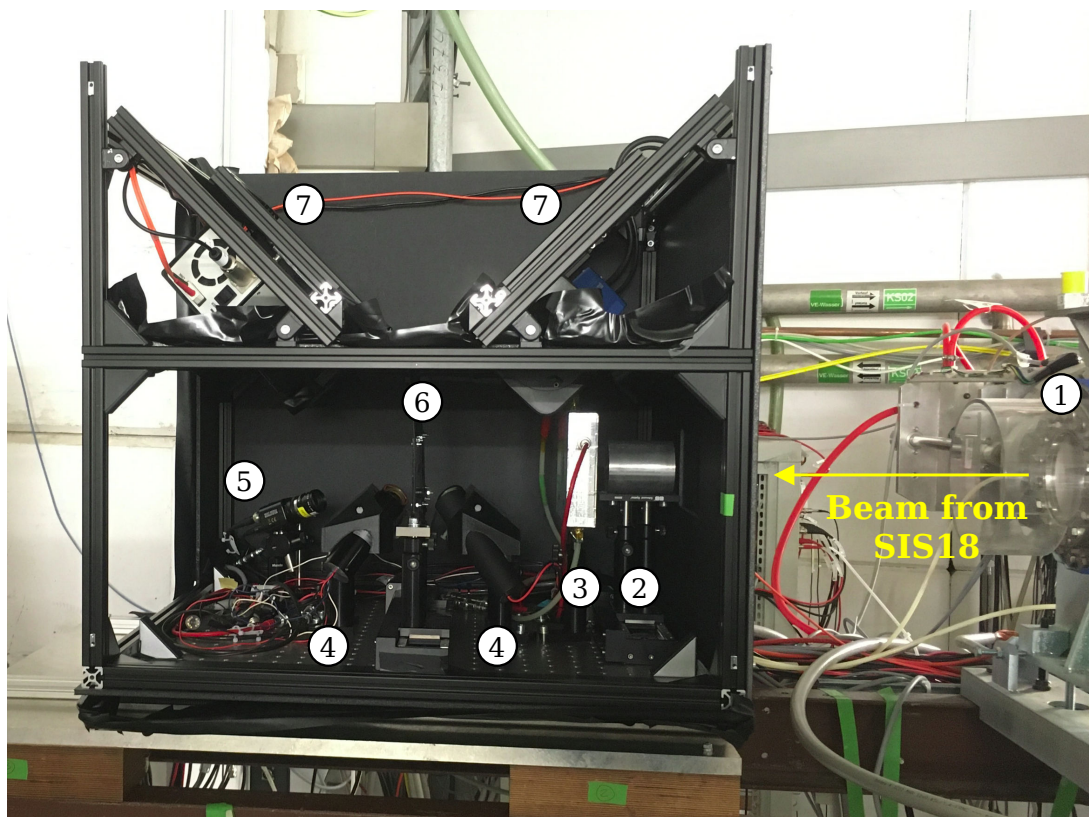


Figure 4.13: Photo of the experimental setup for ionoluminescence measurements under relativistic heavy ion beams. The black box is partially opened to see the insights. The yellow arrow shows the direction of the beam from SIS18 synchrotron. 1 – stainless-steel exit window, 2 – collimator, 3 – ionization chamber, 4 – photo-multipliers, 5 – video camera, 6 – target holder, 7 – spectrometers.

and position of the beam before sample irradiation. A piece of plastic scintillator was used as a reference for both spectroscopy and photo-multiplier measurements. Free spaces on the holder were used to mount various In and Ga doped ZnO ceramic samples.

4.6.1 In-situ ionoluminescence spectroscopy at HTP

The principal scheme of ion induced luminescence light spectra measurement under relativistic heavy ion beam irradiation is shown in Figure 4.15. Luminescence light is emitted in all directions from a region where an ion beam interacts with a sample. The light emitted in the direction of the spectrometer is cut by a slit before entering the Horiba CP 140-202 spectrograph. The light inside the spectrograph is reflected by a mirror towards a 140 gr/mm spherical holographic grating and then after going out from the spectrograph is focused on a light sensor of a high sensitivity camera produced by PCO.

Two spectrometer assemblies with different PCO cameras were used to record spectra of the scintillation light (indicated as (7) in Figure 4.13). “PCO.1600” camera was used in the front and “PCO SensiCam QE” was used in the back spectrometer. Both cameras are based on a CCD chip cooled down to $-15\text{ }^{\circ}\text{C}$ and have a capability to start image acquisition controlled by an external trigger. The key differences between the two cameras is their spectral sensitivity (quantum efficiency). “PCO SensiCam QE” camera sensitivity is optimized to register

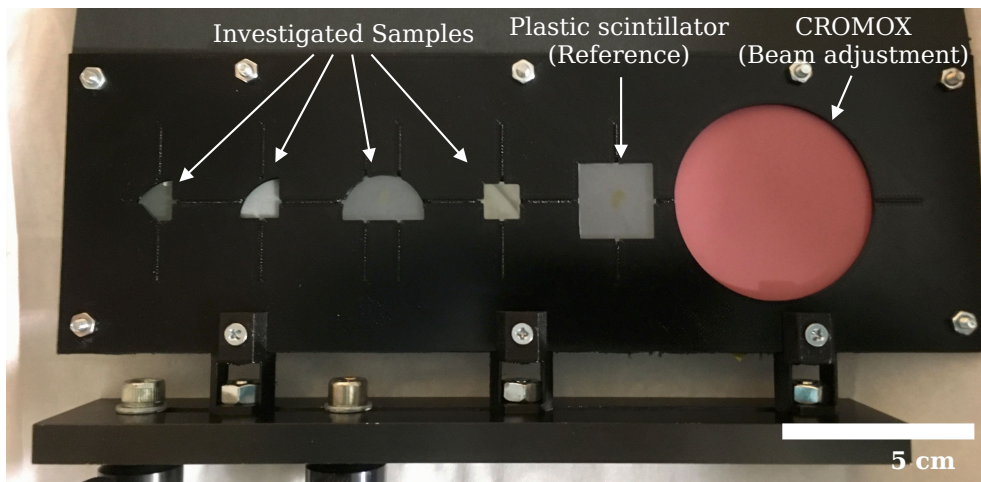


Figure 4.14: Photo of the target holder used in relativistic heavy ion irradiation experiments.

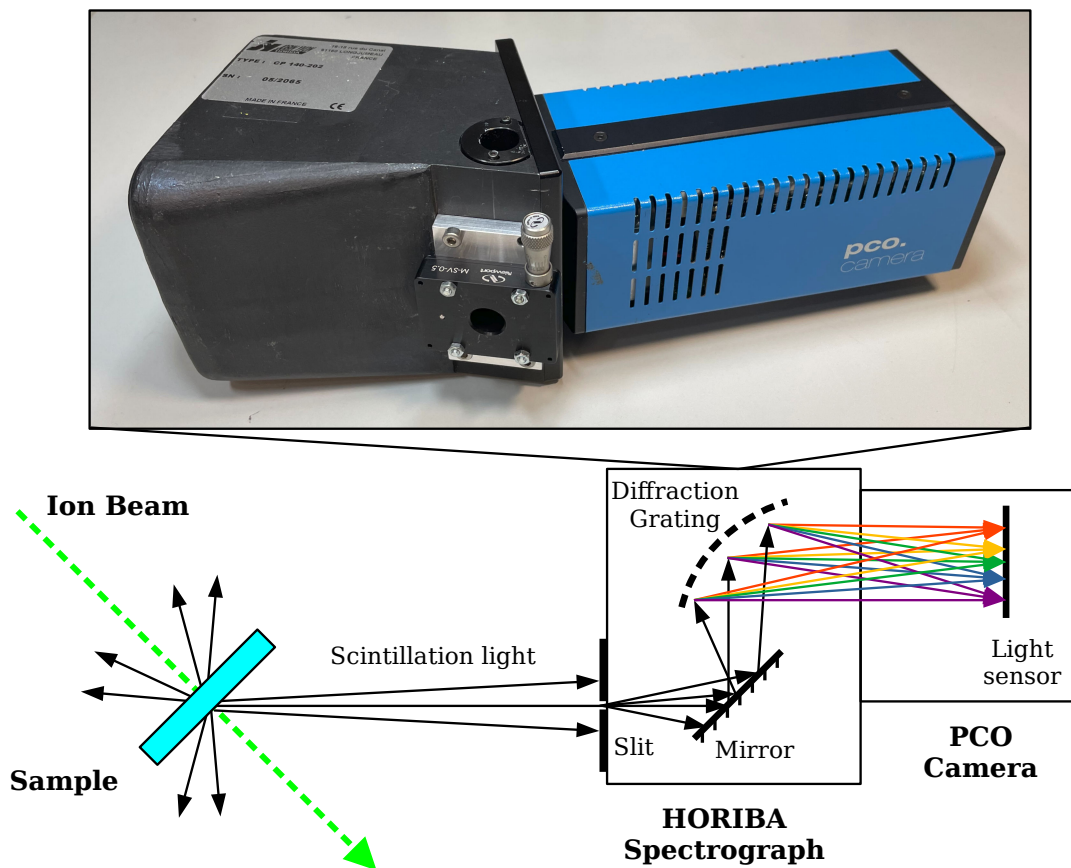


Figure 4.15: Schematic view of scintillation light spectrum measurement under relativistic heavy ion beam irradiation. The inset on top shows a photo of the Horiba CP 140-202 spectrograph attached to the PCO.1600 camera.

light photons in the ultraviolet (UV) and visible (Vis) wavelengths range, while “PCO.1600” is sensitive only to visible light. A more detailed specification of both PCO cameras can be found in references [134, 135].

Before experimental samples characterization, both spectrometer assemblies were calibrated using a discrete mercury–argon wavelength calibration source. Figure 4.16 shows the obtained calibration spectra. There are two lines which are visible in “PCO SensiCam QE” spectrum and missing in “PCO.1600” spectrum. The first line is at 313.16 nm and corresponds to the mercury emission line coming from the first order diffraction. The second line is observed at 507.3 nm and corresponds to the second order diffraction line of the 253.65 nm mercury emission. The absence of these short-wavelength lines in the “PCO.1600” spectrum is due to the low sensitivity of the “PCO.1600” camera to UV light. The broadness of the spectral lines for both spectrometer assemblies is due to the wide slit opening. The spectrometers entrance slits were opened wide to collect a sufficient amount of ionoluminescence light coming from investigated samples during irradiation. The slit opening reduced the resolution of spectrometers. In Figure 4.16 one can note that 404.66 and 407.78 nm as well as 576.96 and 579.07 nm lines are not resolved. Nevertheless, as it is shown further, the resolution of spectrometers is sufficient to resolve the NBE and DL emission bands from ZnO samples. This became possible due to larger separation of NBE and DL bands maxima and rather broad width of the emission bands in comparison to the Hg emission lines.

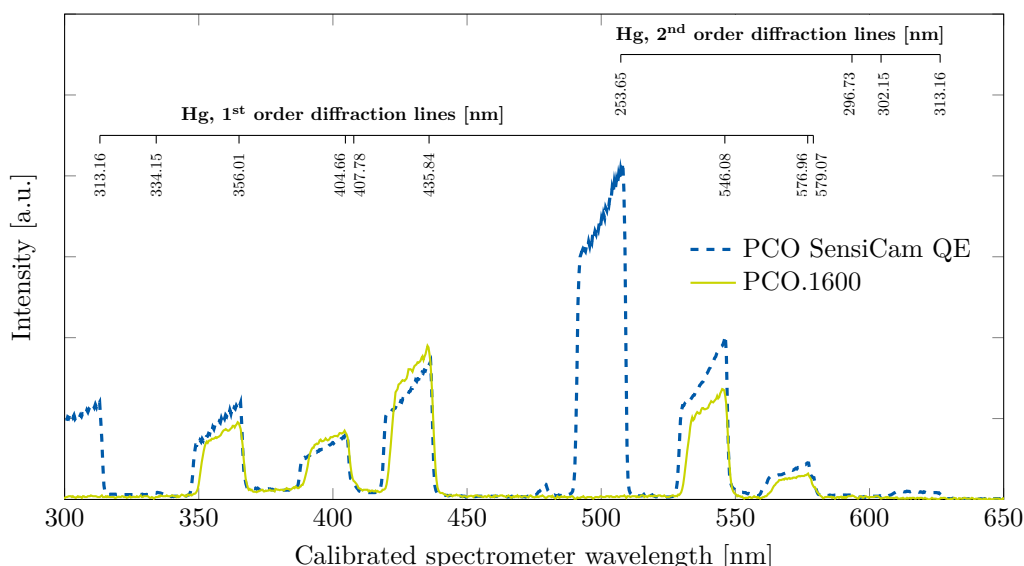


Figure 4.16: Calibration spectra recorded by spectrometer assemblies with “PCO SensiCam QE” (dashed blue line) and “PCO.1600” cameras (solid green line). Both first and second order diffraction lines of mercury emission are visible by “PCO SensiCam QE”. Only the first order lines are registered by “PCO.1600” due to its low sensitivity in the UV range.

During the ionoluminescence spectra measurements at HTP beam line, PCO cameras were acquiring one spectrum image per one spill extracted from SIS18 synchrotron. Thus, the acquisition time varied from 1 to 5 seconds, depending on the spill extraction time. The spectrum acquisition was synchronized with ion spills using the SIS18 timing system. The trigger plastic scintillator shown in Figure 4.5 was moved out from the beam during ionoluminescence spectra acquisition. The spectra images were saved in *.b16 binary format that stores 2D pixels array of the camera with recorded counts (Fig. 4.17). For each recorded spectrum, the number of ions per spill was recorded using an ionization chamber placed in front of the sample behind the aluminum collimator and a secondary electron monitor placed in front of the collimator inside the vacuum tube or the

beam line (see Figure 4.5). The typical beam intensity during the ionoluminescence spectra acquisition was in the order of 10^7 – 10^8 ions/spill.

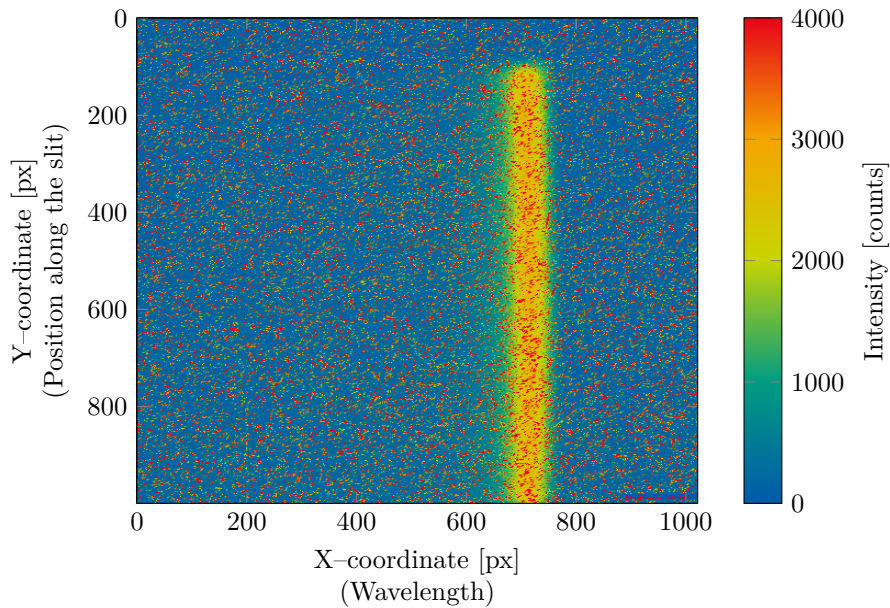


Figure 4.17: An example of the PCO camera image containing an ionoluminescence light spectrum originating from the ZnO(Ga) ceramic. The color map represents the number of counts at each pixel position. The wavelength resolution is along the X-coordinate. The position resolution along the spectrometer slit is on Y-coordinate of the camera image.

During spectra analysis, a horizontal projection of the 2D image from PCO camera was extracted using scripts written in Python. All spectra were corrected for background and normalized by the number of ions taken from ionization chamber and secondary electron monitor measurements.

4.6.2 Light output and scintillation decay times measurement at HTP

Ion induced luminescence light output and decay times were recorded using photomultiplier tubes placed at 60 mm distance from the surface of the sample (see Fig. 4.5 and Fig. 4.13). Photomultiplier signal waveforms, that correspond to individual ion impacts, were recorded using a Tektronix MSO58 oscilloscope with 2 GHz bandwidth. Photomultipliers were connected to the scope using approximately 5 m long coaxial cables with 50 Ohm termination.

The following two photomultiplier assemblies with different responses were used:

- **Hamamatsu (H7415), based on R6427 photomultiplier (PMT)** for light output measurement, because of a linear response of signal in a broad range of the PMT gain;
- **Hamamatsu (H13661)** for scintillation light decay time measurement, because of the fast rise time and short width of the response signal of the assembly.

For simplicity, Hamamatsu H7415 and H13661 assemblies will be referred to as slow-PMT and fast-PMT, respectively.

Voltage on slow PMTs was supplied and controlled remotely via Caen HV power supply. The supply voltage was varied from 700 to 1250 V depending on the ion species to adjust the slow-PMT gain values between 2×10^4 and 2×10^6 . Voltage on fast PMTs was supplied and controlled remotely via Rigol power supply. The fixed voltage of +5 V was sent to supply voltage and +2.2 V sent to control voltage contacts of fast PMTs. This corresponds to the maximum gain of the Hamamatsu (H13661) PMT assembly, around 2.4×10^4 , which was used in measurements with all ion species.

The fast-PMT signal rise time of 0.23 ns is located at the lower limit of the rise times that can be registered with 2 GHz bandwidth in the Tektronix oscilloscope.

Both slow- and fast-PMT response functions were characterized using 373 nm wavelength PicoQuant PDL800D laser providing 44 ps FWHM pulses at a fixed laser power. Slow PMTs response was characterized with short laser pulses at supply voltages varying from 600 to 1300 V, while fast PMT response was characterized only at one fixed supply voltage (+5 V sent to supply voltage and +2.2 V sent to control voltage contacts) as it has been used for samples characterizations. The Figure 4.18 shows responses of slow and fast PMTs used in the HTP experimental setup. One should note, that the slow-PMT signal rise/decay time and pulse width reduce with the increase in supply voltage, as shown in Figure 4.18a. The fast-PMT response signal shape does not change for different laser light intensities (no saturation or non-linearity in the investigated range) as shown in Figure 4.18b. The fast-PMT response is used further for ionoluminescence pulse shape deconvolution and extracting ionoluminescence rise and decay times, measured as it was earlier described in Equation 2.19.

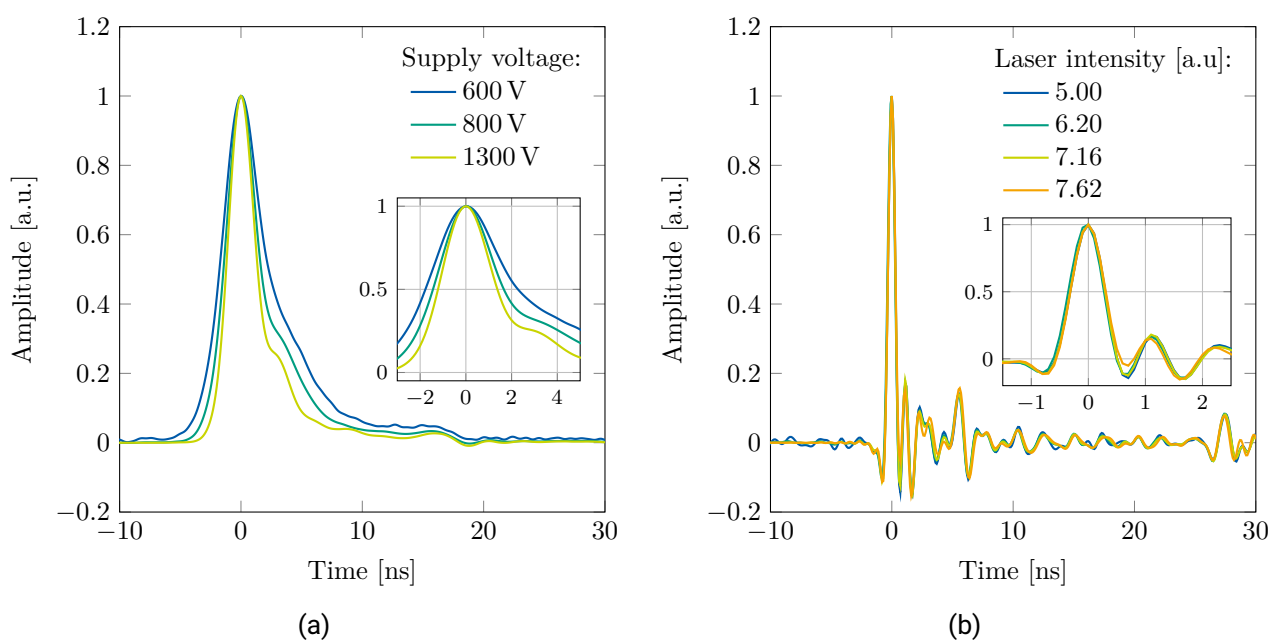


Figure 4.18: Typical response signals of the Hamamatsu H7415 at different supply voltages (a) and Hamamatsu H13661 at +5 V supply and +2.2 V control voltage for different intensity of the laser light (b). The inset plots show the response signals zoomed in around the maximum amplitude. All signals from (a) and (b) are scaled by the maximum amplitude.

The gain values of slow PMTs measured with the laser are shown in Figure 4.19. Further in this work, slow PMTs placed in front and back of the target holder can be distinguished by identification numbers LA4852 and LA4857, respectively.

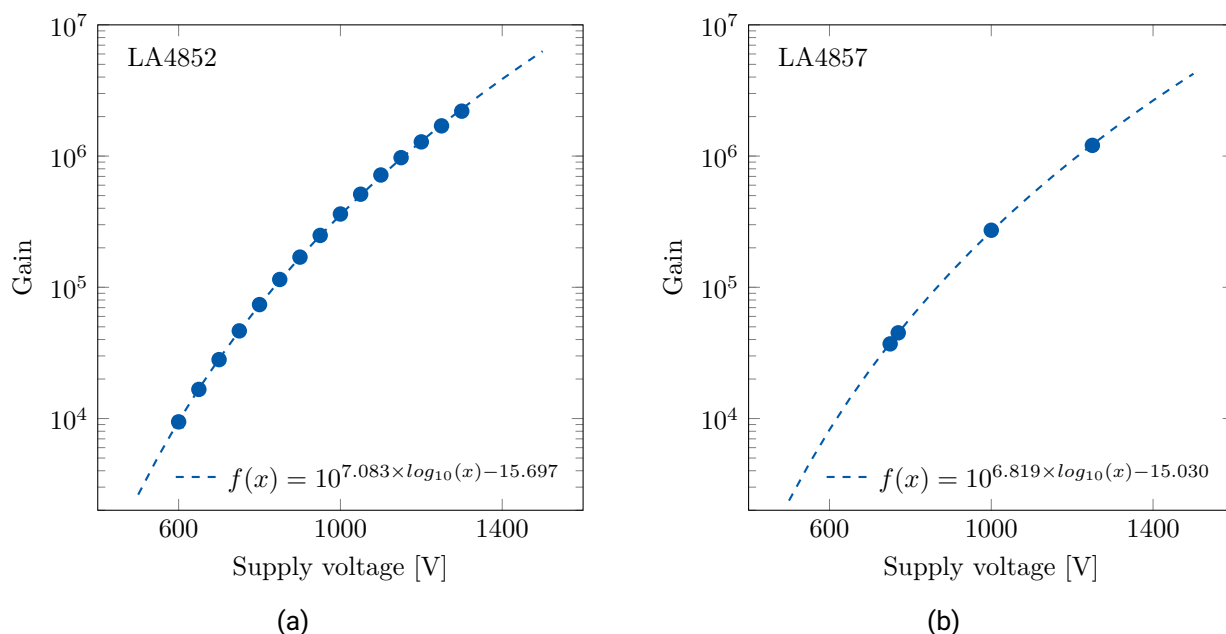


Figure 4.19: Gain of Hamamatsu H7415 slow photomultiplier assemblies placed on the front (a) and back (b) side of the target holder (identification numbers are LA4852 and LA4857, respectively). The dashed lines show the fit of the experimentally measured points.

The gain values shown in Figure 4.19 were used to recalculate PMT anode charge registered at different supply voltages into a PMT photo-cathode charge. The PMT photo-cathode charge is directly proportional to the intensity of the incident light at the PMT entrance window. We used the PMT photo-cathode charge for comparison of the scintillation light output from different samples irradiated with different ion species.

For each characterized sample, we recorded multiple PMT signals corresponding to individual ions passing through the sample. Signals from individual ions were recorded in separate 100 ns long waveform frames. For each sample characterization, we recorded 10000 to 50000 frames at the very initial stage of the irradiation and after reaching various fluences.

Samples irradiation is performed at beam intensities up to 10^7 – 10^8 ions/spill. During the characterization of samples using PMTs, the beam intensity is reduced to 10^3 – 10^4 ions/spill. The intensity is reduced to minimize the probability of two ions hitting the sample within less than 100 ns time window, thus preventing frames with multiple ion signals. For characterized samples, we recorded 10000 to 50000 frames at the very initial stage of the irradiation and after reaching various fluences.

4.7 Beam intensity and irradiation fluence monitoring for experiments at SIS18

The intensity and irradiation fluence during the experiments performed with ion beams delivered from SIS18 synchrotron were measured individually for each SIS18 spill by means of three detector types: scintillation detector, ionization chamber (IC), and secondary electron transmission monitor (SEETRAM). The combination of these detectors allows covering a broad range of beam intensities provided by SIS18. Scintillation detector is used for low beam intensities up to approximately 10^6 ions/s, ionization chamber is used for intermediate

intensities between 10^3 and 10^8 ions/s, and secondary electron transmission monitor is used at high beam intensities from 10^7 and higher.

The scintillation detector provides raw counts which are directly related to the number of ions passing through the detector active area. In contrary to that, IC and SEETRAM provide raw counts that are proportional to a charge created by the ion beam in the detector's active area. IC and SEETRAM provide indirect information on the number of particles in the beam. The raw counts from IC and SEETRAM are recalculated to a real number of ions as a result of a calibration relative to the scintillation detector.

4.7.1 Beam intensity measurements with scintillation detector

In a scintillation detector, each incident ion creates a light flash that is converted into an electric signal by a photosensitive device such as a photomultiplier tube (PMT). Figure 4.20a shows a typical output signal due to a single 300 MeV/u ^{74}Kr ion passage through a plastic scintillation detector. For the plastic scintillation detector based on BC400 or EJ212 scintillators, which are typically used for beam diagnostics at GSI, the signal amplitudes at the detector output are in the order of few tens to a hundred millivolts (depending on the PMT supply voltage, or gain). The output signal rise times are around two to three nanoseconds, and signal full-width-at-half-maximum is in the order of four to five nanoseconds. The amplitude distribution from multiple Kr ion signals is shown in Figure 4.20b. The window of signal amplitudes from 0 to 300 mV is typically used to set up a discriminator and count only high-amplitude pulses above the threshold. Such a discriminator scheme based on surpassing a threshold amplitude value provides raw counts that are directly the number of single ion passages (no need for scintillation detector calibration).

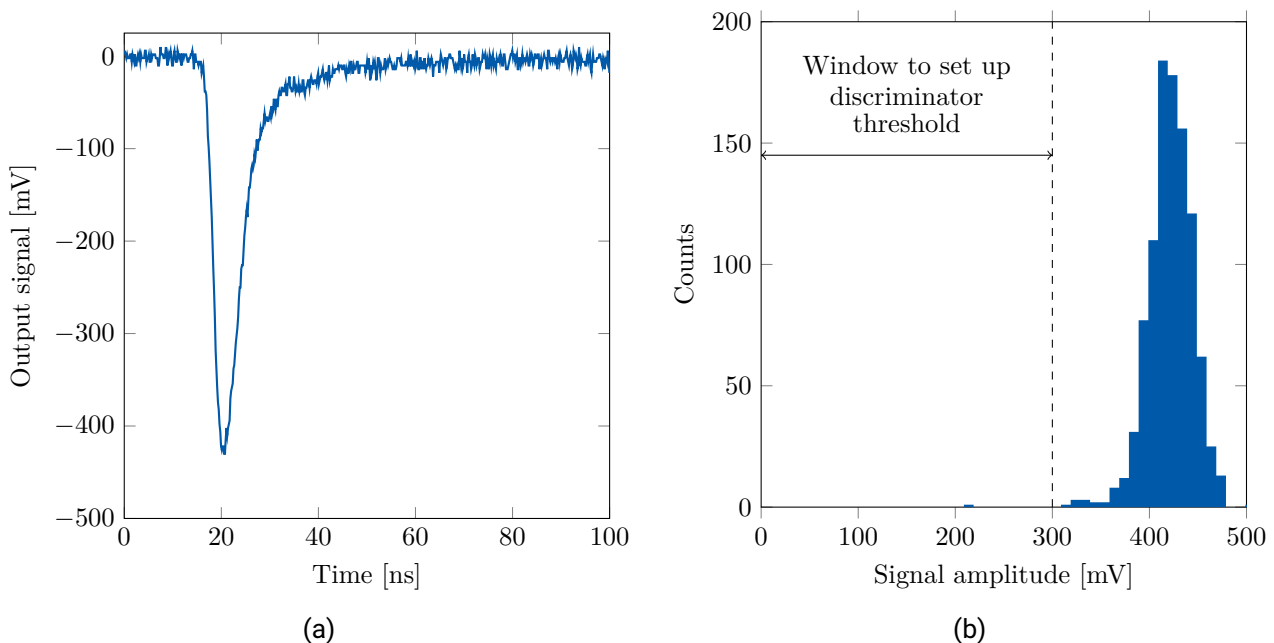


Figure 4.20: Standard signal of plastic scintillation detector created by a single 300 MeV/u ^{74}Kr ion impact (a). Typical amplitude distribution of signal of plastic scintillation detector (b). PMT was operating at 1000 V supply voltage ($\sim 3 \times 10^5$ gain value).

There are two main factors that can cause a systematic error during particles counting with a scintillation detector:

- *Setting a proper discriminator threshold:* on the one hand, the discrimination threshold should be high to exclude peaks that come from background noise. On the other hand, the discrimination threshold should not be too high to let all detector signals originating from real particles overcome the threshold (ions located at the left shoulder of the amplitude distribution from Figure 4.20b). Within the experimental measurements presented in this thesis, the discriminator threshold was set such that the background counting rate was <10 Hz, which leads to $<1\%$ systematic offset error originating from background counts in raw detector counts registered at 1 kHz sampling frequency. In Figure 4.20b an amplitude distribution of the plastic scintillation detector signals from ^{74}Kr ions at 300 MeV/u energy clearly demonstrates that at 100 mV discriminator threshold, 100% of incident ions produce a count (i.e., $\sim 0\%$ systematic scale factor error originating from signal amplitude distribution).
- *Detector dead time:* a raw count from an incident ion can be lost if it occurs too quickly following a preceding ion count. Two or more successive signals can overlap (pile-up) and thus cross the discriminator threshold only once. The dead time of the data acquisition used in the experiments of this thesis was about 50 ns and related to the length of a logical pulse sent by a discriminator to create a count. The loss of ion counts due to the pile-up grows with the increase in beam intensity. A systematic error in scintillation detector raw counts due to signal pile-ups can be estimated using a paralyzable model of dead time behavior [136]:

$$m = n \exp(-n\tau), \quad (4.1)$$

where m being the registered counting rate, n being the true interaction rate, and τ being the system dead time. Thus, the systematic error, ϵ_{syst} , from (4.1) in percent is the following:

$$\epsilon_{syst} = [(n - m)/m] \times 100\% = [1 - \exp(-n\tau)] \times 100\%. \quad (4.2)$$

Figure 4.21 shows that according to the paralyzable model of dead time, the scintillation detector used for experiments in this work is expected to have a systematic scale factor error that results in the miscount of particles. The number of miscounted particles increase with the number of registered counts and reaches $\sim 5\%$ at 10^6 Hz counting rate.

Calibration of the raw experimental counts registered by the plastic scintillator was made by adding the amount of missing counts taken from Figure 4.21b, and subtracting background counts.

It should be noted that Equations 4.1 and 4.2 assume the Poisson time distribution of ions in the beam, which is not the case for experiments at SIS18. Therefore, the paralyzable model provides only a lower limit of possible correction to the scintillation detector counts. It is not possible to completely cancel the contribution of the pile up of detector signals.

When scintillation detector data is used to estimate the number of ions per spill, the average number of ions per spill is calculated as the sum of the calibrated counts per sample recorded within the entire spill. The uncertainty in ion counts per spill is calculated as:

$$\Delta N_{spill} = \sqrt{\sum_{i=0}^{n_{samples}} (\epsilon_{rnd}^i)^2}, \quad (4.3)$$

where ϵ_{rnd}^i is the random error in counts registered for the i -th sample.

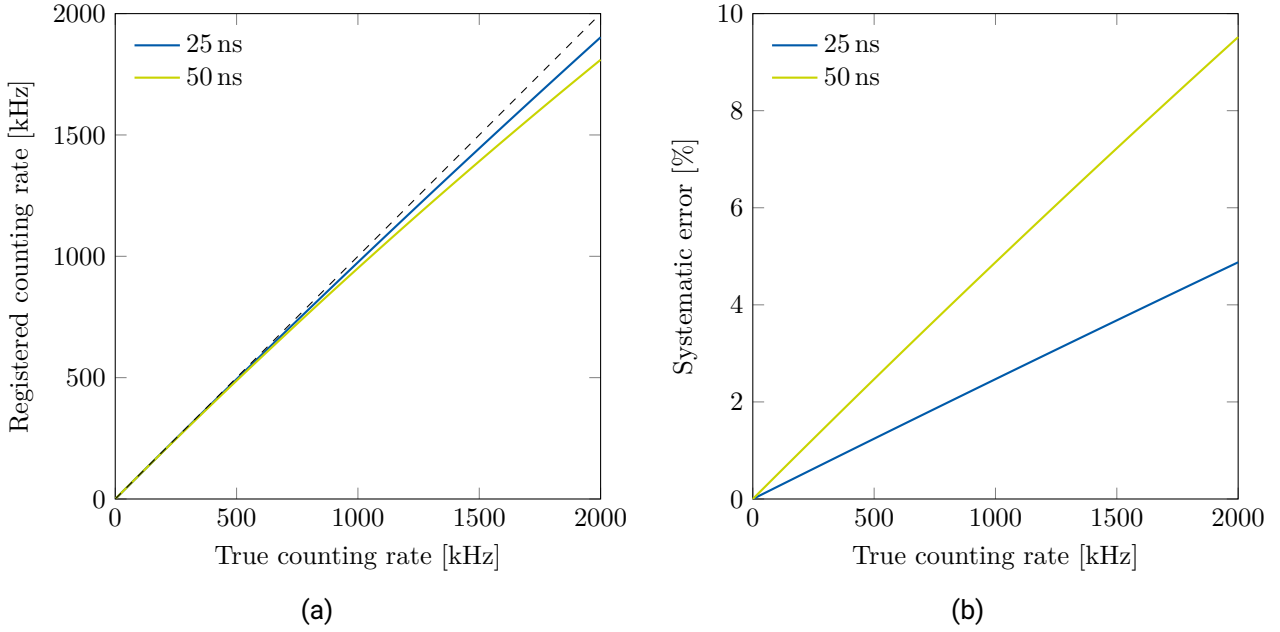


Figure 4.21: True counting rates versus registered counting rate for scintillation detector (a). Blue and green lines show true vs. registered rate calculated according to the paralyzable model from Equation 4.1 for 25 and 50 ns dead time, respectively. The dashed line shows “ $y = x$ ” line. Figure (b) shows the increase in systematic error due to signals pile-up for counts registered by scintillation detector with 25 and 50 ns dead time, according to Equation 4.2.

4.7.2 Beam intensity measurements with ionization chamber

When a charged particle passes through a gas volume of an ionization chamber (IC) it creates a number of positive and negative charges along the path. By applying a high voltage, we tend to collect all charges in gas. The voltage applied to the IC used in the experiments of this work were 1500 and 1200 V for the IC in the black box and in the PDC, respectively (IC1 and IC2 in Figure 4.5). At these voltages, the IC is in the ion saturation region, where ionization current (a charge collected by the IC per unit of time) is proportional to the incident beam intensity. In an IC used particularly for these experiments, the output was read out from an electrode where negative charges were collected.

The charge created by a single heavy ion projectile in the IC filled with Ar(20% CO₂) gas mixture can be estimated by knowing the partial energy losses by the incident particle and the so-called energy dissipation values (W -values) for Ar and CO₂, respectively. The total charge, Q_{tot} , created in the IC by a single ion can be calculated as:

$$Q_{tot} = e \times \left(0.8 \frac{dE_{Ar}}{W_{Ar}} + 0.2 \frac{dE_{CO_2}}{W_{CO_2}} \right), \quad (4.4)$$

where e is elementary charge, dE_{Ar} and dE_{CO_2} are energy losses per ion in Ar and CO₂, W_{Ar} and W_{CO_2} are energy dissipation per incident ion in Ar and CO₂.

The energy loss values were estimated using the ATIMA code [132]. The W -values for Ar and CO₂ are 26.3 and 33.0 eV/ion pair, respectively [136]. Thus, for example, one ²⁰⁹Bi ion at 300 MeV/u energy is expected to generate 1.23×10^{-13} C charge that is created in the active volume of the IC.

To read out the charge from the IC, a current to frequency converter (IFC) was used [137]. The IFC provides a single pulse count when a certain amount of charge is collected at the IC output. Depending on three available operation ranges (100 nA, 1 μ A, and 10 μ A) a single count at the IFC output is triggered after collecting approximately 0.1, 1, and 10 pC. The use of three IFC ranges allows covering beam intensities of the order of magnitude of 10^3 to 10^8 ions/s depending on detected ion species and energies.

Prior to experiments, calibration curves were measured for all IFCs. This was done by means of a Keithley 2450 SourceMeter supplying various DC currents to the IFC input, and Lecroy HDO6104A Oscilloscope reading out the output frequency from the IFC. Figure 4.22 shows an example of calibration curves recorded for one of the IFCs operating in three different ranges. The error in input current comes from the Keithley current source specification. The uncertainty in the output frequency mainly comes from the random error in the number of counts that were registered by the oscilloscope within the five seconds time frame. Since the typical IFC output is in the kHz frequency range, the statistical uncertainty of counts registered within five seconds is less than one percent.

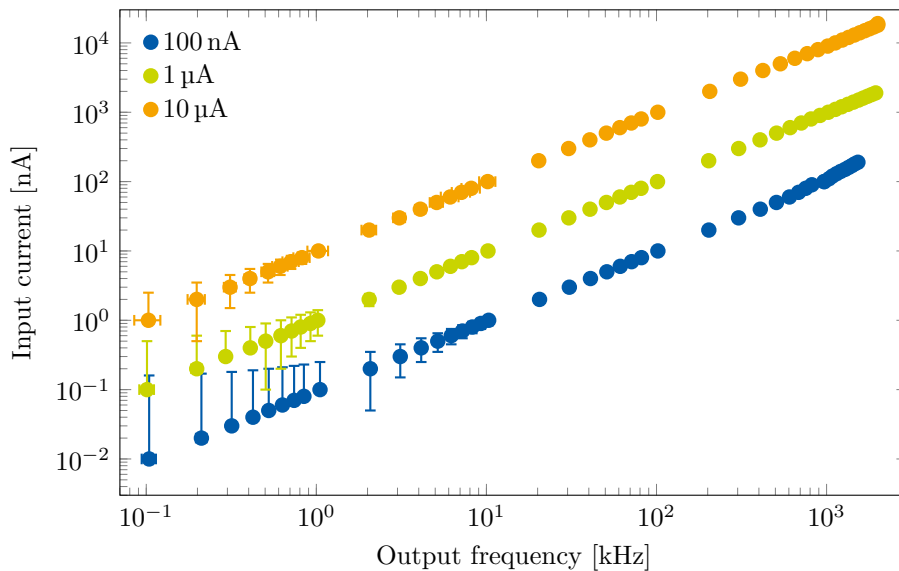


Figure 4.22: Typical current to frequency converter (IFC) calibration in three different operation ranges.

The output of the IFC at each range has an upper limit of 2 MHz. Depending on the beam intensity, the IFC operation range was selected such that 1 MHz output frequency is not exceeded to stay within the range of the linear response of the IFC.

In Figure 4.22 one can see that depending on the IFC range (100 nA, 1 μ A, or 10 μ A) it takes approximately 10^{-13} , 10^{-12} , or 10^{-11} C, respectively, in order to create one raw IFC count. As it has been estimated earlier, one bismuth ion at 300 MeV/u creates 1.23×10^{-13} C/ion, thus, the IFC operating at 100 nA range should produce approximately one raw IFC count per ion. In the case of 1 μ A, and 10 μ A range, IFC should produce one count per approximately 10 and 100 incident Bi ions, respectively.

The lower limit of the IC operation rate is given by the minimum current that can be read out at the IC output, which is about 1 pA and corresponds to approximately 10^3 ions/s. The upper limit of the IC operation range is given by the maximum output current from the IFC at which positive and negative charges in the gas cannot be collected effectively. At high beam intensities, the probability of a secondary electron recombination with a secondary ion increases quadratically with the beam intensity (processes like: $\text{Ar}^+ + e^- = \text{Ar}$). This leads to a

reduction of the registered IC output current. Figure 4.23 shows that the recombination processes start to play a role at about 5 μA , which corresponds to $\sim 5 \times 10^7$ ions/s beam intensity (^{209}Bi @ 300 MeV/u).

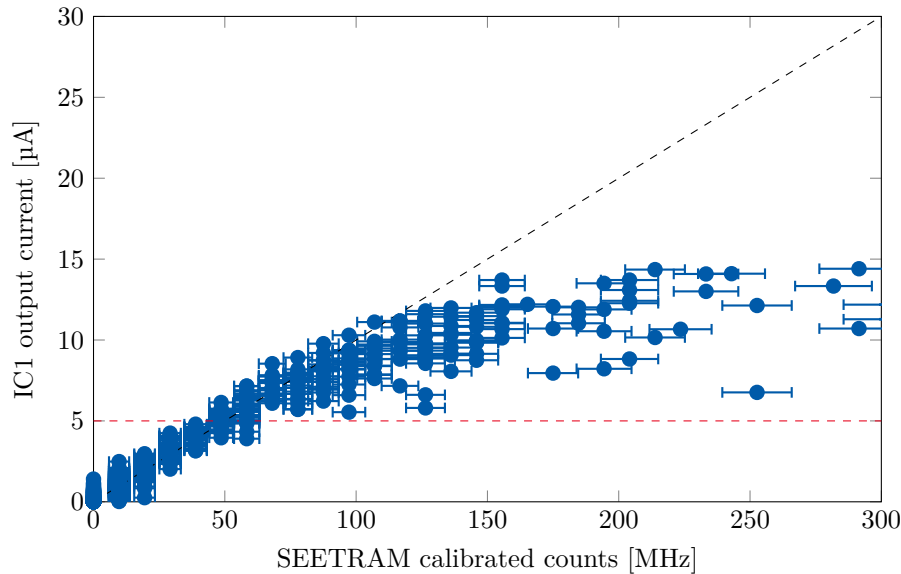


Figure 4.23: Correlation of ionization chamber output current and calibrated ion counts from secondary electron transmission monitor for 300 MeV/u ^{209}Bi ion beam. The black dashed line shows the linear dependency region. The red dashed line shows IC current upper limit around 5 μA at which IC counts linearity beaks down.

The calibration procedure of the IC raw counts consists of the following steps:

1. Check if raw counts of IFC connected to IC do not exceed IFC calibration frequency region and 5 μA output current limit;
2. Recalculate raw counts of IFC into IC output current in nanoamperes using IFC calibration curve;
3. Recalculate IC output current in nanoamperes into number of ions using ATIMA calculated charge per one incident ion.

4.7.3 Beam intensity measurements with secondary electron transmission monitor

When a charged particle hits a material, secondary electrons are emitted from the surface. This effect is used in secondary electron transmission monitors (SEETRAM) to measure high beam intensities above 10^8 ions/s (region where IC is incapable of linear response to the beam intensity). The SEETRAM used for experiments of this work performed at HTP consist of three 100 μm thick Al-foils that were placed in the high vacuum of the ion beam transfer line. A schematic view of the SEETRAM is shown in Figure 4.24. The two outer foils of the SEETRAM are biased by approximately +100 V to attract the secondary electrons emitted from the foils. The foil in the middle is connected to the same type of current to frequency converter as was previously discussed for the ionization chamber.

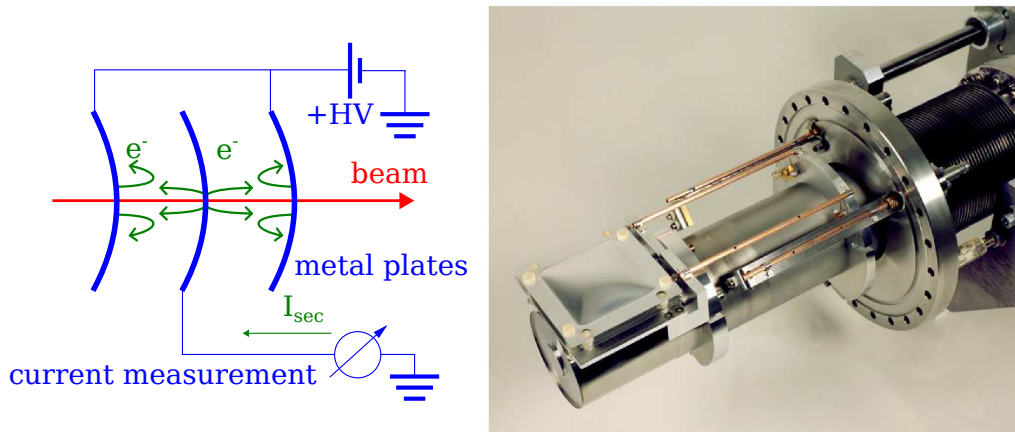


Figure 4.24: Schematic view of SEETRAM working principle (left) and a photo of the SEETRAM mounted in PDC used for experiments (right). The picture is taken from [138].

The secondary emission current registered at the SEETRAM output can be represented as [43]:

$$I_{\text{sec}} = Y \times \left(\frac{dE}{dx} \right) \times I_{\text{beam}}, \quad (4.5)$$

where Y is the yield factor that describes the amount of secondary electrons per ion, which is proportional to the energy deposited at the surface of the Al-foil. The yield factor of the Al-foil has been systematically studied for a large variety of ion species and the average value of $27.4 \text{ e}^- / (\text{MeV}/(\text{mg}/\text{cm}^2))$ with 5% accuracy has been reported [6, 138].

Other investigations indicate that the variation of the yield factor due can reach up to 25% [139]. The variation of the yield value depends on the Al-foil surface quality. The foil surface may vary, depending on the production and cleaning method used. In some cases, the emission yield can also change because of the surface modifications caused by the ion irradiation [140]. Therefore, in our experiments, calibrated counts from SEETRAM were corrected for a systematic scale factor error using experimentally measured calibrated counts from the IC. The SEETRAM calibrations versus the IC were performed at the beam intensities when the IC output current is below $5 \mu\text{A}$ to avoid charge recombination in the IC.

The IFC which was reading the output current from SEETRAM detector was operating at $1 \mu\text{A}$ range. SEETRAM counts were used for beam intensities below 10^9 ions/s. Random error in SEETRAM counts is mainly due to the statistical uncertainty in charge created by one ion and equals to approximately 5%.

5 Samples Characterization Results and Discussion

This chapter presents the results of the measurements as described in the previous chapter. This includes a comparison of ZnO ceramic samples prepared by different processes and having different doping. Luminescence and transmission spectra are compared to discuss the role of self-absorption in the reduction of the light output. The reduction of ionoluminescence light intensity is compared for two methods: spectroscopy and photomultiplier signal characterization. Spectra from X-ray-induced luminescence and ion-induced luminescence are compared. Light output recorded by the photomultiplier is compared for different ion species used to excite the light emission. The reduction of the emitted light intensity with increasing ion fluence is described within the Birks-Black model. Based on the results of the measurements, the best candidates for the scintillation detector prototype are defined.

5.1 In-situ ionoluminescence results under swift heavy ion irradiation

Ionoluminescence (IL) spectra measurements as a function of fluence for thermally-treated ZnO(In) samples exposed to Ca and Au ions at M3 beam line are shown in Figure 5.1. The IL emission is dominated by a peak in the UV spectral region for both ion species. The maximum IL intensity is observed around 388 nm wavelength and corresponds to the sub-nanosecond-fast near-band-edge (NBE) emission. The intensity of the NBE emission drops when increasing the irradiation fluence. No new ionoluminescence emission bands are observed, neither for Ca nor Au ion irradiations.

The change of the wavelength at which the maximum IL intensity is observed during Au and Ca irradiation is shown in Figure 5.2. In the case of Au ion irradiation, the peak position remains at 388 ± 1 nm up to a fluence of approximately 10^{10} Au-ions/cm². At higher Au fluences, the peak position shifts towards longer wavelengths, reaching 394 ± 1 nm at 2×10^{11} Au-ions/cm² fluence. In contrast to this, the maximum IL intensity position for the Ca ion irradiation does not change within the experimental measurement error in the whole investigated range up to 5×10^{12} Ca-ions/cm² fluence.

To get more detailed information about the emitted light, we fitted the measured spectra with a sum of multiple Gaussian peaks. Best fit results are obtained by a convolution of 5 emission peaks (Table 5.1 and Figure 5.3). The evolution of these peaks with increasing fluence shows that the amplitudes of all five peaks become smaller.

By comparing the ratios of amplitudes of peaks 1–3, it was found that the ratios remain constant with the increase in ion fluence, indicating that these peaks lose their amplitudes at a similar rate. Ratios of amplitudes of peaks 4 and 5 to peak 1 increase with the ion fluence, suggesting that the amplitude of peak 1 drops faster with fluence, than peaks 4 and 5. The ratio of amplitudes of peaks 4 and 5 remains constant with the increase in ion fluence, suggesting that the amplitude drop of these peaks occurs at a similar rate.

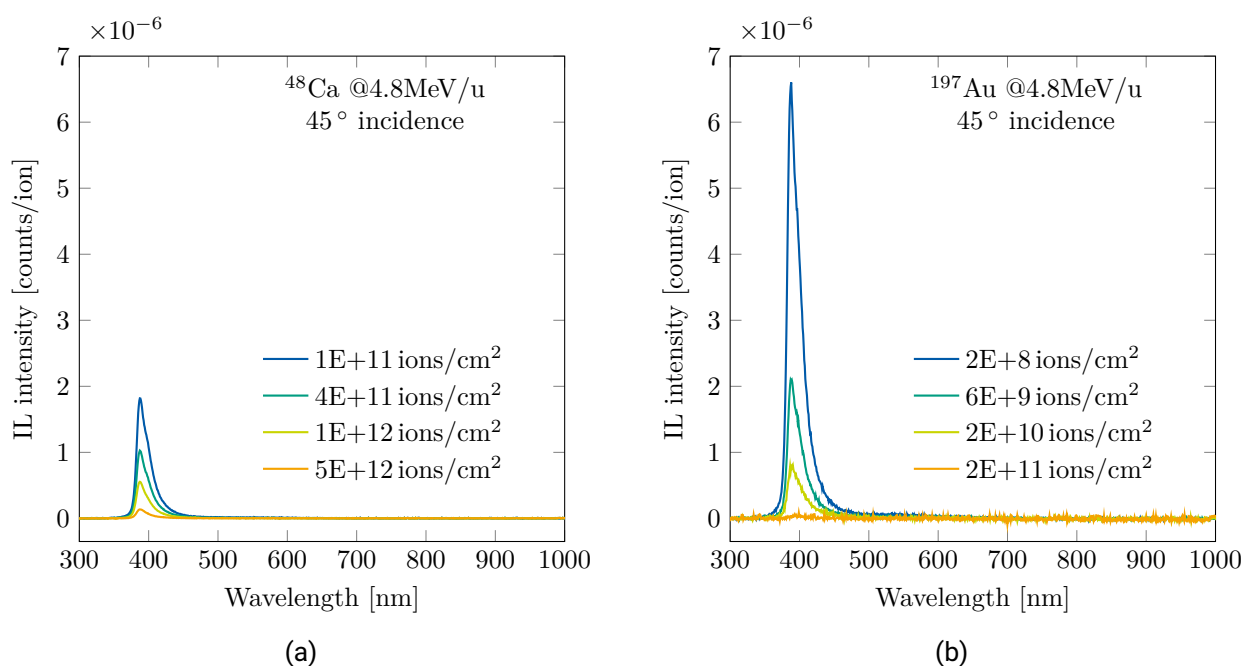


Figure 5.1: Ionoluminescence spectra of thermally-treated ZnO(In) scintillating ceramics. The irradiation was performed with 4.8 MeV/u ⁴⁸Ca (a) and ¹⁹⁷Au (b) ions under an angle of beam incidence of 45°.

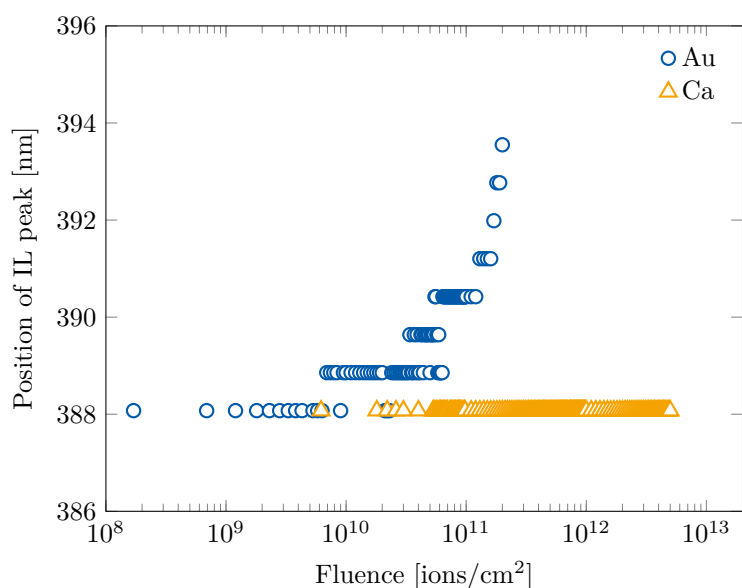


Figure 5.2: Evolution of the ionoluminescence peak position measured with increasing fluence for thermally-treated ZnO(In) scintillating ceramics. Irradiation was performed with 4.8 MeV/u ¹⁹⁷Au (open blue circles) and ⁴⁸Ca (open orange triangles) under an angle of beam incidence of 45°. The uncertainty of position is ±1 nm position.

Table 5.1: Parameters of Gaussian peaks found in thermal-treated ZnO(In) sample irradiated with 4.8 MeV/u Au at 1.7×10^8 fluence. Within the experimental errors, 98% of the measured spectral data points match the fit curve (R^2 of the fit is 0.9998)

	Amplitude (counts/ion)	Mean (nm)	Standard deviation (nm)
Peak-1	3.34×10^{-6}	386.1	3.7
Peak-2	3.24×10^{-6}	393.0	7.7
Peak-3	1.32×10^{-6}	402.3	11.8
Peak-4	5.36×10^{-7}	411.7	24.5
Peak-5	6.36×10^{-8}	503.7	77.3

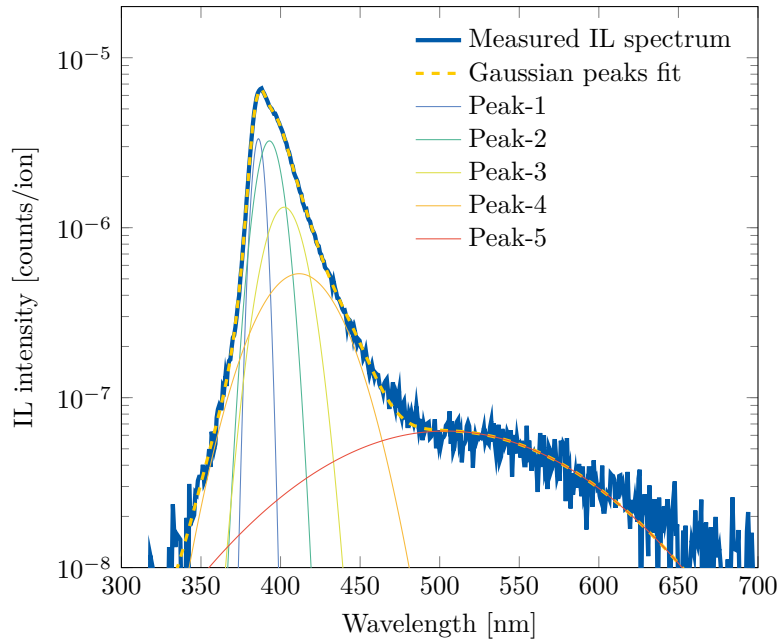


Figure 5.3: Gaussian peaks fit of the ionoluminescence spectrum of thermally-treated ZnO(In) sample irradiated with 4.8 MeV/u ^{197}Au to 1.7×10^8 ions/cm². The thick blue line represents the experimentally measured spectrum. The dashed yellow line is the fit by the sum of multiple Gaussian peaks. Thin color lines represent individual Gaussian peaks of the sum. The parameters of the peaks are listed in Table 5.1.

5.2 In-situ UV/Vis transmission results under swift heavy ion irradiation

The results of the in-situ optical transmission measurements on thermally-treated ZnO(In) samples under Ca and Au ion irradiation are shown in Figure 5.4. Due to the strong diffuse light scattering of the sample, only a small portion of transmitted light reaches the spectrometer, resulting in maximum registered light transmission values of approximately 0.025% for the pristine (not irradiated) sample.

In the UV light region around 387–390 nm, the non-irradiated (initial) samples exhibit a sharp decrease in transmission to zero, which corresponds to the so-called fundamental absorption. Notably, the maximum IL emission is detected in the same range. Therefore, the IL emission generated within the ZnO(In) sample is strongly absorbed.

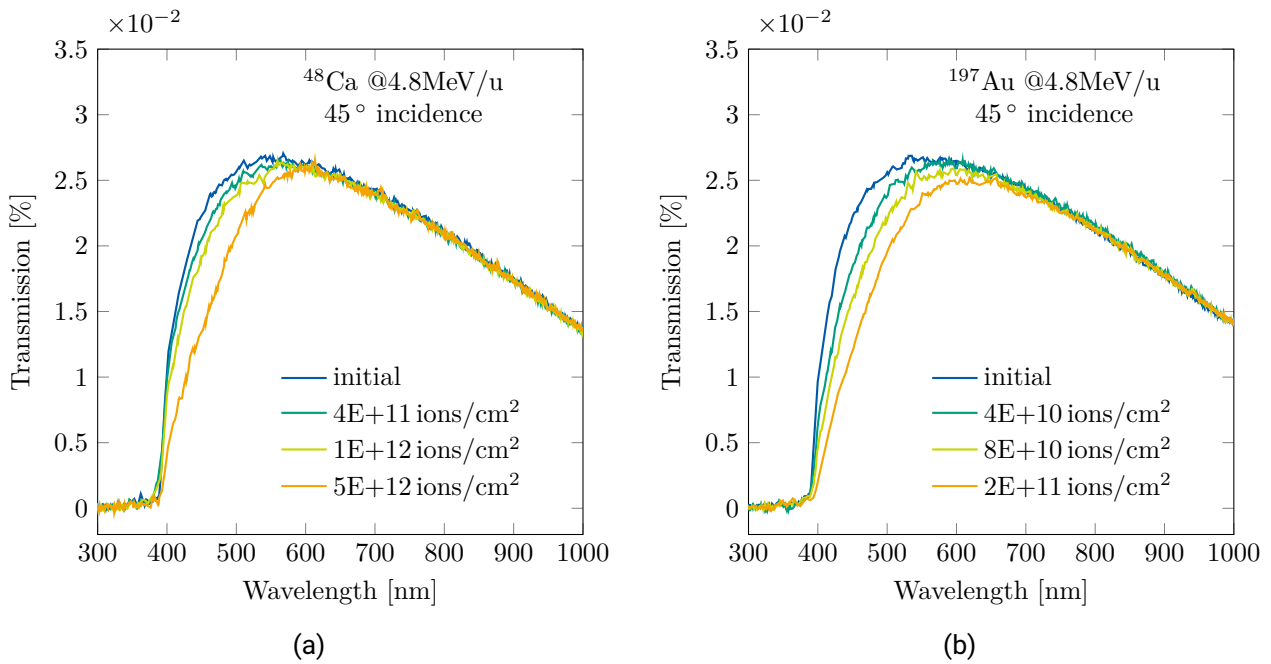


Figure 5.4: In-situ transmission spectra of thermally-treated ZnO(In) scintillating ceramics irradiated at various fluences with 4.8 MeV/u ^{48}Ca (a) and ^{197}Au (b) ions. The ion incidence angle regarding the sample surface was 45° .

In addition to the fundamental absorption edge, there is a lower transmission in the infrared (IR) spectral region between 600 and 1000 nm for non-irradiated samples. Such a lower transmission is not observed in pure non-irradiated ZnO. The loss of transmission of ZnO(In) in the IR region is due to free charge carriers introduced in the conduction band by In^{3+} impurity substituting Zn cations. The concentration of free charge carriers depends on the concentration of the impurity. The position of the absorption maximum shifts to a shorter wavelength with increasing free electron concentration. According to infra-red reflectance measurement [16] the maximum absorption by free electrons in ZnO(In) having 0.13 wt.% indium concentration is observed around $6\ \mu\text{m}$ wavelength, which is not reachable by our equipment.

After exposing our samples to ion irradiation, we observed a reduction in light transmission in the 390–700 nm wavelength range. The transmission remained unchanged for the higher wavelength region of 700–1000 nm, which can be an indirect indication of a constant concentration of free electrons in the conduction band, introduced by In^{3+} impurity.

The most pronounced change of the light transmission spectra after Ca or Au irradiation occurs at the fundamental absorption edge (roughly 395–400 nm). For the sample irradiated with up to 5×10^{12} Ca-ions/ cm^2 , the transmission at 400 nm is reduced by 65% compared to its initial value before irradiation. Whereas, the reduction in ionoluminescence intensity at 400 nm is 95% thus much more pronounced (as seen in Figure 5.5). For the Au ion irradiation to 2×10^{11} ions/ cm^2 , the transmission at 400 nm decreased by 85% and the ionoluminescence intensity at the same wavelength decreased by 99.5% of its initial value (as shown in Figure 5.6). Therefore, the ionoluminescence intensity drops more rapidly than the reduction in light transmission. This suggests that the reduction in sample transmission is not the main cause of the observed IL intensity loss after both Ca and Au irradiation. Instead, the reduction in IL intensity can be attributed to a decrease in the number of luminescent centers in the sample due to radiation damage.

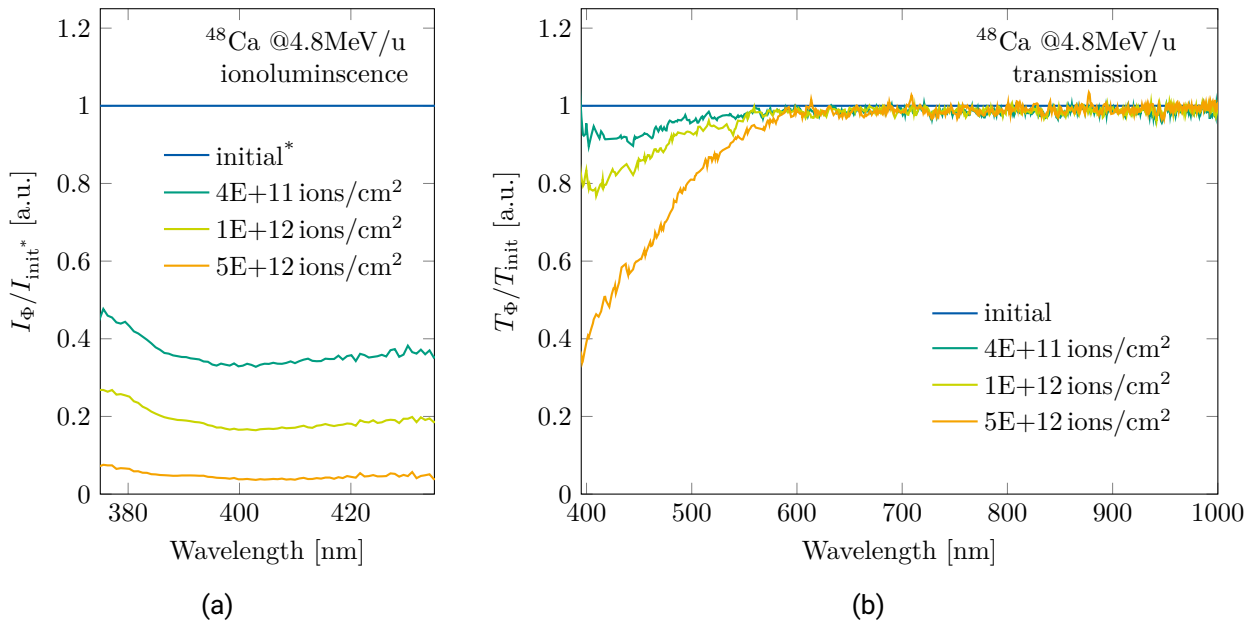


Figure 5.5: Thermally-treated ZnO(In) ceramic at various fluences of 4.8 MeV/u ^{48}Ca ion irradiation at 45° beam incidence. Relative ionoluminescence intensity $I_{\Phi}/I_{\text{init}^*}$ (a) and relative optical transmission T_{Φ}/T_{init} (b) spectra. The initial IL spectrum corresponds to 6×10^9 Ca – ions/cm² fluence.

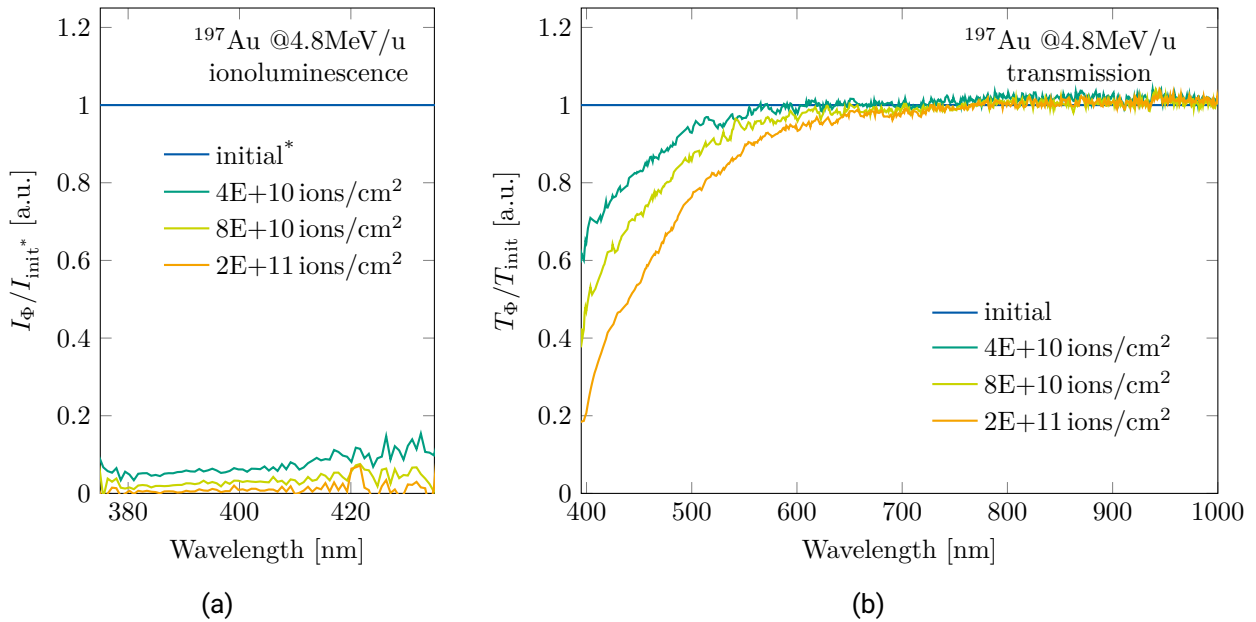


Figure 5.6: Thermally-treated ZnO(In) ceramic at various fluences of 4.8 MeV/u ^{197}Au ion irradiation at 45° beam incidence. Relative ionoluminescence intensity $I_{\Phi}/I_{\text{init}^*}$ (a) and relative optical transmission T_{Φ}/T_{init} (b) spectra. The initial IL spectrum corresponds to 2×10^8 Au – ions/cm² fluence.

In comparison to the thermally-treated ZnO(In) ceramic, Figure 5.7 displays the changes in ionoluminescence and light transmission spectra of a plastic scintillator caused by 4.8 MeV/u Ca ion irradiation at different fluences. The plastic scintillator shows several overlapping emission bands, with two main peaks at 340 nm

and 418 nm wavelengths. The 418 nm band is typically utilized in scintillation detector applications due to the transparency of the scintillator to this wavelength. The 340 nm band is below the absorption edge and therefore is emitted only from the plastic scintillator surface, while it is absorbed in the material volume. The intensity of both peaks decreases as the ion fluence increases. Notably, the rate of damage for both emission bands in plastic is much faster than that observed for the ZnO(In) ceramic sample. The plastic scintillator's emission decreases down to the background noise level approximately between 2×10^{11} – 5×10^{11} Ca-ions/cm², while a similar effect occurs for ZnO at a ten-fold larger fluence.

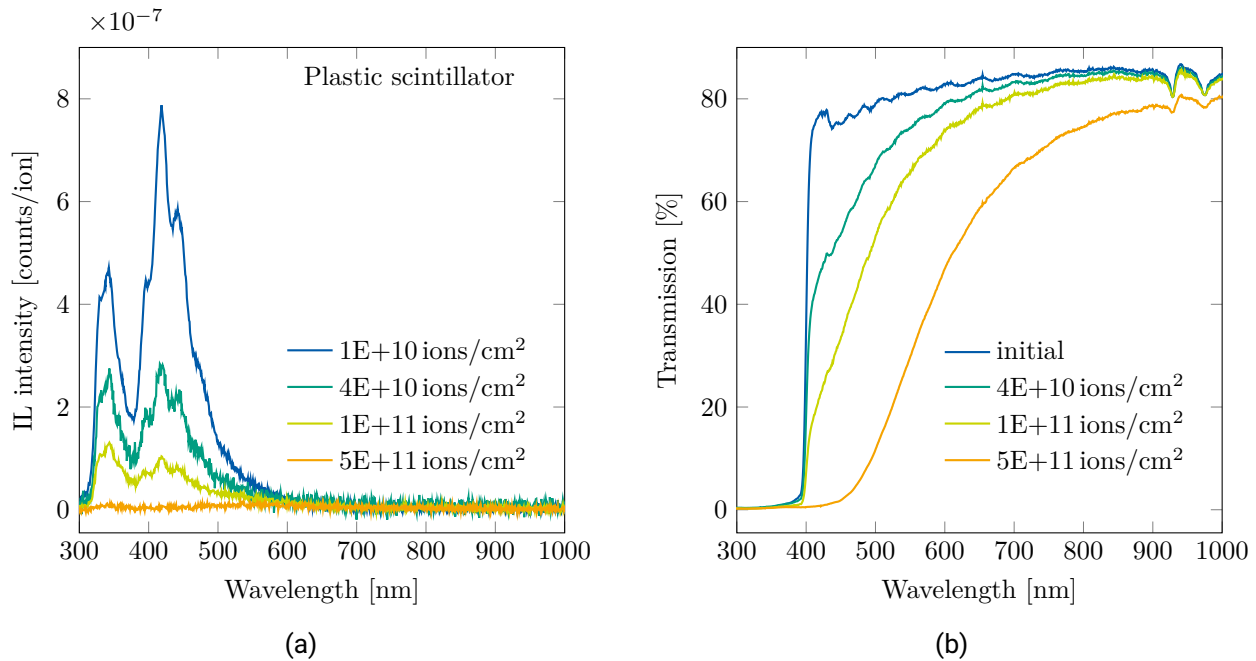


Figure 5.7: Ionoluminescence (a) and light transmission (b) spectra of a plastic scintillator irradiated at various fluences with 4.8 MeV/u ⁴⁸Ca ions. The ion incidence angle with respect to the sample surface was 45°.

5.3 X-ray induced luminescence of pre-irradiated ZnO(In) samples

Figure 5.8 shows X-ray induced luminescence spectra of initial ZnO(In) and thermally-treated ZnO(In) ceramics after 8.3 MeV/u Au ion irradiation at different fluences. Both samples prior to irradiation have a pronounced NBE emission that has a maximum intensity of around 389 nm. It should be noted that for the thermally-treated sample, the NBE emission intensity is approximately 1.6 times larger than for the initial ZnO(In). Both initial and thermally-treated samples exhibit additional deep level (DL) emission with a maximum of around 550 nm for pristine samples, which shifts to around 620 nm for irradiated samples. For both samples, the DL intensity is at least an order of magnitude weaker than the NBE luminescence. No spectra changes were observed at high fluences from 10^{12} to 10^{13} ions/cm². None of the samples showed new emission peaks appearance.

Both samples exhibit an exponential decrease of the NBE intensity with increasing ion fluence. The NBE peak wavelength shifts from 389 to 400 nm with the increase in fluence up to 5×10^{11} Au-ions/cm² for both initial

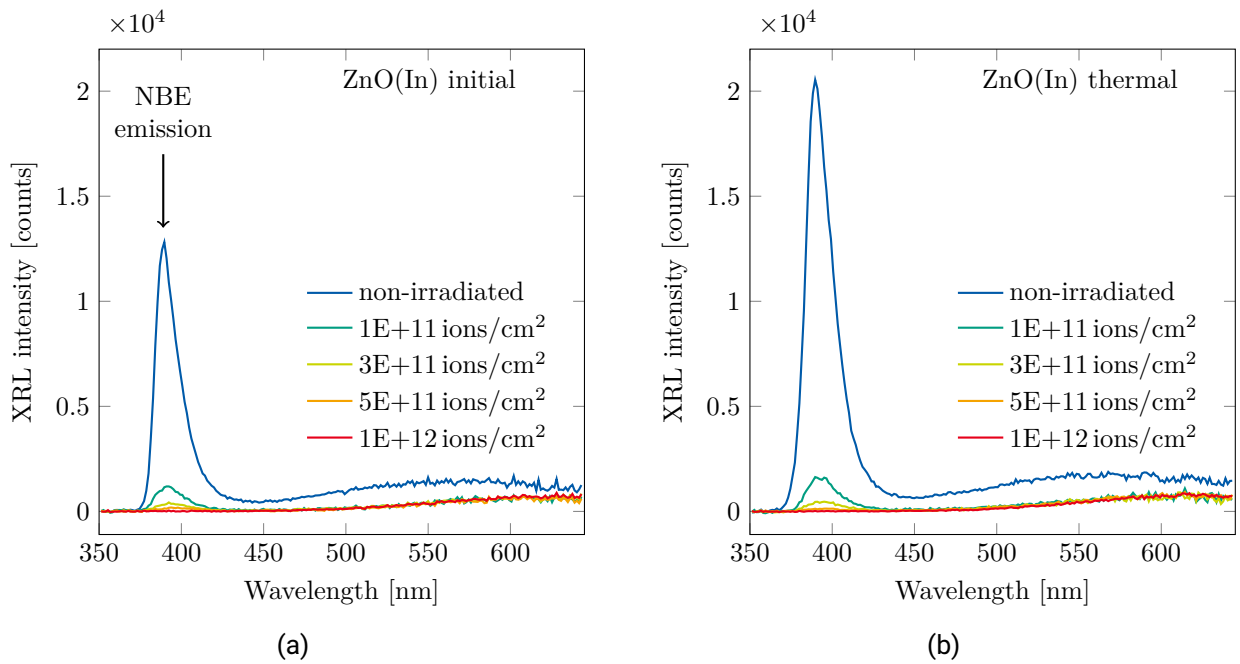


Figure 5.8: X-ray induced luminescence spectra of initial (a) and thermally-treated (b) ZnO(In) ceramic scintillators irradiated at various fluences with 8.3 MeV/u ^{197}Au ions. The peak at 389 nm is assigned to near-band-edge emission (NBE).

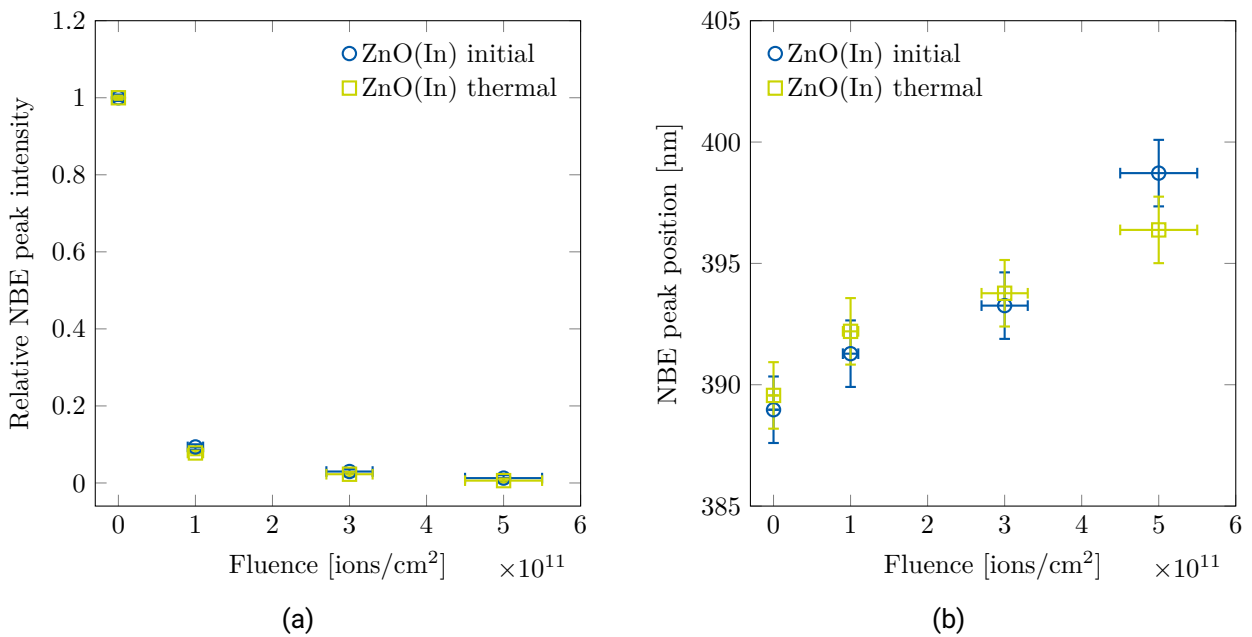


Figure 5.9: Relative change of the X-ray induced luminescence NBE intensity (a) and shift of the NBE peak position (b) for initial and thermally-treated ZnO(In) ceramic samples irradiated at various fluences with 8.3 MeV/u ^{197}Au ions.

and thermally-treated samples. The relative intensity change and wavelength shift of the NBE emission as a function of 8.3 MeV Au fluence for initial and thermally-treated ZnO(In) ceramics are shown in Figure 5.9.

Within the experimental error, there is no difference between the response of the initial and thermally-treated ZnO(In) samples to high fluence irradiation with 8.3 MeV/u Au ions.

5.4 Changes of total optical transmission under swift heavy ion irradiation

Figure 5.10 shows the total transmission spectra of initial and thermally-treated ZnO(In) samples irradiated with 8.3 MeV/u Au ions. Prior to irradiation, materials exhibit the fundamental absorption edge at ~ 390 nm and reduced transmission in the IR region due to indium doping (as was discussed earlier). The maximum transmission of 45% for the initial and 18% for the thermally-treated ZnO(In) sample is observed at 480 nm and 470 nm wavelength, respectively.

The pristine samples were broken into multiple pieces that were irradiated to different fluences. As a result of ion irradiation, both initial and thermally-treated samples exhibit an evident loss of transmission in the wavelength range below 600 nm. At the higher wavelength region from 600 up to 1000 nm, the transmission values scatter around the pristine sample and do not show any clear trend as a function of fluence.

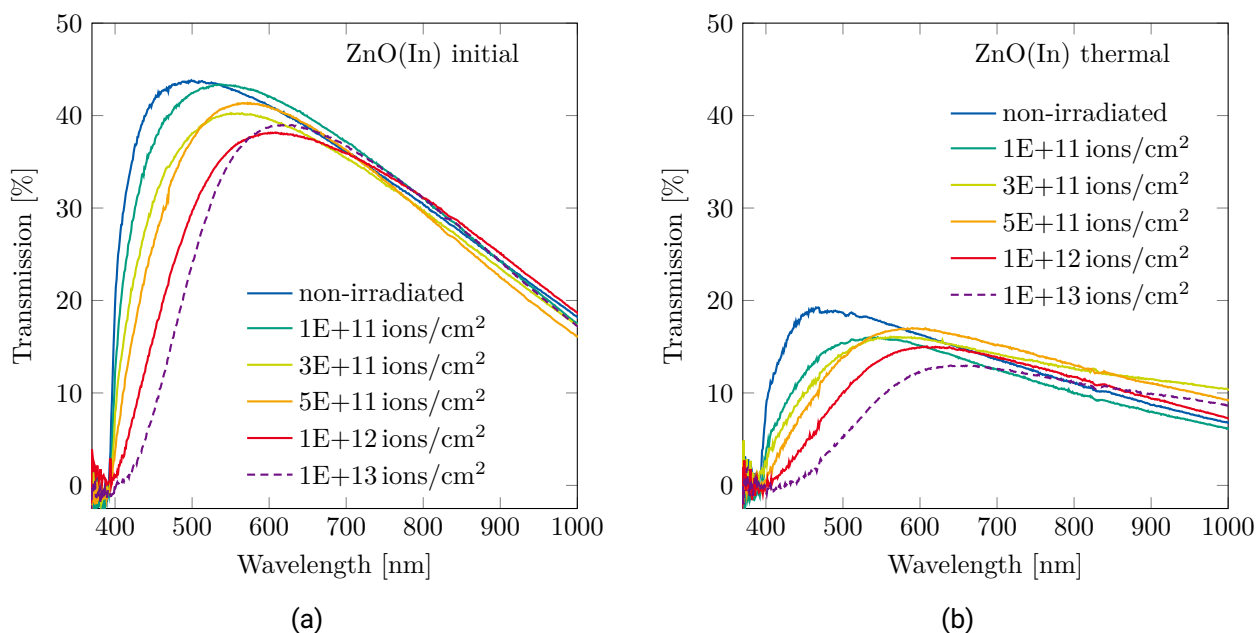


Figure 5.10: Total transmission spectra of initial (a) and thermally-treated (b) ZnO(In) ceramic scintillators irradiated at various fluences with 8.3 MeV/u ^{197}Au ions.

It has been reported that the irradiation of ZnO single crystals with 700 keV O ions and 1.2 MeV Ar ions results in transmission losses in the blue spectral region [28]. The authors discussed the possible role of oxygen vacancy (V_{O}) defects in photon absorption around 409 nm, resulting in sample coloration. However, another report commented on the possible role of zinc vacancies (V_{Zn}) defects for sample coloration [141, 142]. It was suggested that V_{Zn} defects result in absorption at ~ 420 nm. The available experimental data is not sufficient to make a clear statement about whether zinc or oxygen vacancies are responsible for coloration in our samples.

Figure 5.11a shows the evolution of the absorption edge cut-off wavelength as a function of fluence. The cut-off scatters from 390 to 400 nm for both initial and thermally-treated samples, irradiated with 8.3 MeV/u

Au from 0 to 10^{12} ions/cm². The correlation between the NBE peak position shift measured by X-ray-induced luminescence and absorption edge cut-off wavelength measured by total transmission is shown in Figure 5.11b. This plot shows that the change in the band gap leads to the corresponding change in the NBE luminescence peak position.

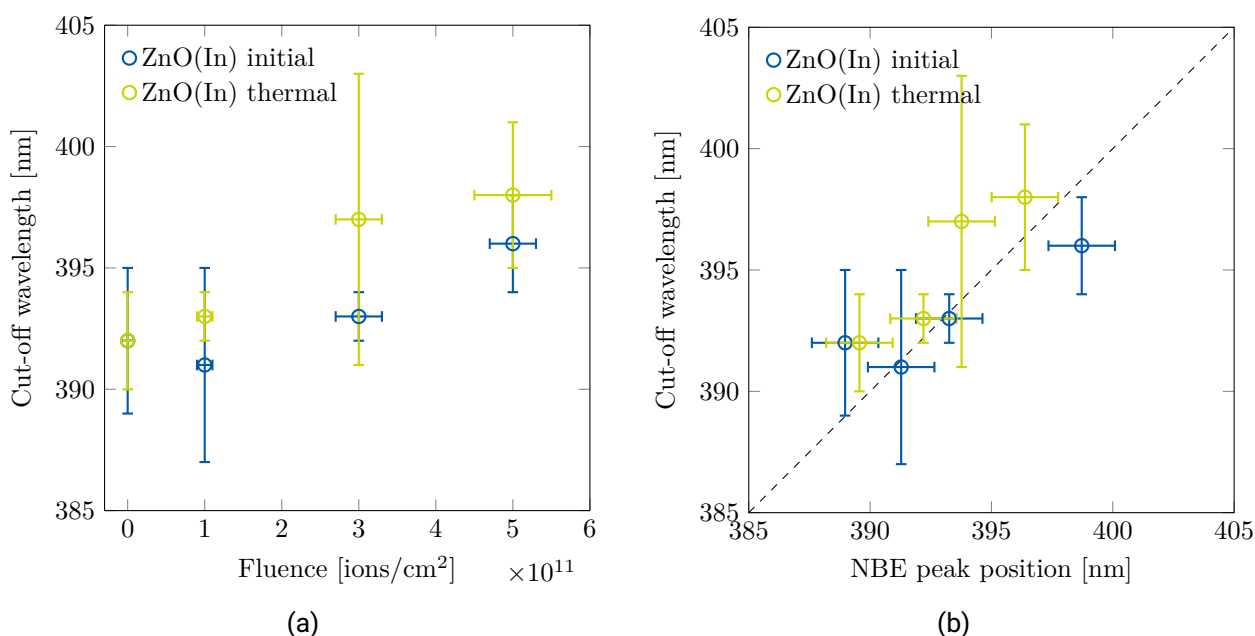


Figure 5.11: Wavelength of absorption edge cut-off as a function of fluence (a) and correlation of the cut-off wavelength vs. NBE luminescence peak position (b) for ZnO(In) ceramic scintillators irradiated at various fluences with 8.3 MeV/u ¹⁹⁷Au ions.

5.5 Raman spectroscopy characterization results

Figure 5.12a shows Raman spectra of pristine single crystalline ZnO with various crystal plane orientations, as well as undoped ZnO ceramic. The Raman peaks between 200 and 1000 cm⁻¹ are in agreement with previously described vibrational modes of ZnO [143].

For <11-20> and <10-10> oriented ZnO single crystals, vibrational modes are observed at 330 (corresponding to $E_2^{\text{high}}-E_2^{\text{low}}$), 375 ($A_1(\text{TO})$), 407 ($E_1(\text{TO})$), and 436 cm⁻¹ (E_2^{high}). In addition to these modes, the ceramic ZnO sample exhibits 535 (corresponding to $E_2^{\text{high}}+E_2^{\text{low}}$), 577 ($A_1(\text{LO})$), and 583 cm⁻¹ ($E_1(\text{LO})$). The absence of $A_1(\text{LO})$, $E_1(\text{LO})$, and second order mode from $E_2^{\text{high}}+E_2^{\text{low}}$ in single crystalline samples is due to the lack of control of the light polarization and sample orientation during Raman spectra measurements.

Figure 5.12b shows Raman spectra of initial and thermally-treated ZnO(In), as well as initial ZnO(Ga) ceramics. An additional band, that is not present in pure ZnO samples, appears around 480 cm⁻¹. It can be possible that In and Ga doping introduce new vibrational bands. For example, the E_2^{high} vibrational mode where Zn^{2+} ions are substituted with In^{3+} or Ga^{3+} impurity may shift from 436 to 480 cm⁻¹. However, the exact nature of the 480 cm⁻¹ band is not clear. Previous studies indicate that the gallium doping of ZnO, depending on its concentration (0.1–5%), results in new bands at 277, 512, 583, 624, 631, and 644 cm⁻¹ [144]. These

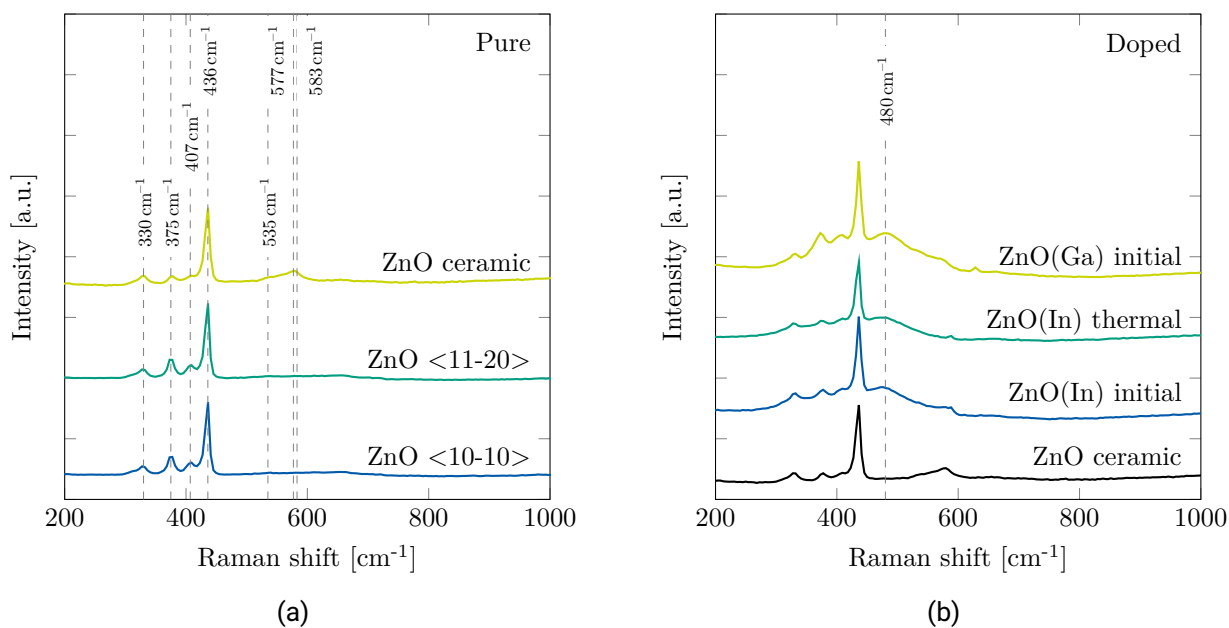


Figure 5.12: Raman spectra of pure ZnO single crystals and ceramic (a). Raman spectra of In- and Ga-doped ZnO ceramics (b).

bands overlap with the main vibrational modes of ZnO and cannot be deconvoluted. To our knowledge, the 480 cm⁻¹ band has not yet been reported previously in the literature.

Regarding the effect of thermal treatment in (Ar/H₂) atmosphere, we could not find any difference in Raman spectra before and after thermal treatment for both In- and Ga-doped ZnO samples.

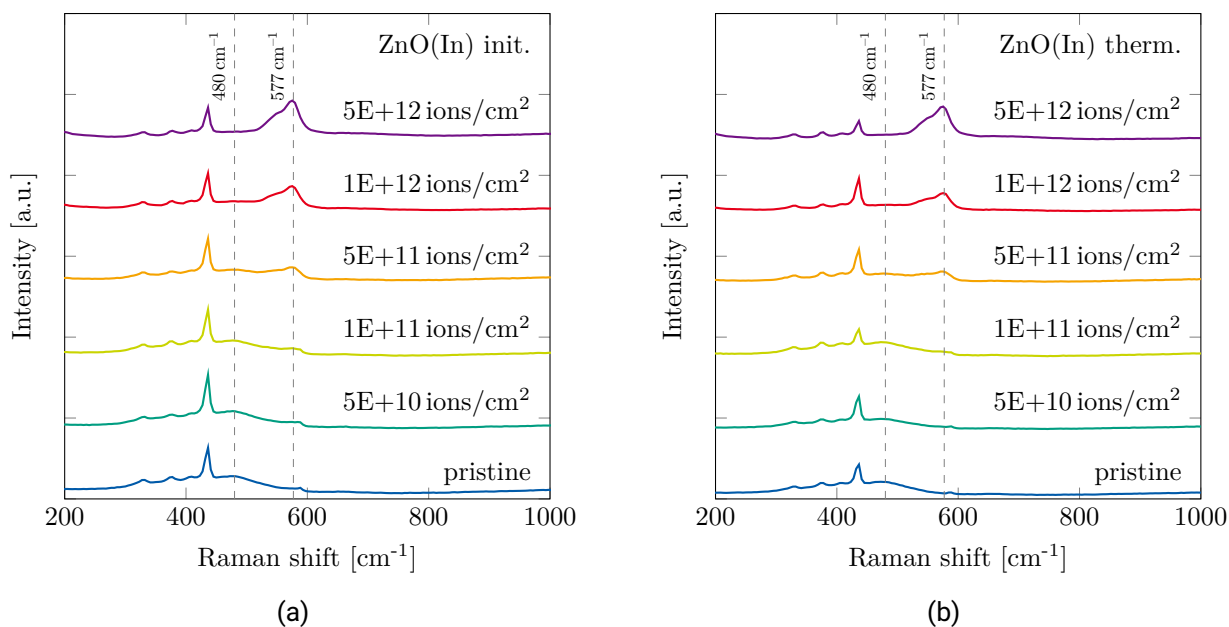


Figure 5.13: Raman spectra of initial (a) and thermally-treated ZnO(In) (b) ceramics irradiated with 8.3 MeV/u Au ions of different fluences.

Figure 5.13 shows Raman spectra of initial and thermally-treated ZnO(In) samples irradiated by 8.3 MeV/u Au to different fluences up to 5×10^{12} ions/cm². There is no significant change in Raman spectra up to approximately 3×10^{11} Au – ions/cm². Starting from 3×10^{11} ions/cm², the intensity of the 480 cm⁻¹ band reduces and simultaneously the band around 535, 577 and 583 cm⁻¹ increase.

The growth of the vibration bands in the 520–600 cm⁻¹ range has been previously attributed to the formation of oxygen vacancies (V_O) by Song *et.al* [29]. The authors investigated pure ZnO single crystals irradiated with 350 MeV $^{56}\text{Fe}^{21+}$ ions. The lowest fluence at which the authors published Raman spectrum of the irradiated ZnO was 5×10^{12} Fe – ions/cm², and this spectrum already had distinctive changes in 520–600 cm⁻¹ bands. Therefore, from the publication by Song *et al.* it is not clear at which fluence the V_O defects start to play a distinctive role in Raman spectra change. In other words, it was not stated whether Zn_i and V_O defects start to change the Raman spectrum immediately from a pristine sample, or if there is some threshold fluence, at which the effect starts to be visible by Raman spectroscopy. In Figure 5.13, one can see that V_O defects formation starts to bring distinctive contribution to the Raman spectra only above 3×10^{11} Au – ions/cm².

Finally, comparing the Raman spectra to X-ray induced luminescence (XRL) spectra shown in Figure 5.8, one can see that the most drastic intensity loss occurs up to 3×10^{11} Au – ions/cm², while no distinctive change in Raman spectra is observed in this fluence range. A similar behavior has also been observed for 300 MeV/u Bi and U ion irradiations. This indicates that the observed loss of luminescence light intensity cannot be directly ascribed to any change in ZnO vibration modes. On the other hand, according to Ref. [29], luminescence deterioration can be very sensitive to formation of Zn_i and V_O defects.

5.6 Ionoluminescence spectroscopy under relativistic heavy ion irradiation

Figure 5.14 compares ionoluminescence spectra of pristine ZnO ceramic samples prepared by different manufacturing processes exposed to U ions at 300 MeV/u energy. Compared to pure ZnO single crystals, doping with In and Ga results in a major increase in the light output. Initial ZnO(In) yields a roughly two times greater NBE emission intensity than initial ZnO(Ga) ceramic. All doped samples exhibit significantly suppressed DL emission and enhanced NBE emission, compared to pure ZnO crystals. This agrees with the results of previous studies (photoluminescence and X-ray-induced luminescence characterization) [16, 117]. Applying thermal treatment in a reducing atmosphere leads to a further increase in NBE intensity, roughly by 50% for In-doped and 180% for Ga-doped samples. As a result of the thermal treatment, both In- and Ga-doped samples exhibit similar NBE luminescence intensity (within 10% uncertainty).

We characterized a limited number of samples. The reproducibility of the manufacturing method is yet to be confirmed. Further investigations are needed to confirm the conclusions about the influence of In and Ga doping and thermal treatment on ZnO luminescence properties.

Ionoluminescence spectra excited by different ion species vary only by the intensity of the emitted light. The spectral shape and emission band positions remain unchanged. For example, Figure 5.15 shows a comparison of ionoluminescence spectra of the initial ZnO(Ga) when excited by Ar at 250 MeV/u and U at 300 MeV/u energy. The NBE emission intensity for U ion excitation is ~ 30 times higher than for Ar ion excitation. Yet, as one can see in Table 4.2, the energy deposited by U ions is roughly 25 times larger than for Ar.

Figure 5.16 shows a 3D plot of thermally-treated ZnO(In) ceramic sample ionoluminescence spectrum change as a function of 300 MeV/u ^{209}Bi ion fluence. As has been previously observed for swift heavy ion irradiation experiments at M3 and X0 beam lines, the irradiation with high energy heavy ions leads to an exponential reduction of both NBE and DL emission intensities, while no new emission bands evolve.

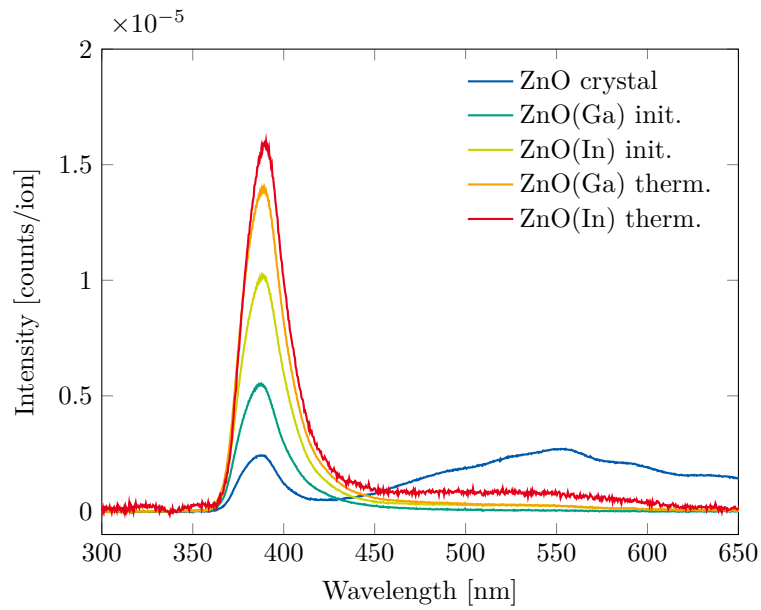


Figure 5.14: Ionoluminescence spectra of pristine ZnO samples prepared with different doping and with/without thermal treatment. The luminescence is induced by 300 MeV/u ^{238}U ions.

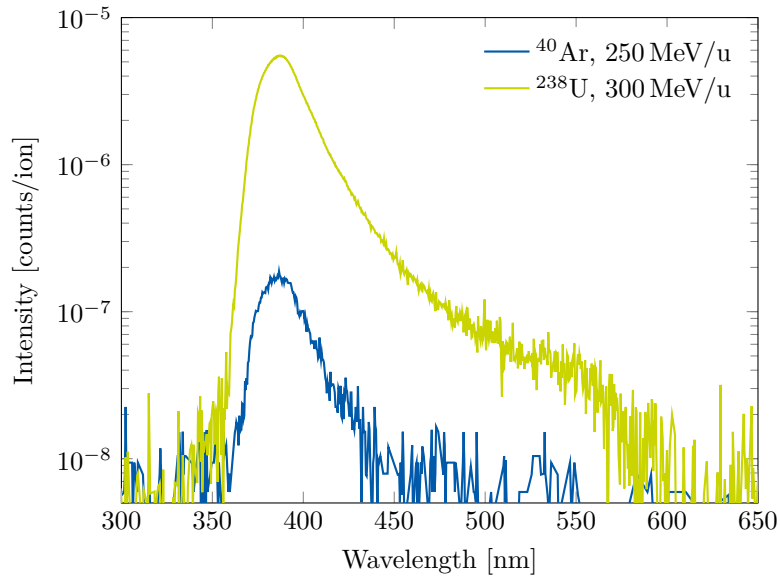


Figure 5.15: Ionoluminescence spectra of initial ZnO(Ga) ceramic sample exposed to 250 MeV/u Ar and 300 MeV/u U ions, corresponding to various electronic stopping powers of 0.66 and 24.36 MeV/(mg cm²), respectively.

Figure 5.17 shows a comparison of ionoluminescence and Raman spectra for an initial ZnO(Ga) sample irradiated with 300 MeV/u Bi ions up to 1.2×10^{12} ions/cm² fluence. As a result of irradiation, the NBE emission intensity reduces roughly by a factor of four (Figure 5.17a), however, no major changes are observed in Raman spectra (Figure 5.17b). This indicates that the radiation damage in ZnO that leads to the observed ionoluminescence intensity reduction cannot be ascribed to changes in vibrational modes.

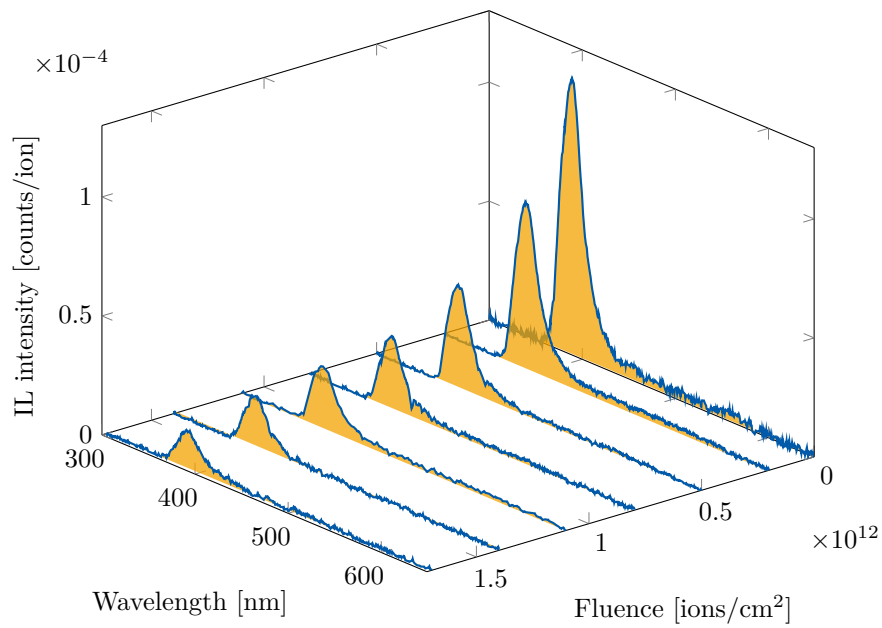


Figure 5.16: 3D representation of the evolution of the ionoluminescence spectra of thermally-treated ZnO(In) ceramic as a function of 300 MeV/u Bi ion fluence.

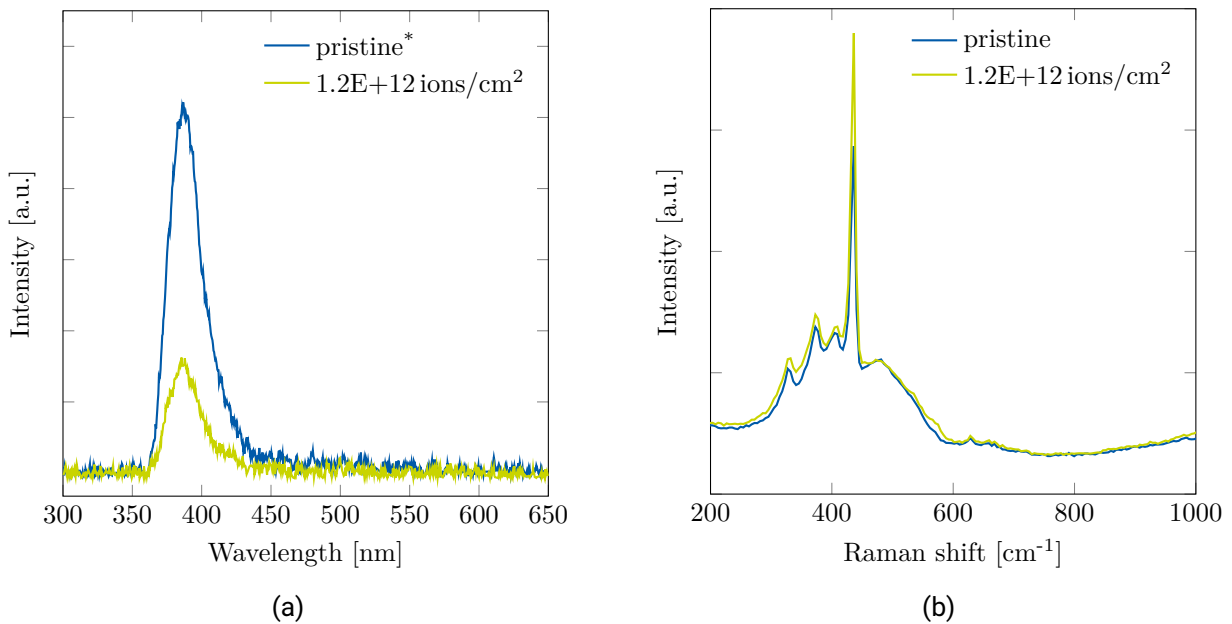


Figure 5.17: Comparison of ionoluminescence (a) and Raman spectra (b) for initial ZnO(Ga) irradiated with Bi at 300 MeV/u. The ionoluminescence of the pristine sample corresponds to 2.9×10^{10} Bi-ions/cm².

5.7 Scintillation light output as a function of stopping power and fluence

Figure 5.18 compares photomultiplier (PMT) signals of initial ZnO(In) and plastic scintillator when irradiated with Kr ions at 300 MeV/u energy. The typical scintillation signals recorded by the slow PMT at 3.6×10^5 gain

(1000 V supply voltage) correspond to scintillation light flashes generated by single ion impacts (Figure 5.18a). The difference between zinc oxide and plastic scintillator signals is the signal amplitude (also signal area), which is proportional to the scintillation light yield of the material.

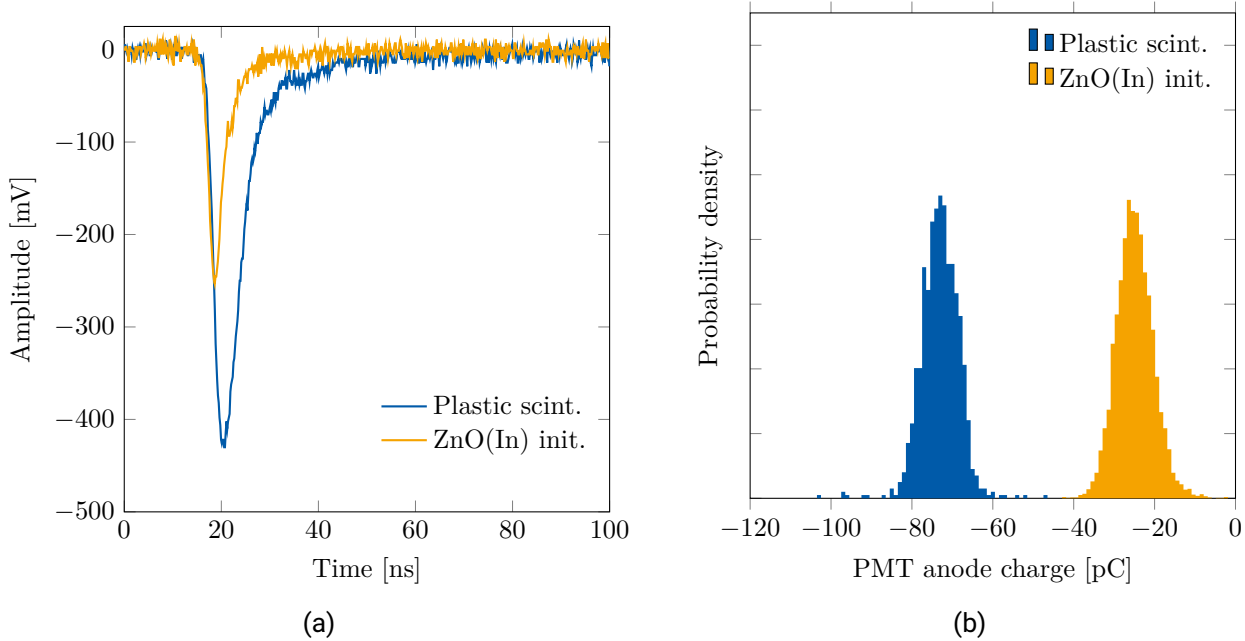


Figure 5.18: Typical PMT signals (a) and anode charge of the PMT (b) recorded for pristine plastic scintillator and ZnO(In) exposed to 300 MeV/u Kr ions. The PMT gain is 3.6×10^5 .

Figure 5.18b shows distributions of the slow PMT anode charge below the signals as from Figure 5.18a. The anode charge in pico coulombs is defined as: $Q_a = A/R$, where A is the area of the signal in pico webers ($\int V(t)dt$, $V(t)$ — signal amplitude in millivolts, dt — time in nanoseconds) and R is the PMT–oscilloscope coupling resistance (50 Ohm).

The charge at the PMT anode registered for initial ZnO(In) ceramic is on average 37% of the plastic scintillator. Another point to note is that the reference plastic scintillator exhibits better energy resolution (FWHM of the PMT anode charge over the mean PMT anode charge) than ZnO-based ceramics. It is 12% and 33% for reference plastic scintillator and initial ZnO(In) ceramic, respectively.

By considering the gain values of the slow PMT (as shown in Figure 4.19), one can calculate the number of photoelectrons, generated on the PMT photocathode as $N_{phe} = Q_a/(g(V) * e)$; $g(V)$ is the PMT gain at the supply voltage V , and e is the electron charge. The number of photoelectrons created in the PMT is directly proportional to the number of scintillation photons emitted from the sample. The proportionality coefficient is a product of the photo-cathode quantum efficiency and the solid angle. This factor was kept the same in comparing the light yield of different samples. This was ensured using the same PMT installed in a reproducible location relative to the investigated samples. Since the exact scintillation photon to photo electron conversion factor is not known, the number of photoelectrons at the PMT cathode is used for further scintillation light output comparison for different samples exposed to different ion species. A rough estimation of light yield from the number of photoelectrons can be done as: $LY = 4\pi N_{phe}/(QE \times \Omega)$, where LY is the light yield in the units of photons/ion, QE is the quantum efficiency of the photocathode (~ 0.2 from the PMT specification), and $\Omega = 0.136$ sr is the solid angle covered by the photocathode.

In Figure 5.19, the N_{phe} values measured for different ZnO ceramic samples and a reference plastic scintillator excited by different ion species (i.e., different stopping power) are shown. The number of photoelectrons (or scintillation light yield) increases with the stopping power. Plastic scintillator exhibits 50–60% larger light output in the entire stopping power range. Initial ZnO(In) ceramic samples exhibit approximately 100% higher N_{phe} than initial ZnO(Ga) ceramic samples. Both ZnO(In) and ZnO(Ga) thermally-treated samples exhibit up to 50% higher light output in comparison to initial ZnO(In) ceramic samples.

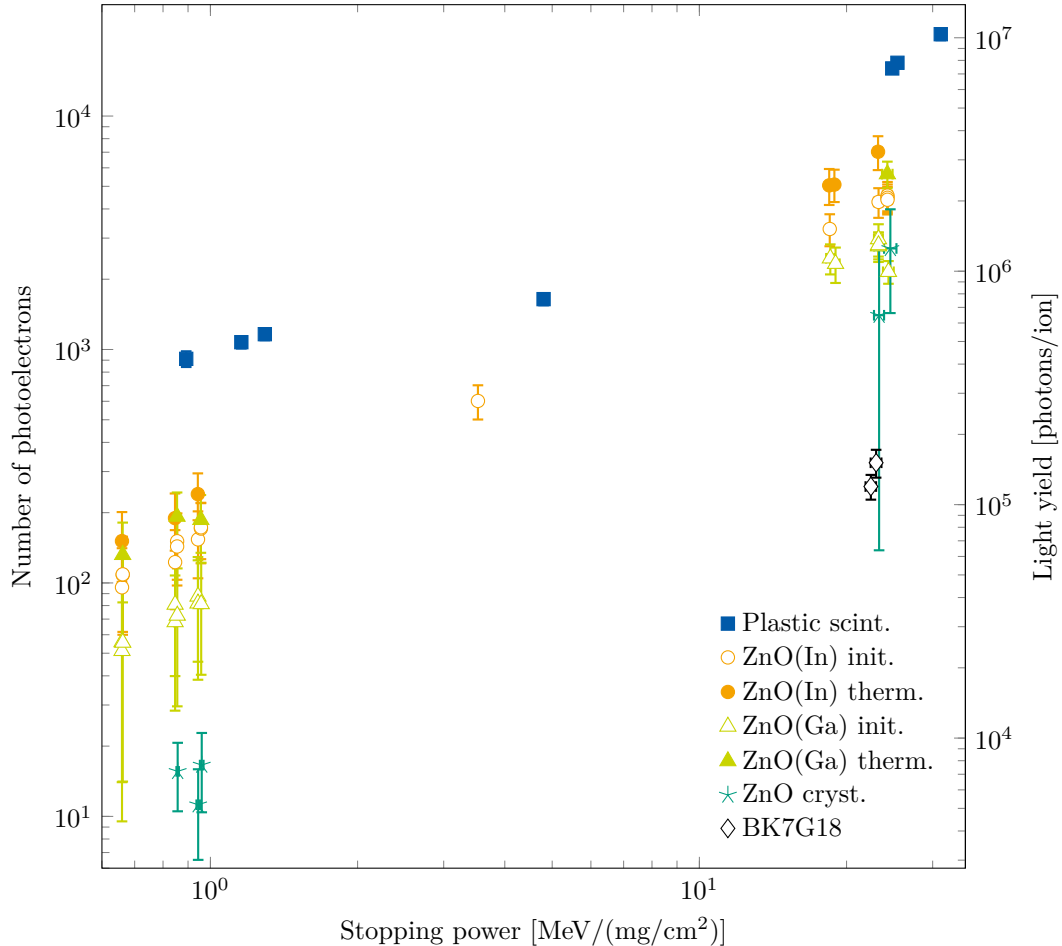


Figure 5.19: Number of photoelectrons generated at PMT input as a result of various samples irradiation with relativistic heavy ions at different stopping power.

Figure 5.20 shows distributions of the N_{phe} value obtained for thermally-treated ZnO(In) sample irradiated with 300 MeV/u Bi ions at different fluences. The number of photoelectrons, and thus the amount of emitted scintillation light, reduces with the increase of fluence. The N_{phe} distribution of a pristine, not irradiated, sample has a Gaussian shape and thus is symmetrical relative to the most probable N_{phe} value. As a result of high fluence irradiation, the most probable N_{phe} value goes down and a longer tail occurs from the higher N_{phe} values side; thus the distribution is no longer symmetric.

The asymmetry of the N_{phe} distribution for irradiated samples is due to the inhomogeneity of the incident ion beam used for irradiation and measurement of samples. In this work, the ion distribution across the irradiated spot is not homogeneous, but a radial Gaussian distribution from the irradiated spot center. Thus, more ions

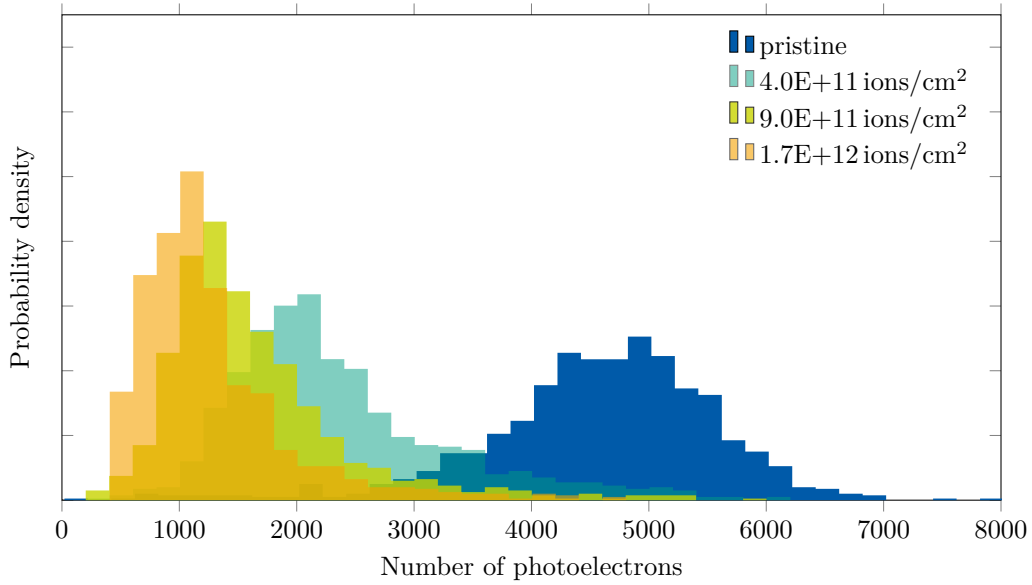


Figure 5.20: Number of photoelectrons generated at PMT input as a result of 300 MeV/u ^{209}Bi ion-induced luminescence in thermally-treated ZnO(In) sample at different fluence.

hit the irradiated spot at the center than at the periphery. This leads to a fluence inhomogeneity across the irradiated spot, with a higher fluence at the center and lower fluence at the periphery of the irradiated spot. At the same time, this means that, during PMTs characterization, more signals are collected from the central (higher fluence) part of the sample than from the periphery (lower fluence) part. The signals from the central part of the sample contribute to the most probable N_{phe} value in the distribution, while the signals from the periphery of the sample contribute to the high values tail.

Due to the beam inhomogeneity, the most probable N_{phe} values in Figure 5.20 correspond to the fluence that is higher than the average fluence shown in Figure 5.20 legend.

Figure 5.21 compares the relative change of the NBE emission intensity from the IL spectroscopy measurement and the relative change of the photo electron number at the slow PMT photocathode as a function of fluence. The relative change of the most probable photo electron number is shifted compared to the relative change of the NBE emission peak intensity. However, the average photo electron number follows the same trend as the NBE emission peak intensity versus fluence.

In addition to samples that were never exposed to an ion beam, we tested one initial ZnO(In) sample that was pre-irradiated with 300 MeV/u ^{238}U ions up to 10^{12} ions/cm 2 and then annealed in air at 500 °C for 30 min. As reported in [10] the pre-irradiation of this sample led to a PMT signal amplitude that was reduced roughly by a factor of five. The subsequent annealing of the pre-irradiated sample recovered luminescent properties, as was reported for the X-ray-induced luminescence measurements [117]. We confirmed the recovery of luminescence in the pre-irradiated sample after annealing by comparing N_{phe} values for pristine and pre-irradiated samples exposed to 300 MeV/u ^{238}U ions (see Figure 5.22).

In general, the ability to recover luminescent properties through thermal annealing is a useful feature of ZnO scintillators compared to plastic scintillators. The same piece of ZnO scintillating ceramic can be used multiple times in a detector, whereas radiation-damaged plastic scintillators must be thrown away after use. That makes ZnO-based scintillators more sustainable and cost-effective compared to plastic scintillators.

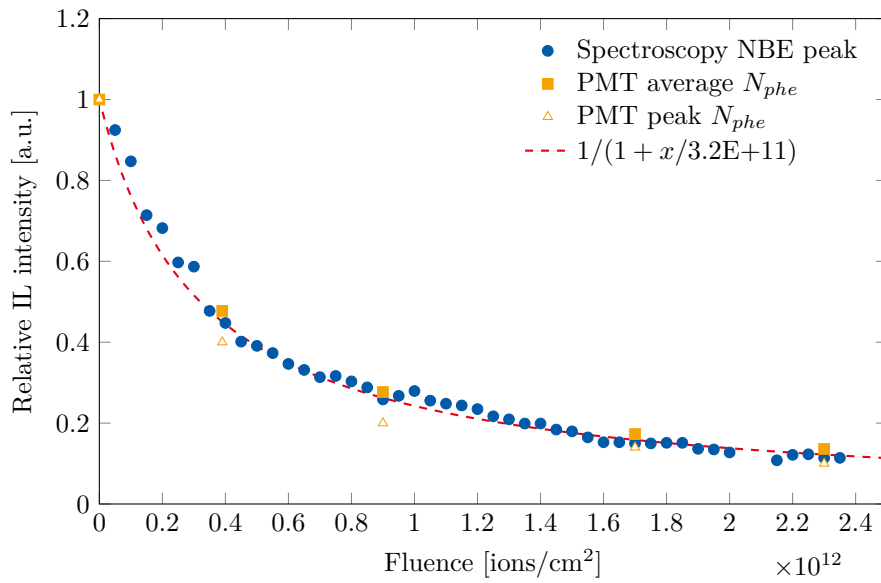


Figure 5.21: Relative IL intensity change measured by different methods as a result of 300 MeV/u ^{209}Bi ion-induced luminescence in thermally-treated ZnO(In) sample at different fluence. The dashed line corresponds to the Birks-Black model fit.

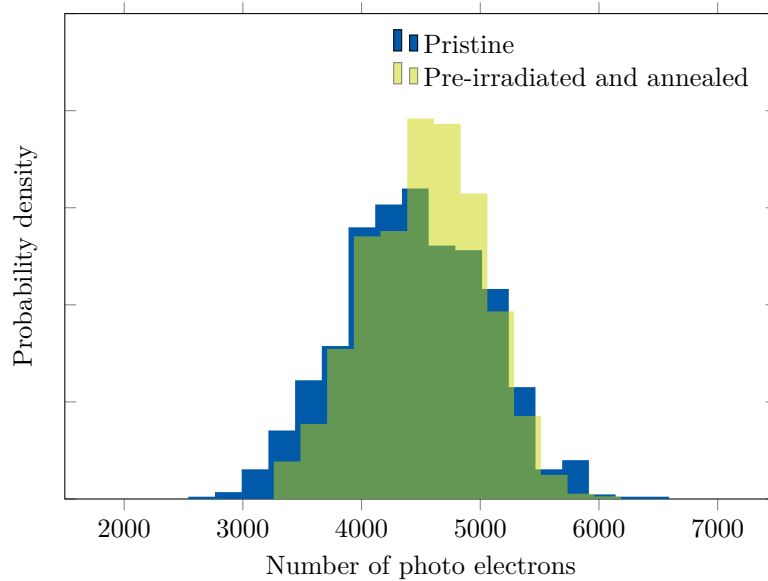


Figure 5.22: Number of photoelectrons generated at PMT input as a result of 300 MeV/u ^{238}U ion-induced luminescence in pristine ZnO(In) sample (blue) and pre-irradiated and annealed ZnO(In) sample (yellow).

5.8 Fitting the IL intensity change as a function of fluence

The relative change in IL intensity from spectrometry measurements and photoelectrons number from PMT measurements as a function of fluence was fitted using the Birks-Black model (Equation 2.20 and

Equation 2.21). It is important to note that heavy ion irradiation may produce not only one type of defect, but a large variety of point defects and defect aggregates. From previous studies of heavy-ion tracks in various materials, e.g., in LiF, it is known that the cross-section of single defects is much larger than for defect aggregates [145]. In this work, the parameters k , σ_e are not associated with any specific defect type. They represent a mixture of different defect types formed along the ion path, and their specific contribution to luminescence cannot be extracted.

When Equation 2.20 was used to fit the experimental data, the iterative fitting procedure based on the orthogonal distance regression implemented in the Python SciPy library did not converge to a unique solution. There is an inverse dependency between the free parameter k and σ_e that leads to an unlimited number of (k, σ_e) pairs providing a good fit based on χ^2 test. Therefore, it was not possible to get stable k and σ_e values output from experimental data fits. Nevertheless, we observed that the product of these two parameters is close to a constant ($k\sigma_e \approx \text{const}$).

Therefore, we used a simplified Birks–Black model, where the exponent is replaced with its first approximation from the Taylor series as shown in Equation 2.21. Figure 5.23 shows examples of the relative IL intensity change observed at the NBE peak as a function of 4.8 MeV/u Ca and Au ion fluence for thermally-treated ZnO(In) as well as the relative N_{phe} values measured by PMT as a function of fluence for 300 MeV/u Bi ions initial ZnO(Ga), together with fits based on the simplified Birks–Black model.

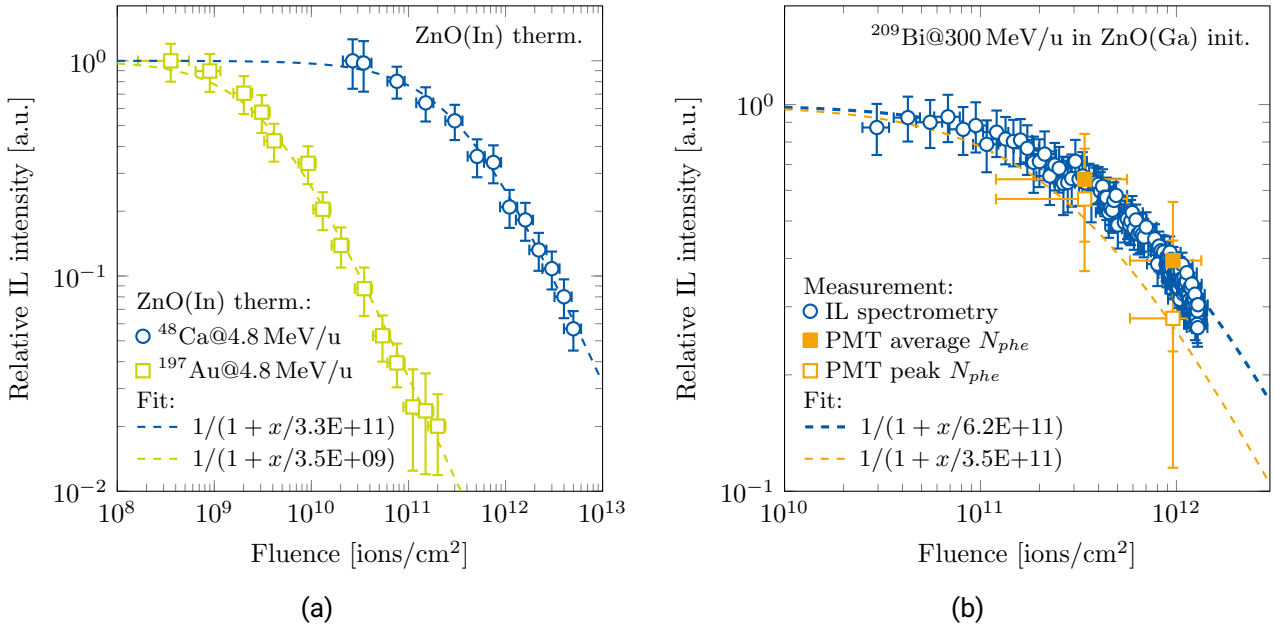


Figure 5.23: Relative IL intensity as a function of fluence measured for thermally-treated ZnO(In) ceramic exposed to 4.8 MeV/u Ca and Au beams (a), and relative IL intensity and relative PMT N_{phe} values as a function of fluence measured for initial ZnO(Ga) sample (b). Dashed lines correspond to the simplified Birks–Black model fits (Equation 2.21).

One should note that in Figures 5.21 and 5.23b the average N_{phe} value follows the relative IL intensity from the spectroscopy measurements, while the value at the peak of N_{phe} distribution is always lower. As mentioned earlier, because of the inhomogeneous beam spot, the peak value of the N_{phe} distribution must correspond to a higher fluence value than the average fluence, estimated for the whole beam spot.

The critical fluence parameter $\Phi_{1/2}$ of the Birks–Black model is used for understanding the asymmetry of N_{phe} distributions observed after high fluence irradiation (e.g., see Figure 5.20). We found that the experimentally measured asymmetric distributions of N_{phe} can be well described by considering a Gaussian beam spot having the dispersion of 1.25 mm.

The asymmetric N_{phe} distribution is simulated by modifying the Birks–Black model as:

$$I(r) = I_0 / (1 + \Phi(r) / \Phi_{1/2}), \quad (5.1)$$

where $I(r)$ is the light output registered for a single ion, hitting the sample at the coordinate r (the radius from the beam spot center), I_0 is the light output that is observed for pristine not irradiated sample, $\Phi(r)$ is the local ion fluence at the radius r from the beam spot center, and $\Phi_{1/2}$ is the critical fluence.

The Gaussian ion beam spot is given by:

$$n(r) = n_0 \exp(-0.5r^2 / \sigma_n^2) \quad (5.2)$$

where $n(r)$ is the radial distribution of ions, n_0 is the number of ions at the beam spot center, and σ_n represents a dispersion of the Gaussian beam. The radial fluence distribution is calculated by multiplying the radial ion beam distribution by a scaling constant: $\Phi(r) = \text{const} \times n(r)$, so that the integral of $\Phi(r)$ equals the average fluence measured by PDC ionization chamber and secondary electron transmission monitor.

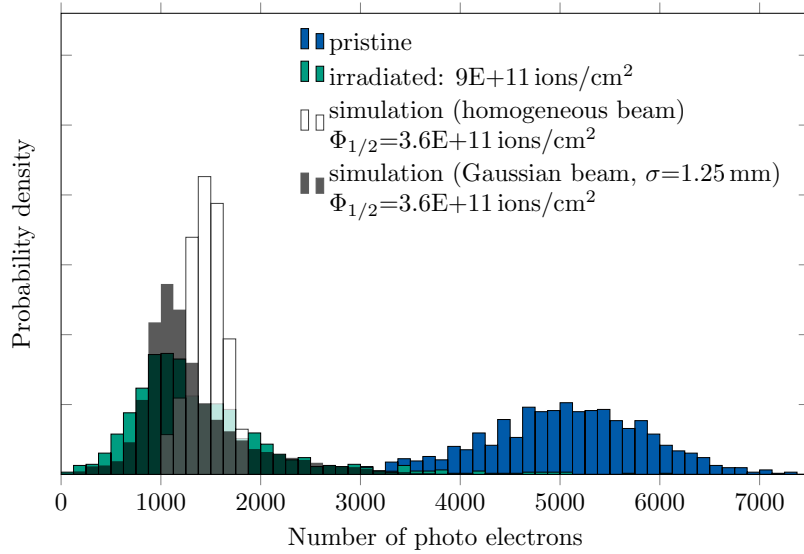


Figure 5.24: The number of photoelectrons measured for the pristine thermally-treated ZnO(In) sample (blue) together with data of the same sample irradiated with 300 MeV/u Bi up to 9×10^{11} ions/cm² (green). The dark gray and white bar plots correspond to the simulated N_{phe} distributions assuming Gaussian and homogeneous ion beams, respectively. The Gaussian beam is assumed to have $\sigma = 1.25$ mm, and both simulations assume $\Phi_{1/2} = 3.6 \times 10^{11}$ ions/cm².

In Figure 5.24, the experimentally measured N_{phe} distribution of thermally-treated ZnO(In) sample irradiated with 300 MeV/u Bi ions to 9×10^{11} ions/cm² is compared to simulations considering homogeneous and Gaussian beam spot. The simulation with the Gaussian beam spot leads to a good match of the experimental result, while the homogeneous beam spot leads to a narrower distribution in which the maximum is shifted to higher values relative to experimental data. The above result is consistent with observation of the beam profile on CROMOX screen. The beam spot was highly asymmetric, elongated in one direction.

The critical fluence values for different samples are summarized in Table 5.2. Within the experimental error, there is a minor difference in critical fluence at fixed ion beam for ZnO-based ceramic samples prepared by different manufacturing processes.

Figure 5.25 shows the critical fluence values of ZnO-based ceramics from Table 5.2 as a function of electronic stopping power. The data of the current work are compared to previously reported critical fluences of the BC400 plastic scintillator measured for various ions and energies [146]. There is a dependency of the critical fluence on the electronic stopping power. The critical fluence values become smaller with increasing stopping power. At a fixed ion specimen (for example 4.8 MeV/u Ca or 253 MeV/u Bi in Table 5.2), the critical fluence value for ZnO-based ceramics is roughly 50 times larger than for the plastic scintillator. This implies that the deterioration of scintillation light output due to heavy ion irradiation of ZnO-based ceramics is at least one order of magnitude slower than for the standard plastic scintillator. The slower IL intensity deterioration of the investigated ZnO ceramic samples results in a longer lifetime during in-beam applications as a scintillation counter.

Table 5.2: Critical fluence values extracted from characterization experiments of this work

Ion	Incident energy MeV/u	Sample	Stopping power MeV/(mg/cm ²)	Critical fluence ions/cm ²	Characterization method
⁴⁸ Ca	4.8	Plastic SCI	27 ± 2	(6.7 ± 1.0) × 10 ⁹	IL spectroscopy
⁴⁸ Ca	4.8	ZnO(In) therm.	19.6 ± 1.8	(3.4 ± 1.0) × 10 ¹¹	IL spectroscopy
¹⁹⁷ Au	4.8	ZnO(In) therm.	87 ± 21	(1.4 ± 0.4) × 10 ⁹	IL spectroscopy
¹⁹⁷ Au	8.3	ZnO(In) init.	66 ± 7	(1.0 ± 0.1) × 10 ¹⁰	XRL
¹⁹⁷ Au	8.3	ZnO(In) therm.	66 ± 7	(8.04 ± 0.8) × 10 ⁹	XRL
¹²⁴ Xe	300	ZnO(In) init.	7.7 ± 0.3	(2.07 ± 0.5) × 10 ¹²	PMT photoelectrons
²⁰⁸ Pb	254.4	ZnO(In) init.	19.3 ± 0.4	(8.46 ± 1.58) × 10 ¹¹	IL spectroscopy
²⁰⁹ Bi	253.5	Plastic SCI	26.6 ± 0.3	(1.36 ± 0.14) × 10 ¹⁰	IL spectroscopy
²⁰⁹ Bi	253.5	Plastic SCI	26.6 ± 0.3	(1.2 ± 0.1) × 10 ¹⁰	PMT photoelectrons
²⁰⁹ Bi	253.5	ZnO(Ga) init.	19.8 ± 0.5	(5.74 ± 0.07) × 10 ¹¹	IL spectroscopy
²⁰⁹ Bi	253.5	ZnO(Ga) init.	19.8 ± 0.5	(6.2 ± 0.2) × 10 ¹¹	PMT photoelectrons
²⁰⁹ Bi	253.5	ZnO(In) therm.	19.7 ± 0.4	(2.88 ± 0.13) × 10 ¹¹	IL spectroscopy
²⁰⁹ Bi	253.5	ZnO(In) therm.	19.7 ± 0.4	(3.7 ± 0.01) × 10 ¹¹	PMT photoelectrons
²³⁸ U	250.6	ZnO(In) init.	24.3 ± 0.5	(1.84 ± 0.8) × 10 ¹¹	IL spectroscopy
²³⁸ U	275.4	ZnO(Ga) init.	23.2 ± 0.5	(3.6 ± 1.1) × 10 ¹¹	IL spectroscopy
²³⁸ U	300	ZnO(In) init.	21.5 ± 0.5	(5.38 ± 1.2) × 10 ¹¹	PMT amplitude

5.9 Fast-PMT signal rise and decay time characterization using relativistic ions

Figure 5.26 shows fast PMT signal waveforms recorded for the reference plastic scintillator and initial ZnO(Ga) exposed to 300 MeV/u bismuth ions. The fast PMT response function recorded as a result of 44 ps short 373 nm laser pulse excitation is also included for comparison. The reference plastic scintillator sample exhibits signals that clearly have longer pulse width and also longer rise time than the ZnO-based ceramic sample. The signal shape of the initial ZnO(Ga) sample is close to the fast PMT response signal, indicating that the scintillation light pulse is comparable to or shorter than the fast PMT response time.

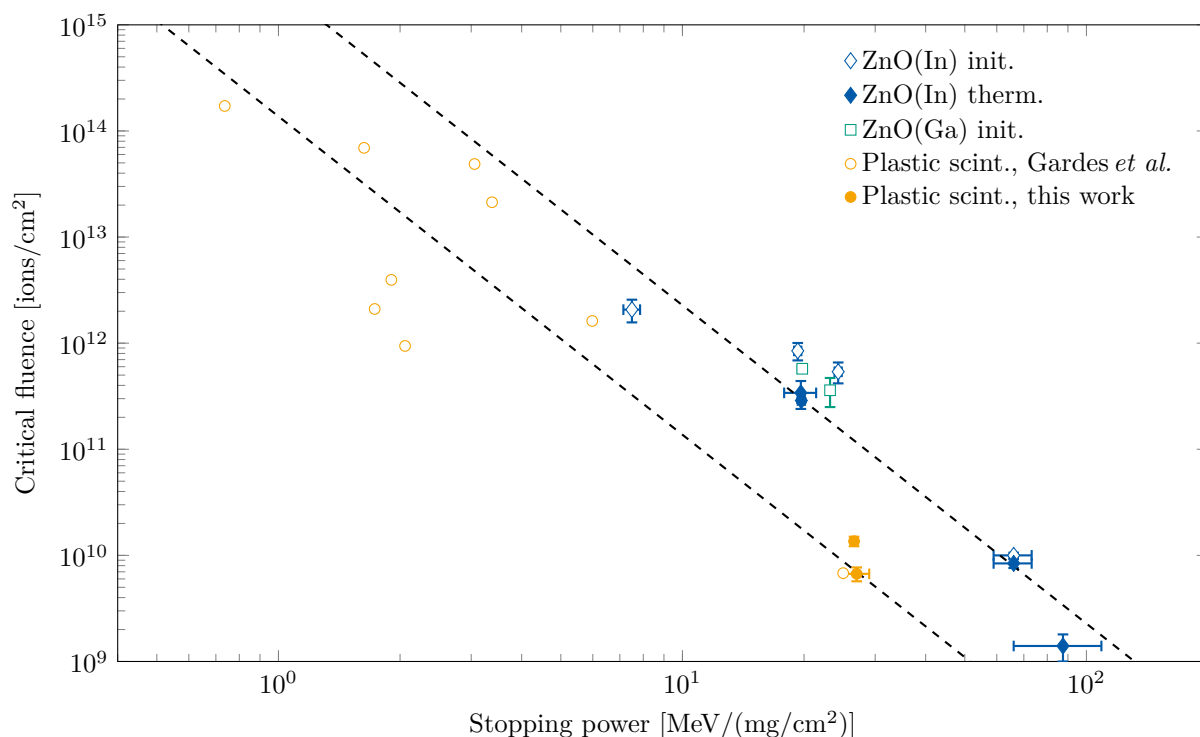


Figure 5.25: Critical fluence values extracted via Birks–Black model from experimental measurements of this work in comparison to previously reported critical fluences for BC400 plastic scintillator by Gardes *et al.* [146]. Dashed lines are used to guide the eye.

The fast PMT signal waveforms recorded for individual ions hitting ZnO and plastic scintillator samples were used to extract scintillation pulse rise and decay times, as earlier described in section 2.2.3. The fast PMT signal waveforms, like those shown in Figure 5.26a, are assumed to be a convolution of the scintillation pulse shape represented by Equation 2.17 and the fast PMT response signal waveform shown in Figure 5.26b.

Equation 2.19 was implemented into a fitting function with 3 free parameters τ , τ_R , and E_{eh} representing scintillation decay time, rise time, and signal amplitude scaling parameter, respectively. The fitting function was applied separately to each sample waveform corresponding to a single ion impact. As a result, the average scintillation decay time was extracted for each sample–ion combination and is shown in Table 5.3.

The scintillation decay time extracted for the reference plastic scintillator is (2.3 ± 0.2) ns, which is in agreement with Table 1.1 value. Because ZnO-based samples exhibit signals hardly varying from the fast PMT response, it was not possible to accurately extract the scintillation decay time. The majority of the fits resulted in decay times less than 0.3 ns, i.e., comparable to the decay time of the fast PMT response signal. In some cases, like thermally-treated ZnO(In) exposed to 300 MeV/u U ions, the fitted decay time reaches (0.77 ± 0.09) ns, which is 3 times shorter than is observed for plastic scintillator. The measured decay time of ZnO-based samples is larger at higher stopping powers. In contrary to this, it stays unchanged for plastic scintillator. Further investigations using methods capable of resolving luminescence in the picosecond timescale are needed to confirm the decay time versus stopping power dependency in ZnO.

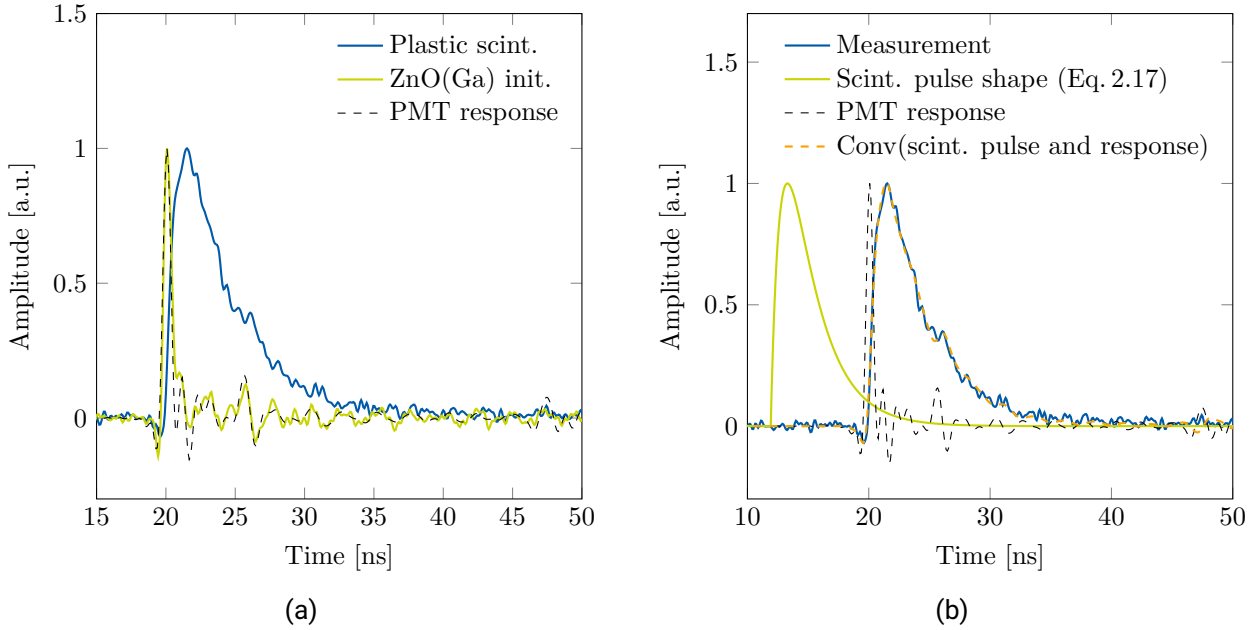


Figure 5.26: Fast PMT signals recorded for 300 MeV/u Bi ion irradiated ZnO(Ga) initial sample and reference plastic scintillator (a). The black dashed line corresponds to the fast PMT response obtained using 44 ps, 373 nm laser pulse excitation. In Figure (b), the orange dashed line corresponds to the convolution of the scintillation pulse shape approximated with Eq. 2.17 and the fast PMT response signal. All signals are scaled by the maximum signal amplitude.

Table 5.3: Scintillation decay times extracted from the experiments using fast PMT characterization

Ion and energy, MeV/u	Decay time, ns				
	Plastic scint.	ZnO(In) init.	ZnO(In) therm.	ZnO(Ga) init.	ZnO(Ga) therm.
Ar, 250	2.3 ± 0.5	0.28 ± 0.14	0.43 ± 0.11	0.12 ± 0.08	0.17 ± 0.08
Pb, 300	2.3 ± 0.1	—	0.77 ± 0.08	0.27 ± 0.19	—
Bi, 300	2.3 ± 0.1	—	0.70 ± 0.10	0.25 ± 0.11	—
U, 300	2.1 ± 0.2	0.55 ± 0.07	0.77 ± 0.09	0.26 ± 0.06	0.39 ± 0.07

6 Development of ZnO-Based Scintillation Detector Prototype

This chapter describes the preparation of a radiation hard and fast scintillation detector prototype based on ZnO(In) scintillating ceramic. This includes the description of the prototype design and results of the radiation-hard glass light guide simulations using the OpenGATE, which is the front end for Geant4 [33]. The simulations allowed us to find the optimal BK7G18 glass light guide thickness and surface quality to provide the highest possible detector signal. Finally, a step-by-step description of the prototype detector assembly is presented.

6.1 Detector layout, description of the main parts and concepts of prototype

Figure 6.1 shows the principal scheme of the ZnO-based scintillation detector prototype. The active volume of the detector consists of a radiation-hard BK7G18 borosilicate glass plate and arrays of ZnO(In) scintillating ceramic tiles on the front and back side of the glass. The scintillation light emitted from the surfaces of ZnO(In) tiles enters the glass, which serves as a guide of the collected light. As a result of internal reflections inside the glass, the scintillation light reaches a plastic light guide coupled on top of the glass. Further, the plastic light guide is coupled to a photomultiplier that converts the input light photons into an electric output signal.

Due to the self-absorption and diffuse scattering of the fast luminescent component in the bulk of ZnO-based ceramics, the scintillating tiles cannot serve themselves as a light guide media to transport the scintillation light. Therefore, the BK7G18 borosilicate glass light guide is used in the active area of the detector to transport the scintillation light from the ZnO ceramic to the PMT.

The borosilicate glass has been chosen as a light guide since this material exhibits a negligible scintillation light emission compared to ZnO-based ceramics. Thus, the contribution of the BK7G18 glass is negligible and thus is not considered further. Moreover, BK7G18 glass remains transparent in the UV light region even at high radiation doses. Therefore, it prevents additional light absorption by the light guide after a long time of irradiation. Details of the BK7G18 radiation-hard glass performance under heavy-ion irradiation are presented in Appendixes A1 and A2.

6.2 Modeling of light propagation in prototype detector using OpenGATE

The registration of a single heavy ion by the prototype detector can be divided into the following stages:

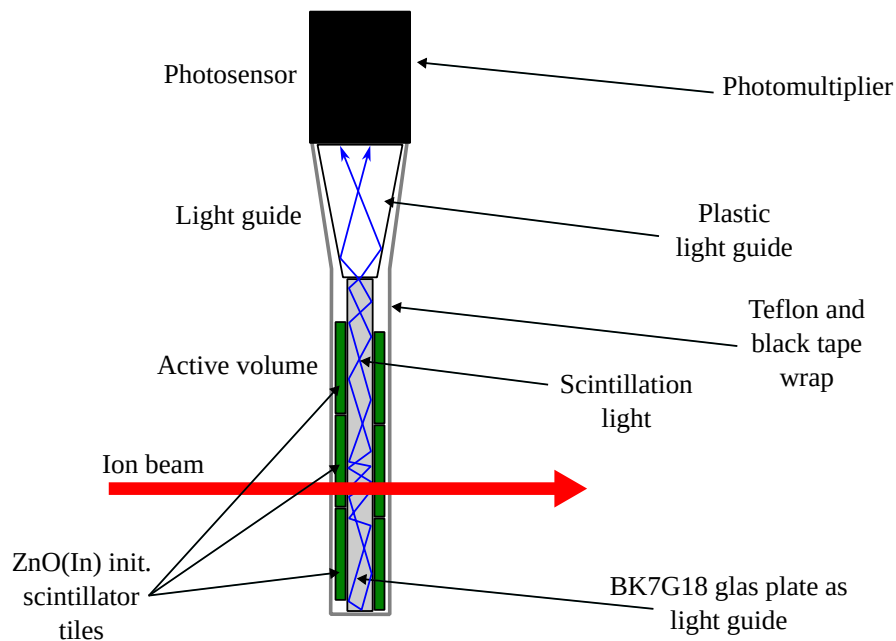


Figure 6.1: Principal scheme of the multi-tile ZnO-based radiation-hard scintillation detector prototype. ZnO(In) tiles are on both sides of the glass, i.e., the BK7G18 glass is sandwiched between two layers of ZnO tiles.

- the incident ion passes through the detector and deposits a part of its energy in the active volume and light guide that consist of ZnO-based scintillating tiles and BK7G18 glass, respectively;
- the energy deposited in ZnO-based ceramic tiles is converted to a scintillation light flash with the intensity related to the amount of the deposited energy;
- part of the scintillation light from ZnO ceramics is emitted towards the BK7G18 glass plate;
- after multiple reflections, the light from the glass enters the plastic light guide that transfers the light to a photomultiplier;
- the photomultiplier generates an electric signal that is proportional to the number of photons interacted with the PMT photocathode;
- the electric signal is processed by the electronics system;
- signals with the amplitude above given threshold are counted.

The scintillation light transmission from the scintillator to the PMT is one of the key factors that defines the amplitude of the detector signal and whether the resulted electric signal can be detected by electronics. For the prototype design presented in this work, light collection and transfer efficiency by the glass light guide was investigated and optimized. This led to our decision to use the BK7G18 light guide.

Before the prototype detector assembly, the light guide performance of the borosilicate glass was simulated using the OpenGATE code [33]. Light collection and transfer efficiency of a rectangular shaped BK7G18 glass light guide were calculated as a function of the thickness and surface quality (roughness) of the glass, as well as the position across the active area where scintillation light enters the glass plate.

6.2.1 Finding an optimal thickness and surface finishing of a radiation-hard light guide

The transfer of the scintillation light through the glass light guide is schematically shown in Figure 6.2. A scintillating tile of a rectangular shape in direct contact with a rectangular glass plate emits N_{tot} scintillation light photons towards it. Depending on the surface properties, N_{in} photons enter the light guide through the interface. As a result of multiple reflections inside the glass, N_{edge} photons reach the upper edge of the glass plate. Finally, N_{out} photons exit the glass light guide and enter the plastic light guide, which further transports them towards the PMT to generate a signal. We denote the glass light guide collection efficiency as $\eta_c = N_{in}/N_{tot}$, and the glass light guide transmission efficiency as $\eta_{tr} = N_{out}/N_{tot}$.

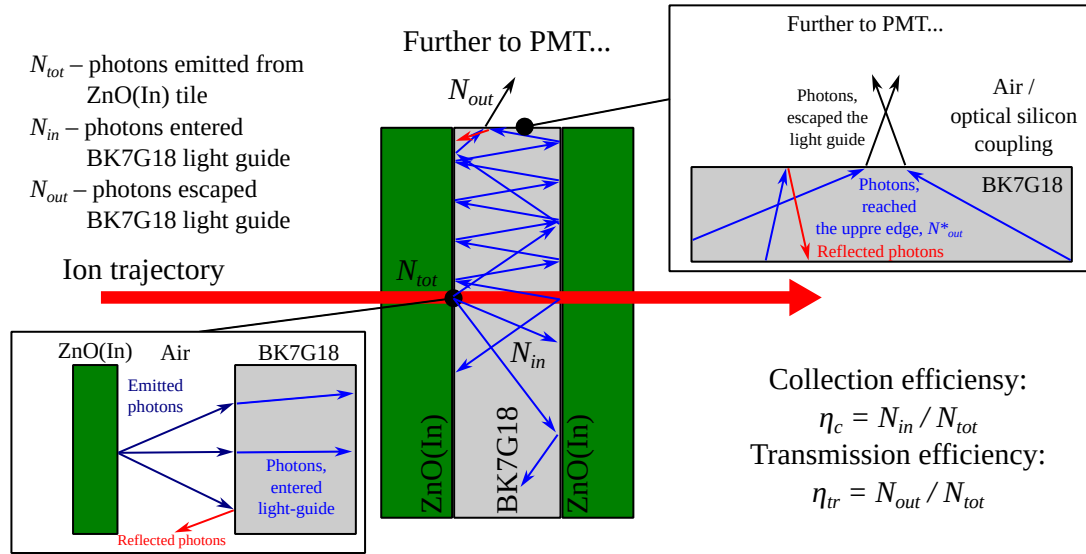


Figure 6.2: Schematic (not in scale) representation of the scintillation light propagation through radiation-hard glass light guide. As a result of the ion impacts, N_{tot} scintillation photons are emitted from ZnO(In) surface. N_{in} photons enter the BK7G18 light guide, thus, defining the light guide collection efficiency as $\eta_c = N_{in}/N_{tot}$. As a result of multiple reflections inside the BK7G18, N_{out} photons exit the light guide further towards PMT, thus, defining the light guide transmission efficiency as $\eta_{tr} = N_{out}/N_{tot}$.

Due to the self-absorption and diffuse scattering in the scintillating tile, we assume for our OpenGATE simulations that the source of scintillation light at the scintillator–glass light guide interface can be represented as a point light source located on the scintillating tile surface and emitting light in 2π solid angle towards the light guide. Also, we assume that there is a 50 μm thick air gap between the scintillator–glass light guide and glass–plastic light guide interfaces.

BK7G18 refraction index of 1.53 and optical absorption length of 0.0371 meters were used in the simulations of the light transport. The information is extracted from the refraction index and optical transmittance tables as a function of wavelength provided by SCHOTT [147].

The effect of the roughness of the glass light guide was simulated according to the UNIFIED model [148, 149]. This model allows controlling the radiant intensity of the surface by specular spike, specular lobe, and diffuse lobe reflection types (see Figure 6.3a). The contribution from each reflection type is defined by scaling constants. The sum of the constants is constrained to unity. For simplicity, we assume that in our situation,

the light reflection from a rough surface is dominated by the specular lobe component (i.e., the specular lobe constant is equal to one and the rest (specular spike and diffuse lobe) constants are equal to zero.) In the UNIFIED model, a rough surface is represented by micro-facets, as shown in Figure 6.3b. For each simulated incident light ray, a normal incidence vector is randomly generated from a Gaussian distribution defined by the parameter σ_α (given in degrees). The σ_α parameter thus defines the standard deviation of the Gaussian distribution of micro-facets tilt angles, α , relative to the average surface normal.

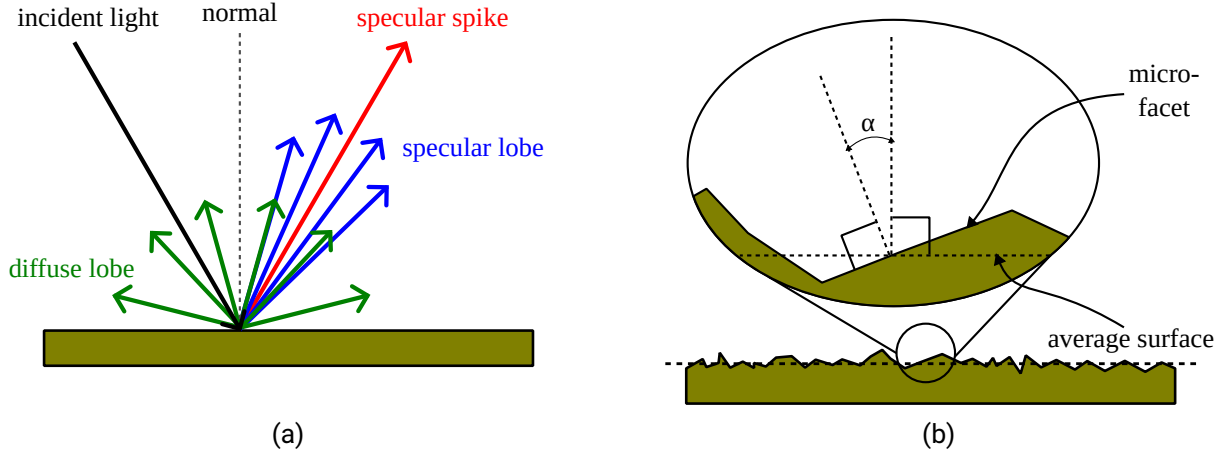


Figure 6.3: Reflection types (a) and micro-facet tilt angle α (b) as simulated in OpenGATE using the UNIFIED model [33].

Figure 6.4 shows the simulated light collection efficiency η_c of a rectangular BK7G18 glass plate as a function of surface roughness controlled by σ_α parameter. One can see that for a perfectly polished surface ($\sigma_\alpha = 0^\circ$) 79% of photons emitted by the scintillator can enter the glass light guide. The collection efficiency increases as the glass surface gets rougher.

At σ_α values above 40° , the collection efficiency saturates at approximately 93%.

One can use Fresnel equations to estimate the light transmission through the BK7G18 glass surface. For non-polarized light, the Fresnel transmittance is:

$$T_{Fr} = 1 - \frac{1}{2}(r_{\parallel}^2 + r_{\perp}^2), \quad (6.1)$$

where r_{\parallel}^2 and r_{\perp}^2 are Fresnel reflectances for parallel and perpendicular polarized light, given as:

$$\begin{aligned} r_{\parallel} &= \frac{n_t \cos(\theta_i) - n_i \cos(\theta_t)}{n_t \cos(\theta_i) + n_i \cos(\theta_t)}, \\ r_{\perp} &= \frac{n_i \cos(\theta_i) - n_t \cos(\theta_t)}{n_i \cos(\theta_i) + n_t \cos(\theta_t)}, \end{aligned} \quad (6.2)$$

with n_i , n_t representing the refraction indexes of the incident and transmitted media, and θ_i , θ_t being the incident and refracted angles, respectively.

According to 6.1 and 6.2, the maximum Fresnel transmittance is observed at zero-incidence angle. In the case of air-glass interface, the maximum Fresnel transmission is 96% ($n_i=1$, and $n_t=1.51$).

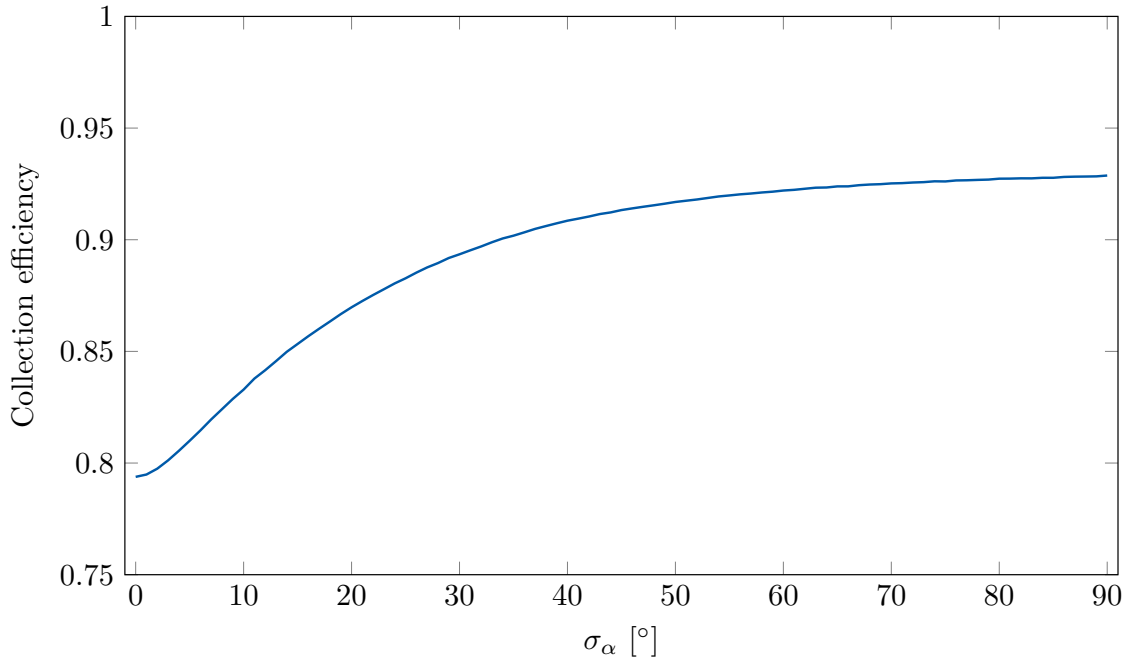


Figure 6.4: Simulated light collection efficiency of BK7G18 glass light guide as a function of surface roughness parameter σ_α .

It should be noted that for the Fresnel transmission, it is assumed that light is emitted along one defined direction. In the OpenGATE simulation, light is emitted from a point source into many directions within a half sphere. In the case of a smooth surface, most of the light emitted by the point source hits the interface surface at a non-zero-incidence angle. Thus, most of the light transmits through the air–glass interface with a reduced efficiency.

In the case of a rough surface, there is a higher chance that the light from the point source hits a micro-facet with a random tilt which results in normal light incidence to the micro-facet, increasing the collection efficiency of the light guide. In order to provide efficient scintillation photons collection through the scintillator–air–glass interface, a rough glass surface characterized by randomly tilted micro-facets is better than a smoothly polished surface.

To investigate the effect of various surface roughness of the glass light guide on the light transmission efficiency, we fixed the light guide area, thickness, and roughness at $5\text{ mm} \times 5\text{ mm}$, 1 mm and 10° , respectively, and varied only the quality of front and back surface (smooth or rough). We define the surface facing the point light source as front surface, and the opposite side as back surface. We compared the η_{tr} value for four different cases of the glass light guide surfaces: (1) both front and back surfaces are smoothly polished; (2) the front surface is rough, the back surface is smooth; (3) the back surface is rough; (4) both front and back surfaces are rough. The simulation results are summarized in Figure 6.5.

For the case (1) when all surfaces are polished and the glass light guide is surrounded by air, zero transmission through the upper side of the light guide is observed. This effect is in agreement with the Snell’s law because any light that hits the upper side of the light guide has an incidence angle greater than the critical angle to cross the glass–air interface. The refraction indexes of air and BK7G18 are 1 and 1.51, respectively. Therefore, the critical angle is $\arcsin(1/1.51) \sim 41.5^\circ$. The minimum angle at which a scintillation light ray can hit the upper surface of the light guide is $(90^\circ - 41.5^\circ = 48.5^\circ)$.

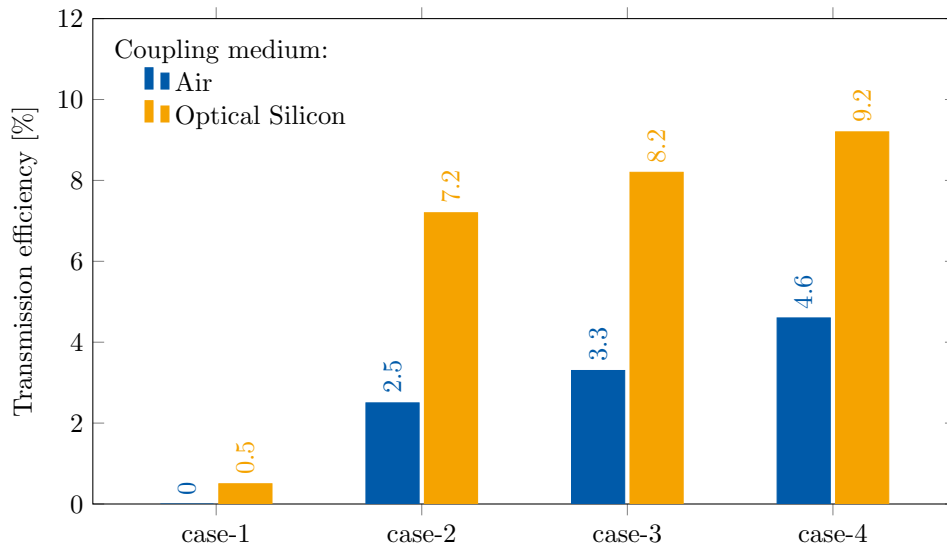


Figure 6.5: Transmission efficiency of the glass plate for different surface finishing (case (1) front and back surfaces are smooth, (2) front surface rough and back smooth, (3) front smooth and back rough, (4) front and back are rough) and different optical coupling from PMT side (air – blue bars, optical silicon – orange bars).

The use of an optical silicon (for example RTV-615, produced by Momentive, having a refraction index of 1.4) is a possible way for extracting the scintillation photons through the upper side of a rectangular glass plate with polished surfaces. In this case, the critical angle through the upper side is increased to approximately 68° ; thus, the photons with $48.5\text{--}68^\circ$ incidence at the upper surface of the glass plate can transmit. The OpenGATE simulation of the glass light guide with all surfaces polished and the glass–silicon coupling at the upper side results in 0.5% transmission efficiency. The transmission efficiency values for the case-1 in Figure 6.5 are the lowest because (1) as shown earlier in Figure 6.4, the polished surface does not provide the most efficient light collection; (2) the majority of scintillation photons escapes through the front and back sides of the light guide; (3) part of the photons is absorbed by the light guide.

For the simulation cases 2–4, the light transmission efficiency is above zero, even with the glass–air coupling at the upper side. This is due to smearing of the light incidence angles by diffuse scattering on the rough surfaces. In the case when only the front side is rough, $\eta_{tr} = 2.5\%$, i.e., slightly smaller compared to case-3 where only the back side is rough (3.3%). The highest transmission is observed when both front and back surfaces are rough. The 4.6% transmission efficiency is observed for glass–air coupling if the front and back surfaces are rough, while glass–optical silicon coupling results in an increase of up to $\eta_{tr} = 9.2\%$.

For our simulations, we conclude that the glass light guide configuration with rough surfaces of the front and back sides and using optical silicon coupling at the glass–plastic interface is the most optimal surface configuration.

Figure 6.6 shows a 2D map of the light transmission efficiency η_{tr} of a rectangular glass light guide coupled with optical silicon on the upper side, with the σ_α roughness parameter for front and back rough surfaces presented on the y-axis and the glass plate thickness presented on the x-axis. The simulated glass plate had $50\text{ mm} \times 50\text{ mm}$ area.

As mentioned earlier, the transmission efficiency for smooth surfaces is zero independently on the glass plate thickness. The transmission efficiency increases with increasing σ_α reaching 2% for $\sigma_\alpha = 10^\circ$ for a 1 mm

thick glass plate. The maximum transmission efficiency is observed for a glass plate thickness between 5 and 15 mm, depending on σ_α and followed by reduction of transmission at larger thickness. The initial increase in transmission with the glass thickness is due to (1) the increase in the number of photons N_{edge} incident on the upper edge of the light guide (thus, increasing the number of photons that can go out, N_{out}) and (2) the reduction of the number of internal reflections (which reduces the probability to lose photons mainly through front and back sides of the light guide). For thicknesses larger than 5 mm, light absorption by the glass light guide starts to contribute more significantly, leading to the loss of transmission efficiency through the glass light guide.

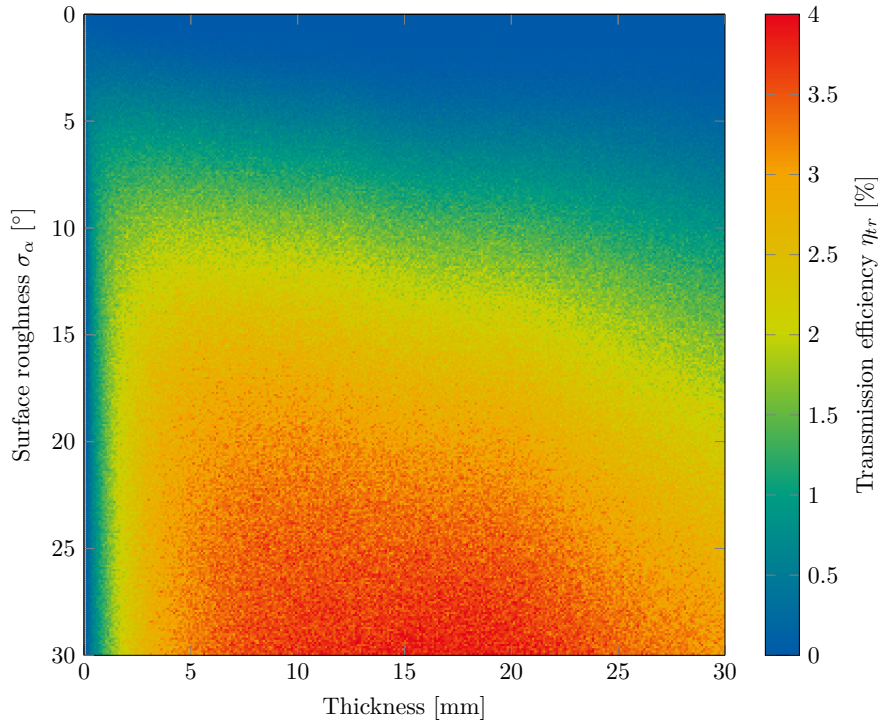


Figure 6.6: Simulated glass light guide transmission efficiency as a function of thickness and surface roughness σ_α . Different colors correspond to different transmission efficiency values η_{tr} .

Another factor, that is important when selecting the optimal thickness of the light guide, is the energy loss of the ion beam in the light guide. It is advantageous to keep the light guide as thin as possible to minimize the amount of material, that can be activated by the incident beam and to make sure that the beam passes through the detector homogeneously depositing its energy along the detector active volume. In the specific case of our experiment, the detector thickness is limited by the range of the 150 MeV/u ^{238}U ions. According to Figure 2.1b, the maximum thickness, where 300 MeV/u ^{238}U has a rather constant stopping power, is around 1–2 mm. The maximum thickness of the light guide is therefore more limited by ion beam energy loss and range, rather than by absorption of scintillation photons within the light guide.

6.2.2 Experimental characterization of a light diffusion by BK7G18 glass used as a light guide

BK7G18 borosilicate glass plate 50 mm \times 50 mm \times 2 mm with mean square roughness 2–4 μm from all sides was purchased from Docter Optics SE. In order to correlate the surface quality of the purchased glass to the σ_α

parameter of the UNIFIED model in Geant4, the light diffusion of the BK7G18 glass plate was characterized. We assembled an experimental setup to measure the diffuse scattering of the 405 nm wavelength laser light by BK7G18 glass, as schematically shown in Figure 6.7.

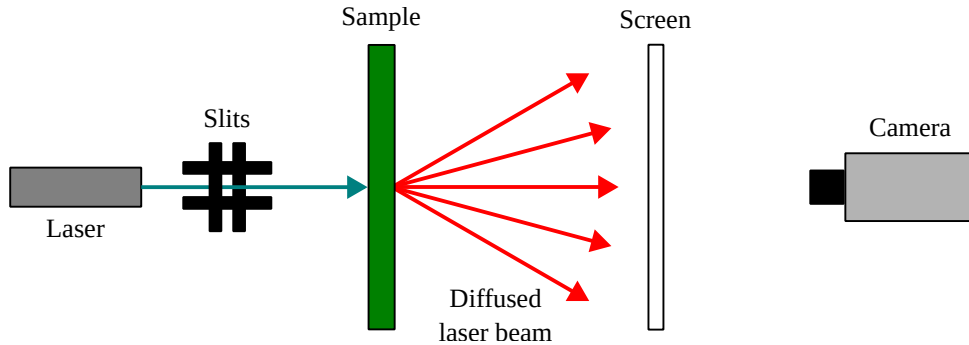


Figure 6.7: Schematic view of the setup used to characterize the BK7G18 light guide roughness with respect to the σ_α roughness parameter of the UNIFIED model.

The incident light beam is provided by a 405 nm wavelength laser (PicoQuant). The laser light is collimated by horizontal and vertical slits, and hits the sample surface at normal beam incidence. Transmitted diffused light is projected to a screen made of a millimeter paper that is located behind the sample. The diffused light projection from the screen is further monitored and recorded by a PCO.1600 camera.

In a first step, the laser beam divergence was measured without the sample by monitoring the spot at various distances between the screen and laser output slit. The resulting projections showed a Gaussian shape of the beam spot along both horizontal and vertical axes of the screen (e.g., see Figure 6.8).

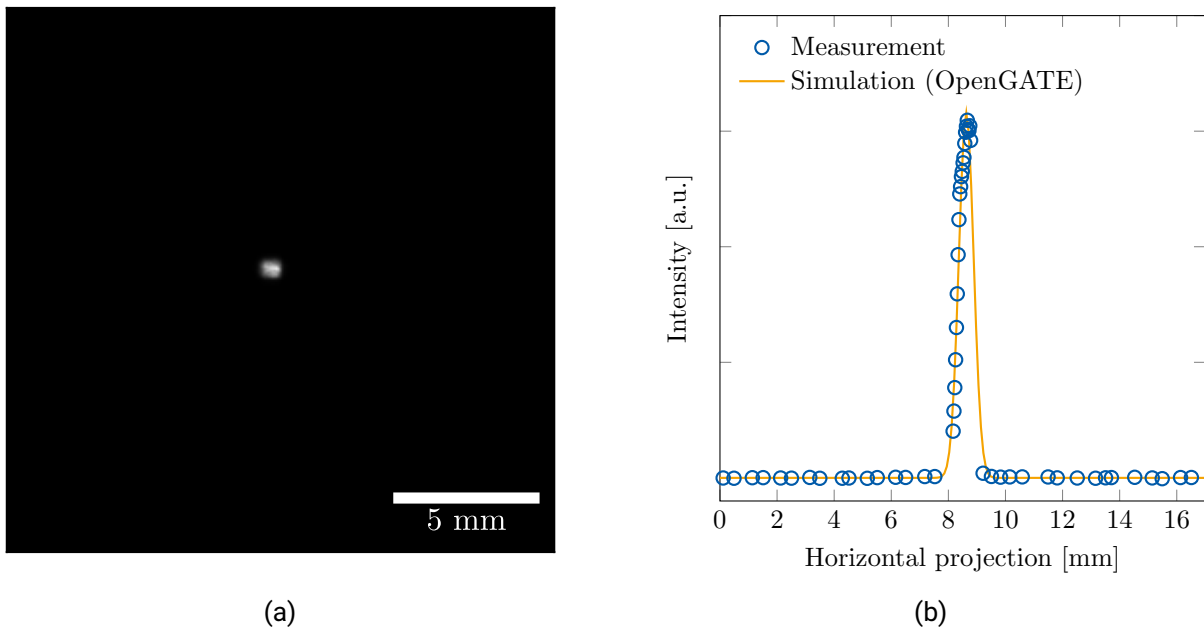


Figure 6.8: The image of the laser beam spot observed on the screen, when no sample is inserted (a). Comparison of the measured laser spot projection with the one simulated using OpenGATE (b).

After characterizing the shape of the laser beam spot, the BK7G18 sample (50 mm × 50 mm × 2 mm) was inserted in front of the screen at a distance of 12.8 mm, and the diffused laser beam spot on the screen was recorded by a camera (see Figure 6.9a). With the OpenGATE simulations, diffused beam images on the screen were simulated for various σ_α values and compared to the experimentally measured data.

Figure 6.9b compares experimental measurements and simulation results. The best simulation to experiment matching is obtained for $\sigma_\alpha = 20^\circ$. This value is used further for the prototype detector performance simulations.

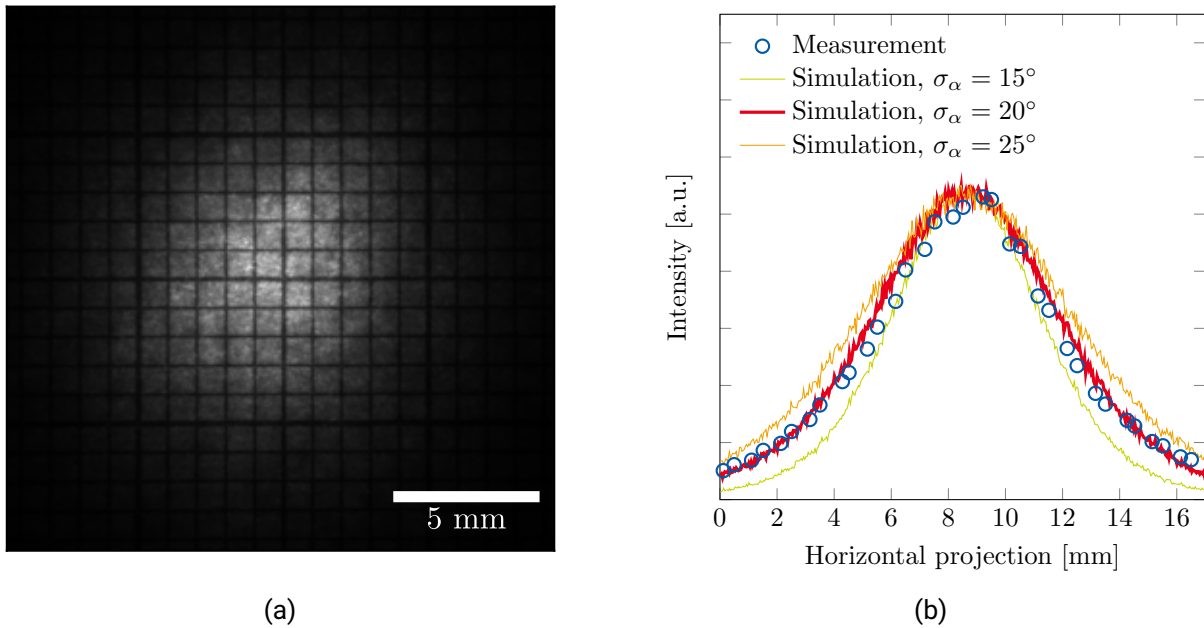


Figure 6.9: Image of laser beam spot observed on screen, when BK7G18 light guide is inserted (a). Comparison of the measured laser spot projection with the one simulated using OpenGATE (b). The best simulation versus experiment match is observed when $\sigma_\alpha = 20^\circ$.

6.2.3 Simulation of the transmission efficiency by BK7G18 glass at various source positions

When the prototype scintillation detector is applied for beam diagnostics, the exact position where an incident ion hits the detector active volume is uncertain. Ions, that hit the detector active volume at different positions, create light emission from cylindrical volumes along ion trajectories. However, due to the self-absorption, it was sufficient to simulate a point light sources on the ZnO surfaces. The glass light guide transmission efficiency for a point light source located at different vertical and horizontal positions of the detector must be investigated to estimate what is the potential spread of the detector signal amplitudes coming from ions that hit the detector in different regions.

Therefore, we simulated the transmission efficiency of the 50 mm × 50 mm × 2 mm BK7G18 glass light guide with 45 mm × 45 mm × 0.5 mm ZnO-based scintillating ceramic plates attached in front and back of the BK7G18 glass as shown in Figure 6.1. The region covered by ZnO(In) tiles is smaller than the BK7G18 light guide area. Scintillating tiles and glass light guide are coupled through an air gap of 50 μm thickness. The glass light guide at the upper side is coupled to an optical silicon (RTV-615, produced by Momentive) as it has

been described earlier. The ZnO-based ceramics had polished surfaces, whereas the BK7G18 glass had rough surface finishing from all sides, characterized by $\sigma_\alpha = 20^\circ$. The entire system is covered with a 0.5 mm layer of Teflon. At each measurement point, the transmission η_{tr} is plotted as a function of the x and y coordinates.

Figure 6.10 shows a 2D map of the simulated glass light guide transmission efficiency with the point scintillation light source placed at various horizontal (x-axis) and vertical (y-axis) positions of the prototype detector active area.

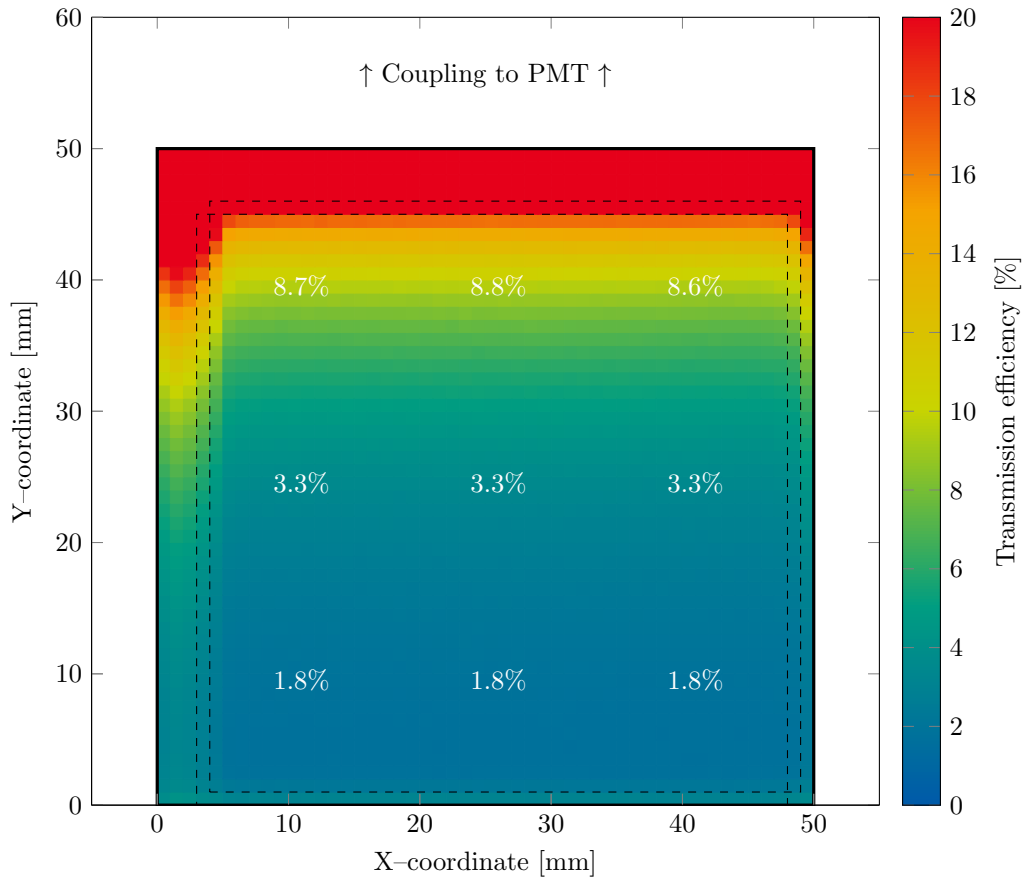


Figure 6.10: 2D map of the transmission efficiency of scintillation detector prototype simulated for scintillation light occurring at different horizontal and vertical positions in the detector active volume. Thick black lines define the boundaries of the BK7G18 glass light guide, while dashed lines show the boundaries of the region covered by ZnO(In) tiles. The upper side of the color map corresponds to the glass light guide region that is coupled to PMT via optical silicon and plastic light guide.

Along the x-axis, the transmission efficiency is lower for the active volume region that is covered with ZnO(In) tiles (x-coordinate from 5 to 49 mm) than the one which is not covered by ZnO(In) tiles (x-coordinate 0–5 mm, and 49–50 mm). This is because, in the region, that is not covered by ZnO(In) tiles, the light escaped through the front or back side of the light guide has a higher chance to be reflected by the Teflon tape back to the light guide rather than being absorbed and lost. In the region covered by ZnO(In) tiles, the light that leaves the light guide through the front or back side can be absorbed by the ZnO(In) tiles and thus gets lost. This

reduces the transmission efficiency, rather than the light is reflected back to the light guide and contributes to the transmitted light intensity.

For the x-coordinates from 4 to 49 mm (where the active volume is covered by ZnO(In) tiles), there is no significant difference in transmission efficiency. Figure 6.11a shows the projection of the transmission efficiency along the x-axis passing through the glass light guide center.

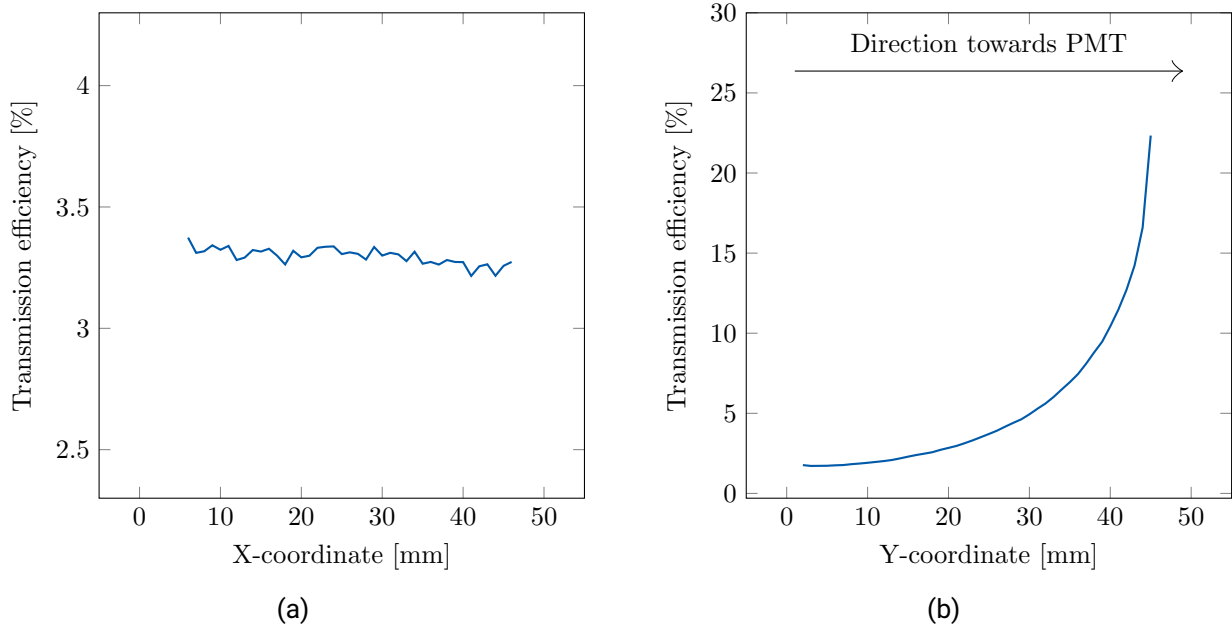


Figure 6.11: Horizontal (a) and vertical (b) projection of the simulated transmission efficiency of the scintillation detector prototype along the x- and y-axes passing through the center of the detector active volume.

There is an exponential growth of the glass light guide transmission efficiency with the increase in y-axis coordinate. The lowest η_{tr} values of $\sim 1.8\%$ are observed at the bottom side of the glass light guide. The transmission efficiency increases up to $\sim 8.7\%$ with approaching the upper side of the glass light guide. Figure 6.11b shows a 2D map projection along the y-axis passing through the glass light guide center.

Based on the simulation result for the presented prototype configuration, one should expect a distinctive difference in the signal amplitudes generated by ions hitting the upper or lower side of the prototype active area, while no difference for the ions hitting the prototype on the left or right side.

6.3 Step-by-step description of the prototype detector assembly

The main steps of the prototype assembly procedure are schematically summarized in Figure 6.12.

1. The plastic light guide is wrapped with two layers of Teflon tape (RS Pro PTFE Band) of thickness 0.2 mm and width 12 mm. The Teflon tape wrapping is necessary to reflect the scintillation light back into the light guide.

-
2. The plastic light guide is fixed on a 3D-printed holder made of white polyethylene terephthalate glycol plastic (PETG). This is used to attach the plastic and BK7G18 glass light guides.
 3. The upper part of the plastic light guide is wrapped with two layers of a black tape. The tape is necessary to avoid external light entering the light guide.
 4. Initial ZnO(In) scintillating ceramic tiles are mounted in 3×3 arrays on the front and back sides of the BK7G18 borosilicate light guide. The tiles are fixed using Kapton tape at the edges of the tiles. The front array of tiles is shifted 1 mm horizontally and vertically relative to the back array of tiles to ensure that an ion that passes between two front tiles still hits the back tile and induces a signal.
 5. The borosilicate glass light guide with the ZnO(In) ceramic tiles is wrapped with two layers of the same type of the Teflon tape as the plastic light guide.
 6. After wrapping, the light guide with the scintillators is mounted to the 3D-printed white PETG holder, which is attached to the plastic light guide. The two light guides are glued together using optical silicon (RTV-615, produced by Momentive). The silicon provides additional mechanical fixation of the light guides and increases the efficiency of the light transfer from the borosilicate glass plate to the UV-transparent plastic light guide.
 7. To avoid possible air bubbles in the two-component silicon mixture, it was stored in vacuum (> 0.1 MPa) and for approximately 0.5 h before and 1 h after applying the silicon between plastic and glass light guides.
 8. The 3D-printed holder is wrapped with two layers of black tape to protect the active volume from external light. A ring mounted on the upper part of the plastic light guide fixes the light guide on the photomultiplier housing.
 9. The PMT is mounted inside the housing and pressed towards the light guide. We used Hamamatsu H7415 assembly like the one used for sample characterizations, described in chapters 4 and 5.
 10. The light guide and PMT are attached to the housing. A silicon optical pad (RTV-615) is placed between the plastic light guide and the PMT to provide a soft mechanical contact, and efficient optical coupling between the two parts. Finally, all the connections are wrapped with a black tape to prevent the entrance of external light.

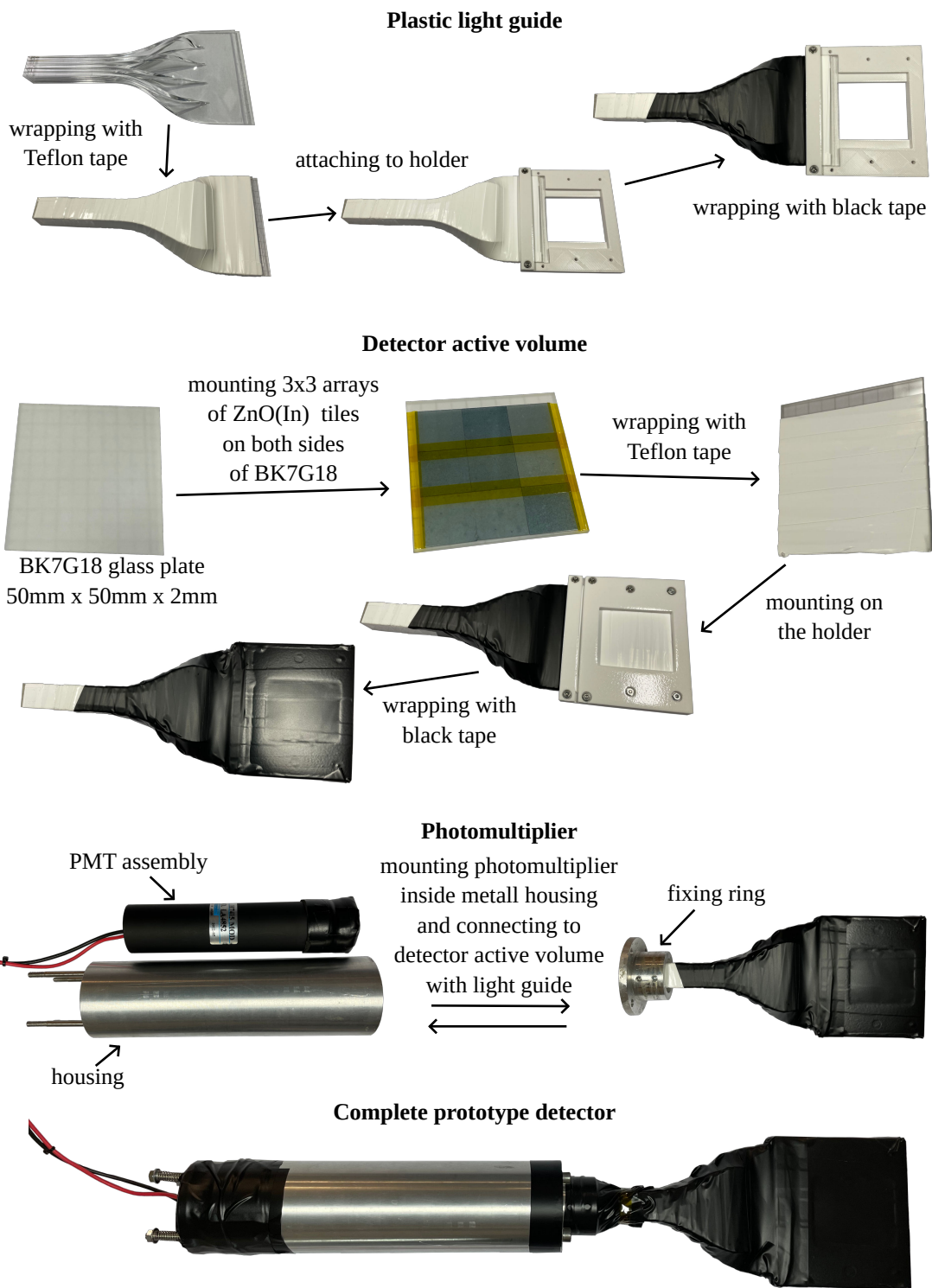


Figure 6.12: Detector components and prototype assembly from top to bottom.

7 Test of ZnO-Based Scintillation Detector Prototype

This chapter describes the experimental tests of the prototype detector performance and its comparison to a standard plastic scintillation detector. This includes the description of the setup and measurements with several ion species, and analysis of the prototype detector signal amplitude and particle counting efficiency at low and high counting rates.

7.1 Experimental setup description

Performance of the detector prototype described in the previous chapter was tested with various relativistic heavy ions and compared to the standard BC400 plastic scintillation detector and ionization chamber. Figure 7.1 shows the experimental setup layout. A 5 mm diameter collimated ion beam from the SIS18 hits the prototype detector mounted on a remotely controllable X/Y movable stage. The scintillating screen is remotely moved IN/OUT from the ion beam in front of the prototype detector, and the beam spot is monitored by the camera. The ion beam which has sufficient energy to punch through the prototype detector is registered by the reference plastic scintillation detector mounted downstream. The plastic scintillation detector is used as a trigger detector to acquire individual ion signals, which are recorded by the fast 2 GHz Tektronix oscilloscope at various x and y-axis coordinates of the ion beam on the detector. The signals on the oscilloscope were used to determine the counting efficiency of the prototype relative to the BC400 reference detector at various (x, y) coordinates on the prototype detector active area as: $\eta_{count} = Count_{prot}/Count_{ref}$. The characterization was performed using ^{40}Ar , ^{197}Au , ^{208}Pb , and ^{238}U ion beams at 300 MeV/u energy.

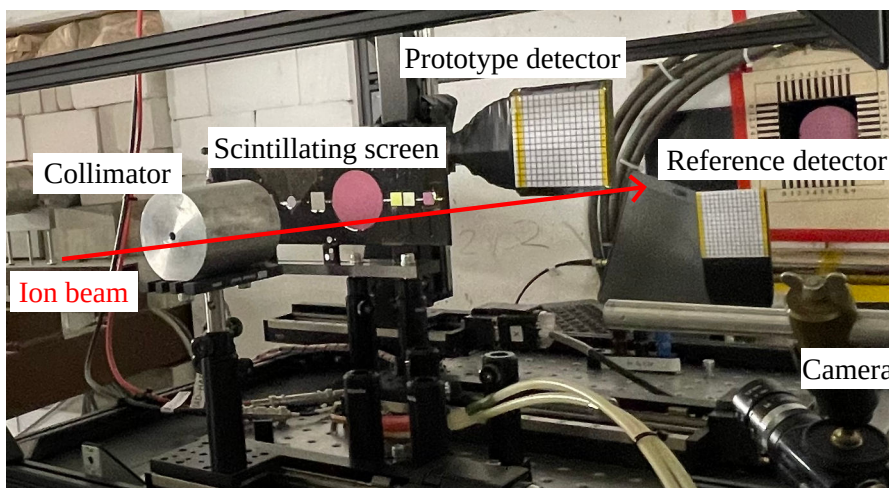


Figure 7.1: Experimental layout used for in-beam tests of the prototype detector.

7.2 Prototype detector signal amplitude variation across the detector active area

Figure 7.2a shows 2D maps of the detector signal amplitudes registered for a 300 MeV/u Au beam hitting the prototype detector at various (x, y) coordinates of the detector active area. Within the region covered by ZnO(In) tiles, no significant change in mean output signal amplitude is observed along the horizontal axis. On the other hand, the vertical axis shows higher signal amplitudes when approaching the side connected to the photomultiplier tube. Figure 7.2b shows the corresponding horizontal and vertical signal amplitude profiles.

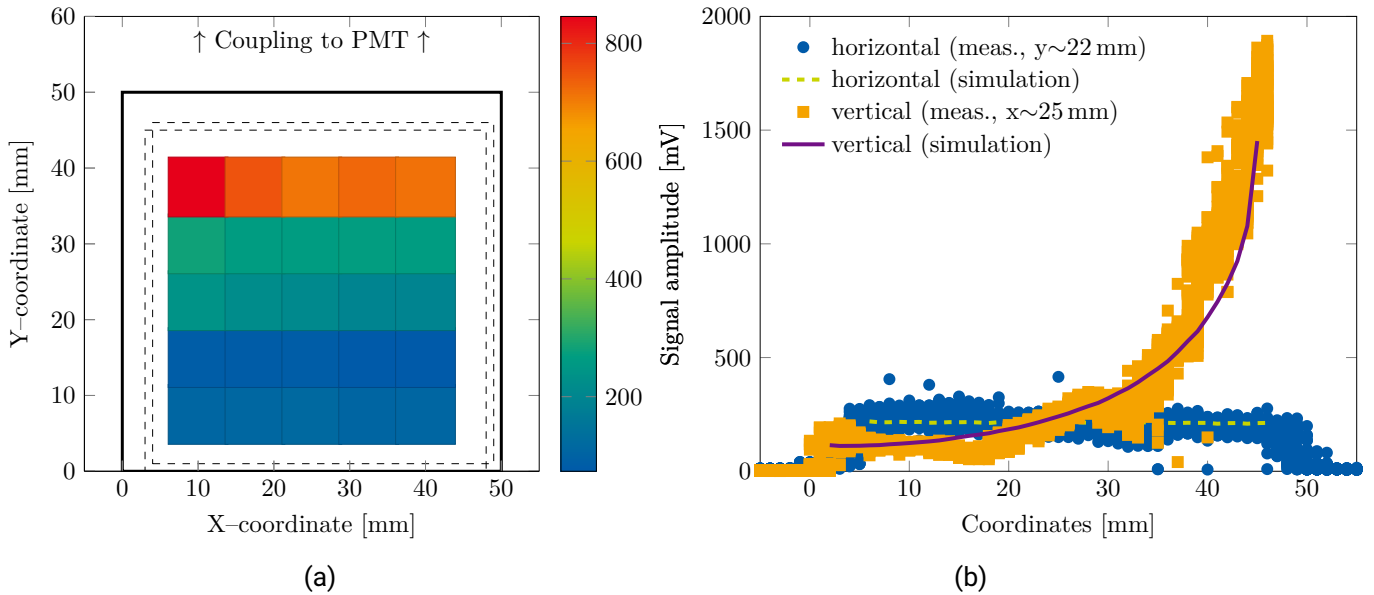


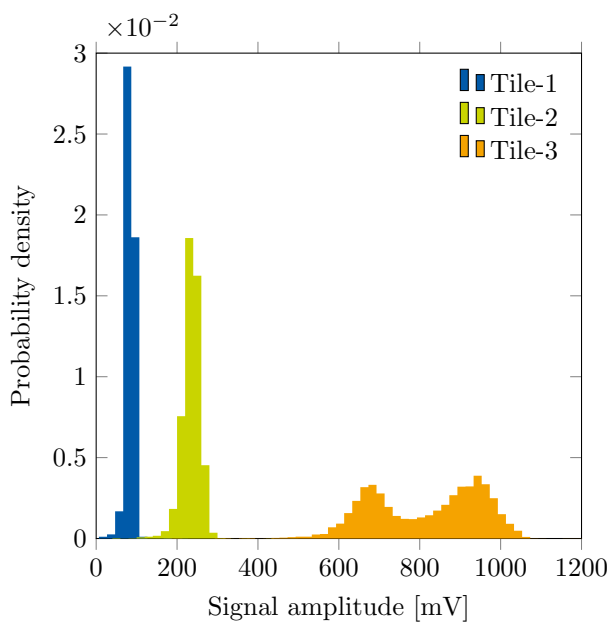
Figure 7.2: 2D color map of the prototype detector performance tests under 300 MeV/u Au beam, showing the amplitude of the output signal(a). The signal amplitude plotted along horizontal and vertical axis across the active volume center (b). Color points correspond to experimental measurements, while dashed lines correspond to OpenGATE simulations.

The amplitude increase in the vertical projection observed experimentally is in agreement with results of simulations and can be associated with the increase in the light collection efficiency of the borosilicate light guide.

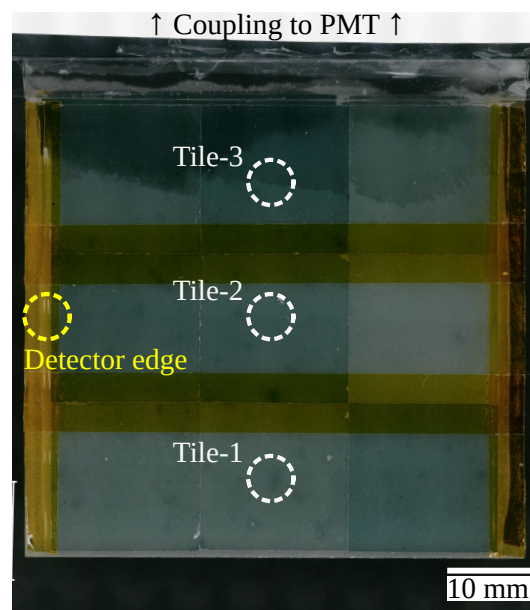
During the experimental test of the prototype, we observed that the upper row of the scintillating tiles provides two peaks in the signal amplitude distribution (see Figure 7.3a). After the experimental test, the active area of the prototype was disassembled and investigated for failures. Figure 7.3b shows that, part of the optical silicon that coupled optically the glass and plastic light guides intruded between the upper row of the scintillating tiles and the glass light guide. This changes the light collection efficiency from the upper row of the scintillating tiles, that is not considered in the OpenGATE simulations.

Figure 7.4 shows the signal amplitude distribution for a 300 MeV/u Pb ion beam hitting the edge of the prototype detector (as shown in Figure 7.3b). During this measurement, the 5 mm diameter beam spot could cover several distinctive regions of the prototype:

- Region 1: the beam passes through the borosilicate glass light guide only;



(a)



(b)

Figure 7.3: Amplitude distributions of the prototype detector output signals recorded when a 300 MeV/u Pb beam hits different ZnO(In) tiles on the detector active area (a). Photo of the prototype detector active area taken after the in-beam tests, showing the upper row of ZnO(In) tiles contaminated with the optical silicon (b). The two peaks in the amplitude distribution of Tile-3 (left figure) are ascribed to a contamination with optical silicon.

- Region 2: the beam passes through the borosilicate glass light guide and the ZnO(In) scintillating tile attached from one side (front or back to be clarified) of the light guide;
- Region 3: the beam passes through the borosilicate glass light guide and ZnO(In) scintillating tiles attached from both sides of the light guide.

The signal amplitude distributions, shown in Figure 7.4, have three distinctive peaks. The lowest amplitude (~ 25 mV) corresponds to signals from the beam passing through the borosilicate glass light guide only. The medium amplitude peak (~ 100 mV) corresponds to signals from the beam passing through one ZnO(In) scintillating tile and the glass light guide. The largest amplitude peak (~ 200 mV) comes from the beam hitting the borosilicate light guide and ZnO(In) scintillating tiles from both front and back sides of the glass light guide.

From Figure 7.4 one can see that the parasitic signal, coming from the borosilicate glass only, has an average amplitude that is 4 times lower than the signal amplitude from region-2, and 8 times less than the signal amplitude from region-3. The contribution of the signal from the borosilicate glass to the total detector signals registered within the prototype detector active area, covered with two ZnO(In) scintillating tiles, is therefore only minor.

The amplitude distributions of the prototype detector measured for various ion species exhibit around 25% resolution (FWHM/Mean) that does not change at different (x, y) positions on the detector active region. In comparison to the prototype detector, we observed 9% resolution for the reference plastic scintillation detector.

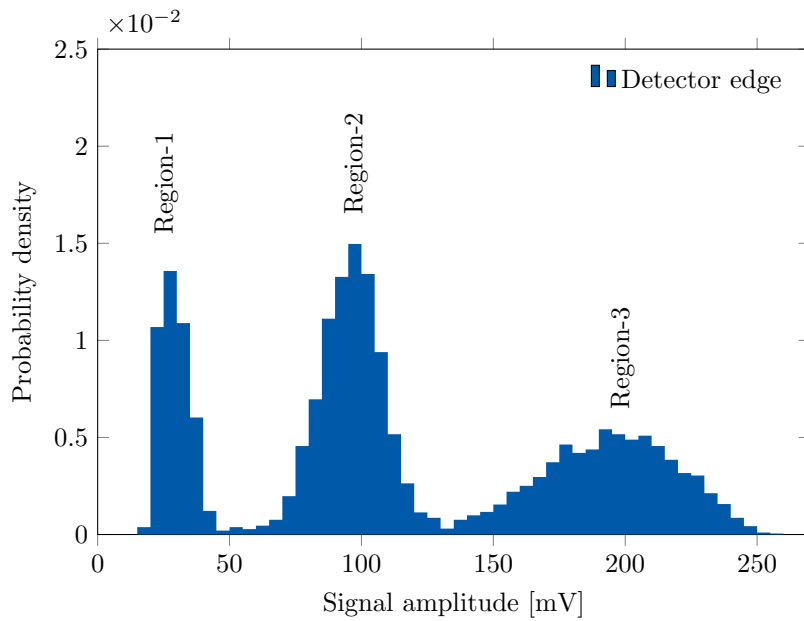


Figure 7.4: Prototype detector output signal amplitude distribution, when 300 MeV/u Pb beam hits the edge of the prototype (see Figure 7.3b), covering three distinctive regions: 1 – beam passes only through the BK7G18 light guide, 2 – beam passes through BK7G18 light guide and ZnO(In) tile on one side, 3 – beam passes through BK7G18 light guide and ZnO(In) tiles on both front and back sides.

7.3 Counting efficiency variation across detector active area

As shown in Figure 7.2a, each individual ion of the beam that passes through the prototype detector active volume creates a signal that, depending on its signal amplitude, can or cannot result in a particle count. The number of individual ion counts registered by the prototype and reference detectors can be used to determine the counting efficiency of the prototype detector relative to the reference BC400 scintillation detector characterized at various (x, y) positions.

Figure 7.5 shows the prototype detector counting efficiency map recorded for 300 MeV/u U ions. The entire active region of the prototype detector exhibits 100 % counting efficiency relative to the plastic scintillation detector. The counting efficiency drops at the edges of the prototype due to the beam partially missing the active region.

7.4 Counting efficiency at high counting rates

A non-collimated 300 MeV/u Au ion beam was used to test the prototype detector performance at different counting rates ranging from 10^4 to 2×10^6 ions/s. To compare the counting rate of the prototype detector at various beam intensities, a 300 MeV/u Au ions passed through an ionization chamber (IC) before reaching the prototype detector.

The comparison of the prototype to the IC counts is shown in Figure 7.6. The counting rate output of the prototype detector is sublinear above 30 nA current registered by the ionization chamber (corresponding to

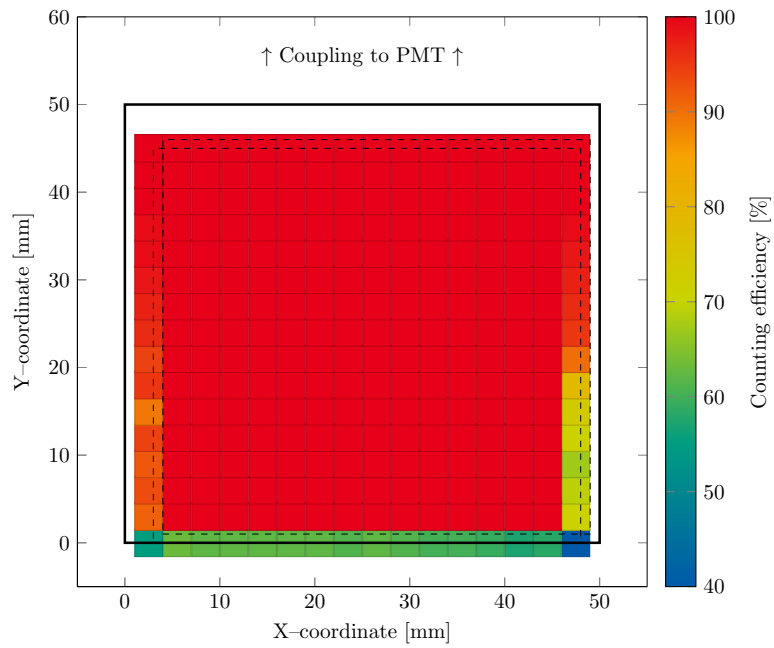


Figure 7.5: Counting efficiency of the prototype detector relative to the reference plastic scintillator measured for 300 MeV/u U ions.

3×10^5 ions/s). The maximum counting rate, at which the nonlinear detector counts are observed, is due to the used electronics limitation, but not due to the properties of the scintillator.

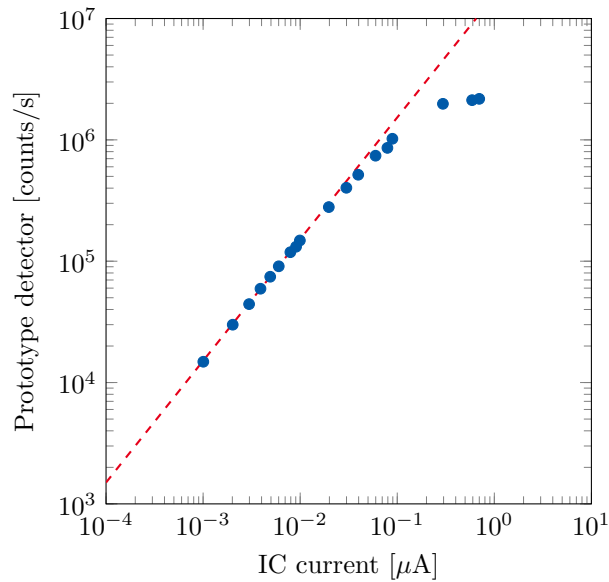


Figure 7.6: Comparison of the counting rate of the prototype detector versus the current in the ionization chamber for 300 MeV/u Au ions.

8 Summary and Outlook

8.1 Summary

The response of In-doped and Ga-doped ZnO ceramics, produced by uni-axial hot pressing in vacuum, to swift and relativistic heavy ions was investigated. Irradiation experiments with ion species varying from Ar to U at energies from 4.8 to 500 MeV/u showed that the decay of the intensity of ion-induced luminescence of ZnO-based ceramics follows the Birks-Black model. The critical fluence (corresponding to 50% intensity loss) was evaluated for different ion species and compared to a plastic scintillator of BC400 type. ZnO ceramic-based scintillation detector exhibits much better radiation stability and promises approximately 100 times longer operation time compared to standard plastic scintillation detectors.

Ionoluminescence spectra, light output, luminescence rise and decay times were characterized for four different ZnO-based scintillating ceramics: ZnO(In)-initial, ZnO(In)-thermally-treated, ZnO(Ga)-initial, and ZnO(Ga)-thermally-treated.

All investigated ceramics exhibit strong near-band-edge (NBE) luminescence in the UV region, with a significantly suppressed deep-level emission component in the yellow/green light spectral region. The evolution of the luminescence spectra as a function of ion fluence showed a reduction of the NBE peak intensity. No new emission peaks appeared, even not at the highest fluences reached in this work. The highest NBE luminescence light output is observed for In-doped and Ga-doped ZnO ceramics thermally treated in Ar/H₂ atmosphere.

The relative changes in the intensity of the ionoluminescence spectra were compared to changes in optical light transmission of the irradiated samples. The in-situ characterization performed with swift heavy ions showed that the relative ionoluminescence intensity drop is faster than the relative transmission loss. Thus, we conclude that the loss of luminescence is negligibly affected by the loss of the sample's transmission. On the other hand, we observed a red shift of the NBE peak wavelength for the Au ion irradiation at 4.8 and 8.3 MeV/u energy (maximum energy loss), which correlates with the red shift of the measured absorption edge.

Scintillation light pulses from individual incident ions, characterized with a photomultiplier tube (PMT), allowed us to compare the light output and luminescence decay times for different ceramic samples and reference plastic scintillators. The light output results from the characterization with PMTs agree with what was observed with ionoluminescence spectroscopy. By deconvolution of the fast PMT signals, the shape of the scintillation light pulses from individual incident ions were extracted, providing information about the scintillation kinetics. All investigated ZnO-based ceramics exhibited scintillation decay time below one nanosecond. No change in the decay time was observed for irradiated samples.

Several ZnO ceramic samples were analyzed by Raman spectroscopy. In the fluence range, where significant changes in the luminescence intensity are observed, the Raman spectra remained unchanged. However, a band at 577 cm⁻¹ starts to grow, when the NBE luminescence intensity is reduced approximately by a factor

of ten. Based on this, we conclude that the loss of the luminescence intensity occurs even before significant changes in vibrational states of the ZnO ceramics lattice occur.

Based on the results obtained from the analysis of beam-induced effects, ZnO(In) ceramic tiles were used to build a scintillation detector prototype with 45 mm × 45 mm large active area. The prototype consists of 18 tiles arranged in two 3 × 3 ZnO arrays attached to a rectangular borosilicate glass plate from front and back sides. The propagation of optical photons through the detector was simulated with OpenGATE (Geant4). Based on the simulation for the rectangular borosilicate light guide, it was predicted that the prototype detector signal amplitude should depend on the location of the beam spot on the active area of the detector.

The prototype detector was assembled, and its performance was tested with various beams from Ar to U ions of 300 MeV/u energy. The tests confirmed the signal amplitude variations depending on the beam spot location on the detector's active region. The particle counting efficiency was 100% compared with a standard plastic scintillation detector. The prototype performance test at high counting rates indicated that non-linearity due to signal pileups starts at approximately 3×10^6 ions/s. The upper limit of the counting rate can be increased using a faster readout electronics.

The resulting ZnO(In)-based scintillation detector is demonstrated to be fast and radiation hard, and as such, a very promising scintillation detector to be used as one of the standard beam diagnostics tools for relativistic ion beams. Using the novel detector prototype would provide orders of magnitude longer operation times with a counting capability (efficiency) as good as the currently used plastic scintillation detectors but requiring less maintenance and beam interruption times during user experiments.

The results of this PhD research yield significant improvements not only at the GSI/FAIR facility, but they also broaden beam inspection capabilities at numerous heavy-ion accelerator facilities around the globe.

8.2 Future prospective for improvement

To further extend the operation time, the possibility of recovering the radiation damage in the ceramic by thermal annealing should be explored. As shown, thermal annealing of irradiated samples leads to the restoration of luminescent properties. Thus, the same scintillating tiles can be reused multiple times, reducing waste from detector maintenance compared to organic plastic scintillators.

Preliminary results indicate the recovery of X-ray-induced luminescence (XRL) properties of ZnO(In) irradiated with 300 MeV/u ^{238}U [117]. As noted in Figure 5.22 (chapter 5), comparing the ionoluminescence from an annealed pre-irradiated sample and pristine sample, one can get complete recovery of ionoluminescence properties by annealing in air at 500 °C for 30 min. More detailed studies of various annealing times and temperatures, as well as various accumulated radiation doses, are needed to find optimal annealing conditions.

8.3 Possible other applications

8.3.1 Beam diagnostics and accelerator physics applications

The investigated ZnO-based ceramics represent interest for other beam diagnostics instrumentation, not only as fast scintillation counters to measure beam intensities but also as fast scintillation screens to characterize

transverse and longitudinal beam profiles including beam spot shape and homogeneity in time and space within the irradiated region.

One of the challenges in beam profile measurements with scintillating screens is the saturation of the emitted scintillation light due to quenching at high incident particle intensities when numerous ions arrive within a short time (short pulsed beam) or a small spatial area (focused beam). The registered intensity of the scintillation light saturates, which leads to artifacts and inadequate evaluation of the beam spot shape or particle distribution within the beam spot.

The short sub-nanosecond scintillation decay times of ZnO-based ceramics are expected to provide saturation effects at higher particle intensities than for CROMOX ($\text{Al}_2\text{O}_3:\text{Cr}$) screens having decay times at the microsecond timescale.

8.3.2 Applications in nuclear and high energy physics

The fast scintillation rise and decay times of ZnO-based ceramics and high radiation hardness will be interesting for various nuclear and high-energy physics experiments. The fast signal rise time of the ZnO-based scintillation detector is ideal for getting precise event timestamps or particle velocity measurements by the time-of-flight (TOF) method.

In experiments requiring long exposure times to collect enough statistics, the use of radiation hard fast detectors would eliminate the time required for detectors maintenance and replacement.

8.3.3 Medical applications

Fast ZnO-based scintillation detectors are of interest in various medical applications. In particular, detection systems based on fast scintillators are required for ultrahigh dose rate dosimetry for FLASH radiotherapy. The FLASH radiotherapy is a novel radiation delivery modality characterized by very fast irradiations (< 300 ms) and ultra-high dose rates (> 40 Gy/s) using charged particles like protons or heavier ions. The dosimetry and beam monitoring of FLASH irradiations are challenging owing to the peculiar characteristics of FLASH beams. Ionization chambers are the gold standard for dosimetry in conventional radiotherapy; however, these detectors feature relatively slow response and saturation at high dose rates. Consequently, they cannot be used for FLASH beams without proper corrections.

Apart from that, materials and detecting systems investigated in this work are of high potential interest for modern medical imaging systems based on positron emission tomography and mammography techniques or single positron emission tomography. Cancer and cardiovascular diseases are often diagnosed at very late stages. The application of faster scintillation detectors with better time resolution could allow the diagnosis of the location of a tumor in a patient with higher precision. Tomography methods are crucial in routine medical checks, cancer treatment, brain mapping, optimum drug dosage, circulation research, etc. Better medical diagnostics is immediately reflected in a better quality of medical care and significantly improved general human health.

Bibliography

- [1] W. Crookes. “Certain properties of the emanations of radium”. In: *Chemical News* 87 (1903), p. 241.
- [2] E. Rutherford. “LXXIX. The scattering of α and β particles by matter and the structure of the atom”. In: *The London, Edinburgh, and Dublin Philosophical Magazine and Journal of Science* 21.125 (1911), pp. 669–688. DOI: 10.1080/14786440508637080.
- [3] W.R. Leo. *Techniques for Nuclear and Particle Physics Experiments: A How-To Approach*. Springer Science & Business Media, 1994.
- [4] FAIR — Facility for Antiproton and Ion Research in Europe. <https://fair-center.eu/overview>. Accessed: 2023-02-27.
- [5] GSI — GSI Helmholtzzentrum für Schwerionenforschung GmbH. https://www.gsi.de/en/researchaccelerators/fair/the_machine. Accessed: 2023-02-27.
- [6] P. Forck, P. Heeg, and A. Peters. “Intensity measurement of high-energy heavy ions at the GSI facility”. In: *AIP Conference Proceedings*. Vol. 390. 1. American Institute of Physics. 1997, pp. 422–429. DOI: 10.1063/1.52298.
- [7] G. Miersch et al. “Fast scintillators as radiation resistant heavy-ion detectors”. In: *Nuclear Instruments and Methods in Physics Research Section A: Accelerators, Spectrometers, Detectors and Associated Equipment* 369.1 (1996), pp. 277–283. DOI: 10.1016/0168-9002(95)00785-7.
- [8] K. Kawade et al. “Study of radiation hardness of Gd₂SiO₅ scintillator for heavy ion beam”. In: *Journal of Instrumentation* 6.09 (2011), T09004. DOI: 10.1088/1748-0221/6/09/T09004.
- [9] P.J. Simpson et al. “Superfast timing performance from ZnO scintillators”. In: *Nuclear Instruments and Methods in Physics Research Section A: Accelerators, Spectrometers, Detectors and Associated Equipment* 505.1-2 (2003), pp. 82–84. DOI: 10.1016/S0168-9002(03)01025-8.
- [10] P. Boutachkov et al. “Radiation hardness investigation of zinc oxide fast scintillators with relativistic heavy ion beams”. In: *Proceedings of the 8th International Beam Instrumentation Conference, IBIC2019, Malmö, Sweden*. JACoW Publishing. 2019, pp. 71–73. DOI: 10.18429/JACoW-IBIC2019-MOPP005.
- [11] W. Lehmann. “Edge emission of *n*-type conducting ZnO and CdS”. In: *Solid-State Electronics* 9.11–12 (1966), pp. 1107–1110. DOI: 10.1016/0038-1101(66)90134-1.
- [12] D. Luckey. “A fast inorganic scintillator”. In: *Nuclear Instruments and Methods* 62.1 (1968), pp. 119–120. DOI: 10.1016/0029-554X(68)90628-9.
- [13] M. Willander et al. “Luminescence from zinc oxide nanostructures and polymers and their hybrid devices”. In: *Materials* 3.4 (2010), pp. 2643–2667. DOI: 10.3390/ma3042643.
- [14] E.D. Bourret-Courchesne, S.E. Derenzo, and M.J. Weber. “Development of ZnO:Ga as an ultra-fast scintillator”. In: *Nuclear Instruments and Methods in Physics Research Section A: Accelerators, Spectrometers, Detectors and Associated Equipment* 601.3 (2009), pp. 358–363. DOI: 10.1016/j.nima.2008.12.206.

-
- [15] E.I. Gorokhova et al. “Development and study of ZnO:In optical scintillation ceramic”. In: *Journal of Optical Technology* 82.12 (2015), pp. 837–842. DOI: 10.1364/JOT.82.000837.
- [16] K.A. Chernenko et al. “Structural, optical, and luminescent properties of ZnO:Ga and ZnO:In ceramics”. In: *IEEE Transactions on Nuclear Science* 65.8 (2018), pp. 2196–2202. DOI: 10.1109/TNS.2018.2810331.
- [17] F. Muktopavela et al. “Effect of in doping on the ZnO powders morphology and microstructure evolution of ZnO:In ceramics as a material for scintillators”. In: *Latvian Journal of Physics and Technical Sciences* 55.6 (2018), pp. 35–42. DOI: 10.2478/lpts-2018-0042.
- [18] E.I. Gorokhova et al. “Structural, optical, and luminescence properties of ZnO:Ga optical scintillation ceramic”. In: *Journal of Optical Technology* 85.11 (2018), pp. 729–737. DOI: 10.1364/JOT.85.000729.
- [19] A. Hassan et al. “Near-band-edge emission enhancement and suppression of the deep levels in Ga-doped ZnO via surface plasmon-exciton coupling without a dielectric spacer”. In: *Journal of Materials Science: Materials in Electronics* 30.23 (2019), pp. 20544–20550. DOI: 10.1007/s10854-019-02418-2.
- [20] D. Millers et al. “ZnO and ZnO:Ga Ceramics for Advanced Scintillators”. In: *Advances in Materials* 9.4 (2020), p. 94. DOI: 10.11648/j.am.20200904.13.
- [21] J.S. Neal et al. “Evaluation of melt-grown, ZnO single crystals for use as alpha-particle detectors”. In: *IEEE Transactions on Nuclear Science* 55.3 (2008), pp. 1397–1403. DOI: 10.1109/TNS.2008.922829.
- [22] C. Liang et al. “Experimental study on scintillation efficiency of ZnO:In to proton response”. In: *Chinese Physics C* 35.11 (2011), p. 1037. DOI: 10.1088/1674-1137/35/11/011.
- [23] M.M.R. Zeidan. “Using Bulk Zinc Oxide as a Neutron Radiation Detector”. PhD thesis. University of Canterbury, 2015. DOI: 10.26021/7207.
- [24] Q. Zhang et al. “An ultrafast X-ray scintillating detector made of ZnO(Ga)”. In: *Journal of Instrumentation* 12.12 (2017), P12033. DOI: 10.1088/1748-0221/12/12/P12033.
- [25] R.M. Sahani et al. “Efficient alpha radiation detector using low temperature hydrothermally grown ZnO:Ga nanorod scintillator”. In: *Scientific Reports* 9.1 (2019), pp. 1–9. DOI: 10.1038/s41598-019-47732-1.
- [26] K. Koike et al. “Radiation hardness of single-crystalline zinc oxide films”. In: *Physica Status Solidi C* 9.7 (2012), pp. 1577–1579. DOI: 10.1002/pssc.201100566.
- [27] A. Sarkar et al. “Defects in 6 MeV H⁺ irradiated hydrothermal ZnO single crystal”. In: *Journal of Physics: Condensed Matter* 25.38 (2013), p. 385501. DOI: 10.1088/0953-8984/25/38/385501.
- [28] S. Pal et al. “Defects in 700 keV oxygen ion irradiated ZnO”. In: *Nuclear Instruments and Methods in Physics Research Section B: Beam Interactions with Materials and Atoms* 311 (2013), pp. 20–26. DOI: 10.1016/j.nimb.2013.06.009.
- [29] Y. Song et al. “Raman spectra and microstructure of zinc oxide irradiated with swift heavy ion”. In: *Crystals* 9.8 (2019), p. 395. DOI: 10.3390/cryst9080395.
- [30] D.R. Kumar et al. “Swift heavy ion induced effects on structural, optical and photo-catalytic properties of Ag irradiated vertically aligned ZnO nanorod arrays”. In: *Nuclear Instruments and Methods in Physics Research Section B: Beam Interactions with Materials and Atoms* 450 (2019), pp. 95–99. DOI: 10.1016/j.nimb.2018.03.015.

-
- [31] P.K. Das et al. “Effect of 120 MeV Ag ion irradiation on the structural and electrical properties of NiO/ZnO heterojunction”. In: *Materials Research Express* 6.12 (2020), p. 126449. DOI: 10.1088/2053-1591/ab6930.
- [32] N. Kato and M. Sugiyama. “Proton irradiation effects on NiO/ZnO visible-light-transparent solar cells for space applications”. In: *Japanese Journal of Applied Physics* 60.4 (2021), p. 048001. DOI: 10.35848/1347-4065/abea54.
- [33] S. Jan et al. “GATE: a simulation toolkit for PET and SPECT”. In: *Physics in Medicine & Biology* 49.19 (2004), p. 4543. DOI: 10.1088/0031-9155/49/19/007.
- [34] R. L. Workman et al. “Review of Particle Physics”. In: *Progress of Theoretical and Experimental Physics* 2022.8 (2022), p. 083C01. DOI: 10.1093/ptep/ptac097.
- [35] P.A. Rodnyi. *Physical processes in inorganic scintillators*. Vol. 14. CRC press, 1997.
- [36] J. Kiefer. *Biologische Strahlenwirkung: eine Einführung in die Grundlagen von Strahlenschutz und Strahlenanwendung*. Springer-Verlag, 2013.
- [37] J.F. Ziegler, M.D. Ziegler, and J.P. Biersack. “SRIM - The stopping and range of ions in matter (2010)”. In: *Nuclear Instruments and Methods in Physics Research Section B: Beam Interactions with Materials and Atoms* 268.11-12 (June 2010), pp. 1818–1823. DOI: 10.1016/j.nimb.2010.02.091.
- [38] H. Weick et al. “Energy-loss straggling of (200–1000) MeV/u uranium ions”. In: *Nuclear Instruments and Methods in Physics Research Section B: Beam Interactions with Materials and Atoms* 193.1-4 (2002), pp. 1–7. DOI: 10.1016/S0168-583X(02)00718-8.
- [39] H. Paul. “On the accuracy of stopping power codes and ion ranges used for hadron therapy”. In: *Advances in Quantum Chemistry*. Vol. 65. Elsevier, 2013, pp. 39–61. DOI: 10.1016/B978-0-12-396455-7.00002-9.
- [40] B. Firsov. “A Qualitative Interpretation of the Mean Electron Excitation Energy in Atomic Collisions”. In: *Journal of Experimental and Theoretical Physics* 36(9).5 (1959), pp. 1076–1080.
- [41] J. Lindhard and M. Scharff. “Energy Dissipation by Ions in the keV Region”. In: *Physical Review* 124 (1 Oct. 1961), pp. 128–130. DOI: 10.1103/PhysRev.124.128.
- [42] J. Lindhard and A.H. Sorensen. “Relativistic theory of stopping for heavy ions”. In: *Physical Review A* 53 (4 1996), pp. 2443–2456. DOI: 10.1103/PhysRevA.53.2443.
- [43] E.J. Sternglass. “Theory of secondary electron emission by high-speed ions”. In: *Physical Review* 108.1 (1957), p. 1. DOI: 10.1103/PhysRev.108.1.
- [44] P. Koschar et al. “Secondary-electron yield as a probe of preequilibrium stopping power of heavy ions colliding with solids”. In: *Physical Review A* 40 (7 Oct. 1989), pp. 3632–3636. DOI: 10.1103/PhysRevA.40.3632.
- [45] N. Medvedev et al. “Frontiers, challenges, and solutions in modeling of swift heavy ion effects in materials”. In: *Journal of Applied Physics* 133.10 (2023). DOI: 10.1063/5.0128774.
- [46] R. Katz, F.A. Cucinotta, and C.X. Zhang. “The calculation of radial dose from heavy ions: predictions of biological action cross sections”. In: *Nuclear Instruments and Methods in Physics Research Section B: Beam Interactions with Materials and Atoms* 107.1-4 (1996), pp. 287–291. DOI: 10.1016/0168-583X(95)01011-4.
- [47] J.A. Gledhill. “The range-energy relation for 0.1–600 keV electrons”. In: *Journal of Physics A: Mathematical, Nuclear and General* 6.9 (1973), p. 1420. DOI: 10.1088/0305-4470/6/9/017.

- [48] A. Menchaca-Rocha. “A simplified scintillator-response formula for multiple-ion energy calibrations”. In: *Nuclear Instruments and Methods in Physics Research Section A: Accelerators, Spectrometers, Detectors and Associated Equipment* 602.2 (2009), pp. 421–424. DOI: 10.1016/j.nima.2009.01.190.
- [49] D. Horn et al. “The mass dependence of CsI(Tl) scintillation response to heavy ions”. In: *Nuclear Instruments and Methods in Physics Research Section A: Accelerators, Spectrometers, Detectors and Associated Equipment* 320.1-2 (1992), pp. 273–276. DOI: 10.1016/0168-9002(92)90785-3.
- [50] E. Belmont-Moreno, A. Menchaca-Rocha, and K. Michaelian. “Application of a specific luminescence model to heavy-ion scintillation detection”. In: *Nuclear Instruments and Methods in Physics Research Section A: Accelerators, Spectrometers, Detectors and Associated Equipment* 332.1-2 (1993), pp. 202–205. DOI: 10.1016/0168-9002(93)90759-B.
- [51] K. Michaelian, A. Menchaca-Rocha, and E. Belmont-Moreno. “Scintillation response of nuclear particle detectors”. In: *Nuclear Instruments and Methods in Physics Research Section A: Accelerators, Spectrometers, Detectors and Associated Equipment* 356.2-3 (1995), pp. 297–303. DOI: 10.1016/0168-9002(94)01252-0.
- [52] J.B. Birks. “The Specific Fluorescence of Anthracene and Other Organic Materials”. In: *Physical Review* 84 (2 Oct. 1951), pp. 364–365. DOI: 10.1103/PhysRev.84.364.2.
- [53] J.B. Birks. *The theory and practice of scintillation counting*. Pergamon Press, Oxford, 1964.
- [54] V.I. Tretyak. “Semi-empirical calculation of quenching factors for ions in scintillators”. In: *Astroparticle Physics* 33.1 (2010), pp. 40–53. DOI: 10.1016/j.astropartphys.2009.11.002.
- [55] A. Meftah et al. “Swift heavy ions in magnetic insulators: A damage-cross-section velocity effect”. In: *Physical Review B* 48.2 (1993), p. 920. DOI: 10.1103/PhysRevB.48.920.
- [56] M. Toulemonde, S. Bouffard, and F. Studer. “Swift heavy ions in insulating and conducting oxides: tracks and physical properties”. In: *Nuclear Instruments and Methods in Physics Research Section B: Beam Interactions with Materials and Atoms* 91.1-4 (1994), pp. 108–123. DOI: 10.1016/0168-583X(94)96200-6.
- [57] A.E. Volkov et al. “Effect of ion velocity on creation of point defects halos of latent tracks in LiF”. In: *Nuclear Instruments and Methods in Physics Research Section B: Beam Interactions with Materials and Atoms* 407 (2017), pp. 80–85. DOI: 10.1016/j.nimb.2017.05.065.
- [58] N. Ishikawa et al. “Ion-velocity effects on defect production in high- T_c superconductors and metals irradiated with swift heavy ions”. In: *Physica Scripta* 1999.T80B (1999), p. 559. DOI: 10.1238/Physica.Topical.080a00559.
- [59] M. Lang et al. “Advances in understanding of swift heavy-ion tracks in complex ceramics”. In: *Current Opinion in Solid State and Materials Science* 19.1 (2015), pp. 39–48. DOI: 10.1016/j.cossms.2014.10.002.
- [60] S.J. Zinkle, V.A. Skuratov, and D.T. Hoelzer. “On the conflicting roles of ionizing radiation in ceramics”. In: *Nuclear Instruments and Methods in Physics Research section B: Beam Interactions with Materials and Atoms* 191.1-4 (2002), pp. 758–766. DOI: 10.1016/S0168-583X(02)00648-1.
- [61] V.A. Skuratov et al. “Surface defects in Al_2O_3 and MgO irradiated with high-energy heavy ions”. In: *Surface and Coatings Technology* 196.1-3 (2005), pp. 56–62. DOI: 10.1016/j.surfcoat.2004.08.095.
- [62] W. Wesch and E. Wendler. “Ion beam modification of solids”. In: *Springer Series in Surface Sciences* 61 (2016). DOI: 10.1007/978-3-319-33561-2.

-
- [63] J.C. Bourgoin, J.W. Corbett, and H.L. Frisch. "Ionization enhanced diffusion". In: *The Journal of Chemical Physics* 59.8 (1973), pp. 4042–4046. DOI: 10.1063/1.1680596.
- [64] S.J. Zinkle. "Effect of irradiation spectrum on the microstructural evolution in ceramic insulators". In: *Journal of Nuclear Materials* 219 (1995), pp. 113–127. DOI: 10.1016/0022-3115(94)00662-8.
- [65] R.L. Fleischer, P.B. Price, and R.M. Walker. "Ion explosion spike mechanism for formation of charged-particle tracks in solids". In: *Journal of Applied Physics* 36.11 (1965), pp. 3645–3652. DOI: 10.1063/1.1703059.
- [66] M. Toulemonde et al. "Transient thermal processes in heavy ion irradiation of crystalline inorganic insulators". In: *Nuclear Instruments and Methods in Physics Research Section B: Beam Interactions with Materials and Atoms* 166 (2000), pp. 903–912. DOI: 10.1016/S0168-583X(99)00799-5.
- [67] P. Lecoq et al. *Inorganic scintillators for detector systems*. 1st edition. Springer, 2006.
- [68] C. Pedrini. "Scintillation mechanisms and limiting factors on each step of relaxation of electronic excitations". In: *Physics of the Solid State* 47.8 (2005), pp. 1406–1411. DOI: 10.1134/1.2014478.
- [69] W. Shockley. "Problems related to p-n junctions in silicon". In: *Czechoslovak Journal of Physics* 11.2 (1961), pp. 81–121. DOI: 10.1007/BF01688613.
- [70] P.A. Rodnyi. "Core–valence luminescence in scintillators". In: *Radiation Measurements* 38.4-6 (2004), pp. 343–352. DOI: 10.1016/j.radmeas.2003.11.003.
- [71] R.A. Glukhov et al. "Simulation of energy conversion and transfer in CeF₃ after VUV photon absorption". In: *Journal of Alloys and Compounds* 275 (1998), pp. 488–492. DOI: 10.1016/S0925-8388(98)00378-8.
- [72] R.G.A. Kumar et al. "Luminescence dynamics and concentration quenching in Gd_{2-x}Eu_xO₃ nanophosphor". In: *Ceramics International* 41.4 (2015), pp. 6037–6050. DOI: 10.1016/j.ceramint.2015.01.051.
- [73] R. Chen, J.L. Lawless, and V. Pagonis. "A model for explaining the concentration quenching of thermoluminescence". In: *Radiation Measurements* 46.12 (2011), pp. 1380–1384. DOI: 10.1016/j.radmeas.2011.01.022.
- [74] P.D. Johnson and F.E. Williams. "Specific Magnetic Susceptibilities and Related Properties of Manganese-Activated Zinc Fluoride". In: *The Journal of Chemical Physics* 18.3 (1950), pp. 323–326. DOI: 10.1063/1.1747625.
- [75] P.D. Johnson and F.E. Williams. "The interpretation of the dependence of luminescent efficiency on activator concentration". In: *The Journal of Chemical Physics* 18.11 (1950), pp. 1477–1483. DOI: 10.1063/1.1747517.
- [76] G. Blasse and B.C. Grabmaier. "A general introduction to luminescent materials". In: *Luminescent Materials*. Springer, 1994, pp. 1–9.
- [77] B.P. Sobolev. *Multicomponent crystals based on heavy metal fluorides for radiation detectors*. Vol. 110. Institut d'Estudis Catalans, 1994.
- [78] Y.I. Gusev et al. "Optical Properties and Radiation Damages of Cerium Fluoride Crystals Doped with Alkali-Earth and Rare-Earth Elements." In: *MRS Online Proceedings Library (OPL)* 348 (1994). DOI: 10.1557/PROC-348-463.
- [79] J.B. Birks and F.A. Black. "Deterioration of anthracene under α -particle irradiation". In: *Proceedings of the Physical Society Section A* 64.5 (1951), p. 511. DOI: 10.1088/0370-1298/64/5/112.

-
- [80] D. Broggio et al. “Degradation of the scintillation yield of anthracene under high-fluence carbon ion beams”. In: *Radiation Measurements* 39.3 (2005), pp. 283–287. DOI: 10.1016/j.radmeas.2004.03.021.
- [81] W.J. Weber. “Models and mechanisms of irradiation-induced amorphization in ceramics”. In: *Nuclear Instruments and Methods in Physics Research Section B: Beam Interactions with Materials and Atoms* 166 (2000), pp. 98–106. DOI: 10.1016/S0168-583X(99)00643-6.
- [82] C. Manfredotti et al. “Luminescence centers in proton irradiated single crystal CVD diamond”. In: *Diamond and Related Materials* 19.7-9 (2010), pp. 854–860. DOI: 10.1016/j.diamond.2010.02.004.
- [83] P.A. Sullivan and R.A. Baragiola. “Ion beam induced luminescence in natural diamond”. In: *Journal of Applied Physics* 76.8 (1994), pp. 4847–4852. DOI: 10.1063/1.357258.
- [84] J.F. Gibbons. “Ion implantation in semiconductors—Part II: Damage production and annealing”. In: *Proceedings of the IEEE* 60.9 (1972), pp. 1062–1096. DOI: 10.1109/PROC.1972.8854.
- [85] R.P. Webb and G. Carter. “The effects of annealing upon the accumulation of amorphousness in a composite model of disorder production”. In: *Radiation Effects* 59.1-2 (1981), pp. 69–76. DOI: 10.1080/00337578108244199.
- [86] M. Kobayashi and M. Ishii. “Effect of cerium doping on the radiation hardness of gadolinium silicate Gd_2SiO_5 ”. In: *Nuclear Instruments and Methods in Physics Research Section B: Beam Interactions with Materials and Atoms* 82.1 (1993), pp. 85–90. DOI: 10.1016/0168-583X(93)95086-K.
- [87] Y. Chen, M.M. Abraham, and D.F. Pedraza. “Radiation damage in Al_2O_3 crystals implanted with 3.8 MeV Fe^{2+} ions”. In: *Nuclear Instruments and Methods in Physics Research Section B: Beam Interactions with Materials and Atoms* 59 (1991), pp. 1163–1166. DOI: 10.1016/0168-583X(91)95786-D.
- [88] M. Izerrouken and T. Benyahia. “Absorption and photoluminescence study of Al_2O_3 single crystal irradiated with fast neutrons”. In: *Nuclear Instruments and Methods in Physics Research Section B: Beam Interactions with Materials and Atoms* 268.19 (2010), pp. 2987–2990. DOI: 10.1016/j.nimb.2010.05.024.
- [89] M. Izerrouken, Y. Djouadi, and H. Zirour. “Annealing process of F^- and F^+ -centers in Al_2O_3 single crystal induced by fast neutrons irradiation”. In: *Nuclear Instruments and Methods in Physics Research Section B: Beam Interactions with Materials and Atoms* 319 (2014), pp. 29–33. DOI: 10.1016/j.nimb.2013.11.009.
- [90] Y.A. Ossipyan and S.Z. Shmurak. “Deformation luminescence and motion of charged dislocations in crystals”. In: *Defects in Insulating Crystals*. 1981.
- [91] J.C. Phillips. “Ionicity of the chemical bond in crystals”. In: *Reviews of Modern Physics* 42.3 (1970), p. 317. DOI: 10.1103/RevModPhys.42.317.
- [92] J.R. Chelikowsky and J.K. Burdett. “Ionicity and the structural stability of solids”. In: *Physical Review Letters* 56.9 (1986), p. 961. DOI: 10.1103/PhysRevLett.56.961.
- [93] A. Janotti and C.G. Van de Walle. “Fundamentals of zinc oxide as a semiconductor”. In: *Reports on Progress in Physics* 72.12 (2009), p. 126501. DOI: 10.1088/0034-4885/72/12/126501.
- [94] Ü. Özgür et al. “A comprehensive review of ZnO materials and devices”. In: *Journal of Applied Physics* 98.4 (2005), pp. 1–103. DOI: 10.1063/1.1992666.
- [95] R.M. Sahani and A. Dixit. “A comprehensive review on zinc oxide bulk and nano-structured materials for ionizing radiation detection and measurement applications”. In: *Materials Science in Semiconductor Processing* 151 (2022), p. 107040. DOI: 10.1016/j.mssp.2022.107040.

- [96] J. Wojnarowicz, T. Chudoba, and W. Lojkowski. “A review of microwave synthesis of zinc oxide nanomaterials: Reactants, process parameters and morphologies”. In: *Nanomaterials* 10.6 (2020), p. 1086. DOI: 10.3390/nano10061086.
- [97] N.H. Nickel and E. Terukov. *Zinc Oxide-A Material for Micro-and Optoelectronic Applications: Proceedings of the NATO Advanced Research Workshop on Zinc Oxide as a Material for Micro-and Optoelectronic Applications, held in St. Petersburg, Russia, from 23 to 25 June 2004*. Vol. 194. Springer Science & Business Media, 2006.
- [98] P.A. Rodnyi and I.V. Khodyuk. “Optical and luminescence properties of zinc oxide”. In: *Optics and Spectroscopy* 111.5 (2011), pp. 776–785. DOI: 10.1134/S0030400X11120216.
- [99] B. K Meyer et al. “Bound exciton and donor–acceptor pair recombinations in ZnO”. In: *Physica Status Solidi B* 241.2 (2004), pp. 231–260. DOI: 10.1002/pssb.200301962.
- [100] R. Dingle. “Luminescent transitions associated with divalent copper impurities and the green emission from semiconducting zinc oxide”. In: *Physical Review Letters* 23.11 (1969), p. 579. DOI: 10.1103/PhysRevLett.23.579.
- [101] Y.I. Alivov, M.V. Chukichev, and V.A. Nikitenko. “Green luminescence band of zinc oxide films copper-doped by thermal diffusion”. In: *Semiconductors* 38.1 (2004), pp. 31–35. DOI: 10.1134/1.1641129.
- [102] A.F. Kohan et al. “First-principles study of native point defects in ZnO”. In: *Physical Review B* 61.22 (2000), p. 15019. DOI: 10.1103/PhysRevB.61.15019.
- [103] B. Guo, Z.R. Qiu, and K.S. Wong. “Intensity dependence and transient dynamics of donor–acceptor pair recombination in ZnO thin films grown on (001) silicon”. In: *Applied Physics Letters* 82.14 (2003), pp. 2290–2292. DOI: 10.1063/1.1566482.
- [104] F.K. Shan et al. “Aging effect and origin of deep-level emission in ZnO thin film deposited by pulsed laser deposition”. In: *Applied Physics Letters* 86.22 (2005), p. 221910. DOI: 10.1063/1.1939078.
- [105] F. Leiter et al. “Oxygen vacancies in ZnO”. In: *Physica B: Condensed Matter* 340 (2003), pp. 201–204. DOI: 10.1016/j.physb.2003.09.031.
- [106] M. Liu, A.H. Kitai, and P. Mascher. “Point defects and luminescence centres in zinc oxide and zinc oxide doped with manganese”. In: *Journal of Luminescence* 54.1 (1992), pp. 35–42. DOI: 10.1016/0022-2313(92)90047-D.
- [107] D.C. Reynolds et al. “Time-resolved photoluminescence lifetime measurements of the Γ_5 and Γ_6 free excitons in ZnO”. In: *Journal of Applied Physics* 88.4 (2000), pp. 2152–2153. DOI: 10.1063/1.1305546.
- [108] T Batsch, B Bengtson, and M Moszyński. “Timing properties of a ZnO(Ga) scintillator (NE843)”. In: *Nuclear Instruments and Methods* 125.3 (1975), pp. 443–446. DOI: 10.1016/0029-554X(75)90262-1.
- [109] T. Yanagida et al. “Scintillation properties of in doped ZnO with different In concentrations”. In: *IEEE Transactions on Nuclear Science* 57.3 (2010), pp. 1325–1328. DOI: 10.1109/TNS.2009.2035120.
- [110] J.S. Neal et al. “Investigation of ZnO-Based Polycrystalline Ceramic Scintillators for Use as α -Particle Detectors”. In: *IEEE Transactions on Nuclear Science* 56.3 (2009), pp. 892–898. DOI: 10.1109/TNS.2008.2004702.
- [111] K. Ellmer and A. Klein. “ZnO and its applications”. In: *Transparent Conductive Zinc Oxide*. Springer, 2008, pp. 1–33.
- [112] M. Asadian. “Thermodynamic analysis of ZnO crystal growth from the melt”. In: *Journal of Crystallization Process and Technology* 3.3 (2013). DOI: 10.4236/jcpt.2013.33012.

-
- [113] E.V. Kortunova et al. “Hydrothermal synthesis of improved ZnO crystals for epitaxial growth of GaN thin films”. In: *Journal of Materials Science* 43.7 (2008), pp. 2336–2341. DOI: 10.1007/s10853-007-2036-5.
- [114] L. Grigorjeva et al. “Luminescence properties of ZnO nanocrystals and ceramics”. In: *IEEE Transactions on Nuclear Science* 55.3 (2008), pp. 1551–1555. DOI: 10.1109/TNS.2008.921931.
- [115] P.A. Rodnyi et al. “Novel scintillation material—ZnO transparent ceramics”. In: *IEEE Transactions on Nuclear Science* 59.5 (2012), pp. 2152–2155. DOI: 10.1109/TNS.2012.2189896.
- [116] E.I. Gorokhova et al. “Structural, optical, and scintillation characteristics of ZnO ceramics”. In: *Journal of Optical Technology* 78.11 (2011), pp. 753–760. DOI: 10.1364/JOT.78.000753.
- [117] P. Rodnyi et al. “Fast, efficient, and radiation hard ZnO:In ceramic scintillator”. In: *2019 IEEE International Conference on Electrical Engineering and Photonics (EExPolytech)*. IEEE, 2019, pp. 197–200. DOI: 10.1109/EExPolytech.2019.8906846.
- [118] R. German. *Sintering: from empirical observations to scientific principles*. Butterworth-Heinemann, 2014.
- [119] J. Binner and T. Murthy. “Structural and thermostructural ceramics”. In: *Encyclopedia of Materials: Technical Ceramics and Glasses*. Elsevier Masson, 2021, pp. 3–24.
- [120] M. Pomeroy. *Encyclopedia of materials: technical ceramics and glasses*. Elsevier, 2021.
- [121] C. Hu et al. “Developments in hot pressing (HP) and hot isostatic pressing (HIP) of ceramic matrix composites”. In: *Advances in Ceramic Matrix Composites*. Elsevier, 2014, pp. 177–202.
- [122] V.A. Demidenko et al. “Scintillation properties of ceramics based on zinc oxide”. In: *Radiation Measurements* 42.4-5 (2007), pp. 549–552. DOI: 10.1016/j.radmeas.2007.01.050.
- [123] E.I. Gorokhova et al. “Optical, luminescence, and scintillation properties of ZnO and ZnO:Ga ceramics”. In: *Journal of Optical Technology* 75.11 (2008), pp. 741–746. DOI: 10.1364/JOT.75.000741.
- [124] P.A. Rodnyi et al. “Scintillating ceramics based on zinc oxide”. In: *IOP Conference Series: Materials Science and Engineering*. Vol. 38. 1. IOP Publishing, 2012, p. 012002. DOI: 10.1088/1757-899X/38/1/012002.
- [125] L. Grigorjeva et al. “The luminescence of ZnO ceramics”. In: *Radiation Measurements* 45.3-6 (2010), pp. 441–443. DOI: 10.1016/j.radmeas.2010.03.012.
- [126] L. Grigorjeva et al. “Radioluminescence, thermoluminescence and dosimetric properties of ZnO ceramics”. In: *Ceramics International* 43.8 (2017), pp. 6187–6191. DOI: 10.1016/j.ceramint.2017.02.016.
- [127] GSI — GSI Helmholtzzentrum für Schwerionenforschung GmbH. <https://www.eljentechnology.com/>. Accessed: 2023-07-19.
- [128] B. Speit et al. “Radiation resistant optical glasses”. In: *Nuclear Instruments and Methods in Physics Research Section B: Beam Interactions with Materials and Atoms* 65.1-4 (1992), pp. 384–386. DOI: 10.1016/0168-583X(92)95071-X.
- [129] TIE-42. *Radiation resistant optical glasses*. Technical Information, Advanced Optics. Version April 2018.
- [130] C. Hubert. “Characterization of radiation damage induced by swift heavy ions in graphite”. PhD thesis. Technische Universität Darmstadt, 2016.
- [131] P. Bolz. “Analyzation of radiation resistance of carbon-based materials for accelerator components”. PhD thesis. Technische Universität Darmstadt, 2023, p. 138. DOI: 10.26083/tuprints-00023113.

-
- [132] H. Geissel et al. “Experimental studies of heavy-ion slowing down in matter”. In: *Nuclear Instruments and Methods in Physics Research Section B: Beam Interactions with Materials and Atoms* 195.1-2 (2002), pp. 3–54. DOI: 10.1016/S0168-583X(02)01311-3.
- [133] A. Romanenko. “Radiation damage produced by swift heavy ions in rare earth phosphates”. PhD thesis. Technische Universität Darmstadt, 2016.
- [134] *PCO 1600 data sheet*. https://www.pco.de/fileadmin/user_upload/pco-product_sheets/pco.1600_2000_4000_data_sheet.pdf. Accessed: 2021-09-09.
- [135] *PCO SensiCam QE data sheet*. https://www.pco.de/fileadmin/user_upload/db/products/datasheet/sensicam_qe_20080624.pdf. Accessed: 2021-09-09.
- [136] G.F. Knoll. *Radiation detection and measurement*. John Wiley & Sons, 2010.
- [137] H. Reeg. “A current digitizer for ionisation chambers/SEMs with high resolution and fast response”. In: *DIPAC Proceedings*. Chester, UK, 1999, p. 147.
- [138] P. Forck. *Lecture notes on beam instrumentation and diagnostics*. English. 2011. 152 pp. URL: https://www-bd.gsi.de/conf/juas/juas_script.pdf.
- [139] P. Boutachkov et al. “In-beam tests of the new secondary electron detector for FAIR”. In: *GSI Scientific Report* (2017), p. 465. DOI: 10.15120/GR-2017-1.
- [140] V. Baglin et al. *The secondary electron yield of technical materials and its variation with surface treatments*. Technical Report. 2000.
- [141] W.E. Vehse et al. “Radiation damage in ZnO single crystals”. In: *Physical Review* 167.3 (1968), p. 828. DOI: 10.1103/PhysRev.167.828.
- [142] X.D. Wang et al. “Space radiation damage in ZnO induced by subthreshold electrons: Defect identity and optical degradation”. In: *Radiation Research* 176.2 (2011), pp. 264–268. DOI: 10.1667/RR2518.1.
- [143] V. Russo et al. “Multi-wavelength Raman scattering of nanostructured Al-doped zinc oxide”. In: *Journal of Applied Physics* 115.7 (2014), p. 073508. DOI: 10.1063/1.4866322.
- [144] C. Bundesmann et al. “Raman scattering in ZnO thin films doped with Fe, Sb, Al, Ga, and Li”. In: *Applied Physics Letters* 83.10 (2003), pp. 1974–1976. DOI: 10.1063/1.1609251.
- [145] C. Trautmann et al. “Damage structure in the ionic crystal LiF irradiated with swift heavy ions”. In: *Nuclear Instruments and Methods in Physics Research Section B: Beam Interactions with Materials and Atoms* 164 (2000), pp. 365–376. DOI: 10.1016/S0168-583X(99)01066-6.
- [146] E. Gardès et al. “SPORT: A new sub-nanosecond time-resolved instrument to study swift heavy ion-beam induced luminescence—Application to luminescence degradation of a fast plastic scintillator”. In: *Nuclear Instruments and Methods in Physics Research Section B: Beam Interactions with Materials and Atoms* 297 (2013), pp. 39–43. DOI: 10.1016/j.nimb.2012.12.039.
- [147] *SCHOTT — BK7G18 520636.252 glass data sheet*. <https://www.schott.com/shop/advanced-optics/en/Optical-Glass/BK7G18/c/glass-BK7G18>. Accessed: 2023-09-04.
- [148] S. Nayar, K. Ikeuchi, and T. Kanade. “Surface reflection: physical and geometrical perspectives”. In: *Proceedings: Image Understanding Workshop*. 1990, pp. 185–212. DOI: 10.1109/34.85654.
- [149] A. Levin and Ch. Moisan. “A more physical approach to model the surface treatment of scintillation counters and its implementation into DETECT”. In: *1996 IEEE Nuclear Science Symposium. Conference Record*. Vol. 2. IEEE. 1996, pp. 702–706. DOI: 10.1109/NSSMIC.1996.591410.

Appendixes

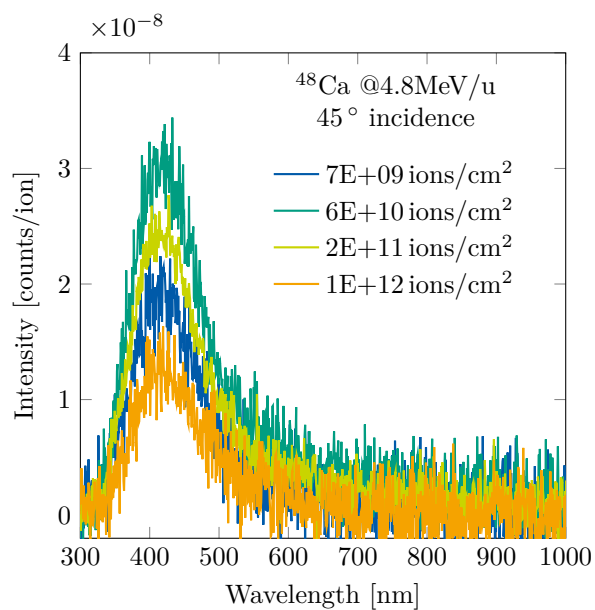
A1 Luminescent properties of BK7G18 exposed to heavy-ion beams

Figure A1.1 shows the luminescence spectra of the BK7G18 glass under excitation with different ion species and fluences, as well as the X-ray-induced luminescence before and after ion bombardment. The luminescence spectra have a single band with a maximum intensity located around 400–420 nm. It is worth noting, that the BK7G18 glass luminescence emission intensity is more than 10 times weaker compared to ZnO-based ceramic scintillators (see Figure A1.3b). X-ray-induced luminescence characterization of irradiated samples was performed approximately one year after ion irradiation. Compared to ionoluminescence measurements, the X-ray-induced luminescence spectra indicate possible self-recovery within one year after ion exposure.

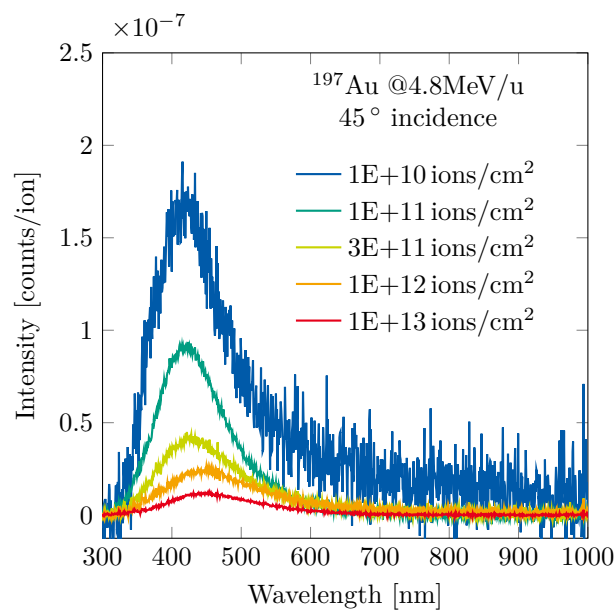
As a result of the heavy-ion irradiation, no new emission bands are formed. The intensity of the emission band first increases by a factor of twos, reaching maximum intensity at approximately 10^{10} ions/cm², or 7×10^{10} ions/cm² fluence of 4.8 MeV/u ¹⁹⁷Au, or ⁴⁸Ca, respectively. Then, the luminescence intensity reduces when further increasing the fluence. Within the investigated range of fluences, the wavelength of the maximum emission intensity remains unchanged up to 10^{12} Ca-ions/cm², 10^{11} Au-ions/cm², and 8×10^{11} Bi-ions/cm². For the Au irradiation the emission wavelength shifts from 420 to 450 nm in the fluence range from 10^{11} to 10^{12} ions/cm². Figure A1.2 shows the evolution of the intensity and position wavelength of the luminescence peak as a function of fluence for BK7G18 sample exposed to different heavy-ion species.

BK7G18 glass exposure to heavy ions stimulates the formation of defects in the glass matrix. Some defects absorb energy deposited by the incident ions and subsequently emit luminescent light. Meanwhile, other defects absorb the luminescent light photons without further light emission. As the irradiation fluence increases, the number of these two defect types in the glass also increases. As a result of a complex interplay of different defect types, ion irradiation at lower fluences leads to an increase in the measured ionoluminescence intensity. However, at higher fluences, the number of defects becomes so numerous that they interact with each other and interfere with the ion-induced luminescent process, causing a decrease in the measured ionoluminescence intensity.

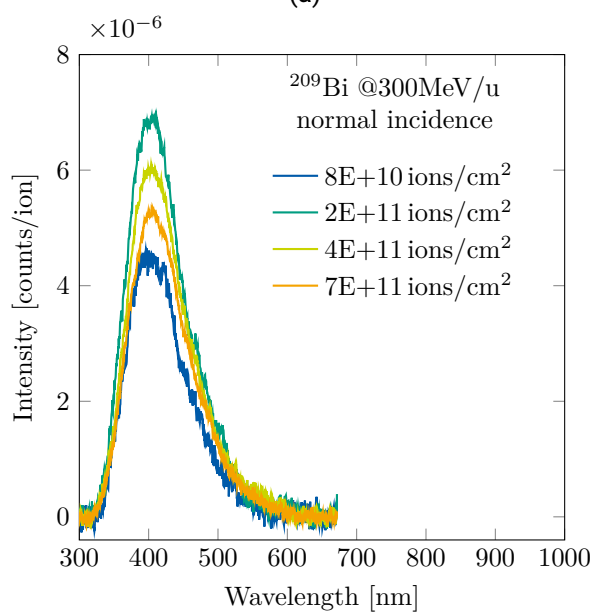
BK7G18 glass exhibits two luminescence decay components, with decay times of the order of 4.64 ns (80 % of the light) and 36.13 ns (20 % of the light). The luminescence kinetics of the pristine BK7G18 measured using X-rays and the two-exponential decay fit curve are shown in Figure A1.3a. Also, typical BK7G18 slow PMT signals in comparison to initial and thermally-treated ZnO(In) are shown in Figure A1.3b.



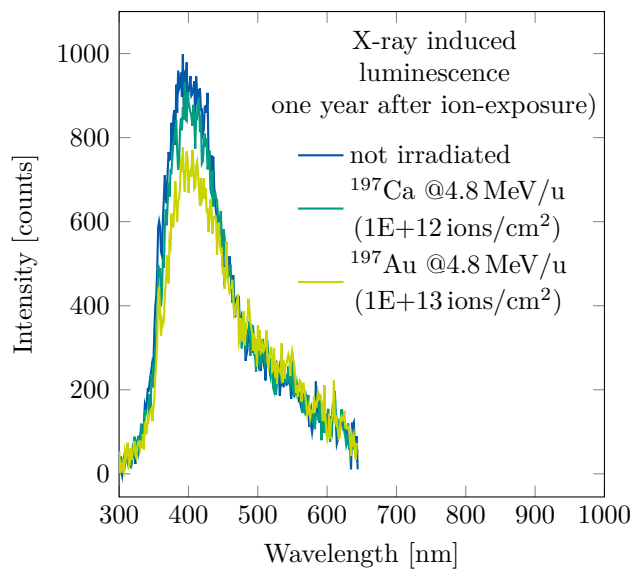
(a)



(b)

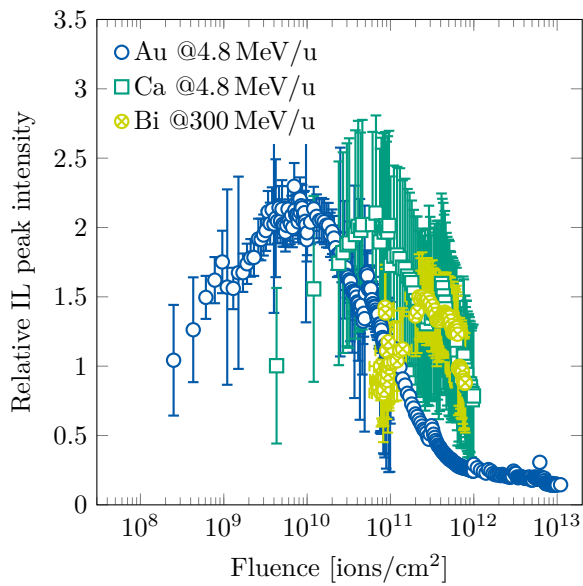


(c)

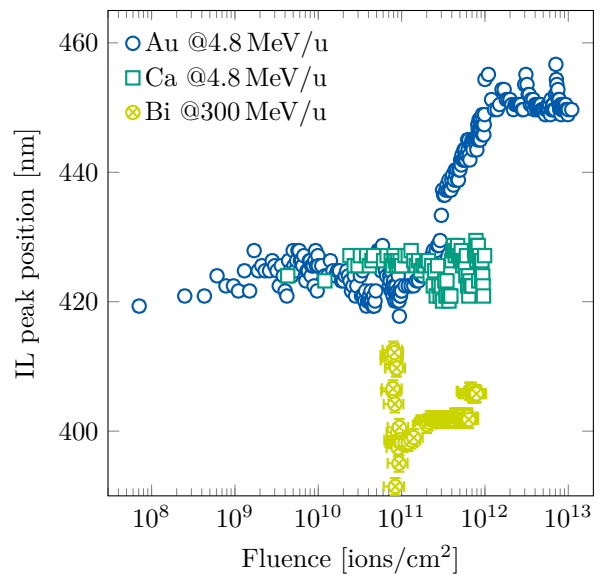


(d)

Figure A1.1: Ion-induced luminescence spectra of BK7G18 borosilicate glass exposed to 4.8 MeV/u Ca (a), Au (b), and 300 MeV/u Bi (c) ions at various fluences, and X-ray-induced luminescence spectra of pristine and ion-irradiated BK7G18 samples (d). X-ray-induced luminescence spectra (d) were measured one year after ion exposure.

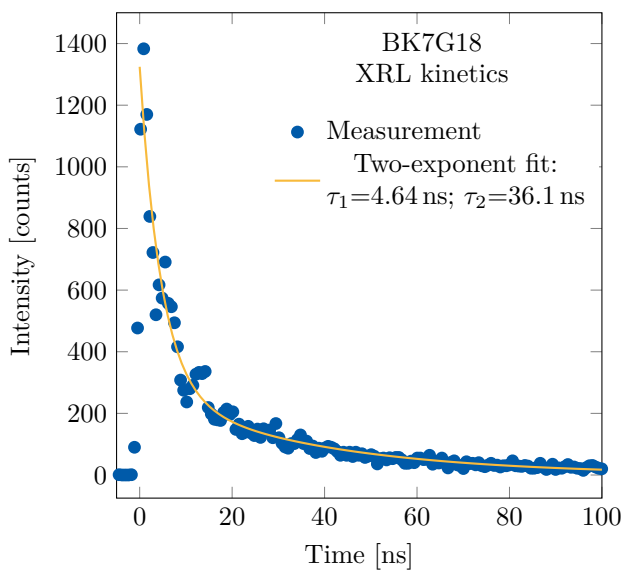


(a)

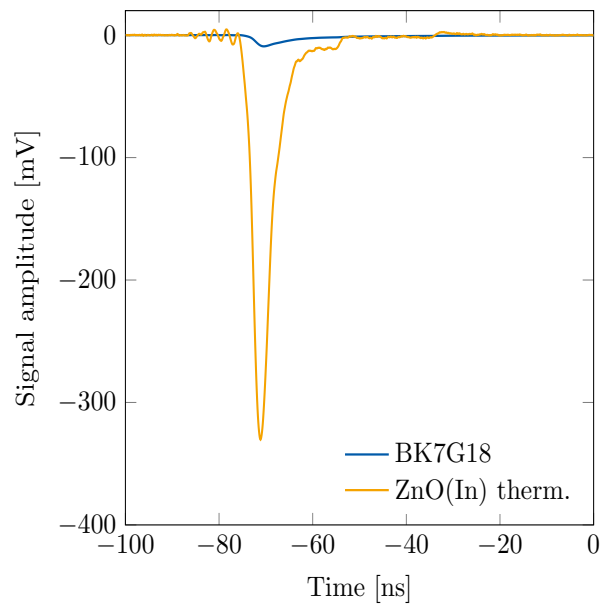


(b)

Figure A1.2: Relative intensity (a) and wavelength (b) changes of BK7G18 borosilicate glass ionoluminescence as a function of fluence of various heavy ions.



(a)



(b)

Figure A1.3: X-ray-induced luminescence kinetics of BK7G18 glass (a) and typical photomultiplier signals due to a heavy-ion impact in BK7G18 in comparison to ZnO(In) scintillating ceramics (b).

A2 Optical transmission of BK7G18 exposed to heavy-ion beams

The material exhibits high tolerance of optical transmission properties to heavy ion exposure, as presented in Figure A2.1. Transmission at 390–400 nm wavelength is reduced roughly from 90% to 80% due to 4.8 MeV/u ^{197}Au ion irradiation, which is negligible compared to the loss of light output registered in ZnO-based ceramics at a similar fluence (for example, see Figure 5.10).

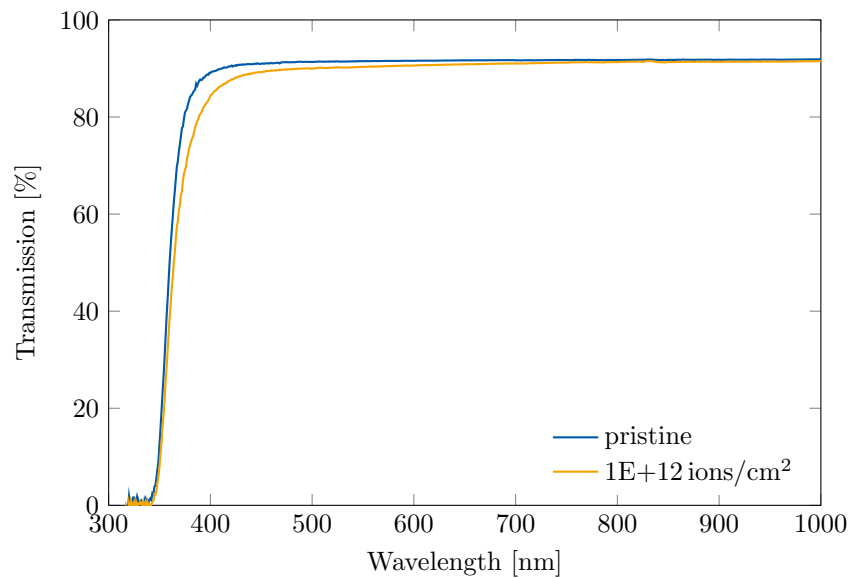


Figure A2.1: Optical transmission spectra of pristine and 4.8 MeV/u Au ion irradiated BK7G18 glass.

Curriculum Vitae

Maxim Saifulin

Born 16.07.1991 in Astana, Kazakhstan
E-Mail: M.Saifulin@gsi.de

Education

Doctoral studies

2019 – 2023: Technical University Darmstadt (Darmstadt, Germany)

Master studies

2014 – 2016: Dubna State University (Dubna, Russia)

Bachelor studies

2013 – 2014: Dubna State University (Dubna, Russia)

2009 – 2014: L.N. Gumilyov Eurasian National University (Astana, Kazakhstan)

Awards

Giersch grant for PhD students, 2020

Publications

- **M. Saifulin**, P. Boutachkov, E. Gorokhova, P. Rodnyi, C. Trautmann, I. Venevtsev, and B. Walasek-Höhne “Multi-tile zinc-oxide-based radiation-hard fast scintillation counter for relativistic heavy-ion beam diagnostics: prototype design and test” *Journal of Physics: Conference Series*, 2023 (in press).
- **M. Saifulin**, P. Boutachkov, E. Gorokhova, P. Rodnyi, P. Simon, C. Trautmann, I. Venevtsev, and B. Walasek-Höhne “Ionoluminescence and optical transmission investigation of ZnO(In) fast ceramic scintillator irradiated with swift heavy ions” *Journal of Applied Physics*, **132**, 195901 (2022), DOI: 10.1063/5.0110205.
- **M. Saifulin**, P. Boutachkov, C. Trautmann, B. Walasek-Höhne, P. Rodnyi, I. Venevtsev, and E. Gorokhova “ZnO(In) scintillation light spectra investigation for heavy ion detector application” *In Proceedings of the 11th International Beam Instrumentation Conference IBIC2022*, Krakow, Poland, JACoW Publishing, 2022, DOI: 10.18429/JACoW-IBIC2022-TUP29.

-
- P. Boutachkov, **M. Saifulin**, C. Trautmann, B. Walasek-Höhne, E.I. Gorokhova, P. Rodnyi, and I. Venevtsev “Novel fast radiation-hard scintillation detectors for ion beam diagnostics” *In Proceedings of the 11th International Beam Instrumentation Conference IBIC2022*, Krakow, Poland, JACoW Publishing, 2022, DOI: 10.18429/JACoW-IBIC2022-WE3I1.
 - P. Rodnyi, I. Venevtsev, E. Gorokhova, S. Eron’ko, P. Boutachkov, and **M. Saifulin** “Fast, Efficient, and Radiation Hard ZnO:In Ceramic Scintillator” *In Proceedings of the 2019 IEEE International Conference on Electrical Engineering and Photonics (EExPolytech)*, St. Petersburg, Russia, IEEE, 2019, DOI: 10.1109/EExPolytech.2019.8906846.
 - P. Boutachkov, A. Reiter, **M. Saifulin**, B. Walasek-Höhne, E. Gorokhova, P. Rodnyi, and I. Venevtsev “Radiation hardness investigation of zinc oxide fast scintillators with relativistic heavy ion beams” *In Proceedings of the 8th International Beam Instrumentation Conference IBIC2019*, Malmö, Sweden, JACoW Publishing, 2019, DOI: 10.18429/JACoW-IBIC2019-MOPP005.

Acknowledgements

The completion of this PhD thesis would have been unimaginable without the unwavering support of numerous people. I would like to express my heartfelt gratitude to all those who have provided guidance, inspiration, and support throughout this academic journey.

First and foremost, I extend my deepest thanks to my doctoral mother, Prof. Dr. Christina Trautmann, for granting me the invaluable research opportunity to undertake this PhD thesis. Your expertise, encouragement, and insightful feedback have been instrumental in shaping the direction and quality of my work.

I would also like to express my deep respect and appreciation to Dr. Plamen Boutachkov for his exceptional supervision and transfer of precious research experience. Your expertise, understanding, generous guidance, and continuous support have been readily available to me, and I am truly grateful for the invaluable guidance you have provided!

My gratitude also goes to Dr. Peter Forck, my mentor at the HGS-HIRe Graduate School. Your expertise in beam instrumentation and your willingness to share your knowledge has greatly contributed to my growth as a scientist.

Beata Walasek-Höhne and Dr. Marcus Schwickert deserve my gratitude for providing an excellent working environment within the GSI beam diagnostic group. Your efforts fostered a positive and supportive atmosphere, allowing me to focus on my research with enthusiasm and dedication.

I would like to express my sincere acknowledgment to Prof. Dr. Ralph Krupke, Prof. Dr. Adrian Finch, and Prof. Dr. Jan Philipp Hofmann for their kindness and willingness to serve as members of my PhD examination board. In particular, I am grateful to Prof. Trautmann and Prof. Krupke for their roles as referees for this thesis.

I would like to thank Dr. Piotr Rodnyi, Dr. Elena Gorokhova, and Dr. Ivan Venevtsev for their invaluable contributions, particularly considering the global challenges and obstacles that arose during the course of this project. I am especially grateful for their dedicated efforts in synthesizing scintillating ceramic samples, which served as the decisive component for my PhD work.

My appreciation also goes to Dr. Rahul Singh for his interest in my work, for engaging in discussions during group seminars, and for his willingness to offer assistance with constructive advice when needed.

A special word of thanks goes to PhD students of the beam diagnostics department. My office mates: Jiangyan, Philipp, Lorenzo, and Dr. David Haider. The pleasant moments we shared at work and leisure time will always be cherished. I wish each of you continued success in your research endeavors.

I acknowledge DLR for the funding provided under the ERA.NET RUS Plus Project number RUS_ST2017-051. I thank GSI for their financial support within the F&E projects “Radiation hard scintillators for FAIR” and “Particle counter for the HEBT section of FAIR”. Furthermore, I am grateful to the HGS-HIRe graduate school for its soft-skill courses and financial support dedicated to attending conferences.

I express my deepest appreciation to my parents, who have played an extraordinary role in shaping the person I am today. Their sacrifices, guidance, and belief in my abilities have been the driving force behind my academic achievements. I am forever grateful for their tireless care and dedication, without which this journey would not have been possible.

Lastly, I express my deepest appreciation to my wife Daria for her unwavering support and understanding throughout this thesis. Her willingness to listen to my complaints, share my challenges and excitement, and believe in my abilities were invaluable. To my precious daughter Maria, who brings joy to my life every day, thank you for your bright smiles and for helping me forget all my research worries.

To all those mentioned above and to those who may not have been explicitly named, I am forever grateful for your belief in my abilities and for being an integral part of my academic journey. Your contributions have left an indelible mark on my personal and professional growth.

Thank you all from the bottom of my heart!